NMR-spektroskopische Untersuchungen der Adsorptionsprozesse in porösen Funktionsmaterialien mittels hyperpolarisiertem ^{129}Xe

Dissertation

zur Erlangung des akademischen Grades eines
Doktors der Naturwissenschaften (Dr. rer. nat.)
an der Fakultät für Biologie, Chemie und Geowissenschaften
der Universität Bayreuth

Vorgelegt von

Tobias Willi Kemnitzer
aus Hof
Bayreuth, 2023

Die vorliegende Arbeit wurde in der Zeit von Januar 2014 bis September 2019 in Bayreuth am Lehrstuhl für Anorganische Chemie III unter Betreuung von Herrn Professor Dr. Jürgen Senker angefertigt.

Vollständiger Abdruck der von der Fakultät für Biologie, Chemie und Geowissenschaften der Universität Bayreuth genehmigten Dissertation zur Erlangung des akademischen Grades eines Doktors der Naturwissenschaften (Dr. rer. nat.)

Art der Dissertation: Kumulative Dissertation
Dissertation eingereicht am: 30.10.2023
Zulassung durch die Promotionskommision: 08.11.2023
Wissenschaftliches Kolloquium: 21.06.2024

Amtierender Dekan: Prof. Dr. Cyrus Samimi

Prüfungsausschuss:
Prof. Dr. Jürgen Senker (Gutachter)
Prof. Dr. Josef Breu (Gutachter)
Prof. Dr. Anna Schenk (Vorsitz)
Prof. Dr. André Gröschel

Der Beginn aller Wissenschaft ist das Erstaunen,
dass die Dinge sind, wie sie sind.

- Aristoteles

Danksagung

An erster Stelle möchte ich mich ganz besonders bei meinem Doktorvater Prof. Dr. Jürgen Senker bedanken, nicht nur für die Möglichkeit der Promotion in einem solch spannenden Forschungsthema, auch für die aufmerksame Betreuung, sowie der Freiheiten, die er seinen Doktoranden einräumt. Bei Fragen stand er mir stets mit Rat zur Seite und gab mir die Möglichkeit, mich wissenschaftlich aber auch persönlich weiterzuentwickeln.

Zudem bedanke ich mich bei Dr. Caroline Keenan und Robert Stäglich für die Zusammenarbeit in diesem Forschungsthema. Die gemeinsame Arbeit war geprägt von Geduld, regem Austausch und einer freundschaftlichen Atmosphäre, in der immer Zeit für Fragen und Diskussionen war.

Ich danke Dr. Renée Siegel für die technische Unterstützung rund um NMR-Spektroskopie und die allabendlichen Gespräche, sowie die konstante Versorgung mit Schokolade.

Ebenso möchte ich mich bei allen Kollegen und Freunden, besonders aus den Lehrstühlen AC I und AC III bedanken, für die schöne gemeinsame Zeit, die fachlichen, sowie fachfremden Diskussionen und die Freundschaften, die bis heute noch andauern. Danke Beate und Helen für die angenehme Zeit im Büro und der B7. Danke Marion, für die unterhaltsamen Kaffeepausen und die gemeinsamen Spieleabende. Danke Dominik, für die jahrelange Freundschaft, über das Studium und die Promotion hinaus und die schönen Terrassenabende. Danke Thomas, für die fachliche und praktische Unterstützung in der Laborarbeit. Danke Wolfgang, für die engagierte Unterstützung in kristallographischen Themen. Danke Christoph, Adrian, Carsten, Lisa, Kevin, Katja, Thomas, Simon, Kasper und alle die ich namentlich nicht genannt habe. Danke an meine Studierenden, die ich während meiner Zeit an der Universität Bayreuth betreuen durfte.

Ich möchte mich auch bei allen Freunden und Kollegen der Studiobühne Bayreuth und der Sübkültür bedanken. Das gemeinsame Schaffen in der Kulturlandschaft Bayreuths war für mich immer eine angenehme Abwechslung zum Universitätsalltag.

Ein großer Dank geht an meine Familie und meine Freunde für die viele Unterstützung. Danke an Stephen für die vielen wertvollen Gespräche. Vor allem danke ich meiner Mutter, die mich in jeder Lebenslage unterstützt hat, immer ein offenes Ohr hatte und mich stets bekräftigte, meinen eigenen Weg zu gehen.

Inhaltsverzeichnis

Abkürzungsverzeichnis

2D-EXSY	2D Exchange Spectroscopy
CAU	Christian-Albrechts-Universität
CF	Continuous Flow
COPD	Chronic obstructive pulmonary disease
CSA	Chemical Shift Anisotropy
DFT	Density Functional Theory
GIPAW	Gauge-including projector augmented Wave
HP	Hyperpolarisiert
IBU	Inorganic Building Unit
IR	Infrarot
IRMOF	Isoreticular Metalorganic Framework
MAS	Magic Angle Spinning
MIL	Matériaux de l’Insitute Lavoisier
MOF	Metalorganic Framework
MPR	Magnetization Production Rate
MRI / MRT	Magnet Resonance Imaging
NLDFT	Non-local Density Functional Theory
NMR	Nuclear Magnetic Resonance
PBE	Perdew-Burke-Ernzerhof
PXRD	Powder X-Ray Diffraction
QCPMG	Quadrupolar Carr-Purcell-Meiboom-Gill
SEOP	Spin Exchange Optical Pumping
UV-VIS	Ultraviolett – Sichtbares (Visible) Licht
VT-NMR	Variable Temperature NMR

Zusammenfassung

Diese Arbeit beschäftigt sich mit der Nutzung von hyperpolarisiertem ^{129}Xe für die NMR-spektroskopische Analyse des Porenraumes und Adsorptionsprozessen von Xe innerhalb der aluminiumbasierten MOFs CAU-1 und MIL-53, sowie poröser Silicahohlkugeln. Für die Anwendung von ^{129}Xe-NMR-Spektroskopie zur Analyse von Porenräumen gibt es zum Stand der bisherigen Forschung keine allgemeingültigen Analysemodelle. Daher wurden die genannten MOFs als Modellsubstanzen genutzt, um Effekte wie lokale Ordnung und bevorzugte Adsorptionspositionen, sowie die Flexibilität des Wirtsnetzwerks zu untersuchen. Die experimentellen Daten wurden hierbei mit aus DFT-Rechnungen erhaltenen NMR-Parametern verglichen. Diese sind unter Zuhilfenahme von Modellstrukturen erzeugt worden, um einen direkten Zusammenhang zwischen ^{129}Xe Shift und den strukturellen Eigenschaften eines porösen Materials herzustellen.

Im ersten Teil der Arbeit wurde ein an der Universität Bayreuth entwickelter ^{129}Xe-Polarisator in seinem Aufbau und Betrieb optimiert, um eine maximale ^{129}Xe Polarisation bei möglichst hoher Produktionsrate zu erzeugen. Dieser zeichnet sich durch seine einzigartigen Charakteristika einer zweischenkligen Pumpzelle, sowie eines separaten Rb-Reservoirs aus. Durch die gezielte Optimierung einer Vielzahl von Parametern, wie Laserleistung, Gasdruck und Rb-Beladung konnte eine maximale ^{129}Xe Kernspinpolarisation von 22 % erreicht werden. Die über Stunden konstante Polarisation konnten wir erfolgreich für 2D-EXSY Experimente unter stop-and-flow Bedingungen für die Modellsubstanz CAU-1-AmMe nutzen.

Hyperpolarisiertes ^{129}Xe wurde anschließend genutzt, um die Porosität von Silicahohlkugeln in Abhängigkeit der Kalzinierungstemperatur zu charakterisieren. Die Silicahohlkugeln wurden zum Entfernen des Polymerkerns im Temperaturbereich von 500 °C bis 950 °C kalziniert, wobei sich mit steigender Temperatur der Quervernetzungsgrad des Silica erhöht und das Mikroporenvolumen abnimmt. Bei maximaler Kalzinierungstemperatur wurde hierbei noch eine geringe Menge an Mikroporen nachgewiesen, die in N_2-Physisorptionsexperimenten nicht mehr aufgelöst werden konnte.

Im folgenden Teil dieser Arbeit wurde ^{129}Xe-NMR-Spektroskopie verwendet, um ein besseres Verständnis der Adsorptionsprozesse in MOFs zu gewinnen und die Wirkung von Netzwerkveränderungen auf die chemische Verschiebung von ^{129}Xe zu untersuchen.

Wir haben den MOF CAU-1, sowie zwei postsynthetische Modifikationen CAU-1-AmMe und CAU-1-UrMe hinsichtlich lokaler Ordnung, sowie bevorzugter Adsorptionspositionen untersucht. Durch die Kombination gemessener ^{129}Xe-NMR Spektren und der Berechnung von ^{129}Xe Shifts mittels DFT-Methoden wurden bevorzugte Adsorptionspositionen für Xe im Zentrum der Tetraederpore von CAU-1 ermittelt. Die Berechnung eines Boltzmann-gewichteten Mittelwerts des ^{129}Xe Shifts über alle Adsorptionspositionen zeigte eine gute Übereinstimmung

mit den experimentellen Werten in Temperaturbereichen, in denen Xe-Xe-Wechselwirkungen vernachlässigt werden konnten. Darüber hinaus lieferten die Ergebnisse das Verhältnis von adsorbiertem Xe in Tetraeder und Oktaederpore des Netzwerks in Abhängigkeit der Umgebungstemperatur. Die postsynthetische Modifikation von CAU-1 zur Verkleinerung des Porenraumes verlagerte den experimentellen ^{129}Xe Shift mit längeren Seitengruppen schrittweise zu höheren Werten.

Anhand des zweiten Modellsystems MIL-53 wurde die Bi-Stabilität dieses Netzwerks, sowie die Austauschdynamik mittels ^{129}Xe untersucht. Die Adsorption von Xe durch Verringerung der Temperatur oder Erhöhen des Drucks bewirkt einen Übergang der kanalförmigen Poren von der offenen in die geschlossene Form. ^{129}Xe-NMR Spektren erhielten dadurch eine charakteristische CSA und änderten mit höherer Beladung ihr Vorzeichen. Diese CSA konnte durch isolierte Xe-Atome in den Poren nicht simuliert werden und zeigte einen starken Effekt von Xe-Xe-Wechselwirkungen. Für beide Signaturen konnten passende NMR-Parameter durch Strukturmodelle von Xe in den Poren ermittelt werden. 2D-EXSY Experimente von ^{129}Xe im Temperaturbereich, in dem beide Netzwerkformen koexistieren und die daraus ermittelten Diffusionsgeschwindigkeiten von Xe zwischen offener und geschlossener Form zeigten, dass der Übergang nicht schlagartig stattfindet, sondern sich Domänen beider Formen innerhalb eines Kristallits bilden.

Die hier dargestellten Ergebnisse demonstrierten die Erzeugung von hyperpolarisiertem ^{129}Xe mit hoher Polarisation, sowie die erfolgreiche Anwendung in der Analyse poröser Funktionsmaterialien, wobei neue Methoden zur Analyse des Porenraumes mittels ^{129}Xe-NMR-Spektroskopie entwickelt werden konnten.

Abstract

This work deals with the usage of hyperpolarized ^{129}Xe for the NMR spectroscopic analysis of the pore space and adsorption processes of ^{129}Xe within the Al-based MOFs CAU-1 and MIL-53, as well as porous silica hollow spheres. For the application of ^{129}Xe-NMR spectroscopy, there are no state of the art analysis models available. Therefore, the aforementioned MOFs were used as model substances to investigate effects such as local order, preferred adsorption sites, as well the hosts network flexibility. The experimental data was compared with NMR parameters obtained from DFT calculations, which were generated using model structures to establish a direct relationship between ^{129}Xe shift and the structural properties of a porous material.

In the first part of the work, the polarizer developed at University of Bayreuth was improved in its design and operation to produce maximum ^{129}Xe polarization together with high production rates. This apparatus is characterized by its unique design of the two-bodied pumping cell, as well as a separate Rb reservoir. A maximum polarization of 22% was achieved by optimizing a number of parameters, such as laser power, operating pressure and Rb loading. By keeping the polarization constant for hours we were able to use it for 2D-EXSY experiments under stop-and-flow conditions for the model substance CAU-1-AmMe.

Hyperpolarized ^{129}Xe was then used to characterize the porosity of hollow silica nanospheres as a function of calcination temperature. The hollow silica spheres were calcined in order to remove the polymer core at a temperature range from 500 °C to 950 °C. The degree of cross-linking of the silica increases and the micropore volume decreases with rising temperature. At maximum calcination temperature, a small amount of micropores was still detected, which could no longer be resolved in N_2-physisorption experiments.

In the following part of this work, ^{129}Xe NMR spectroscopy was used to gain a better understanding of the adsorption processes in MOFs and investigate the effect of network changes on the chemical shift of ^{129}Xe.

We investigated the MOF CAU-1, as well as two modifications CAU-1-AmMe and CAU-1-UrMe with respect to local order, as well as preferred adsorption sites. The combination of measured ^{129}Xe NMR spectra and the calculation of ^{129}Xe shifts using DFT methods, preferred adsorption positions for Xe in the center of the tetrahedral pore of CAU-1 were determined. The calculation of a Boltzmann-weighted average ^{129}Xe NMR shift over all adsorption positions showed good agreement with experimental values in temperature ranges where Xe-Xe interactions could be neglected. Furthermore, the results provided the ratio of adsorbed Xe in tetrahedral and octahedral pore of the network as a function of ambient temperature.

The post-synthetic modification of CAU-1 reduced the accessible pore space gradually and moved the experimental ^{129}Xe shift downfield with longer side chains.

Based on the model system MIL-53, the bi-stability of two forms of the network as well adsorption dynamics were investigated using ^{129}Xe. Adsorption of Xe at low temperatures or high pressure causes a transition of the channel-shaped pores from the open to the closed form. ^{129}Xe-NMR spectra of the closed form acquired a characteristic CSA pattern which changes its sign with higher loading. The unique lineshape could not be simulated by isolated Xe atoms within the pores proving a strong effect of Xe-Xe interactions. For both lineshapes, suitable NMR parameters could be determined using structural models of Xe in the pores. 2D-EXSY experiments of ^{129}Xe as well as resulting diffusion velocities in the temperature range, where both network forms coexist reveals that the transition between open and closed form does not occur abruptly but domains form within a crystallite.

This works findings demonstrate the generation of hyperpolarized ^{129}Xe with high polarization and its successful application in analyzing porous functional materials. New methods for pore space analysis using ^{129}Xe NMR spectroscopy were developed as a result.

1. Einleitung

Die Materialklasse der porösen Funktionsmaterialien, wie Silicate, MOFs oder poröser organischer Netzwerke bietet eine große potentielle Anwendungsbreite aufgrund porenspezifischer Eigenschaften.[1–3] Da hier sowohl die strukturelle, morphologische und chemische Funktionalität sehr präzise den gewünschten Anwendungen angepasst werden kann, handelt es sich um auf die gewünschten Anwendungen maßgeschneiderte Stoffe. Vor allem die Materialklasse der metallorganischen Gerüstverbindungen (MOFs) wird aufgrund ihrer hohen strukturellen Variabilität, dem geringen Materialgewicht und der einfachen chemischen Funktionalisierbarkeit intensiv untersucht. Die Anwendungsgebiete reichen hier von Gasspeicherung und Trennung[4–13], Drug Delivery[14–18] und Sensorik[19–22] bis zur Katalyse[23–26]. Um die Eigenschaften solcher Materialien noch besser verstehen zu können, ist ein genaues Wissen über die Dynamik und strukturelle Ordnung im Innern des Porenraumes von großer Bedeutung. Methoden wie Kristallstrukturanalysen und Gasphysisorption stellen hierbei die wichtigsten Instrumente zur Porencharakterisierung dar. Diese Bulk-Methoden analysieren die Materialeigenschaften aber nur als Ganzes. Lokale Unterschiede wie Fehlordnungen oder die Ermittlung von Diffusionswegen und Adsorptionsplätzen innerhalb des porösen Netzwerks können auf diese Weise nur begrenzt dargestellt werden.[27]

Um diese Lücke zu schließen bietet sich hier die Anwendung von NMR-Spektroskopie unter Anwendung von gasförmigem, hyperpolarisiertem ^{129}Xe an. ^{129}Xe als NMR-aktiver Kern kann aufgrund seiner guten Adsorptionseigenschaft, des inerten Charakters, sowie einer auf die Gasumgebung sehr empfindlich reagierenden chemischen Verschiebung δ hervorragend für solche Zwecke genutzt werden.[28,29] Einflüsse sind dabei beispielhaft die mittlere freie Weglänge, die Xe zurücklegen kann oder die unterschiedliche Orientierung funktioneller Gruppen innerhalb des Wirtsnetzwerks.[30–32] Auch die Adsorptions- bzw. Desorptionsdynamik spielt bei dem resultierenden Shift von ^{129}Xe eine Rolle, da ein Sampling aller möglichen Adsorptionspositionen innerhalb des Netzwerks stattfindet und die zeitliche Dauer des Aufenthalts von hoher Relevanz ist.[30]

Durch optische Pumpen von Alkalimetallatomen und dem nachfolgenden Spintransfer kann die Polarisation des Kernspins von ^{129}Xe vergleichsweise einfach um mehrere Größenordnungen hyperpolarisiert werden, was die Messzeit, aufgrund der Erhöhung der Empfindlichkeit, dramatisch verkürzt. Dies ermöglicht auch die Aufnahme von 2D-NMR-Experimenten und damit die Erfassung zeitabhängiger Parameter. Somit eröffnen sich die Möglichkeiten, Diffusionswege und -geschwindigkeiten in größerem Detail zu untersuchen.[33,34] Diese Methode besitzt damit den Vorteil zeitaufgelöste Informationen zu gewinnen, um so noch mehr Rückschlüsse auf mögliche Diffusionsprozesse des Xe Atoms in und aus dem

Netzwerk, sowie Interporendiffussion, zu gewinnen.[35–37] Die Hyperpolarisation von ^{129}Xe ist dabei apparativ sehr aufwendig und eine kommerziell erhältliche Version eines solchen Hyperpolarisators ist bisher nicht verfügbar. Die bedeutendsten Herausforderungen liegen in diesem Zusammenhang in der Handhabung von gasförmigen Alkalimetallen unter Inertgasatmosphäre unterschiedlicher Gaszusammensetzung, sowie der Nutzung von Hochleistungsdiodenlasern mit den entsprechenden Optiken. Ferner müssen transparente Zellen zum optischen Pumpen entwickelt und hergestellt werden. Eine Reihe von Arbeitsgruppen hat solche Polarisatoren entwickelt und nutzt diese für die Untersuchung poröser Materie, aber auch in klinischer, bildgebender Anwendung.[38–41]

Die Interpretation solcher NMR-spektroskopischen Daten ist dabei nicht trivial, da keine allgemeinen Modelle existieren und die chemische Verschiebung von vielen Faktoren beeinflusst werden kann. Aus diesem Grund müssen Modellstudien an bereits gut untersuchten Materialien durchgeführt werden, um Einflüsse von Struktur, Dynamik und Funktionalisierung auf die gemessene chemische Verschiebung von ^{129}Xe zu bestimmen. Der Zugang zu theoretisch berechneten NMR-Parametern auf Basis quantenmechanischer Rechnungen ist dabei ein wertvolles Werkzeug, da hier mittels einer Vielzahl von Modellen einzelne Parameter variiert und somit der Einfluss auf gemessene NMR-Parameter quantifiziert werden kann.[42,43]

Die Kombination aus experimentellen Studien und quantenmechanischer Modellierung der beobachteten Ergebnisse aus der ^{129}Xe-NMR-Spektroskopie stellt bei dieser Fragestellung daher eine wichtige Methode dar, um experimentelle Daten richtig zu interpretieren und letztendlich neue Informationen über die Eigenschaften des Porenraumes funktioneller poröser Feststoffe zu gewinnen.[44–46]

1.1. Metallorganische Gerüstverbindungen

Unter der Materialklasse der metalorganic frameworks (Metallorganische Gerüstverbindungen, MOFs) versteht man ein koordinatives Netzwerk aus Metallclustern als anorganische Knotenpunkte, die über organische Linkermoleküle vernetzt sind. Auf dieser Basis können eine Vielzahl von kristallinen Netzwerken ausgebildet werden, die zudem eine periodische Porenstruktur besitzen.[2]

Bei den anorganischen Knotenpunkten handelt es sich um mehrkernige Oxometall-Cluster, welche auch *Inorganic Building Unit* (IBU) genannt werden. An diese IBUs binden die organischen Linker mittels koordinativer Bindungen. Bei den Linkern handelt es sich meist um starre, aromatische und mehrzähnige Polycarbonsäuren.[47] Da sowohl die verwendeten Linker als auch die ausgebildeten IBUs sehr variabel in ihrer Geometrie und der Anzahl ihrer Anknüpfungspunkte sind, resultieren hieraus eine Vielzahl an realisierbaren ein-, zwei- oder dreidimensionalen Strukturmotiven und Netzwerkgeometrien.[2,48,49] Die Größe der Wiederholeinheiten und damit auch der vorhandenen Poren kann gezielt durch die Größe der Linkermoleküle gesteuert werden, wie es bei den isoretikulären MOFs (IRMOF-X) deutlich gezeigt wird. Das bekannteste Beispiel hier ist MOF-5 (Abb. 1.1).

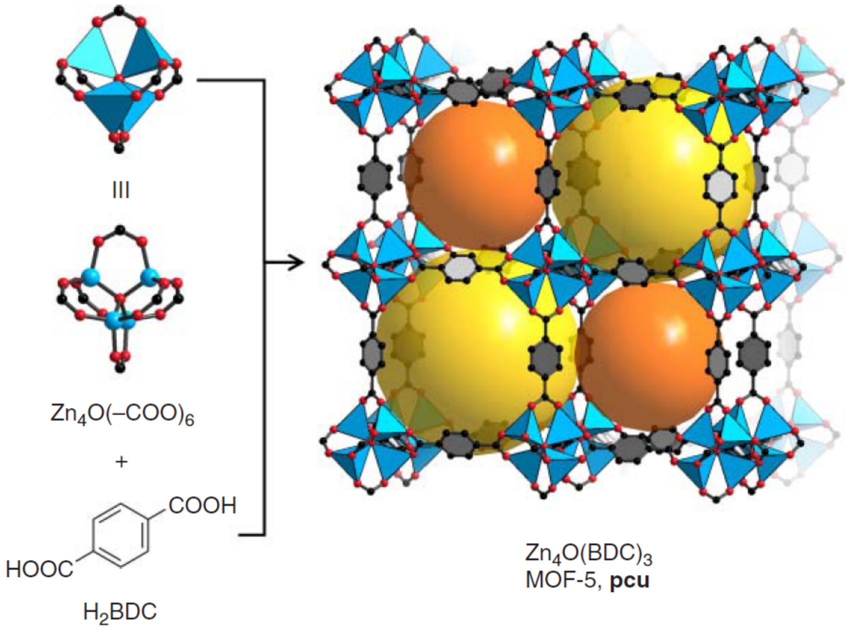

Abb. 1.1 Darstellung der Zusammensetzung eines MOFs am Beispiel von MOF-5. Ein Zn_4O-Cluster bildet die IBU, an welche insgesamt 6 Terephthalsäureeinheiten koordinieren. Die Zn^{2+} Ionen sind somit tetraedrisch von Sauerstoff koordiniert. Es bildet sich ein poröses kubisches Kristallsystem aus. Reprint mit Genehmigung von [130] Copyright Wiley 2016.

MOF-5 bildet aus einer Kombination aus Zn_4O-IBUs, die von 6 Terephthalat-Einheiten umgeben sind, ein kubisches Netzwerk.[50] Nutzt man nun längere Linker, wie beispielsweise Biphenyl-4,4‘-dicarbonsäure (IRMOF-10) oder Triphenyl-4,4‘-dicarbonsäure (IRMOF-16), so steigt schrittweise die Porengröße unter Erhalt des ursprünglichen kubischen Strukturmotivs.[51] Diese Bildung isoretikulärer Reihen von MOFs kann genutzt werden, um beispielsweise die Änderung der Porengröße unter Beibehaltung der Netzwerkkonfiguration oder der chemischen Zusammensetzung des MOFs genauer zu untersuchen.[52]

Durch die Form und die räumliche Geometrie der IBUs wird die Anordnung der Linkermoleküle und als Resultat die Geometrie des Netzwerks bestimmt. So entsteht im Fall von MOF-5 aufgrund der pseudooktaedrischen Struktur der IBUs in Kombination mit Terephthalsäure als linearer Linker ein kubisches Netzwerk. Im Vergleich dazu bildet Al-MIL-53 Ketten aus eckenverknüpften $AlO_4(OH)_2$-Oktaedern aus, welche über lineare Linkermoleküle quervernetzt sind. Das Resultat ist eine 2D-Struktur mit kanalförmigen Poren (Abb. 1.2).[53,54]

Im Vergleich zu porösen anorganischen Materialien wie Zeolithen, die auf Silikatverbindungen basieren, besitzen MOFs aufgrund ihrer Zusammensetzung viele Vorteile. Durch die hohe Variabilität im Einsatz von Linkermolekülen kann eine große Zahl von Strukturmotiven und

Netzwerken realisiert werden, wie auch unter Verwendung verschiedenster Metalle innerhalb der IBUs. Dabei können vor allem die Größen der Kavitäten für potentielle Anwendungen maßgeschneidert werden.

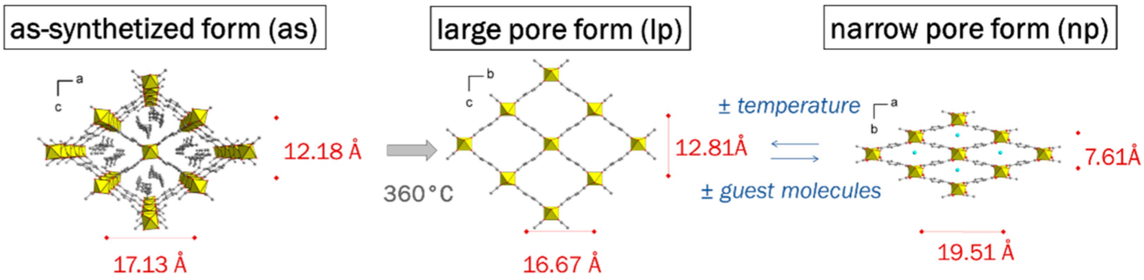

Abb. 1.2: Darstellung der kanalförmigen Porenstruktur von Al-MIL-53 in as-Form mit Resten von Linkermolekülen im Porenraum, sowie der lp- und der np-Form in Abhängigkeit von adsorbierten Gastmolekülen. Reprint aus [54], Verwendung unter Open Access Creative Commons CC BY Lizenz.

Zudem kann durch den Einsatz verschiedenster funktioneller Gruppen an den verwendeten Linkermolekülen zusätzliche Funktionalität eingeführt werden. Diese funktionellen Gruppen können nach der Synthese des jeweiligen Netzwerkes chemisch weiter funktionalisiert werden. Man spricht an dieser Stelle von postsynthetischer Modifikation.[55–59] Ebenfalls ist man in der Lage flexible Netzwerke auszubilden, die sich unter Variation physikalischer Parameter wie dem Umgebungsdruck oder der Temperatur in Ihrer Struktur ändern. Man spricht häufig auch von „atmenden“ MOFs.[60–64] Nachteilig im Vergleich zu Zeolithen hingegen ist die deutlich geringere chemische und thermische Stabilität, da die organischen Linker niedrigere Zersetzungstemperaturen im Bereich von 300 - 600 °C aufweisen und viele MOFs geringere Stabilität gegen Wasser aufweisen, da die koordinative Bindung der Metallionen leicht durch Hydratation gelöst werden kann.[56,59,65,66]

Durch die genannten Optionen zum Maßschneidern solcher Netzwerke, sowie der Funktionalisierung, ergeben sich eine Vielzahl potentieller Anwendungsmöglichkeiten von MOFs. Hier stehen vor allem die Möglichkeiten zur Gastrennung und -speicherung zur Diskussion. Aufgrund der vielfältigen Möglichkeiten den Porenraum in Größe, Form und Funktionalität zu gestalten, eignen sich MOFs für die potentielle Anwendung zur Abtrennung verschiedener Gase in Form von Membranen oder Adsorbentien.[9,10,67] Besonders die Abtrennung von CO_2 aus Industrieabgasen stellt, aufgrund des stetigen Bedarfs von Emissionssenkungen, einen wichtigen Anwendungsaspekt dar.[68–72] Im selben Zusammenhang ist es für die anstehende Energiewende ebenfalls von entscheidender Bedeutung moderne, verlässliche und einfach herzustellende Energiespeicher zu entwickeln. Aus diesem Grund gibt es ebenfalls Ansätze, MOFs als mögliche elektrochemische Energiespeicher oder in Supercapacitors zu verwenden, da diese Netzwerke ebenfalls konfiguriert werden können, um Ladung zu transportieren und zu speichern.[7,54,73,74]

Eine Anwendung im Bereich des Transports und der gezielten Freisetzung von Wirkstufen wurde untersucht, da MOFs auch in der Lage sind durch gezielte Stimuli eingelagerte Stoffe freizugeben. Zudem sind die meisten MOFs aufgrund der verwendeten Hauptgruppenmetalle und Linkermoleküle nicht toxisch. Damit bieten sich MOFs ebenfalls im Bereich pharmazeutischer Anwendungen, vor allem Drug Delivery, an. Hierbei kann der MOF als schützende Hülle genutzt werden, so dass der Wirkstoff während des Transports nicht zersetzt wird und gezielt durch physikalische oder chemische Einflüsse wie Hitze, Magnetismus oder Änderung der Ionenkonzentration (pH-Wert) freigesetzt wird.[14–18,75–77]

1.2. Polarisation in der NMR-Spektroskopie

Bei jeder Art von Spektroskopie handelt es sich um die Anregung von einem Grundzustand in einen energetisch höher gelegenen, angeregten Zustand durch die Absorption von Energie in Form von elektromagnetischer Strahlung. Dieser Zustandsübergang kann beispielsweise die Anregung von Schwingungs- oder Rotationsniveaus innerhalb eines Moleküls (IR-Spektroskopie), oder die Anregung von Bindungselektronen (UV-VIS) darstellen. Die absorbierte Energie entspricht dabei immer dem Energieunterschied der beiden beschriebenen Niveaus, weshalb sich mittels einzigartiger Absorptionsmuster viele analytische Fragestellungen beantworten lassen. In der NMR-Spektroskopie findet eine Anregung der Kernspinniveaus statt. Besitzt ein Atomkern einen Kernspin $I \neq 0$, so spalten sich die Kernspinniveaus aufgrund des Zeeman-Effekts beim Anlegen eines statischen Magnetfeldes B_0 in $2I + 1$ Energielevel auf.[78]

Die Energiedifferenz E_{mag} der Aufspaltung hängt dabei vom jeweiligen gyromagnetischen Verhältnis γdes entsprechenden Kernes und B_0 ab und definiert sich wie folgt[33,34]:

$$E_{mag} = -\hbar\gamma m_l B_0 \tag{1.1}$$

Bei m_l handelt es sich um die magnetische Quantenzahl, die die Ausrichtung des magnetischen Moments zum externen Magnetfeld beschreibt. Geht man beispielsweise von ^{1}H-Kernen aus, welche einen Kernspin von $I = 1/2$ besitzen, so existieren ein Grundzustand N_- (m_l = ½) und ein angeregter Zustand N_+ (m_l = -½). Die Wahrscheinlichkeit der Besetzung dieser Zustände in einem Vielteilchensystem folgt aufgrund thermischer Anregung der Boltzmann-Statistik und ist somit abhängig von der Größe des Energieunterschiedes:

$$\frac{N_+}{N_-} = exp\left(-\frac{\gamma\hbar B_0}{k_B T}\right) \tag{1.2}$$

Bei dem Begriff der Polarisation P handelt es sich nun um die prozentualen Besetzungsunterschiede dieser beiden Niveaus in Referenz zur Gesamtteilchenzahl entsprechend folgender Formel:

$$P = \frac{|N_{-} - N_{+}|}{|N_{-} + N_{+}|} \cdot 100\ \% \tag{1.3}$$

Die Polarisation spielt damit eine wichtige Rolle bei der Beschreibung der Sensitivität und Durchführbarkeit spektroskopischer Messungen. In der NMR-Spektroskopie ist die Gesamtmagnetisierung, und damit die Sensitivität des jeweiligen Spinensembles, abhängig von der Polarisation. Ist ΔE deutlich kleiner als die thermische Energie der Umgebung, so kann im Falle eines Kernspins von I = ½ für die Berechnung der Polarisation die sogenannte Hochtemperaturnäherung angenommen werden:

$$P = \frac{1}{2} \frac{\gamma \hbar B_0}{k_B T} \cdot 100\ \% \tag{1.4}$$

Betrachtet man an dieser Stelle als repräsentatives Beispiel die Polarisation von ^{1}H-Kernen bei Standardbedingungen in einem statischen Magnetfeld von 7.05 T (300 MHz-Magnet), so beläuft sich die Polarisation, und damit der Anteil der für ein NMR-Experiment verwendbarer Kerne, auf 0.0151 %. Im Falle von Kernen mit deutlich kleinerem gyromagnetischem Verhältnis reduziert sich diese Zahl noch weiter, wie im Falle von ^{129}Xe auf 0.00067 %. Eine solch geringe Polarisation macht sich bei spektroskopischen Experimenten vor allem in hoher Messzeit bei gleichzeitig sehr geringem Signal/Rausch-Verhältnis bemerkbar.

Betrachtet man nun den Zusammenhang zwischen Energie und Polarisation, gibt es zwei konventionelle Möglichkeiten um die Empfindlichkeit zu verbessern: Die Erhöhung des statischen Magnetfeldes B_0 und die Verringerung der Temperatur. Mit Erhöhung des Magnetfeldes steigt die Polarisation linear an, jedoch werden hier sehr schnell technische Grenzen erreicht, da bereits jetzt supraleitende Kryomagneten verwendet werden, um die nötigen Flussdichten zu realisieren. Die größten Feldstärken von kommerziell zugänglichen Magneten belaufen sich im Moment auf 28.2 T, was einer Protonenresonanzfrequenz von 1.2 GHz entspricht.[79] Aufgrund der Kosten von ca. 12.5 Millionen Euro finden sich entsprechende Geräte nur in Großforschungseinrichtungen mit begrenzter Verfügbarkeit wieder.[80] Die Verringerung der Temperatur kann die Polarisation ebenfalls erhöhen, ist jedoch ebenfalls durch die technische Möglichkeit der Probenkühlung begrenzt. Zudem stößt diese Methode bei flüssigen Proben schnell an ihre Grenzen und kann zudem aufgrund niedriger Relaxationsraten die Dauer eines Experiments stark erhöhen.

Die Verwendung größerer Probenmengen zur Verbesserung der Sensitivität ist ebenfalls möglich und von allen Beispielen vermutlich am einfachsten umzusetzen. Dabei sollte beachtet werden, dass der zu untersuchende Stoff meist nicht in beliebiger Menge zur Verfügung steht und das Volumen des Probenconfinements hier die Grenze darstellt.

Neben diesen Methoden, die die Polarisation nur im geringen Maß und innerhalb technischer Grenzen verbessern kann, gibt es die Möglichkeit der Hyperpolarisation des Kernspins mittels *Dynamic Nuclear Polarization* (DNP)[81,82] oder *Spin Exchange Optical Pumping* (SEOP), welches im folgenden Kapitel näher erläutert werden soll.

1.3. Hyperpolarisation mittels Spin Exchange Optical Pumping

Bei *Spin Exchange Optical Pumping* oder SEOP handelt es sich um eine Methode des optischen Pumpens von Alkalimetallatomen und dem anschließenden Transfer des polarisierten Elektronenspins auf den Kernspin eines NMR-aktiven Kerns. Dieser Effekt wurde bereits in den 60er Jahren anhand der Polarisation von ^{3}He mittels Rb experimentell von Bouchiat, Carver und Varnum beschrieben.[83] Dieses Modell wurde 1978 von Bhaskar, Happer und McClelland auf ^{129}Xe ausgeweitet.[84] Im ersten Schritt, dem optischen Pumpen, wird Licht verwendet, um den Elektronenspin S eines Alkalimetallatoms innerhalb eines statischen Magnetfeldes zu polarisieren. Befindet sich ein dieses Atom innerhalb eines entlang der z-Achse ausgerichteten Magnetfeldes, so wird der Hamilton-Operator H_a folgendermaßen beschrieben:

$$\hat{H}_a = A_a \hat{I}_a \cdot \hat{S} + g_s \mu_B \hat{S}_z B_0 - \frac{\mu_a}{I_a} \hat{I}_{az} B_0 \tag{1.5}$$

Der erste Teil der Gleichung beschreibt hierbei die Hyperfeinwechselwirkung zwischen Kernspin $\hat{I}$ und Elektronenspin $\hat{S}$, während der zweite und dritte Teil die Wechselwirkung des Elektrons bzw. des Kerns mit dem externen Magnetfeld B_0 beschreibt.[85–87] Bei kleinen magnetischen Feldern, wie sie üblicherweise für SEOP verwendet werden (~20 G), können die Eigenzustände von H_a mit den Eigenzuständen des Gesamtdrehimpulses $F = S + I_a$ und dessen Projektion entlang der z-Achse F_z gleichgesetzt werden, da hier die Hyperfeinwechselwirkung der Zeeman-Wechselwirkung überwiegt.[88] Wird nun Alkalimetallatomdampf mit zirkular polarisiertem Licht angeregt, dessen Wellenlänge dem D_1-Übergang des Alkalimetallatoms entspricht, so werden Elektronen vom $^2S_{1/2}$-Zustand in den $^2P_{1/2}$ Zustand angeregt. Dabei muss die Erhaltung des Gesamtdrehimpulses berücksichtigt werden, so dass sich aufgrund der Polarisation des Lichtes bei der Anregung von $m_J = -\frac{1}{2}$ zu $+\frac{1}{2}$ ändert (Abb. 1.3).[86] Durch Kollisionen der Rb-Atome werden die angeregten Zustände in ihrem Gesamtdrehimpuls gemischt und relaxieren mit gleichen Raten wieder in ihre Grundzustände.

Das dabei emittierte Licht muss von einem Fluoreszenzquencher[89] absorbiert werden und in Schwingungs-Rotationsniveaus relaxieren, da es sonst aufgrund stimulierter Emission zur Depolarisierung des Rubidiums kommt. Häufig werden hierfür geringe Mengen an Stickstoff beigemischt.

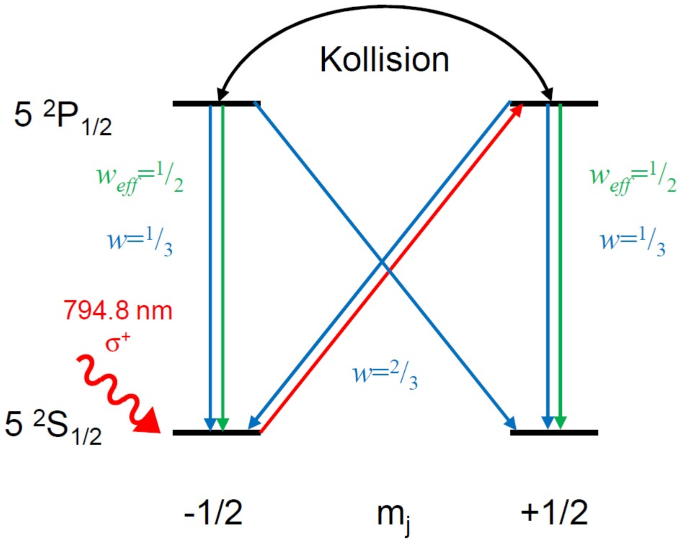

Abb. 1.3: Schematische Darstellung der elektronischen Niveaus des Valenzelektrons von Rubidium und der optische Pumpvorgang (rot) mit zirkular polarisiertem (σ⁺) Laserlicht. Relaxationsvorgänge werden durch blaue (natürliche) und grüne (stoßinduzierte) Pfeile inklusive deren Clebsch-Gordon Koeffizienten *w* dargestellt.

Aufgrund konstanter Pump- und Relaxationsprozesse reichert sich in diesem Beispiel der elektronische Zustand mit einem Gesamtdrehimpuls von $m_J = +½$ an, wodurch eine starke Polarisation des Elektronenspins stattfindet. Die mittlere Rate zur Absorption von Photonen $\langle \delta\Gamma \rangle$ wird dabei wie folgt beschrieben[88]:

$$\langle \delta\Gamma \rangle = (1 - 2\langle S_z \rangle) R_p \tag{1.6}$$

Hierbei beschreibt R_p die Absorptionsrate für unpolarisierte Atome in Abhängigkeit des spektralen Profils des Anregungslichtes, wobei das Photon einen Beitrag zum Drehmoment leistet und damit der mittlere Gesamtspin $\langle Fz \rangle$ steigt:

$$\frac{d\langle F_z \rangle}{dt} = R_p \left(\frac{1}{2} - \langle S_z \rangle\right) \tag{1.7}$$

Während durch den optischen Pumpprozess die Polarisation immer weiter aufgebaut wird, so führen Kollisionen zwischen Rb-Atomen zu einer Zerstörung ebendieser. Die Rate der Spinzerstörung hängt vom Kollisionsquerschnitt ab und liegt im Fall von Rb bei $2 \cdot 10^{-14} cm^2$.[88] Aus diesem Grund wird der vorhandene Rb-Dampf durch ein Puffergas mit einem deutlich geringerem Stoßquerschnitt, meist Helium, verdünnt. Die effektive hieraus resultierende

Polarisation der Rb-Atome P_{Rb} ergibt sich also aus der optischen Pumprate ρ_{OP}, sowie der *Spin destruction rate* ρ_{SD} und kann wie folgt beschrieben werden:

$$P_{Rb} = \frac{\rho_{OP}}{\rho_{OP}+\rho_{SD}} \tag{1.8}$$

Der eigentliche Polarisationsübertrag auf den Kernspin des Xe-Atoms erfolgt anschließend mittels verschiedener Kollisionen zwischen Rb und Xe Atomen, die sich je nach Umgebungsdruck unterscheiden. Während es bei einem Gasdruck von bis zu 1 bar um die kurzlebige Bildung von Van-der-Waals Molekülen von Xe, Rb und N_2 handelt, findet der Spinaustausch bei höherem Druck fast ausschließlich durch binäre Kollisionen zwischen Rb und Xe Atomen statt (Abb. 1.4).[88,90]

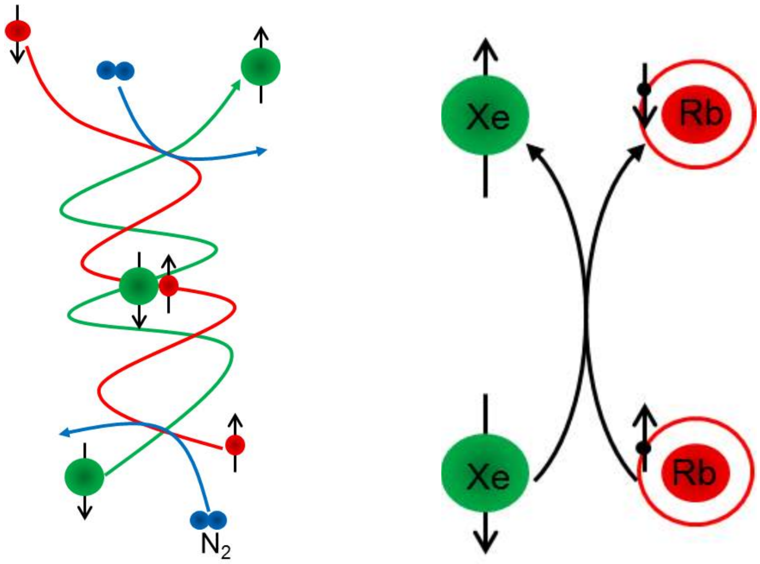

Abb. 1.4: Darstellung der Arten von Spinaustausch durch Kollisionen zwischen optisch gepumptem Rb und Xe. Der Spinaustausch findet hier bei niedrigem Druck durch die Bildung von Van-der-Waals Molekülen (links) und bei hohem Druck durch binäre Kollisionen (rechts) statt,

Obwohl der Spinaustausch mittels der Bildung von Van-der-Waals-Molekülen deutlich effizienter ausfällt, ist die Lebensdauer dieser bei höherem Druck aufgrund der höheren Frequenz von Teilchenkollisionen zu kurz.[84–86]

Die erzeugte Kernspinpolarisation ist selbst sehr langlebig, kann aber durch Faktoren wie Kollisionen zwischen verschiedenen Gasatomen, sowie der Kollision von Xe mit den Wänden der Pumpzelle, zerstört werden. Auch hier wird eine *Spin destruction rate* ρ_0 definiert, welche sämtliche Prozesse vereint, die die Relaxation der Hyperpolarisation beeinflussen und somit die letztendlich erhaltene Kernspinpolarisation von ^{129}Xe bestimmen.

Zusammen mit der Rate des Spinaustauschs zwischen polarisierten Elektronen im Rubidiumatom und dem Kernspin des Xenon Atoms ρ_{SE} ergibt sich ein Term, der parallel zu

Formel 1.8 aufgestellt werden kann. Bei der Berechnung wird hier ein Spinaustausch angenommen, der ausschließlich über binäre Kollisionen realisiert wird. Zusätzlich zeigt ein nachgestellter Term die Zeitabhängigkeit der Polarisationsentwicklung, die aufgrund ständiger Polarisations- und Relaxationseffekte einen *steady-state* Zustand erreicht, dessen Höhe vom Verhältnis der Austauschrate zur Relaxationsrate abhängig ist.[90,91]

$$P_{Xe} = \frac{\rho_{SE}}{\rho_{SE}+\rho_0} P_{Rb}\left[1 - e^{-(\rho_{SE}+\rho_0)t}\right] \tag{1.9}$$

Praktisch kann die Erzeugung von hyperpolarisiertem ^{129}Xe in einem *single batch*- oder *continuous flow*-Verfahren umgesetzt werden. In Ersterem wird Xenon nach erfolgter Hyperpolarisation mittels einer Kühlfalle kondensiert und kann vorübergehend in einem statischen Magnetfeld gelagert werden. Im *continuous flow*-Verfahren wird dem Gasgemisch lediglich der Rubidiumdampf entzogen und der kontinuierliche Fluss kann direkt verwendet werden. Hierbei ist auch eine Wiederverwendung des Gasgemisches möglich.[92]

In der Praxis ist ein solches Gerät aufgrund der gewissen Nischenanwendung, sowie der Komplexität des Polarisationsprozesses, bisher nicht kommerziell erhältlich. Jedoch gibt es mittlerweile eine große Anzahl an experimentellen Aufbauten. Diese unterscheiden sich dabei in ihrem Design, dem Anwendungsbereich, sowie der erreichten, beziehungsweise gemessenen Polarisation.[92–94]

Als Beispiel seien hier Apparaturen mit hoher Effizienz an Laserabsorption[95] oder Niederdruck-Polarisatoren unter Verwendung von Diodenlasern mit schmaler Emissionslinie[96–99] genannt. Ebenso werden Polarisatoren zur klinischen Anwendung der ^{129}Xe-MRT entwickelt.[41,100] In der nachfolgenden Tabelle soll ein kurzer Überblick über verschiedene publizierte Polarisatoren und die erreichte maximale ^{129}Xe-Polarisation gegeben werden.

Tabelle 1.1 Übersicht verschiedener und veröffentlichter ^{129}Xe-Polarisatortypen und deren maximal erreichte Polarisation.

POLARISATOR	**TYP**	**POLARISATION**
Rosen, 1999[101]	Batch, in-vivo	7.5 %
Driehuys, 1996[102]	Continuous flow	5 %
Nikolaou, 2014[40]	Temperature ramped	21 – 85 %
Russet, 2006[97]	Continuous flow	64 %
Senker, 2022[38]	Continuous flow, separate Rb-Zelle	22 %

1.4. Anwendung von ^{129}Xe-NMR-Spektroskopie

Während die Hyperpolarisation von Edelgasen ursprünglich nur einen beobachteten physikalischen Effekt darstellte, wurde dieser schließlich auch praktisch in der NMR-Spektroskopie, sowie bildgebender Verfahren genutzt. Neben der hohen erreichten Polarisation eignen sich Edelgase wie Xenon gut als chemisch inerte Sonden für verschiedene Fragestellungen.

^{129}Xe mit einem Kernspin von I = ½, einem gyromagnetischen Verhältnis von γ = -7.3997 x 10^7 rad s^{-1} T^{-1} und einer natürlichen Isotopenhäufigkeit von 26.4 % stellt aufgrund seiner verhältnismäßig einfachen Messbarkeit einen besonders attraktiven Kern in der NMR-Spektroskopie dar. Die Empfindlichkeit ist mit der des ^{13}C Kerns bei deutlich höherer natürlicher Häufigkeit zu vergleichen. Aufgrund der hohen Polarisierbarkeit der vergleichsweise großen Elektronenhülle reagiert die chemische Verschiebung ausgesprochen empfindlich auf äußere Einflüsse. Aus diesen Gründen und des vergleichsweise niedrigen Preises, ist Xenon das am häufigsten verwendete Edelgas im Bereich von Hyperpolarisationsexperimenten.[34,103]

Eine der ersten analytischen Anwendungen fand ^{129}Xe-NMR-Spektroskopie in der Physisorption und anschließenden NMR-spektroskopischen Betrachtung in Molekularsieben. In der Pionierarbeit von Demarquay und Fraissard wurde schon in den Anfängen der ^{129}Xe-NMR-Spektroskopie eine Verbindung zwischen der chemischen Verschiebung des in Zeolithen adsorbierten Xenons und der mittleren freien Weglänge der Gasatome hergestellt.[31,32] Dies war aufgrund des sehr homogenen Aufbaus und der gleichmäßigen Oberflächenbeschaffenheit möglich. Die Ergebnisse bildeten die Grundlagen des Zusammenhangs zwischen Porengrößen in einem interkonnektiven anorganischen Netzwerk und der direkt messbaren chemischen Verschiebung des ^{129}Xe Kerns.[104] Neben der Porengröße des untersuchten Materials können eine große Anzahl an Eigenschaften näher untersucht werden, da sich die Umgebung adsorbierten Xenons direkt auf chemische Verschiebung und Signalform auswirkt. Auf diese Weise können Informationen über die Mikrostrukturierung und Geometrie der Poren von Festkörpern ermittelt werden, wie beispielsweise die Morphologie von mesoporösem TiO_2[37], oder Carbon-Nanotubes[105]. Ebenfalls kann die Interkonnektivität von Porensystemen oder hierarchisch strukturierten Materialien bestimmt werden, was gerade bei amorphen Substanzen mittels Beugungsmethoden kaum zu bewältigen ist.[106–108] Da sich die gemessene chemische Verschiebung aus dem Mittel aller verfügbarer Adsorptionspositionen zusammensetzt, kann auch durch Änderungen der Diffusionsdynamik, beispielsweise einer Temperaturabsenkung, genauere Aussagen über spezifische oder bevorzugte Adsorptionspositionen innerhalb des porösen Wirtsnetzwerks getroffen werden (vgl. Abb. 1.5). [109]

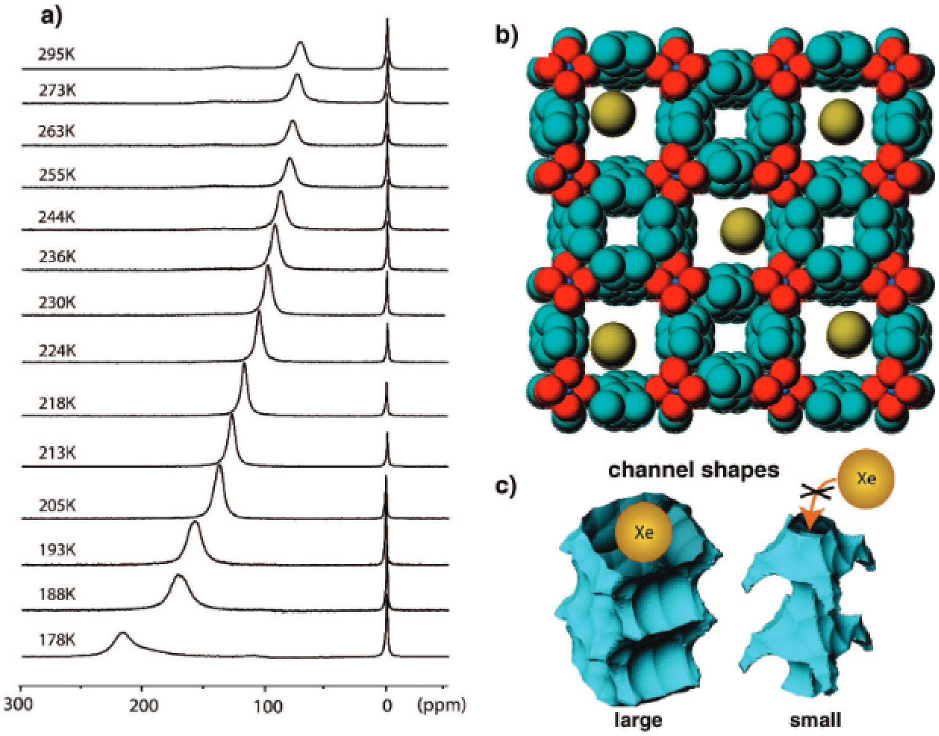

Abb. 1.5: a) ^{129}Xe-NMR Spektren eines Al-basierten MOFs Al(OH)(1,4-NDC) unter Verwendung von hyperpolarisiertem ^{129}Xe bei variabler Temperatur. b) Kristallstruktur des MOFs. Deutlich erkennbar ist die Kanalstruktur der Poren. c) Räumliche Darstellung der Nanokanäle und der Diffusionswege von Xe. Reprint mit Genehmigung von [109]. Copyright 2008 American Chemical Society.

Die bereits angesprochene Änderung der Signalform ist besonders gut bei zweidimensionalen Systemen wie Kanälen oder Röhren zu beobachten und zeigt sich in einer ausgeprägten *Chemical Shift Anisotropie* (CSA). Die Form der CSA ändert sich je nach Grad der Porenbeladung mit Xenon und gibt so Aufschluss über die Gasdichte innerhalb der Poren.[45,110–112] Diese Veränderung der Signalform kann ebenfalls dazu genutzt werden, dynamische Prozesse des Materials selbst zu betrachten. So führen sogenannte *atmende* MOFs eine Strukturänderung bei bestimmter Gasbeladung und Temperatur durch, welche mittels Xenon induziert und NMR-spektroskopisch sehr genau verfolgt werden kann.[46,113–116] So ist beispielsweise bei MIL-53 ein ausgeprägter *gate opening*-Effekt bei einer bestimmten Xe-Beladung zu beobachten, der auch vollständig reversibel ist und zudem ein Übergangsbereich der Konfigurationen, sowie der relevante Mechanismus bestimmt werden können.

Neben der Untersuchung poröser Materialien wird hyperpolarisiertes ^{129}Xe auch *in vivo* für bildgebende Verfahren mittels MRI verwendet. Xenon ist als Edelgas dabei nicht toxisch und wirkt als Anästhetikum. Wird es eingeatmet, so kann ein detailliertes Bild des zugänglichen Lungenvolumens aufgenommen werden. Da die Kontrastgebung in der Magnetresonanzbildgebung üblicherweise über die T_1- bzw. T_2-Zeit der im Wasser enthaltenen Protonen stattfindet und dieses im freien Lungenvolumen kaum vorhanden ist, kann mittels ^{129}Xe-MRI ein deutlich

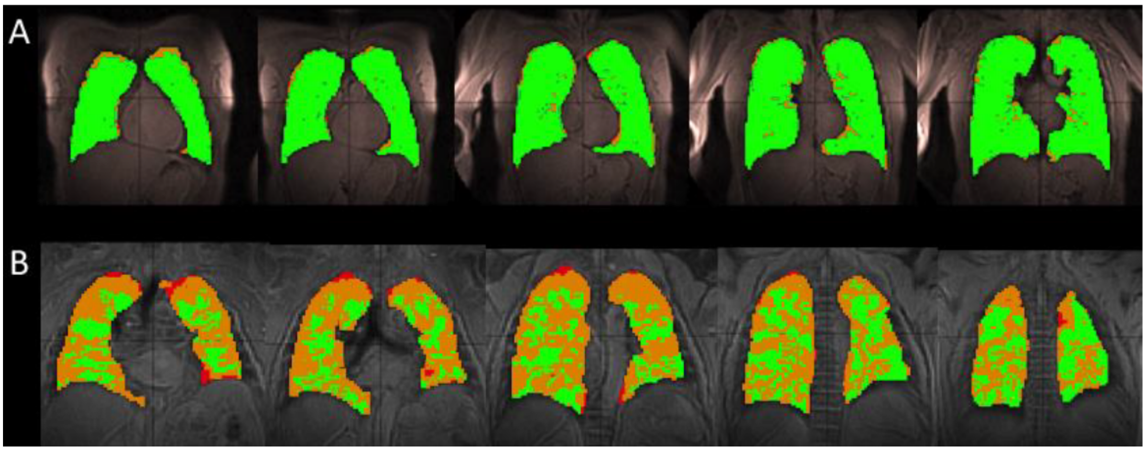

Abb. 1.6: Mittels ^{129}Xe-MRI erzeugtes Bild der Lunge einer gesunden Person (A) und einer Person, die an idiopatischer Lungenfibrose erkrankt ist (B). Die grünen Bereiche zeigen frei zugängliches, die orangen Bereiche unterversorgtes und die roten Bereiche nicht versorgtes Lungenvolumen. Das umliegende Gewebe wurde mittels ^{1}H-MRI abgebildet. Reprint aus [118], Verwendung unter Open Access Creative Commons CC BY Lizenz.

besseres Bild erzeugt werden und so beispielsweise krankhafte Veränderungen der Lunge durch COVID-19 oder COPD näher untersucht werden (siehe Abb. 1.6).[117–122]

Eine deutlich fortgeschrittenere Methode der Bildgebung unter Verwendung von hyperpolarisiertem ^{129}Xe ist die Hyper-CEST Methode.[123] Hierfür wird zuvor hyperpolarisiertes Xe-Gas in einem Shuttle-Molekül fixiert, meist Cryptophane, an deren Käfigstruktur weitere funktionelle Seitengruppen angebracht sind.[124–126] Das fixierte Xe-Atom kann somit gezielt an Stellen innerhalb eines Patienten transportiert und dort für die Bildgebung verwendet werden. Durch Funktionalisierung der Cryptophane können sogar bestimmte Zellmerkmale von Krebszellen angesteuert und damit Tumore sichtbar gemacht werden.[127,128] Die CEST-Methode sorgt dabei für eine Kontrastierung auf Basis des Austausches von hyperpolarisiertem ^{129}Xe in freier und gebundener Form. Somit dient ^{129}Xe neben Gadolinium als sehr spezifisches Kontrastmittel mit einer großen Breite an Anwendungen.[117,129]

Anhand der hier genannten Beispiele zeigt sich nur ein Bruchteil der großen Anwendungsbreite von hyperpolarisiertem ^{129}Xe in NMR- und MRI-Methoden. Aus diesem Grund ist die Anwendung von ^{129}Xe wichtiger Bestandteil bestimmter Forschungszweige. In den nachfolgenden Kapiteln wird dies an den eigens veröffentlichten Arbeiten zur Verwendung von hyperpolarisiertem ^{129}Xe im Bereich der Materialforschung noch einmal deutlich gemacht.

2. Literaturverzeichnis

(1) Li, J.-R.; Sculley, J.; Zhou, H.-C. Metal–Organic Frameworks for Separations. *Chem. Rev.* **2012**, *112* (2), 869–932.

(2) Foo, M. L.; Matsuda, R.; Kitagawa, S. Functional Hybrid Porous Coordination Polymers. *Chem. Mater.* **2014**, *26* (1), 310–322.

(3) Xu, R.; Pang, W.; Yu, J.; Huo, Q.; Chen, J. *Chemistry of Zeolites and Related Porous Materials*; Wiley, 2007.

(4) Connolly, B. M.; Madden, D. G.; Wheatley, A. E. H.; Fairen-Jimenez, D. Shaping the Future of Fuel: Monolithic Metal–Organic Frameworks for High-Density Gas Storage. *J. Am. Chem. Soc.* **2020**, *142* (19), 8541–8549.

(5) Hu, Z.; Wang, Y.; Shah, B. B.; Zhao, D. CO_2 Capture in Metal–Organic Framework Adsorbents: An Engineering Perspective. *Adv. Sustain. Syst.* **2019**, *3* (1), 1800080.

(6) Xue, D.-X.; Wang, Q.; Bai, J. Amide-Functionalized Metal–Organic Frameworks: Syntheses, Structures and Improved Gas Storage and Separation Properties. *Coord. Chem. Rev.* **2019**, *378*, 2–16.

(7) Zhang, X.; Chen, A.; Zhong, M.; Zhang, Z.; Zhang, X.; Zhou, Z.; Bu, X. H. Metal–Organic Frameworks (MOFs) and MOF-Derived Materials for Energy Storage and Conversion. *Electrochem. Energy Rev.* **2019**, *2* (1), 29–104.

(8) Liang, Z.; Qu, C.; Guo, W.; Zou, R.; Xu, Q. Pristine Metal–Organic Frameworks and Their Composites for Energy Storage and Conversion. *Adv. Mater.* **2018**, *30* (37).

(9) Li, L.; Lin, R.-B.; Krishna, R.; Wang, X.; Li, B.; Wu, H.; Li, J.; Zhou, W.; Chen, B. Flexible–Robust Metal–Organic Framework for Efficient Removal of Propyne from Propylene. *J. Am. Chem. Soc.* **2017**, *139* (23), 7733–7736.

(10) Banerjee, D.; Simon, C. M.; Plonka, A. M.; Motkuri, R. K.; Liu, J.; Chen, X.; Smit, B.; Parise, J. B.; Haranczyk, M.; Thallapally, P. K. Metal–Organic Framework with Optimally Selective Xenon Adsorption and Separation. *Nat. Commun.* **2016**, *7*, ncomms11831.

(11) Hu, Z.; Kang, Z.; Qian, Y.; Peng, Y.; Wang, X.; Chi, C.; Zhao, D. Mixed Matrix Membranes Containing UiO-66(Hf)-$(OH)_2$ Metal–Organic Framework Nanoparticles for Efficient H_2 / CO_2 Separation. *Ind. Eng. Chem. Res.* **2016**, *55* (29), 7933–7940.

(12) Qiu, S.; Xue, M.; Zhu, G. Metal–Organic Framework Membranes: From Synthesis to Separation Application. *Chem. Soc. Rev.* **2014**, *43* (16), 6116–6140.

(13) Chavan, S.; Vitillo, J. G.; Gianolio, D.; Zavorotynska, O.; Civalleri, B.; Jakobsen, S.; Nilsen, M. H.; Valenzano, L.; Lamberti, C.; Lillerud, K. P.; Bordiga, S. H_2 Storage in Isostructural UiO-67 and UiO-66 MOFs. *Phys. Chem. Chem. Phys.* **2012**, *14* (5), 1614.

(14) Cao, J.; Li, X.; Tian, H. Metal-Organic Framework (MOF)-Based Drug Delivery. *Curr. Med. Chem.* **2019**, *27* (35), 5949–5969.

(15) Horcajada, P.; Serre, C.; Vallet-Regí, M.; Sebban, M.; Taulelle, F.; Férey, G. Metal-Organic Frameworks as Efficient Materials for Drug Delivery. *Angew. Chem. Int. Ed. Engl.* **2006**, *45* (36), 5974–5978.

(16) Lawson, H. D.; Walton, S. P.; Chan, C. Metal-Organic Frameworks for Drug Delivery: A Design Perspective. *ACS Appl. Mater. Interfaces* **2021**, *13* (6), 7004–7020.

(17) Gordon, J.; Kazemian, H.; Rohani, S. MIL-53(Fe), MIL-101, and SBA-15 Porous Materials: Potential Platforms for Drug Delivery. *Mater. Sci. Eng. C* **2015**, *47*, 172–179.

(18) Abánades Lázaro, I.; Wells, C. J. R.; Forgan, R. S. Multivariate Modulation of the Zr MOF UiO-66 for Defect-Controlled Combination Anticancer Drug Delivery. *Angew. Chemie Int. Ed.* **2020**, *59* (13), 5211–5217.

(19) Li, H. Y.; Zhao, S. N.; Zang, S. Q.; Li, J. Functional Metal-Organic Frameworks as Effective Sensors of Gases and Volatile Compounds. *Chem. Soc. Rev.* **2020**, *49* (17), 6364–6401.

(20) Rauf, S.; Vijjapu, M. T.; Andrés, M. A.; Gascón, I.; Roubeau, O.; Eddaoudi, M.; Salama, K. N. Highly Selective Metal-Organic Framework Textile Humidity Sensor. *ACS Appl. Mater. Interfaces* **2020**, *12* (26), 29999–30006.

(21) Liu, C. Sen; Li, J.; Pang, H. Metal-Organic Framework-Based Materials as an Emerging Platform for Advanced Electrochemical Sensing. *Coord. Chem. Rev.* **2020**, *410*, 213222.

(22) Li, Q.; Zhang, W.; Miljanić, O. Š.; Sue, C. H.; Zhao, Y. L.; Liu, L.; Knobler, C. B.; Stoddart, J. F.; Yaghi, O. M. Docking in Metal-Organic Frameworks. *Science* **2009**, *325* (5942), 855–859.

(23) Yuan, S.; Zou, L.; Li, H.; Chen, Y.-P.; Qin, J.; Zhang, Q.; Lu, W.; Hall, M. B.; Zhou, H.-C. Flexible Zirconium Metal-Organic Frameworks as Bioinspired Switchable Catalysts. *Angew. Chemie Int. Ed.* **2016**, *55* (36), 10776–10780.

(24) Lu, G.; Li, S.; Guo, Z.; Farha, O. K.; Hauser, B. G.; Qi, X.; Wang, Y.; Wang, X.; Han, S.; Liu, X.; Duchene, J. S.; Zhang, H.; Zhang, Q.; Chen, X.; Ma, J.; Loo, S. C. J.; Wei, W. D.; Yang, Y.; Hupp, J. T.; Huo, F. Imparting Functionality to a Metal-Organic Framework Material by Controlled Nanoparticle Encapsulation. *Nat. Chem.* **2012**, *4* (4), 310–316.

(25) Lee, J.; Farha, O. K.; Roberts, J.; Scheidt, K. A.; Nguyen, S. T.; Hupp, J. T. Metal-Organic Framework Materials as Catalysts. *Chem. Soc. Rev.* **2009**, *38* (5), 1450–1459.

(26) Ma, L.; Abney, C.; Lin, W. Enantioselective Catalysis with Homochiral Metal–Organic Frameworks. *Chem. Soc. Rev.* **2009**, *38* (5), 1248.

(27) Ruckdeschel, P.; Kemnitzer, T. W.; Nutz, F. A.; Senker, J.; Retsch, M. Hollow Silica Sphere Colloidal Crystals: Insights into Calcination Dependent Thermal Transport. *Nanoscale* **2015**, *7* (22), 10059–10070.

(28) Boventi, M.; Mauri, M.; Simonutti, R. 129Xe: A Wide-Ranging NMR Probe for Multiscale Structures. *Appl. Sci.* **2022**, *12* (6), 3152.

(29) Pietraiß, T.; Gaede, H. C. Optically Polarized ^{129}Xe in NMR Spectroscopy. *Adv. Mater.* **1995**, *7* (10), 826–838.

(30) Kemnitzer, T. W.; Tschense, C. B. L.; Wittmann, T.; Rössler, E. A.; Senker, J. Exploring Local Disorder within CAU-1 Frameworks Using Hyperpolarized ^{129}Xe NMR Spectroscopy. *Langmuir* **2018**, *34* (42), 12538–12548.

(31) Springuel-Huet, M.; Demarquay, J.; Ito, T.; Fraissard, J. 129Xe-NMR of Xenon Adsorbed on Zeolites: Determination of the Dimensions of the Void Space from the Chemical Shift ΔdL(^{129}Xe). *Stud. Surf. Sci. Catal.* **1988**, *Volume 37* (C), 183–189.

(32) Demarquay, J.; Fraissard, J. 129Xe NMR of Xenon Adsorbed on Zeolites. *Chem. Phys. Lett.* **1987**, *136* (3–4), 314–318.

(33) Brunner, E. Enhancement of Surface and Biological Magnetic Resonance Using Laser-Polarized Noble Gases. *Concepts Magn. Reson.* **1999**, *11* (5), 313–335.

(34) Goodson, B. M. Nuclear Magnetic Resonance of Laser-Polarized Noble Gases in Molecules, Materials, and Organisms. *J. Magn. Reson.* **2002**, *155* (2), 157–216.

(35) Ooms, K. J.; Campbell, K.; Tykwinski, R. R.; Wasylishen, R. E. Hyperpolarized ^{129}Xe NMR Spectroscopic Investigation of Potentially Porous Shape-Persistent Macrocyclic Materials. *J. Mater. Chem.* **2005**, *15* (40), 4318–4327.

(36) Weiland, E.; Springuel-Huet, M.-A.; Nossov, A.; Gédéon, A. ^{129}Xenon NMR: Review of Recent Insights into Porous Materials. *Microporous Mesoporous Mater.* **2016**, *225*, 41–65.

(37) Wang, L.-Q.; Wang, D.; Liu, J.; Exarhos, G. J.; Pawsey, S.; Moudrakovski, I. Probing Porosity and Pore Interconnectivity in Crystalline Mesoporous TiO_2 Using Hyperpolarized ^{129}Xe NMR. *J. Phys. Chem. C* **2009**, *113* (16), 6577–6583.

(38) Stäglich, R.; Kemnitzer, T. W.; Harder, M. C.; Schmutzler, A.; Meinhart, M.; Keenan, C. D.; Rössler, E. A.; Senker, J. Portable Hyperpolarized Xe-129 Apparatus with Long-Time Stable Polarization Mediated by Adaptable Rb Vapor Density. *J. Phys. Chem. A* **2022**, *126* (16), 2578–2589.

(39) Nikolaou, P.; Coffey, A. M.; Walkup, L. L.; Gust, B. M.; LaPierre, C. D.; Koehnemann, E.; Barlow, M. J.; Rosen, M. S.; Goodson, B. M.; Chekmenev, E. Y. A 3D-Printed High Power Nuclear Spin Polarizer. *J. Am. Chem. Soc.* **2014**, *136* (4), 1636–1642.

(40) Nikolaou, P.; Coffey, A. M.; Barlow, M. J.; Rosen, M. S.; Goodson, B. M.; Chekmenev, E. Y. Temperature-Ramped ^{129}Xe Spin-Exchange Optical Pumping. *Anal. Chem.* **2014**, *86* (16), 8206–8212.

(41) Norquay, G.; Parnell, S. R.; Xu, X.; Parra-Robles, J.; Wild, J. M. Optimized Production of Hyperpolarized ^{129}Xe at 2 Bars for in Vivo Lung Magnetic Resonance Imaging. *J. Appl. Phys.* **2013**, *113* (4), 44908.

(42) Komulainen, S.; Roukala, J.; Zhivonitko, V. V.; Javed, M. A.; Chen, L.; Holden, D.; Hasell, T.; Cooper, A.; Lantto, P.; Telkki, V.-V. Inside Information on Xenon Adsorption in Porous Organic Cages by NMR. *Chem. Sci.* **2017**, *8* (8), 5721–5727.

(43) Trepte, K.; Schaber, J.; Schwalbe, S.; Drache, F.; Senkovska, I.; Kaskel, S.; Kortus, J.; Brunner, E.; Seifert, G. The Origin of the Measured Chemical Shift of ^{129}Xe in UiO-66 and UiO-67 Revealed by DFT Investigations. *Phys. Chem. Chem. Phys.* **2017**, *108*, 4751–4758.

(44) Jameson, C. J.; Jameson, A. K.; Gerald, R.; de Dios, A. C. Nuclear Magnetic Resonance Studies of Xenon Clusters in Zeolite Na A. *J. Chem. Phys.* **1992**, *96* (3), 1676–1689.

(45) Jameson, C. J.; de Dios, A. C. Xe Nuclear Magnetic Resonance Line Shapes in Nanochannels. *J. Chem. Phys.* **2002**, *116* (9), 3805–3821.

(46) Hoffmann, H. C.; Assfour, B.; Epperlein, F.; Klein, N.; Paasch, S.; Senkovska, I.; Kaskel, S.; Seifert, G.; Brunner, E. High-Pressure in Situ ^{129}Xe NMR Spectroscopy and Computer Simulations of Breathing Transitions in the Metal--Organic Framework $Ni_2(2,6\text{-}Ndc)_2(Dabco)$ (DUT-8(Ni)). *J. Am. Chem. Soc.* **2011**, *133* (22), 8681–8690.

(47) Cheetham, A. K.; Rao, C. N. R.; Feller, R. K. Structural Diversity and Chemical Trends in Hybrid Inorganic–Organic Framework Materials. *Chem. Commun.* **2006**, No. 46, 4780–4795.

(48) Janiak, C.; Vieth, J. K. MOFs, MILs and More: Concepts, Properties and Applications for Porous Coordination Networks (PCNs). *New J. Chem.* **2010**, *34* (11), 2366.

(49) Férey, G. Hybrid Porous Solids: Past, Present, Future. *Chem. Soc. Rev.* **2008**, *37* (1), 191–214.

(50) Li, H.; Eddaoudi, M.; O'Keeffe, M.; Yaghi, O. M. Design and Synthesis of an Exceptionally Stable and Highly Porous Metal-Organic Framework. *Nature* **1999**, *402* (6759), 276–279.

(51) Eddaoudi, M.; Kim, J.; Rosi, N.; Vodak, D.; Wachter, J.; O'Keeffe, M.; Yaghi, O. M. Systematic Design of Pore Size and Functionality in Isoreticular MOFs and Their Application in Methane Storage. *Science.* **2002**, *295* (5554), 469–472.

(52) Ooms, K. J.; Wasylishen, R. E. ^{129}Xe NMR Study of Xenon in Iso-Reticular Metal–Organic Frameworks. *Microporous Mesoporous Mater.* **2007**, *103* (1–3), 341–351.

(53) Loiseau, T.; Serre, C.; Huguenard, C.; Fink, G.; Taulelle, F.; Henry, M.; Bataille, T.; Férey, G. A Rationale for the Large Breathing of the Porous Aluminum Terephthalate (MIL-53) Upon Hydration. *Chem. - A Eur. J.* **2004**, *10* (6), 1373–1382.

(54) Zhang, Y.; Gikonyo, B.; Khodja, H.; Gauthier, M.; Foy, E.; Goetz, B.; Serre, C.; Coste Leconte, S.; Pimenta, V.; Surblé, S. MIL-53 Metal–Organic Framework as a Flexible Cathode for Lithium-Oxygen Batteries. *Materials (Basel).* **2021**, *14* (16), 4618.

(55) Banerjee, M.; Das, S.; Yoon, M.; Hee, J. C.; Myung, H. H.; Se, M. P.; Seo, G.; Kim, O. Postsynthetic Modification Switches an Achiral Framework to Catalytically Active Homochiral Metal-Organic Porous Materials. *J. Am. Chem. Soc.* **2009**, *131* (22), 7524–7525.

(56) Wittmann, T.; Siegel, R.; Reimer, N.; Milius, W.; Stock, N.; Senker, J. Enhancing the Water Stability of Al-MIL-101-NH_2 via Postsynthetic Modification. *Chem. - A Eur. J.* **2015**, *21* (1), 314–323.

(57) Tanabe, K. K. K.; Cohen, S. M. M. Postsynthetic Modification of Metal–Organic Frameworks—a Progress Report. *Chem. Soc. Rev.* **2011**, *40* (2), 498–519.

(58) Tanabe, K. K.; Wang, Z.; Cohen, S. M. Systematic Functionalization of a Metal-Organic Framework via a Postsynthetic Modification Approach. *J. Am. Chem. Soc.* **2008**, *130* (26), 8508–8517.

(59) Garibay, S. J.; Cohen, S. M. Isoreticular Synthesis and Modification of Frameworks with the UiO-66 Topology. *Chem. Commun.* **2010**, *46* (41), 7700.

(60) Serre, C.; Millange, F.; Thouvenot, C.; Nogués, M.; Marsolier, G.; Louër, D.; Férey, G. Very Large Breathing Effect in the First Nanoporous Chromium(III)-Based Solids: MIL-53 or $Cr^{III}(OH)\cdot\{O_2C\text{-}C_6H_4\text{-}CO_2\}\cdot\{HO_2C\text{-}C_6H_4\text{-}CO_2H\}x\cdot H_2O$. *J. Am. Chem. Soc.* **2002**, *124* (45), 13519–13526.

(61) Férey, G.; Serre, C. Large Breathing Effects in Three-Dimensional Porous Hybrid Matter: Facts, Analyses, Rules and Consequences. *Chem. Soc. Rev.* **2009**, *38* (5), 1380–1399.

(62) Serra-Crespo, P.; Gobechiya, E.; Ramos-Fernandez, E. V.; Juan-Alcañiz, J.; Martinez-Joaristi, A.; Stavitski, E.; Kirschhock, C. E. A.; Martens, J. A.; Kapteijn, F.; Gascon, J. Interplay of Metal Node and Amine Functionality in NH_2-MIL-53: Modulating Breathing Behavior through Intra-Framework Interactions. *Langmuir* **2012**, *28* (35), 12916–12922.

(63) Alhamami, M.; Doan, H.; Cheng, C. H. A Review on Breathing Behaviors of Metal-Organic-Frameworks (MOFs) for Gas Adsorption. *Materials*. April 2014, pp 3198–3250.

(64) Schneemann, A.; Bon, V.; Schwedler, I.; Senkovska, I.; Kaskel, S.; Fischer, R. A. Flexible Metal-Organic Frameworks. *Chemical Society Reviews*. August 21, 2014, pp 6062–6096.

(65) Ding, M.; Cai, X.; Jiang, H. L. Improving MOF Stability: Approaches and Applications. *Chemical Science*. Royal Society of Chemistry 2019, pp 10209–10230.

(66) Healy, C.; Patil, K. M.; Wilson, B. H.; Hermanspahn, L.; Harvey-Reid, N. C.; Howard, B. I.; Kleinjan, C.; Kolien, J.; Payet, F.; Telfer, S. G.; Kruger, P. E.; Bennett, T. D. The Thermal Stability of Metal-Organic Frameworks. *Coord. Chem. Rev.* **2020**, *419*.

(67) Lin, R. B.; Li, L.; Wu, H.; Arman, H.; Li, B.; Lin, R. G.; Zhou, W.; Chen, B. Optimized Separation of Acetylene from Carbon Dioxide and Ethylene in a Microporous Material. *J. Am. Chem. Soc.* **2017**, *139* (23), 8022–8028.

(68) Serra-Crespo, P.; Berger, R.; Yang, W.; Gascon, J.; Kapteijn, F. Separation of CO_2/CH_4 Mixtures over NH_2-MIL-53 - An Experimental and Modelling Study. *Chem. Eng. Sci.* **2015**, *124*, 96–108.

(69) Boutin, A.; Coudert, F. X.; Springuel-Huet, M. A.; Neimark, A. V; Férey, G.; Fuchs, A. H. The Behavior of Flexible MIL-53(Al) upon CH_4 and CO_2 adsorption. *J. Phys. Chem. C* **2010**, *114* (50), 22237–22244.

(70) Si, X.; Jiao, C.; Li, F.; Zhang, J.; Wang, S.; Liu, S.; Li, Z.; Sun, L.; Xu, F.; Gabelica, Z.; Schick, C. High and Selective CO2 Uptake, H2 Storage and Methanol Sensing on the Amine-Decorated 12-Connected MOF CAU-1. *Energy Environ. Sci.* **2011**, *4* (11), 4522.

(71) Liu, H.; Zhao, Y.; Zhang, Z.; Nijem, N.; Chabal, Y. J.; Peng, X.; Zeng, H.; Li, J. Ligand Functionalization and Its Effect on CO2 Adsorption in Microporous Metal-Organic Frameworks. *Chem. - An Asian J.* **2013**, *8* (4), 778–785.

(72) Mihaylov, M.; Chakarova, K.; Andonova, S.; Drenchev, N.; Ivanova, E.; Pidko, E. A.; Sabetghadam, A.; Seoane, B.; Gascon, J.; Kapteijn, F.; Hadjiivanov, K. Adsorption of CO_2 on MIL-53(Al): FTIR Evidence of the Formation of Dimeric CO_2 Species. *Chem. Commun.* **2016**, *52* (7), 1494–1497.

(73) Baumann, A. E.; Burns, D. A.; Liu, B.; Thoi, V. S. Metal-Organic Framework Functionalization and Design Strategies for Advanced Electrochemical Energy Storage Devices. *Communications Chemistry*. Springer Nature December 1, 2019, pp 1–14.

(74) Li, S. L.; Xu, Q. Metal-Organic Frameworks as Platforms for Clean Energy. *Energy and Environmental Science*. The Royal Society of Chemistry 2013, pp 1656–1683.

(75) Horcajada, P.; Gref, R.; Baati, T.; Allan, P. K.; Maurin, G.; Couvreur, P.; Férey, G.; Morris, R. E.; Serre, C. Metal-Organic Frameworks in Biomedicine. *Chemical Reviews*. February 8, 2012, pp 1232–1268.

(76) Horcajada, P.; Chalati, T.; Serre, C.; Gillet, B.; Sebrie, C.; Baati, T.; Eubank, J. F.; Heurtaux, D.; Clayette, P.; Kreuz, C.; Chang, J.-S.; Hwang, Y. K.; Marsaud, V.; Bories, P.-N.; Cynober, L.; Gil, S.; Férey, G.; Couvreur, P.; Gref, R. Porous Metal–Organic-Framework Nanoscale Carriers as a Potential Platform for Drug Delivery and Imaging. *Nat. Mater.* **2010**, *9* (2), 172–178.

(77) Teplensky, M. H.; Fantham, M.; Li, P.; Wang, T. C.; Mehta, J. P.; Young, L. J.; Moghadam, P. Z.; Hupp, J. T.; Farha, O. K.; Kaminski, C. F.; Fairen-Jimenez, D. Temperature Treatment of Highly Porous Zirconium-Containing Metal-Organic Frameworks Extends Drug Delivery Release. *J. Am. Chem. Soc.* **2017**, *139* (22), 7522–7532.

(78) Atkins, P. W.; De Paula, J. *Physikalische Chemie*, 4. Auflage.; WILEY-VCH: Weinheim, 2006.

(79) Wikus, P.; Frantz, W.; Kümmerle, R.; Vonlanthen, P. Commercial Gigahertz-Class NMR Magnets. *Supercond. Sci. Technol.* **2022**, *35* (3), 033001.

(80) Schwalbe, H. Editorial: Die Neuen 1.2-GHz-NMR-Spektrometer Und Ihr Beitrag Zur Forschung. *Angew. Chemie* **2017**, *129* (35), 10386–10387.

(81) Biedenbänder, T.; Aladin, V.; Saeidpour, S.; Corzilius, B. Dynamic Nuclear Polarization for Sensitivity Enhancement in Biomolecular Solid-State NMR. *Chem. Rev.* **2022**, *122* (10), 9738–9794.

(82) Lilly Thankamony, A. S.; Wittmann, J. J.; Kaushik, M.; Corzilius, B. Dynamic Nuclear Polarization for Sensitivity Enhancement in Modern Solid-State NMR. *Prog. Nucl. Magn. Reson. Spectrosc.* **2017**, *102–103*, 120–195.

(83) Bouchiat, M. A.; Carver, T. R.; Varnum, C. M. Nuclear Polarization in He-3 Gas Induced by Optical Pumping and Dipolar Exchange. *Phys. Rev. Lett.* **1960**, *5* (8), 373–375.

(84) Bhaskar, N. D.; Happer, W.; McClelland, T. Efficiency of Spin Exchange between Rubidium Spins and Xe129 Nuclei in a Gas. *Phys. Rev. Lett.* **1982**, *49* (1), 25–28.

(85) Happer, W.; Miron, E.; Schaefer, S.; Schreiber, D.; van Wijngaarden, W. A.; Zeng, X.; van Wijngaarden, W.; Zeng, X. Polarization of the Nuclear Spins of Noble-Gas Atoms by Spin Exchange with Optically Pumped Alkali-Metal Atoms. *Phys. Rev. A* **1984**, *29* (6), 3092–3110.

(86) Appelt, S.; Ben-Amar Baranga, A.; Erickson, C. J.; Romalis, M. V.; Young, A. R.; Happer, W. Theory of Spin-Exchange Optical Pumping Of3He And129Xe. *Phys. Rev. A - At. Mol. Opt. Phys.* **1998**, *58* (2), 1412–1439.

(87) Grover, B. C. Noble-Gas NMR Detection through Noble-Gas-Rubidium Hyperfine Contact Interaction. *Phys. Rev. Lett.* **1978**, *40* (6), 391–392.

(88) Walker, T. G.; Happer, W. Spin-Exchange Optical Pumping of Noble-Gas Nuclei. *Rev. Mod. Phys.* **1997**, *69* (2), 629–642.

(89) Hrycyshyn, E. S.; Krause, L. Inelastic Collisions between Excited Alkali Atoms and Molecules. VII. Sensitized Fluorescence and Quenching in Mixtures of Rubidium with H_2, HD, D_2, N_2, CH_4, CD_4, C_2H_4 and C_2H_6. *Can. J. Phys.* **1970**, *48* (22), 2761–2768.

(90) Cates, G.; Fitzgerald, R.; Barton, A.; Bogorad, P.; Gatzke, M.; Newbury, N. R.; Saam, B. Rb-^{129}Xe Spin-Exchange Rates Due to Binary and Three-Body Collisions at High Xe Pressures. *Phys. Rev. A* **1992**, *45* (7), 4631–4639.

(91) Jau, Y.-Y. High-Field Measurement of the ^{129}Xe-Rb Spin-Exchange Rate Due to Binary Collisions. *Phys. Rev. A* **2002**, *66* (5), 52710.

(92) Knagge, K.; Prange, J.; Raftery, D. A Continuously Recirculating Optical Pumping Apparatus for High Xenon Polarization and Surface NMR Studies. *Chem. Phys. Lett.* **2004**, *397* (1–3), 11–16.

(93) Wojna-Pelczar, A.; Pa?asz, T. A High Volume, Batch Mode ^{129}Xe Polarizer. *Nucl. Instruments Methods Phys. Res. Sect. A Accel. Spectrometers, Detect. Assoc. Equip.* **2017**, *856*, 65–71.

(94) Moudrakovski, I. L.; Lang, S.; Ratcliffe, C. I.; Simard, B.; Santyr, G.; Ripmeester, J. A. Chemical Shift Imaging with Continuously Flowing Hyperpolarized Xenon for the Characterization of Materials. *J. Magn. Reson.* **2000**, *144* (2), 372–377.

(95) Norquay, G.; Collier, G. J.; Rao, M.; Stewart, N. J.; Wild, J. M. Xe-129 - Rb Spin-Exchange Optical Pumping with High Photon Efficiency. *Phys. Rev. Lett.* **2018**, *121* (15), 153201.

(96) Schrank, G.; Ma, Z.; Schoeck, A.; Saam, B. Characterization of a Low-Pressure High-Capacity Xe-129 Flow-through Polarizer. *Phys. Rev. A - At. Mol. Opt. Phys.* **2009**, *80* (6), 063424.

(97) Ruset, I. C.; Ketel, S.; Hersman, F. W. Optical Pumping System Design for Large Production of Hyperpolarized ^{129}Xe. *Phys. Rev. Lett.* **2006**, *96* (5), 053002.

(98) Freeman, M. S.; Emami, K.; Driehuys, B. Characterizing and Modeling the Efficiency Limits in Large-Scale Production of Hyperpolarized Xe-129. *Phys. Rev. A* **2014**, *90* (2), 023406.

(99) Whiting, N.; Nikolaou, P.; Eschmann, N. A.; Barlow, M. J.; Lammert, R.; Ungar, J.; Hu, W.; Vaissie, L.; Goodson, B. M. Using Frequency-Narrowed, Tunable Laser Diode Arrays with Integrated Volume Holographic Gratings for Spin-Exchange Optical Pumping at High Resonant Fluxes and Xenon Densities. *Appl. Phys. B Lasers Opt.* **2012**, *106* (4), 775–788.

(100) Nikolaou, P.; Coffey, A. M.; Walkup, L. L.; Gust, B. M.; Whiting, N.; Newton, H.; Muradyan, I.; Dabaghyan, M.; Ranta, K.; Moroz, G. D.; Rosen, M. S.; Patz, S.; Barlow, M. J.; Chekmenev, E. Y.; Goodson, B. M. XeNA: An Automated ‘Open-Source’ ^{129}Xe Hyperpolarizer for Clinical Use. *Magn. Reson. Imaging* **2014**, *32* (5), 541–550.

(101) Rosen, M. S.; Chupp, T. E.; Coulter, K. P.; Welsh, R. C.; Swanson, S. D. Polarized 129Xe Optical Pumping/Spin Exchange and Delivery System for Magnetic Resonance Spectroscopy and Imaging Studies. *Rev. Sci. Instrum.* **1999**, *70* (2), 1546–1552.

(102) Driehuys, B.; Cates, G. D.; Miron, E.; Sauer, K.; Walter, D. K.; Happer, W. High-volume Production of Laser-polarized ^{129}Xe. *Appl. Phys. Lett.* **1996**, *69* (12), 1668–1670.

(103) Brunner, E. Applications of Laser-Polarized ^{129}Xe under Continuous Flow. *Magn. Reson. Chem.* **1999**, *37* (13), S14–S22.

(104) Cros, F.; Korb, J.-P.; Malier, L. Spectroscopic Mesopore Size Characterization and Diffusion Measurement in Closed Porosity by Xenon NMR. *Langmuir* **2000**, *16* (26), 10193–10197.

(105) Clewett, C. F. M.; Morgan, S. W.; Saam, B.; Pietraß, T. Optically Polarized ^{129}Xe Investigation of Carbon Nanotubes. *Phys. Rev. B* **2008**, *78* (23), 235402.

(106) Romanenko, K. V.; Lapina, O. B.; Py, X.; Fraissard, J. Xe-129 NMR Spectroscopy of Adsorbed Xenon: Possibilites for Exploration of Microporous Carbon Materials. *Russ. J. Gen. Chem.* **2008**, *78* (11), 2171–2181.

(107) Oschatz, M.; Hoffmann, H. C.; Pallmann, J.; Schaber, J.; Borchardt, L.; Nickel, W.; Senkovska, I.; Rico-Francés, S.; Silvestre-Albero, J.; Kaskel, S.; Brunner, E. Structural Characterization of Micro- and Mesoporous Carbon Materials Using In Situ High Pressure ^{129}Xe NMR Spectroscopy. *Chem. Mater.* **2014**, *26* (10), 3280–3288.

(108) Weiland, E.; Springuel-Huet, M.-A.; Nossov, A.; Guenneau, F.; Quoineaud, A.-A.; Gédéon, A. Exploring the Complex Porosity of Transition Aluminas by ^{129}Xe NMR Spectroscopy. *J. Phys. Chem. C* **2015**, *119* (27), 15285–15291.

(109) Comotti, A.; Bracco, S.; Sozzani, P.; Horike, S.; Matsuda, R.; Chen, J.; Takata, M.; Kubota, Y.; Kitagawa, S. Nanochannels of Two Distinct Cross-Sections in a Porous Al-Based Coordination Polymer. *J. Am. Chem. Soc.* **2008**, *130* (41), 13664–13672.

(110) Meersmann, T.; Logan, J. W.; Simonutti, R.; Caldarelli, S.; Comotti, A.; Sozzani, P.; Kaiser, L. G.; Pines, A. Exploring Single-File Diffusion in One-Dimensional Nanochannels by Laser-Polarized ^{129}Xe NMR Spectroscopy. *J. Phys. Chem. A* **2000**, *104* (50), 11665–11670.

(111) Springuel-Huet, M. A.; Fraissard, J. ^{129}Xe NMR of Xenon Adsorbed on the Molecular Sieves $AlPO_4$-11 and SAPO-11. Chemical Shift Anisotropy Related to the Asymmetry of the Adsorption Zones. *Chem. Phys. Lett.* **1989**, *154* (4), 299–302.

(112) Moudrakovski, I.; Soldatov, D. V; Ripmeester, J. A.; Sears, D. N.; Jameson, C. J. Xe NMR Lineshapes in Channels of Peptide Molecular Crystals. *Proc. Natl. Acad. Sci.* **2004**, *101* (52), 17924–17929.

(113) Klein, N.; Herzog, C.; Sabo, M.; Senkovska, I.; Getzschmann, J.; Paasch, S.; Lohe, M. R.; Brunner, E.; Kaskel, S. Monitoring Adsorption-Induced Switching by ^{129}Xe NMR Spectroscopy in a New Metal-Organic Framework $Ni_2(2,6\text{-ndc})_2(\text{dabco})$. *Phys. Chem. Chem. Phys.* **2010**, *12* (37), 11778–11784.

(114) Klein, N.; Hoffmann, H. C.; Cadiau, A.; Getzschmann, J.; Lohe, M. R.; Paasch, S.; Heydenreich, T.; Adil, K.; Senkovska, I.; Brunner, E.; Kaskel, S. Structural Flexibility and Intrinsic Dynamics in the $M_2(2,6\text{-ndc})_2(\text{dabco})$ (M = Ni, Cu, Co, Zn) Metal–Organic Frameworks. *J. Mater. Chem.* **2012**, *22* (20), 10303.

(115) Giovine, R.; Volkringer, C.; Springuel-Huet, M.-A.; Nossov, A.; Blanc, F.; Trébosc, J.; Loiseau, T.; Amoureux, J.-P.; Lafon, O.; Pourpoint, F. Study of Xenon Mobility in the Two Forms of MIL-53(Al) Using Solid-State NMR Spectroscopy. *J. Phys. Chem. C* **2017**, *121* (35), 19262–19268.

(116) Boutin, A.; Springuel-Huet, M.-A.; Nossov, A.; Gédéon, A.; Loiseau, T.; Volkringer, C.; Férey, G.; Coudert, F.-X.; Fuchs, A. H. Breathing Transitions in MIL-53(Al) Metal-Organic Framework Upon Xenon Adsorption. *Angew. Chemie Int. Ed.* **2009**, *48* (44), 8314–8317.

(117) Khan, A. S.; Harvey, R. L.; Birchall, J. R.; Irwin, R. K.; Nikolaou, P.; Schrank, G.; Emami, K.; Dummer, A.; Barlow, M. J.; Goodson, B. M.; Chekmenev, E. Y. Enabling Clinical Technologies for Hyperpolarized ^{129}Xenon Magnetic Resonance Imaging and Spectroscopy. *Angew. Chemie - Int. Ed.* **2021**, *60* (41), 22126–22147.

(118) Mata, J.; Guan, S.; Qing, K.; Tustison, N.; Shim, Y.; Mugler, J. P.; Altes, T.; Huaromo, J.; Mehrad, B. Evaluation of Regional Lung Function in Pulmonary Fibrosis with Xenon-129 MRI. *Tomography* **2021**, *7* (3), 452–465.

(119) Qing, K.; Tustison, N. J.; Mugler, J. P.; Mata, J. F.; Lin, Z.; Zhao, L.; Wang, D.; Feng, X.; Shin, J. Y.; Callahan, S. J.; Bergman, M. P.; Ruppert, K.; Altes, T. A.; Cassani, J. M.; Shim, Y. M. Probing Changes in Lung Physiology in COPD Using CT, Perfusion MRI, and Hyperpolarized Xenon-129 MRI. *Acad. Radiol.* **2019**, *26* (3), 326–334.

(120) Grist, J. T.; Chen, M.; Collier, G. J.; Raman, B.; Abueid, G.; McIntyre, A.; Matthews, V.; Fraser, E.; Ho, L.-P.; Wild, J. M.; Gleeson, F. Hyperpolarized ^{129}Xe MRI Abnormalities in Dyspneic Patients 3 Months after COVID-19 Pneumonia: Preliminary Results. *Radiology* **2021**, *301* (1), E353–E360.

(121) Li, H.; Zhang, Z.; Zhao, X.; Han, Y.; Sun, X.; Ye, C.; Zhou, X. Quantitative Evaluation of Pulmonary Gas-Exchange Function Using Hyperpolarized ^{129}Xe CEST MRS and MRI. *NMR Biomed.* **2018**, *31* (9), e3961.

(122) Möller, H. E.; Chen, X. J.; Chawla, M. S.; Driehuys, B.; Hedlund, L. W.; Johnson, G. A. Signal Dynamics in Magnetic Resonance Imaging of the Lung with Hyperpolarized Noble Gases. *J. Magn. Reson.* **1998**, *135* (1), 133–143.

(123) Kunth, M.; Witte, C.; Schröder, L. Continuous-Wave Saturation Considerations for Efficient Xenon Depolarization. *NMR Biomed.* **2015**, *28* (6), 601–606.

(124) Spence, M. M.; Rubin, S. M.; Dimitrov, I. E.; Ruiz, E. J.; Wemmer, D. E.; Pines, A.; Yao, S. Q.; Tian, F.; Schultz, P. G. Functionalized Xenon as a Biosensor. **2001**, *98* (19), 10654–10657.

(125) Bartik, K.; Luhmer, M.; Dutasta, J. P.; Collet, A.; Reisse, J. 129Xe and 1H NMR Study of the Reversible Trapping of Xenon by Cryptophane-A in Organic Solution. *J. Am. Chem. Soc.* **1998**, *120* (4), 784–791.

(126) Schröder, L.; Lowery, T. J.; Hilty, C.; Wemmer, D. E.; Pines, A. Molecular Imaging Using a Targeted Magnetic Resonance Hyperpolarized Biosensor. *Science* **2006**, *314* (5798), 446–449.

(127) Zhang, H.; Chen, S.; Yuan, Y.; Li, Y.; Jiang, Z.; Zhou, X. ^{129}Xe Hyper-CEST/ ^{19}F MRI Multimodal Imaging System for Sensitive and Selective Tumor Cells Detection. *ACS Appl. Bio Mater.* **2019**, *2* (1), 27–32.

(128) Wu, Y.; Wood, T. C.; Arzanforoosh, F.; Hernandez-Tamames, J. A.; Barker, G. J.; Smits, M.; Warnert, E. A. H. 3D APT and NOE CEST-MRI of Healthy Volunteers and Patients with Non-Enhancing Glioma at 3 T. *Magn. Reson. Mater. Physics, Biol. Med.* **2022**, *35* (1), 63–73.

(129) McHugh, C. T.; Durham, P. G.; Kelley, M.; Dayton, P. A.; Branca, R. T. Magnetic Resonance Detection of Gas Microbubbles via HyperCEST: A Path Toward Dual Modality Contrast Agent. *ChemPhysChem* **2021**, *22* (12), 1219–1228.

(130) *The Chemistry of Metal-Organic Frameworks: Synthesis, Characterization, and Applications*; Kaskel, S., Ed.; Wiley-VCH Verlag GmbH & Co. KGaA: Weinheim, Germany, 2016.

3. Synopsis

Die vorliegende Arbeit besteht aus drei Publikationen und einem Manuskript, welche sich mit der Erzeugung von hyperpolarisiertem (HP) ^{129}Xe, sowie dessen Verwendung zur Charakterisierung des Porenraumes poröser Funktionsmaterialien (Kapitel 3 und 4) mittels ^{129}Xe-NMR-Spektroskopie beschäftigen.

Neben dem hier dokumentierten Aufbau und der Charakterisierung einer an der Universität Bayreuth entwickelten Polarisationsapparatur, die sich besonders durch ihr erreichtes Polarisationsvolumen auszeichnet, wird HP ^{129}Xe-NMR spektroskopisch dazu verwendet, um strukturelle und dynamische Eigenschaften im Porenraum von metallorganischen Gerüstverbindungen, sowie porösen Silica-Hohlkugeln zu analysieren. Über die üblichen Charakterisierungsmethoden poröser Funktionsmaterialien, wie Gasphysisorption oder Pulverröntgendiffraktion hinausgehend, kann ^{129}Xe-NMR-Spektroskopie kleinste Änderungen im Porenraum detektieren. Um hierbei eine möglichst präzise Interpretation der ^{129}Xe-NMR Spektren zu ermöglichen, wurden Strukturmodelle von Xe Atomen im Porenraum erzeugt und mittels quantenchemischer Rechnungen entsprechende NMR Parameter modelliert. Hierbei fand die *gauge including projector augmented wave* (GIPAW) Methode unter periodischen Randbedingungen Anwendung. Aus den in dieser Arbeit präsentierten Ergebnissen wurde damit die Anwendungsreife der Porenanalytik mittels ^{129}Xe-NMR-Spektroskopie bewiesen.

3.1. Entwicklung einer Apparatur zur Erzeugung von hyperpolarisiertem ^{129}Xe

Eines der Hauptziele dieser Arbeit bestand in der Weiterentwicklung einer Apparatur zur Bereitstellung eines kontinuierlichen Gasstroms an hyperpolarisiertem ^{129}Xe. Da eine solche Apparatur nicht kommerziell erhältlich ist, wurde das Design, sowie die Konstruktion vollständig an der Universität Bayreuth entwickelt. Die zugrundeliegenden Herausforderungen beim Design einer solchen Anlage liegen vor allem in der Handhabung gasförmigen Rubidiums, dem Umgang von Gasen bei Drücken im Bereich von 2 bis 6 bar, sowie der Entwicklung einer transparenten Bewegungsstrecke des Gasgemisches zur maximalen Absorption von Laserlicht (Pumpzelle). Ferner reagiert die erzeugte Polarisation empfindlich auf metallische Werkstoffe, wodurch vor allem auf Glas und Kunststoffe als Materialien zurückgegriffen werden musste. Neben der eigentlichen Konstruktion ist die Höhe der erzeugten Polarisation, die sich im zweistelligen Prozentbereich befindet, von einer Anzahl an Betriebsparametern abhängig. Daher musste zur Charakterisierung der Apparatur und dem Ermitteln optimaler Betriebsbedingungen ein mehrdimensionaler Parameterraum abgetastet werden. Aus diesem Grund beschäftigt sich die vorliegende Arbeit mit der Weiterentwicklung des ursprünglichen Designs, welches grundlegend von Caroline Keenan entwickelt wurde, sowie der Optimierung der Parameter mit dem Ziel einer hohen und stabilen ^{129}Xe Polarisation.

Beim entwickelten Design des konstruierten Polarisators entschied man sich für eine Hochdruckapparatur ($p > 2$ bar), um die Druckverbreiterung der Laserabsorptionslinie des Rubidiums zu nutzen. Damit konnte auf komplexe optische Bauelemente zur Linienverschmälerung des Laserprofils verzichtet werden. Zwei konstruktive Merkmale der Apparatur, welche im bereits bestehenden Design implementiert wurden, sind an dieser Stelle besonders erwähnenswert und in dieser Form einzigartig, nämlich die Pumpzelle und das Rb-Reservoir. Der Entwurf der Pumpzelle besteht in seiner Form aus zwei parallelen zylindrischen Kammern, die senkrecht in der Apparatur angebracht sind. Dies verringert die Entstehung von Turbulenzen im Gasstrom aufgrund von Konvektionseffekten.

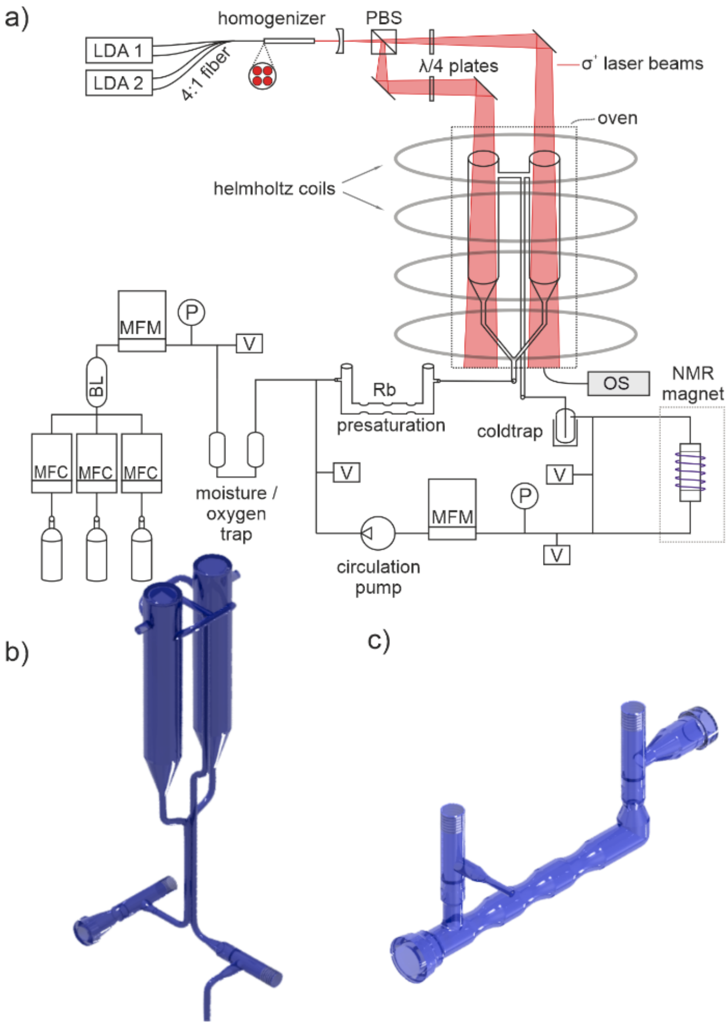

Abb. 3.1: Details der konstruierten und verwendeten Apparatur zur Erzeugung von HP ^{129}Xe. a) Schematischer Aufbau inkl. Laserpfad. LDA: laser diode array, PBS: polarizing beam splitter, MFC: mass flow controller, BL: ballast tank, MFM: mass flow meter, P: pressure meter, V: turbomolecular pump access, OS: optical spectrometer. b) CAD-Modell der zweischenkligen, optischen Pumpzelle in vertikaler Ausrichtung. c) CAD-Modell der Rb-Vorsättigungszelle mit mehreren Kammern. Die realen Bauteile sind aus Glas gefertigt, die blaue Farbe dient der Verbesserung des Kontrasts. Abdruck mit Genehmigung Stäglich, R.; Kemnitzer, T. et al. J. Phys. Chem. A 2022, 126 (16), 2578–2589. Copyright 2022 American Chemical Society.

Auf diese Weise können Wandkontakte des Gases vermieden werden, was zu einer zusätzlichen Depolarisation führen würde. Das Radius-Längen-Verhältnis beträgt 0.07 und wurde auf ein optimales Oberflächen-zu-Volumen-Verhältnis eingestellt.

Um die Länge der Zelle möglichst kompakt zu halten, fließt das Gasgemisch parallel durch die beiden zuvor genannten Zylinder. Der Strahlweg des Lasers verläuft dabei entgegengesetzt zur Flussrichtung des Gasgemisches. Dies sorgt für eine optimale Ausleuchtung und einer Maximierung der Photonendichte innerhalb der Pumpzelle. Das notwendige Rb wird nicht direkt in der Pumpzelle vorgelegt, sondern in einer Vorsättigungszelle verdampft, die zur Oberflächenvergrößerung über mehrere Kammern verfügt und separat beheizt werden kann. Das verwendete Gasgemisch strömt dabei vor Eintritt in die Pumpzelle durch die Vorsättigungszelle und trägt durch Erhitzen erzeugten Rb-Dampf mit sich. Auf diese Weise kann sowohl durch die Wahl der Temperatur der Vorsättigungszelle, aber auch über die Beladung und Verteilung von Rubidium die Rate der Erzeugung von Rb-Dampf kontrolliert werden. Zudem verhindert dieser Aufbau die Gefahr des sogenannten *Rubidium runaway*, bei dem durch Hitze und hohe Photonendichte die Verdampfungsrate von Rb immer weiter ansteigt. Der schematische Aufbau der Polarisationsapparatur, inklusive dem Laserpfad, sowie das Design der verwendeten Pump- und Vorsättigungszelle sind in Abb. 3.1 a), respektive b) und c) dargestellt.

Zur Charakterisierung der optimalen Betriebsbedingungen wurden mehrere Messreihen unter Einsatz unterschiedlicher Rb-Beladung durchgeführt. In allen Experimenten wurde dabei die erreichte Polarisation von ^{129}Xe als Ergebnis betrachtet, da das Ziel eine Maximierung ebendieser Polarisation ist. Ein wichtiger Faktor bei der Charakterisierung ist die Verweilzeit des Gasgemisches innerhalb der Pumpzelle. Das Gas wird mittels einer ölfreien Drehschieberpumpe durch das gesamte System zirkuliert und der Volumenstrom mit einem Massenflussmesser aufgezeichnet. Durch Veränderung der Zirkulationsgeschwindigkeit kann somit auch die Verweilzeit τ_{res}^{tot} innerhalb der Pumpzelle bestimmt werden und beträgt in Abhängigkeit des Drucks P und des Volumenstroms $\dot{V}$ unter Normalbedingungen:

$$\tau_{res}^{tot} = 31240 \frac{mL \cdot s}{bar \cdot min} \cdot \frac{P}{\dot{V}}$$

In Messreihe I wurde eine voreingestellte Gasmischung (1 vol% Xe, 3 vol% N_2, 96 vol% He) vorgelegt, die während der Testreihen nicht mehr verändert wurde. Unter Verwendung dieser Gasmischung wurden systematisch Druck, Laserleistung und Flussrate / Verweilzeit variiert. Das Ergebnis muss aufgrund des mehrdimensional abgetasteten Parameterraums in mehreren Teilen aufgezeigt und diskutiert werden. Wird die Polarisation als Funktion der Laserleistung aufgetragen (siehe Abb. 3.2a), so zeigt sich in fast allen Fällen, dass diese mit zunehmender

Leistung ansteigt. Dies ist im Einklang mit Formel 1.2, welche zeigt, dass die Rb-Polarisation mit zunehmender optischer Pumprate ansteigt und damit ebenfalls die an ^{129}Xe transferierte Polarisation, welche einen Maximalwert von 22 % erreicht. Es zeigte sich, dass im niedrigen Druckbereich die erreichte Polarisation von der Verweilzeit in der Pumpzelle nahezu unabhängig ist und bereits bei kleinstmöglichen Verweilzeiten die maximale Polarisation erreicht wurde. Bei einem Systemdruck von 4 und 5 bar, sank die erreichbare Polarisation deutlich und es war ein zunehmender Einfluss der Verweilzeit erkennbar.

Bei hohem Druck und hoher Verweilzeit zeigte sich sogar ein zunehmender Depolarisationseffekt. Wird die Polarisation gegen die Verweilzeit aufgetragen, ist am Kurvenverlauf sehr deutlich erkennbar, dass sowohl Aufbau und Zerfall der Polarisation in verschiedenen Verweilzeitregimen unterschiedlich stark ausgeprägt sind (siehe Abb. 3.2b). Die Polarisation baute sich zu höheren Verweilzeiten zu einem Maximum auf und fiel anschließend asymptotisch wieder ab. Dieser Effekt war bei einer höheren Beladung der Vorsättigungszelle noch ausgeprägter, da hier bei minimal möglicher Verweilzeit bereits das Polarisationsmaximum erreicht war.

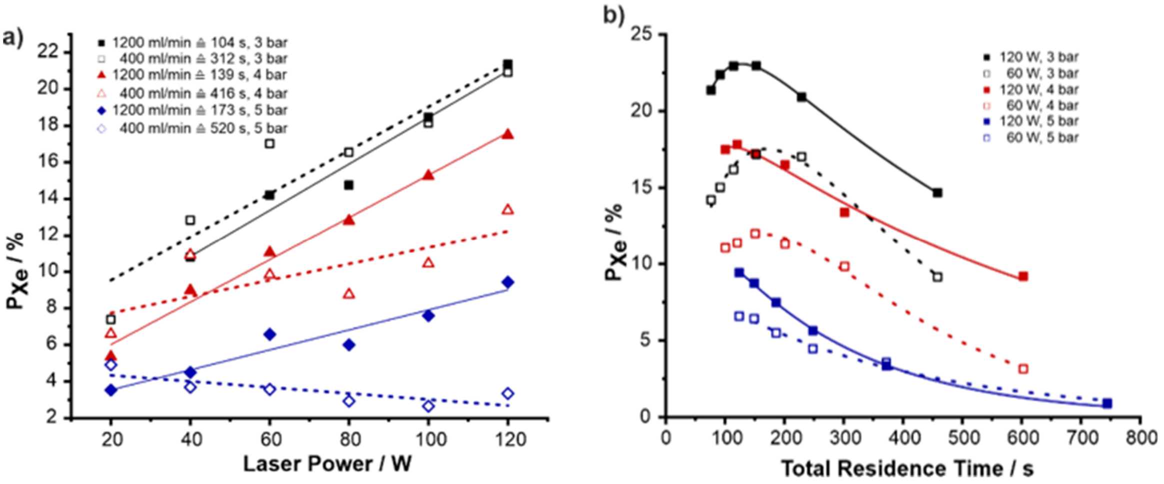

Abb. 3.2 Darstellung der gemessenen ^{129}Xe Polarisation von Messreihe I in Abhängigkeit unterschiedlicher Betriebsparameter des Polarisators bei halb gefüllter Vorsättigungszelle und unterschiedlichem Betriebsdruck (schwarz: 3 bar, rot: 4 bar, blau: 5 bar). a) Polarisation in Abhängigkeit der Laserleistung bei minimaler (offene Symbole, gestrichelte Trendlinie) und maximaler (geschlossene Symbole, durchgängige Trendlinie) Flussrate. b) Polarisation in Abhängigkeit der Verweilzeit bei minimaler (offene Symbole, gestrichelte Trendlinie) und maximaler (geschlossene Symbole, durchgängige Trendlinie) Laserleistung. Abdruck mit Genehmigung Stäglich, R.; Kemnitzer, T. et al. J. Phys. Chem. A 2022, 126 (16), 2578–2589. Copyright 2022 American Chemical Society.

Aus der Variation der Verhältnisse zwischen Xe, N_2 und He bei unterschiedlichen Betriebsdrücken in Messreihe II konnte eine optimale Gaszusammensetzung für maximale ^{129}Xe Polarisation ermittelt werden. Diese liegt bei einer Zusammensetzung von 0.5 vol% Xe, 5 vol% N_2 und 95.5 vol% He. Die hier maximal erreichten Polarisationswerte bei einem Gesamtdruck von 2.5 bar und einer Laserleistung von 120 W liegen ebenfalls bei ca. 22 %. Unter Berücksichtigung der optimalen Verweilzeiten und der damit verbundenen Menge an polarisiertem

Volumen von ^{129}Xe erreichte der Polarisator *magnetization production rate* (MPR) von ca. 70 mL/h.

Neben der Maximalpolarisation spielt die Stabilität der erreichten Polarisation von ^{129}Xe, vor allem bei der Anwendung in 2D-NMR Experimenten, eine wichtige Rolle. Die Aufnahmezeit solcher 2D-Spektren kann mehrere Stunden betragen. Während dieser Zeit muss eine konstante Polarisation gewährleistet werden, da eine Fluktuation unweigerlich zu einer Veränderung der aufgenommenen Signalintensitäten führen würde. Dies hätte Signalartefakte zur Folge und macht eine quantitative Auswertung solcher Messungen unmöglich. Aus diesem Grund wurden ^{129}Xe-2D-EXSY Spektren (siehe Abb. 3.3) von postsynthetisch modifiziertem CAU-1 aufgenommen, um die Langzeitstabilität der erhaltenen Polarisation zu beweisen. Zusätzlich wurde hier die *stop-and-flow* Technik eingesetzt, wobei der Gasfluss während eines NMR-Experiments gestoppt wurde. In der Wartezeit zwischen den Experimenten wurde dieser Fluss wiederaufgenommen, um neu polarisiertes Gas in den Probenraum fließen zu lassen. Dies verhindert ein Ausströmen von angeregten ^{129}Xe Kernen in der Gasphase während der einzelnen Transienten der EXSY-Sequenz.

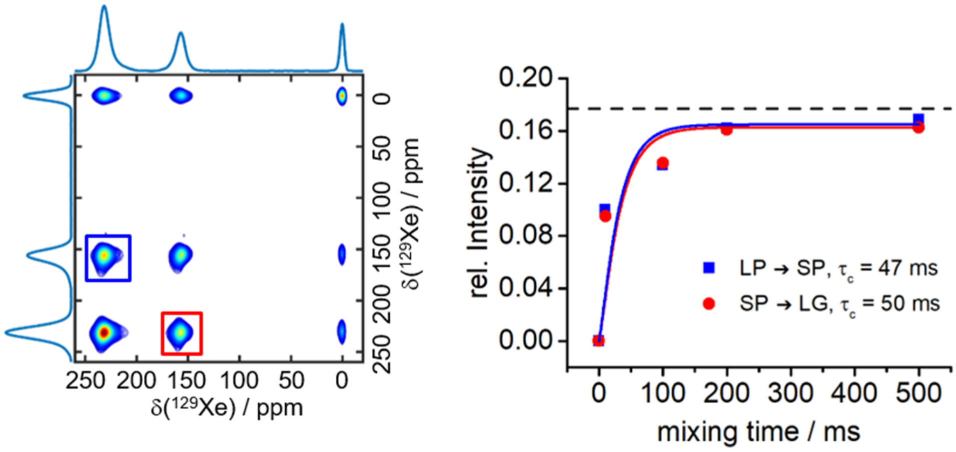

Abb. 3.3 links: ^{129}Xe-2D-EXSY Spektrum von CAU-1-AmMe bei 160K und τ_{mix} = 500ms, aufgenommen unter stop-and-flow Bedingungen. Es sind deutlich ausgeprägte Kreuzintensitäten zwischen den unterschiedlichen Porentypen (large pore = LP, small pore = SP) zu erkennen. Rechts: Aufbaukurve der Kreuzintensitäten für den Gasaustausch LP ↔ SP und der daraus berechneten Korrelationszeiten τ_c. Abdruck mit Genehmigung Stäglich, R.; Kemnitzer, T. et al. J. Phys. Chem. A 2022, 126 (16), 2578–2589. Copyright 2022 American Chemical Society.

Die Messung bei unterschiedlichen Austauschzeiten im Bereich von 2 – 500 ms zeigte keinerlei Anzeichen der besagten Artefakte. Zudem wurden die Signale adsorbierten Xenons innerhalb der verschiedenen Kavitäten genutzt, um Austauschraten und somit Diffusionsgeschwindigkeiten erfolgreich zu bestimmen. Zwischen den unterschiedlichen Porengrößen wurde eine Austauschkorrelationszeit t_c von ca. 50 ms bestimmt (siehe Abb. 3.3.)

Die vorgestellten Ergebnisse zeigen den großen Erfolg in der Weiterentwicklung und Optimierung der verwendeten ^{129}Xe-Polarisationsapparatur. Neben dem einzigartigen Design der Pumpzelle konnte eine Polarisation von bis zu 22 % erreicht werden und liegt damit um eine Größenordnung höher als bei *continuous flow* Polarisatoren anderer Arbeitsgruppen. Die erreichte Langzeitstabilität ermöglichte die Aufnahme von quantitativen 2D-Austauschspektren. Die Ermittlung optimaler Betriebsparameter für maximale ^{129}Xe Polarisation gestaltete sich aufgrund des mehrdimensionalen Parameterraums als aufwändig. Als Resultat gab diese aber Aufschluss über das Verweilzeitverhalten innerhalb der Pumpzelle und dessen Einfluss auf den Aufbau der letztlich gemessenen ^{129}Xe Polarisation bei unterschiedlicher Rb-Beladung, Druck und Laserleistung.

3.2. Strukturelle Veränderung kalzinierter Silica-Hohlkugeln

Die Leistungsfähigkeit und Sensitivität von ^{129}Xe-NMR-Spektroskopie als lokal auflösende Methode neben der klassischen Festkörper NMR-Spektroskopie zeigt sich beispielhaft in der Untersuchung kolloidaler Kristalle von Silica-Hohlkugeln in Abhängigkeit der Kalzinierungstemperatur. Bei den hier untersuchten Proben handelt es sich um eine Materialklasse, für die bereits Korrelationen in der ^{129}Xe-NMR-Spektroskopie untersucht wurden. Herausfordernd in diesem Zusammenhang ist jedoch die sehr geringe Porosität der Hohlkugeln, welche mit klassischen Physisorptionsmethoden teilweise nicht mehr aufgelöst werden konnte.

Diese Hohlkugeln wurden durch die Beschichtung von monodispersen Polystyrol-Latexpartikeln mit Silica unter Verwendung des Stöber-Prozesses hergestellt. Der organische Precursor wurde anschließend durch Kalzinieren bei Temperaturen von 500 – 950 °C für 12 h entfernt. Die Hohlkugeln erzeugten kolloidale Kristalle mit äußerst geringen Wärmeleitfähigkeitskoeffizienten. Es zeigte sich, dass die resultierende Wärmeleitfähigkeit κ stark von der Temperatur während des Kalzinierungsprozesses abhängig ist und ändert sich von $\kappa = 71\ \mathrm{mW\ m^{-1}\ K^{-1}}$ bei 500 °C Kalzinierungstemperatur auf $\kappa = 140\ \mathrm{mW\ m^{-1}\ K^{-1}}$ bei 950 °C. Die Größe und Dichte der Hohlkugeln wurde hierbei kaum beeinflusst, was eine temperaturbedingte Veränderung der mikroskopischen Struktur des Silica-Materials zur Folge haben muss.

Aufgrund der fehlenden Fernordnung konnten keine Diffraktionsmethoden zur Strukturklärung verwendet werden, weshalb hier die Anwendung von NMR-Spektroskopie als lokale Methode hilfreich erschien. Anhand von ^{29}Si-NMR-Spektroskopie konnte der Anteil von Q^3 und Q^4-Einheite für jede Kalzinierungstemperatur ermittelt werden, um Rückschlüsse auf den Vernetzungsgrad der $(\mathrm{Si{-}O})_n$ Einheiten zu ziehen. Mit Erhöhung der Kalzinierungstemperatur stieg die Anzahl an Q^4-Einheiten von 88 % (500 °C) auf bis zu 94 % (950 °C), und damit der Grad der Quervernetzung. Gleichzeitig wurde ein signifikanter Anstieg der Spin-Gitter Relaxationszeit (T_1) beobachtet, der auch als ein Maß der Beweglichkeit der Si-Atome innerhalb des Netzwerks fungiert. Diese stieg mit der Kalzinierungstemperatur von 33 s (500 °C) auf 6400 s (950 °C) an. Anhand von ^{129}Xe-NMR-Spektroskopie in Kombination mit N_2 Physisorption wurde die Entwicklung der vorhandenen Porosität des Materials in

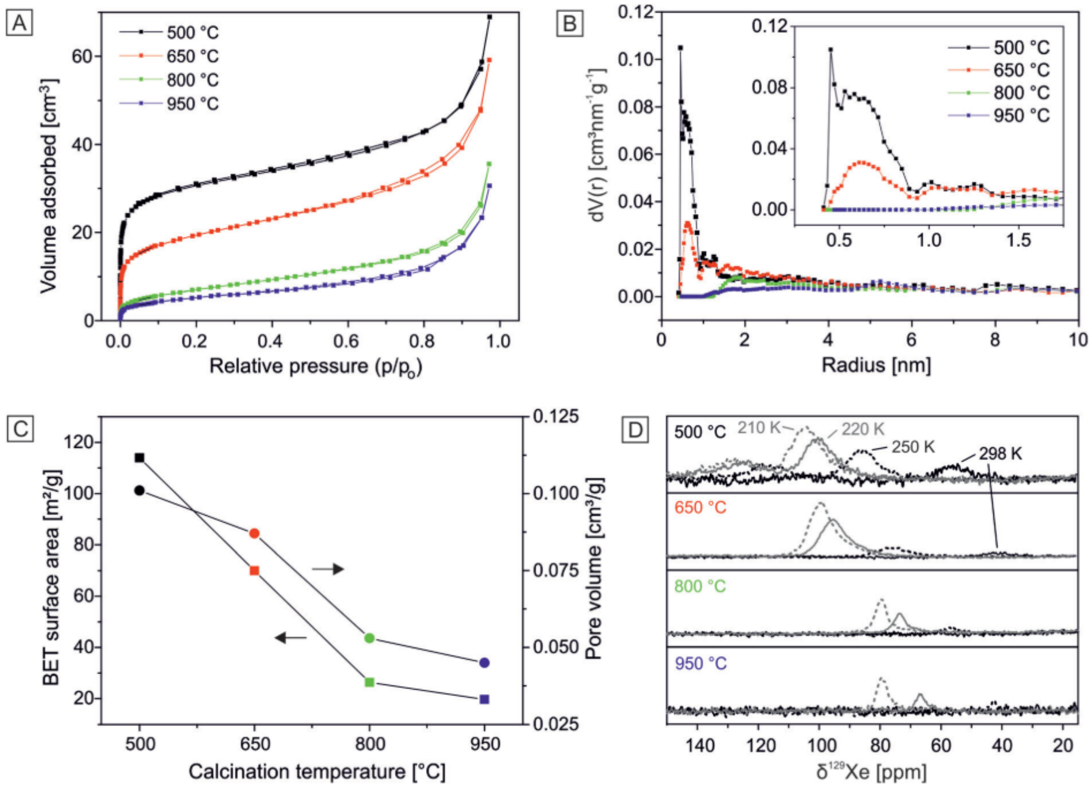

Abb. 3.4 Charakterisierung der mikroskopischen Struktur von Silica-Hohlkugeln in Abhängigkeit der Kalzinierungstemperatur. A: N_2 Physisorptionsisothermen bei 77 K zur Ermittlung der inneren Oberfläche. B. Porengrößenverteilung berechnet mittels NLDFT Kernel. C. BET-Oberfläche und inneres Porenvolumen. D. HP-^{129}Xe-NMR Spektren bei verschiedenen Messtemperaturen: 210 K (grau, gestrichelt), 220 K (grau ununterbrochen), 250 K (schwarz, gestrichelt), 298 K (schwarz, ununterbrochen). Abdruck mit Genehmigung von Ruckdeschel, P. et al. Nanoscale 2015, 7 (22), 10059–10070. Copyright 2015 Royal Society of Chemistry.

Abhängigkeit der Kalzinierungstemperatur bestimmt (siehe Abb. 3.4). So ist das Silica-Material selbst kaum porös, bildet aber an den Kontaktflächen der Kugeln mikroporöse Porenräume aus. Bei höherer Kalzinierungstemperatur sank das gesamte Porenvolumen und ab 800 °C konnten mittels N_2 Physisorption keine Porenvolumina mehr beobachtet werden (Abb. 3.4 B). ^{129}Xe-NMR Spektren zeigten anhand der auftretenden chemischen Verschiebung von 80 – 120 ppm, dass dennoch Mikroporen verblieben sind. Bei einer Kalzinierungstemperatur von 800 °C und 950 °C kann adsorbiertes Xe erst bei niedrigen Messtemperaturen im NMR-Spektrum nachgewiesen werden. Die Resonanzen liegen im Verschiebungsbereich für Mikroporen ohne auftretende Xe-Xe Wechselwirkungen. Die dargestellten Ergebnisse belegen die herausragende Sensitivität für das Auftreten von Mikroporen in zu untersuchenden Materialien, die über die Detektionsgrenzen der üblichen N_2-Physisorption hinausgehen.

3.3. Untersuchung des Porenraums und Diffusionsverhalten von ^{129}Xe in CAU-1

Im Vergleich zu den im vorherigen Kapitel beschriebenen Silica-Materialen besitzen MOFs eine sehr heterogene innere Oberfläche. Hier wechseln sich hochgeladene IBUs mit organischen Linkermolekülen ab. Aus diesem Grund ist hier die gemessene chemische Verschiebung von ^{129}Xe stark von der Position innerhalb des Netzwerks abhängig. Der Porenraum der Al-basierten MOFs CAU-1 in verschiedenen Modifikationen wurde mittels HP ^{129}Xe-NMR untersucht. Unter Zuhilfenahme von modellbasierten Rechnungen der chemischen Verschiebung durch DFT-Methoden konnte Aufschluss über Struktur und bevorzugte Adsorptionspositionen innerhalb des Wirtsnetzwerks gewonnen werden. Dem gegenüber wurde die konventionelle Untersuchung der Porosität mittels isothermer Ar-Physisorption gestellt.

CAU-1 besteht aus 8 zu Ringen verbundener AlO_6-Oktaeder. Diese sind über Amino-terepthalsäureeinheiten miteinander zu einem Netzwerk verknüpft. Hierbei entstehen zwei unterschiedliche Porenräume. Eine größere Oktaederpore, welche auf den Flächen der Einheitszelle liegt, sowie einer deutlich kleineren Tetraederpore, die sich formal in den Tetraederlücken einer pseudokubischen Kugelpackung befindet. Die Struktur sowie die Kavitäten sind in Abb. 3.5 dargestellt.

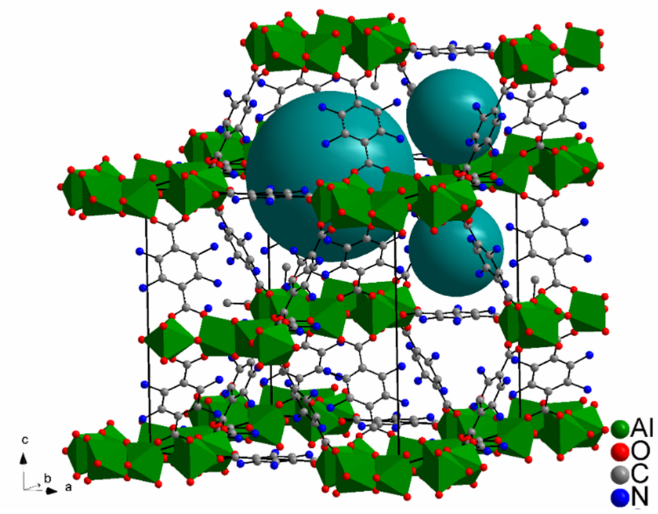

Abb. 3.5: Kristallstruktur von CAU-1. Die cyanfarbenen Kugeln deuten die unterschiedlichen Porenräume an. Die Stickstoffpositionen sind mit einer Wahrscheinlichkeit von 25 % besetzt und andernfalls durch Wasserstoff auszutauschen. Abdruck mit Genehmigung von Kemnitzer, T. W et al. Langmuir 2018, 34 (42), 12538–12548, Copyright 2018 American Chemical Society.

CAU-1 wurde hierbei in drei verschiedenen Modifikationen untersucht, die sich in der Funktionalisierung des verwendeten Linkermoleküls unterscheiden. Hierzu wurde die bei CAU-1 vorhandene Aminogruppe der 2-Aminotherephthalsäure postsynthetisch durch eine Amidmethyl- (CAU-1-AmMe) und eine Ureamethylgruppe (CAU-1-UrMe) ersetzt, wie in Abb. 3.6 zu erkennen ist. Die Einführung dieser sterisch deutlich anspruchsvolleren Gruppen mittels postsynthetischer Modifikation wurde hier genutzt, um den Porenraum schrittweise zu verkleinern. Dies diente anschließend der Untersuchung des Einflusses der Porengröße auf die chemische Verschiebung von ^{129}Xe und dem Gewinn möglicher Einblicke über die geometrische Anordnung der funktionellen Gruppen innerhalb des Porenraumes. Bereits die Analyse mittels Ar-Physisorption (NLDFT-Kernel), sowie der Betrachtung von Kristallstrukturdaten hinsichtlich freier Volumina innerhalb des Netzwerkes zeigte, dass das Porenvolumen, vor allem im Bereich der Oktaederpore, in der Reihe CAU-1, CAU-1-AmMe, CAU-1-UrMe schrittweise abnimmt.

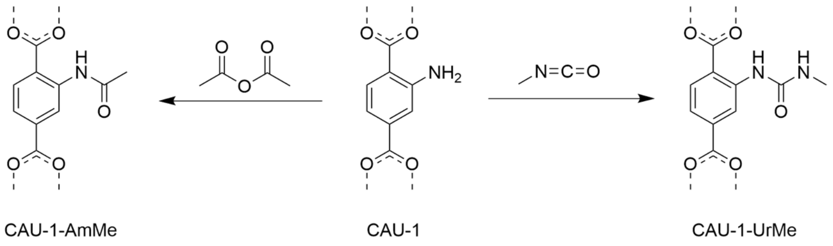

Abb. 3.6: Übersicht der postsynthetischen Modifikation des Linkers von CAU-1 mittels Acetanhydrid zu CAU-1-AmMe (links) und mittels Methylisocyanat zu CAU-1-UrMe (rechts).

Bei der Analyse der ^{129}Xe-Spektren des unmodifizierten CAU-1 erkennt man selbst bei niedriger Temperatur lediglich eine breite Resonanz für adsorbiertes Xe. Daher ist selbst hier die Diffusion zu schnell im Vergleich zur Dauer des NMR-Experiments (FID-Abfall), um unterschiedliche Adsorptionspositionen innerhalb des Netzwerks zu differenzieren. Aus diesem Grund wurden NMR-Parameter mittels *Gauge Including Projector Augmented Waves* (GIPAW) berechnet, um die chemische Verschiebung aus einem großen Ensemble spezifischer Adsorptionspositionen innerhalb des Netzwerks zu berechnen.

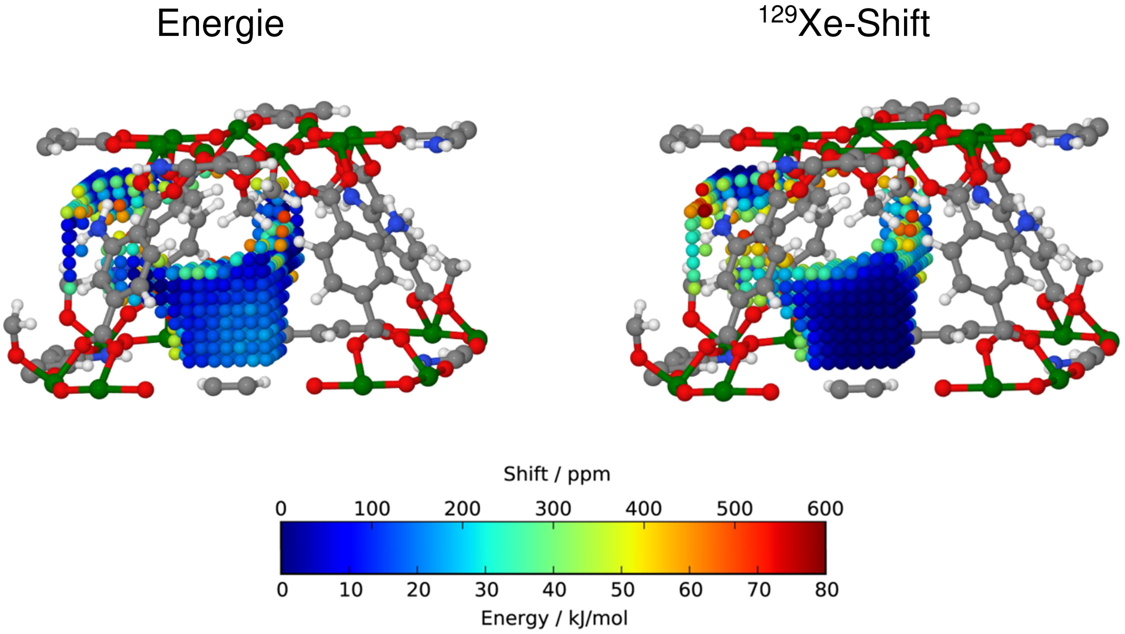

Abb. 3.7: Aus den quantenchemischen Berechnungen resultierende Werte der Systemenergie und chemische Verschiebung für ^{129}Xe in Abhängigkeit der Position innerhalb der asymmetrischen Einheit von CAU-1. Positionen, die zu stark mit dem Wirtsnetzwerk überlappen wurden nicht berücksichtigt. Die hier vorliegende Skala der Energie bezieht sich zum Modell des Energieminimums. Abdruck mit Genehmigung von Kemnitzer, T. W et al. Langmuir 2018, 34 (42), 12538–12548, Copyright 2018 American Chemical Society.

Hierzu wurde ein Xe Atom in die asymmetrische Einheit der CAU-1 schrittweise an jede erreichbare Position platziert. Für jede dieser Positionen wurde anschließend die chemische Verschiebung sowie die Systemenergie berechnet. Diese Berechnungen wurden auf quantenchemischer Basis ohne Einflüsse von relativistischen Effekten erzeugt. In Abb. 3.7 sind die Ergebnisse dieser Berechnungen dargestellt, wobei anhand des Farbcodes der Wert der chemischen Verschiebung sowie der Systemenergie in Abhängigkeit der Adsorptionsposition verdeutlicht wird. Während die Position mit der niedrigsten chemischen Verschiebung in der Mitte der Oktaederpore liegt, so ist die energetisch am meisten bevorzugte Position das Zentrum der Tetraederpore. Hier ist das Xe-Atom zwischen den aromatischen Ringen der Terephthalsäureeinheiten positioniert.

Die hier erhaltenen Werte der chemischen Verschiebung und der korrespondierenden Energie des Systems wurden im Anschluss genutzt, um in Abhängigkeit der Temperatur und der Verwendung einer Boltzmann-Verteilung, einen mittleren gewichteten ^{129}Xe-NMR Shift zu bestimmen. Ich Vergleich zu den aus den Experimenten erhaltenen Werten, zeigt der berechnete Shift eine Abweichung von 41.5 ppm. Diese Abweichung kann durch die fehlenden Einflüsse relativistischer Effekte, sowie der häufig beobachteten Überschätzung der berechneten Werte aus der DFT basierten Rechnung erklärt. Aus diesem Grund wurden die erhaltenen Werte um 41.5 ppm korrigiert. Dieser so erzeugte Shift zeigte nahezu das gleiche lineare Verhalten in Abhängigkeit der Temperatur wie das beobachtete Signal im Limiting Shift Bereich von CAU-1 (siehe Abb. 3.8).

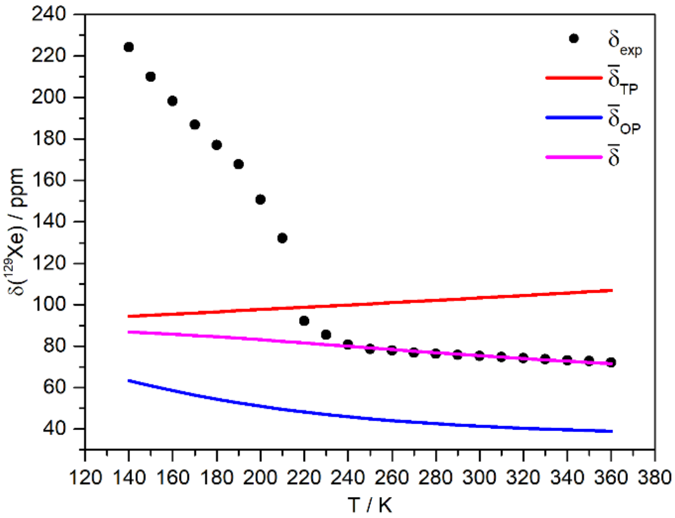

Abb. 3.8: Experimentelle δ_{exp} und mittlere theoretische $\bar{\delta}$ Werte für die isotrope chemische Verschiebung von ^{129}Xe für jede gemessene Temperatur von CAU-1. Aufgezeigte Werte resultieren aus dem energetisch gewichteten Mittel der chemischen Verschiebung der Tetraederpore $\bar{\delta}_{TP}$ und Oktaederpore $\bar{\delta}_{OP}$. Zudem wurden berechnete Verschiebungen um den konstanten Wert von 41.5 ppm korrigiert um den Versuchsdaten zu entsprechen. Abdruck mit Genehmigung von Kemnitzer, T. W et al. Langmuir 2018, 34 (42), 12538–12548, Copyright 2018 American Chemical Society.

Dies beweist, dass es sich beim beobachteten NMR Signal um ein Ensemble verschiedener Adsorptionspositionen innerhalb des Netzwerks im thermischen Gleichgewicht handelt. Ebenso zeigt es den Einfluss energetisch favorisierter Adsorptionspositionen zur beobachteten chemischen Verschiebung, da gerade bei niedrigen Temperaturen der Einfluss der Absorptionspositionen innerhalb der Tetraederpore deutlich zunimmt, wobei diese nur ca. 20 % des gesamten freien Adsorptionsvolumens bereitstellen.

Betrachtet man in diesem Zusammenhang nun die modifizierten Varianten des CAU-1, die sterisch deutlich anspruchsvollere funktionelle Gruppen besitzen, so kann die deutlich höhere beobachtete chemische Verschiebung ebenfalls mit diesem Adsorptionsmodell erklärt werden. Modellrechnungen zeigten, dass durch größere funktionelle Gruppen an den Terephthalsäureeinheiten vor allem Bereiche blockiert wurden, die mit einem sehr niedrigen ^{129}Xe Shift verbunden sind, also vor allem Volumina innerhalb der Oktaederpore (Abb. 3.9 a und b). Stehen diese nicht mehr zur Adsorption zur Verfügung, so verschiebt sich der mittlere Shift zu deutlich höheren Werten. In diesem Fall für CAU-1-AmMe um 14 ppm und für CAU-1-UrMe um 16 ppm, verglichen zu den Werten von unmodifiziertem CAU-1 (Abb. 3.9 c).

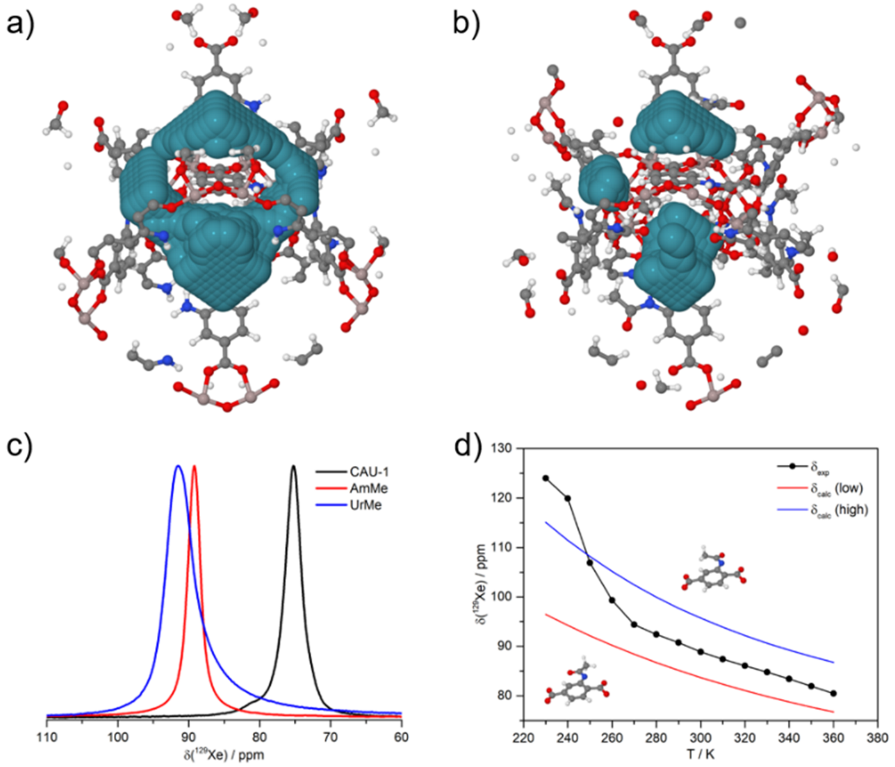

Abb. 3.9 oben: Übersicht aller möglichen Adsorptionspositionen von Xe innerhalb der asymmetrischen Einheit von a) CAU-1 und b) CAU-1-AmMe. c) ^{129}Xe NMR Signal von adsorbiertem Xe bei Raumtemperatur für CAU-1 (schwarz) und den postsynthetischen Modifikationen CAU-1-AmMe (rot) und CAU-1-UrMe (blau). d) Experimentelle chemische Verschiebung δ_{exp} von CAU-1-Am-Me sowie simulierte Grenzwerte der chemischen Verschiebung bei unterschiedlicher Ausrichtung der funktionellen Gruppe der Terephthalsäure (rot und blau). Abdruck mit Genehmigung von Kemnitzer, T. W et al. Langmuir 2018, 34 (42), 12538–12548, Copyright 2018 American Chemical Society.

Mittels der oben beschriebenen Methode zur Berechnung einer gewichteten mittleren chemischen Verschiebung wurde dies ebenfalls anhand zweier Modelle von CAU-1-AmMe unter Berücksichtigung der Orientierung der Methylamid-Gruppe durchgeführt. Der berechnete Shift für die beiden Grenzfälle zeigt zwei Extrema um die realen Werte (Abb. 3.9 d). Somit zeigt das Experiment hier eine kinetische Mittelung über alle möglichen Orientierungen der funktionellen Gruppe innerhalb eines MOF-Kristallits.

Diese Resultate belegen, dass bei heterogenen Materialklassen wie MOFs die Position von ^{129}Xe, sowie bevorzugte Adsorptionsplätze, einen großen Einfluss auf das letztendlich beobachtete NMR-Signal hat. Die energetische Mittelung zum experimentell beobachteten ^{129}Xe Shift konnte erfolgreich nachvollzogen werden. Zudem wurde bewiesen, dass der Ausschluss bestimmter zugänglicher Volumina des Porenraumes durch raumfordernde Ankergruppen den beobachteten Shift durch Veränderung der Adsorptionsstatistik beeinflusst.

3.4. Untersuchung der strukturellen Bi-Stabilität und des Gate-Opening Effekts von Al-MIL-53 mittels ^{129}Xe

Die NMR-Spektroskopie von in porösen Festkörpern adsorbiertem ^{129}Xe kann ebenfalls der Aufklärung struktureller Veränderungen dienen, die durch den Adsorptionsprozess selbst induziert werden. Al-MIL-53 ist bekannt für seinen *Gate-Opening* Effekt, also der Veränderung der Kristallstruktur ab einer definierten Aufnahmemenge eines Adsorptivs. Mittels der Adsorption von Xe in den Porenraum, konnte ein struktureller Übergang des Materials induziert werden. Dieser Übergang der Netzwerkstruktur, der über einen breiten Temperaturbereich verläuft, wurde mittels ^{129}Xe-NMR-Spektroskopie untersucht. Man unterscheidet bei MIL-53 hierbei die *Large Pore*-Form (LP) mit offenen Kanälen und die *Narrow Pore*-Form (NP) mit kontrahierten Kanälen. Bei statischen VT-^{129}Xe-NMR Messungen (Abb. 3.10 A) zeigt sich bei Temperaturen von 298 K bis 250 K ein isotropes Signalbild, das der ausgehenden LP-Form zugeordnet werden kann. Dieses wandelte sich bei tieferen Temperaturen (240 – 255 K) in ein Signal mit hoher chemischer Anisotropie um (Abb. 3.10A). Bei genauer Betrachtung besteht diese Linienform aus einer Überlagerung zweiter anisotroper ^{129}Xe Signale (Abb. 3.10 B). Dieses Signalmuster wird dem Übergang in die NP-Form zugeordnet. Ab 200 K bildeten sich erneut ein sehr schmales Signal aus, dass das NMR-Spektrum dominiert und eine Rückkehr in die LP-Form indiziert. Die anisotropen Signale konnten ebenfalls unter MAS-Bedingungen nachgewiesen werden. Experimente unter Variation des Druckes (Abb. 3.10 C) anstatt der Temperatur wurden durchgeführt, um die beobachteten Signalformen unter diesen Bedingungen zu reproduzieren.

Dies beweist, dass die Effekte des *Gate-Opening* durch die Beladung des Host-Materials entweder mittels Druck oder Temperatur initiiert werden kann. So wurden die diskutierten CSA-

Pattern der NP-Form bei Beladung von 0.9 – 1.75 bar mit 100% thermisch polarisiertem ^{129}Xe, sowie der vollständige Übergang in die LP-Form ab 3.0 atm (Abb. 3.10 C) gemessen. Die Detektion von NMR Signalen der NP- und LP-Form nebeneinander beweist die Bi-Stabilität beider Formen in einem definierten Temperatur- und Druckbereich.

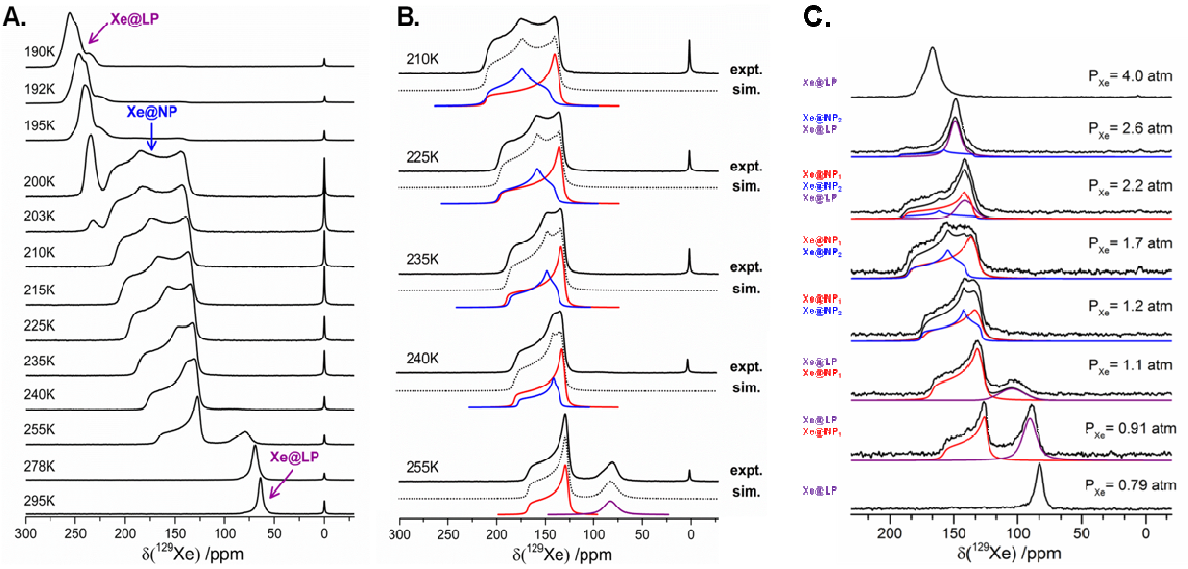

Abb. 3.10: Temperaturabhängige (A, B) HP-^{129}Xe NMR-Spektren von Xenon adsorbiert in Al-MIL-53, sowie druckabhängige (C) Spektren unter Verwendung von 100% thermisch polarisiertem ^{129}Xe. Markiert sind die Large Pore (Xe@LP) und Narrow Pore (Xe@NP) Phasen. NMR Spektren mit komplexer Überlagerung verschiedener CSA-Pattern wurden in B und C deutlicher inklusive einer Entfaltung der Signalbestandteile dargestellt.

So kann ein breiter Übergangsbereich definiert werden, in dem beide Phasen stabil nebeneinander beobachtet werden. Der Übergang kann auch strukturell mittels QCPMG-Spektren von ^{27}Al beobachtet werden. Zeitgleich mit dem Übergang von LP zu NP-Form aufgrund höherer Beladung ändert sich das Quadrupolmoment C_Q von 8.70 MHz zu 8.3 MHz und invers bei der Rückkehr in die LP-Form bei sehr hohen Drücken mit $C_Q = 9.1$ MHz. Diese sehr kleine Änderung verdeutlicht, dass der Übergang der einzelnen Strukturphasen nur einen geringfügigen Einfluss auf die direkte Umgebung der Aluminiumatome innerhalb der IBUs hat und somit keine Änderung oder Neuverknüpfung des MOF-Gerüsts stattfindet.

Um die beobachteten ^{129}Xe Resonanzen und ihre Formen genauer zu verstehen, bediente man sich erneut der Modellierung der chemischen Verschiebung mittels DFT-Methoden, wie bereits in Kapitel 3.3 beschrieben. Hierbei wurde jede mögliche Position eines einzelnen Xe Atoms in der Pore von MIL-53 mit der berechneten chemischen Verschiebung und der Systemenergie korreliert und eine energetisch gemittelte chemische Verschiebung in Kombination mit der CSA berechnet. Dies wurde sowohl für die NP- als auch die LP-Form des MIL-53-Netzwerks durchgeführt und anschließend mit den experimentellen Ergebnissen verglichen.

Die Ergebnisse zeigen eine gute Übereinstimmung für die LP-Form bei geringer Beladung (hohe Temperatur). Bei der Berechnung in der NP-Form mit deutlich kleinerem Porenraum konnte zwar auch in den *ab initio* berechneten Werten eine ausgeprägte CSA ermittelt werden, diese stimmt aber sowohl in ihrer Größe sowie des Vorzeichens nicht mit den experimentellen Daten überein. Aus diesem Grund wurde eine Reihe verschiedener Konstellationen bestehend aus mehreren Xe-Atomen modelliert und die entsprechenden CSA-Parameter der ^{129}Xe-Kerne berechnet. Aus den Ergebnissen wurden mögliche Anordnungen von Xe Atomen innerhalb der Pore ausgesucht, deren NMR-Parameter die beste Übereinstimmung mit den experimentellen Werten erzielten. Die sehr asymmetrische Form, die bei 255 K beobachtet wurde, konnte mit einer gewinkelten Kette von Xe Atomen (NP angle) modelliert werden, während die bei tieferen Temperaturen auftretende zweite anisotrope Signalform mittels Paaren in abwechselnder Formation mit einzelnen Xe Atomen (NP ppe) dargestellt werden (siehe Abb. 3.11). Natürlich stellen diese Modelle mögliche Grenzfälle von Xe-Anordnungen im Porenraum dar, da es sich um statische Betrachtungen eines sehr dynamischen Prozesses handelt. Dies ist auch an den vergleichsweise sehr hohen simulierten isotropen Verschiebungswerten zu erkennen.

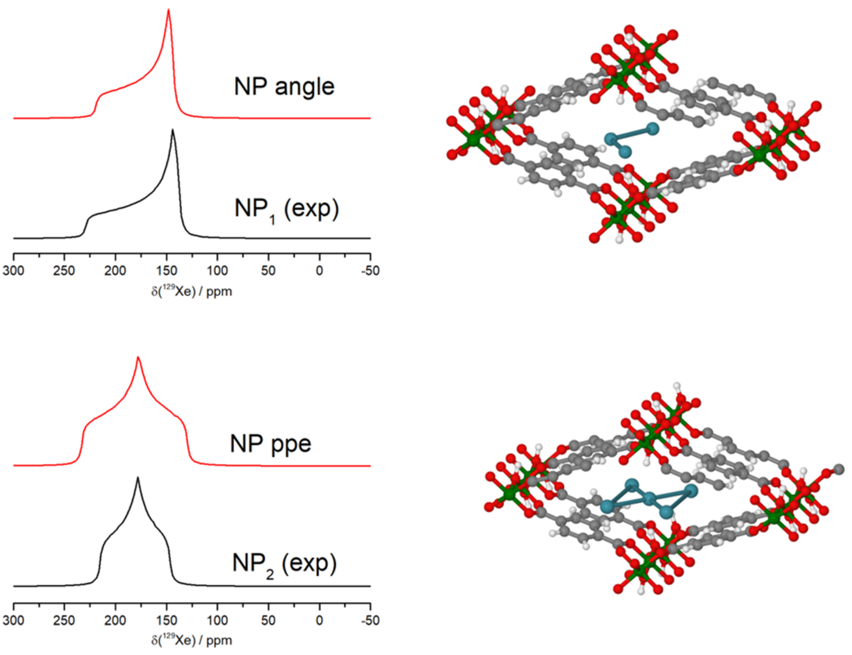

Abb. 3.11: Vergleich der ermittelten CSA-Formen von ^{129}Xe in zwei verschiedenen NP-Formen von MIL-53 zu berechneten Pattern aus *ab-initio* Berechnungen unter Verwendung verschiedener Xe-Atomkonfigurationen innerhalb des Porenraums. Da es sich lediglich um strukturelle Grenzfälle handelt, wurde der isotrope Shift der theoretisch ermittelten Signalformen an die der experimentellen angepasst. Die NP angle Form zeigt dabei gute Übereinstimmung mit dem NP1-Signal und die NP ppe Form zu der des NP2-Signals (vgl. Abb. 3.10 B)

Die Verteilung der Domänen von LP- und NP-Form in ihrer bistabilen Phase konnte mittels 2D-EXSY-Spektroskopie aufgrund der Sensitivität hinsichtlich Diffusionsgeschwindigkeiten erklärt werden (Abb. 3.12). Bereits bei kurzen Korrelationszeiten wurde ein deutlicher Austausch zwischen Gasphase und adsorbiertem Xe gemessen. Somit sind die Poren im Allgemeinen für Xe aus der Gasphase sehr gut zugänglich. Der Austausch, der innerhalb des anisotropen Signals ab einer Korrelationszeit von 100 ms detektiert wurde (Abb. 3.12, Korrelation 4), und auch als *butterfly pattern* bezeichnet wird, belegt einen Austausch zwischen einzelnen Kristalliten in der NP-Form. Besonders interessant ist der Austausch LP↔NP in diesem bistabilen Temperaturbereich. Es zeigten sich bereits bei Korrelationszeiten von unter 1 ms deutliche Austauschsignale. Diese sind auf der entsprechenden Zeitskala zu kurz für interkristallinen Austausch, was die Existenz von Domänen der verschiedenen Strukturphasen von MIL-53 innerhalb eines Kristallits beweist. Zudem sind die Austauschkorrelationen zwischen den einzelnen Strukturformen erkennbar, die keinen Zwischenweg über die Gasphase aufzeigen. Die Umwandlung von LP-Form in die NP-Form aufgrund höherer Beladung muss daher in kleinen Domänen innerhalb eines MOF-Kristallits beginnen und sich bei höherer Beladung schrittweise ausdehnen, wodurch das *Gate-Opening* nicht im gesamten Kristallit geschieht. Hierbei geht man von einem Schichtmodell aus. Einzelne schichtartige Domänen entlang der porösen Kanäle beginnen mit höherer Beladung zur NP-Form umzuklappen. Dieser dynamische Prozess wird durch eine immer höhere Beladung vorangetrieben und diese Domänen breiten sich über mehrere Schichten aus, bis schließlich der gesamte Kristallit in der NP-Form vorliegt. Xenon kann sich dabei zwischen diesen Domänen selbst auf sehr kurzen Zeitskalen frei bewegen.

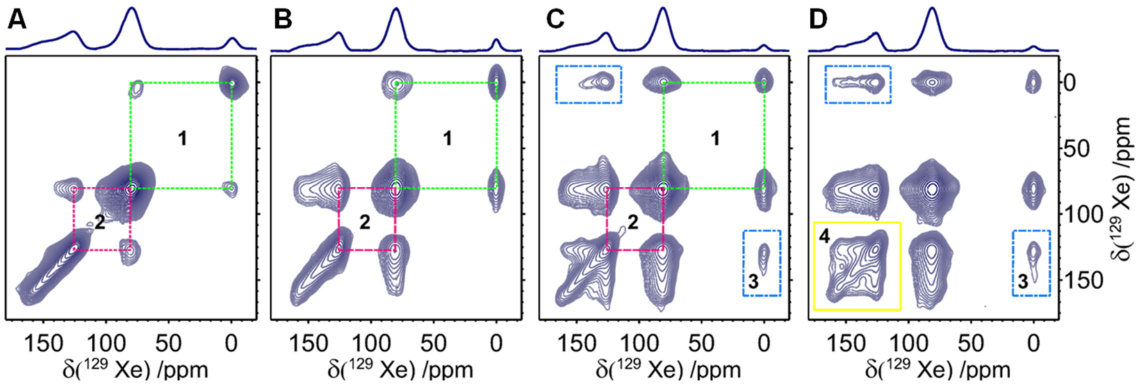

Abb. 3.12: 2D CF-HP ^{129}Xe-EXSY Spektren unter statischen Bedingungen. Die Messungen wurden bei 263K und unter Verwendung verschiedener Mischzeiten τ_{mix} gemessen: A) 1ms, B) 20ms, C) 100 ms, D) 250 ms. Die farblich markierten Bereiche 1-4 zeigen spezifische Austauschprozesse innerhalb und zwischen den strukturellen Phasen von MIL-53.

Zusammengefasst veranschaulichen diese Ergebnisse, dass HP ^{129}Xe-NMR-Spektroskopie genutzt werden kann, um Strukturveränderungen in einem sehr dynamischen und flexiblen System, wie MIL-53 genau zu untersuchen. Wird die Beladung mit Xe durch Verringerung der Temperatur oder Erhöhung des Gasdrucks erhöht, so kann der auftretende Phasenübergang, sowie der *gate-opening* Effekt direkt detektiert werden. DFT-Berechnungen zeigen, wie Xe-Xe-Wechselwirkungen in der NP-Form großen Einfluss auf die CSA-Parameter haben und geben Hinweise auf bestimmte Xe-Konstellationen innerhalb der Porenkanäle. Letztendlich kann aber vor allem mit 2D-Austauschspektren das Diffusionsverhalten und der Mechanismus des *Gate-Openings* geklärt werden. Dieser komplexe Informationsgehalt kann mittels Beugungsmethoden und einfacher Physisorptionsexperimente nicht ermittelt werden.

4. Darstellung der Eigenanteile

Die Ergebnisse dieser Dissertation wurden in Zusammenarbeit mit weiteren Autoren gewonnen und sind in wissenschaftlichen Zeitschriften, welche ein Begutachtungsverfahren unterhalten, veröffentlicht oder werden noch zur Veröffentlichung eingereicht. In den folgenden Kapiteln wird der Anteil der einzelnen Autoren kurz dargestellt. Der korrespondierende Autor wird dabei mit einem Stern markiert.

Kapitel 5.1

Portable Hyperpolarized Xe-129 Apparatus with Long-Time Stable Polarization Mediated by Adaptable Rb Vapor Density

Robert Stäglich, Tobias Kemnitzer, Marie Harder, Adrian Schmutzler, Marcel Meinhart, Caroline Keenan, Ernst Rössler, Jürgen Senker*

Das Konzept der Publikation wurde von Robert Stäglich und mir entwickelt. Die grundlegende Planung und Konstruktion des Polarisators wurden von Caroline Keenan durchgeführt. Die konzeptionelle und technische Weiterentwicklung von Bauteilen des Polarisators wurden von mir durchgeführt. Die Messstrategie von ^{129}Xe-NMR Spektren zur Optimierung der erhaltenen ^{129}Xe Polarisation wurden von R. Stäglich und mir mit Unterstützung von Marie Harder aufgestellt und durchgeführt. Die technischen Zeichnungen des Polarisators, sowie die Modelle zum Verweilzeitverhalten von ^{129}Xe wurden von R. Stäglich erstellt. 1D-, sowie 2D-EXSY-^{129}Xe-NMR Spektren an CAU-1-AmMe unter stop-and-flow Bedingungen wurden von mir realisiert und interpretiert. Marcel Meinhart und Adrian Schmutzler waren an wissenschaftlichen Diskussionen involviert.

Die Publikation wurde von Robert Stäglich und mir verfasst, während sie von Ernst Rössler und Jürgen Senker überarbeitet wurde.

Kapitel 5.2

Hollow silica sphere colloidal crystals insights into calcination dependent thermal transport

Pia Ruckdeschel, Tobias Kemnitzer, Fabian Nutz, Jürgen Senker, Markus Retsch*

Das Konzept der Publikation wurde von Pia Ruckdeschel entwickelt. Die Experimente und die Synthese der Partikel wurden von Pia Ruckdeschel geplant und realisiert. Die Charakterisierung der Partikel mittels TEM, SAXS, Elementaranalyse, DSC, CLEM, sowie thermischer Leitfähigkeitsmessung wurden von Pia Ruckdeschel durchgeführt. Ich habe ^{1}H, ^{29}Si, sowie hyperpolarisierte ^{129}Xe-NMR Spektren bei variabler Temperatur gemessen und ausgewertet. Analysen mittels N_2-Physisorption und PXRD wurden von mir durchgeführt und interpretiert. Fabian Nutz war an wissenschaftlichen Diskussionen beteiligt.
Die Publikation wurde von Pia Ruckdeschel, mir und Markus Retsch verfasst und von Jürgen Senker überarbeitet.

Kapitel 5.3

Exploring Local Disorder within CAU-1 Frameworks Using Hyperpolarized ^{129}Xe-NMR Spectroscopy

Tobias Kemnitzer, Carsten Tschense, Thomas Wittmann, Ernst Rössler, Jürgen Senker*

Das Konzept und die experimentellen Arbeiten für diese Publikation wurden von mir erarbeitet. Ich habe sämtlich HP ^{129}Xe-NMR Experimente durchgeführt und interpretiert. Die DFT-Berechnungen zur Ermittlung von NMR Parametern, sowie deren Auswertung und Interpretation wurden von mir realisiert, wobei ich ebenfalls die verwendeten Strukturmodelle konzipiert habe. Ich habe die Charakterisierung der MOFs mittels Physisorption, ^{1}H und ^{13}C NMR, sowie PXRD durchgeführt und ausgewertet. Carsten Tschense hat bei der skriptbasierten Erstellung von DFT-Rechnungen und deren Analyse unterstützt und war an wissenschaftlichen Diskussionen beteiligt. Thomas Wittmann hat die verwendeten MOFs synthetisiert und modifiziert.
Die Publikation wurde von mir angefertigt und von Ernst Rössler und Jürgen Senker überarbeitet.

Kapitel 5.4

Probing the Structural Bi-stability during Gate-Opening of MIL-53(Al) via Hyperpolarized ^{129}Xe and Chemical Modelling

Tobias Kemnitzer, Caroline Keenan, Renée Siegel, Ernst Rössler, Jürgen Senker*

Es handelt sich hier um ein Manuskript, das zur Veröffentlichung eingereicht wird. Das Konzept des Manuskripts wurde von Caroline Keenan und mir entwickelt. Die HP ^{129}Xe-NMR Experimente bei variable Temperatur und variablem Druck, sowie 2D-EXSY Experimente wurden von Caroline Keenan und mir realisiert und interpretiert. Xe-Physisorptionsexperimente wurden von mir durchgeführt und ausgewertet. Struktur- und Adsorptionsmodelle zur quantenmechanischen Berechnung von NMR-Parametern wurden von mir entwickelt und mittels DFT-Rechnungen umgesetzt und interpretiert. Renée Siegel hat ^{27}Al NMR Spektren aufgenommen und war an wissenschaftlichen Diskussionen beteiligt.

Das Manuskript wurde von mir mit Unterstützung von Caroline Keenan angefertigt und von Ernst Rössler und Jürgen Senker überarbeitet.

5. Publikationen

5.1. Portable Hyperpolarized Xe-129 Apparatus with Long-Time Stable Polarization Mediated by Adaptable Rb Vapor Density

R. Stäglich,[a] T. W. Kemnitzer,[a] M. C. Harder,[a] A. Schmutzler,[a] M. Meinhart,[a] C. D. Keenan,[b]
E. A. Rössler[c] und J. Senker[a]*

Erschienen in:

The Journal of Physical Chemistry A **2022**, *126(16)*, 2578-2589
DOI: 10.1021/acs.jpca.2c00891

[a] Department of Inorganic Chemistry III, University of Bayreuth, Universitätsstr. 30, 95447 Bayreuth (Germany)

[b] Department of Chemistry and Biochemistry, Carson-Newman University, Jefferson City, Tennessee 37760 (United States of America)

[c] Department of Experimental Physics II, University of Bayreuth, Universitätsstr. 30, 95447 Bayreuth (Germany)

* juergen.senker@uni-bayreuth.de

THE JOURNAL OF PHYSICAL CHEMISTRY A
A JOURNAL OF THE AMERICAN CHEMICAL SOCIETY

pubs.acs.org/JPCA Article

Portable Hyperpolarized Xe-129 Apparatus with Long-Time Stable Polarization Mediated by Adaptable Rb Vapor Density

Robert Stäglich,[§] Tobias W. Kemnitzer,[§] Marie C. Harder, Adrian Schmutzler, Marcel Meinhart, Caroline D. Keenan,* Ernst A. Rössler,* and Jürgen Senker*

Cite This: J. Phys. Chem. A 2022, 126, 2578−2589

Read Online

ACCESS | Metrics & More | Article Recommendations | Supporting Information

ABSTRACT: The extraordinary sensitivity of ^{129}Xe, hyperpolarized by spin-exchange optical pumping, is essential for magnetic resonance imaging and spectroscopy in life and materials sciences. However, fluctuations of the polarization over time still limit the reproducibility and quantification with which the interconnectivity of pore spaces can be analyzed. Here, we present a polarizer that not only produces a continuous stream of hyperpolarized ^{129}Xe but also maintains stable polarization levels on the order of hours, independent of gas flow rates. The polarizer features excellent magnetization production rates of about 70 mL/h and ^{129}Xe polarization values on the order of 40% at moderate system pressures. Key design features include a vertically oriented, large-capacity two-bodied pumping cell and a separate Rb presaturation chamber having its own temperature control, independent of the main pumping cell oven. The separate presaturation chamber allows for precise control of the Rb vapor density by restricting the Rb load and varying the temperature. The polarizer is both compact and transportable—making it easily storable—and adaptable for use in various sample environments. Time-evolved two-dimensional (2D) exchange spectra of ^{129}Xe absorbed in the microporous metal−organic framework CAU-1-AmMe are presented to highlight the quantitative nature of the device.

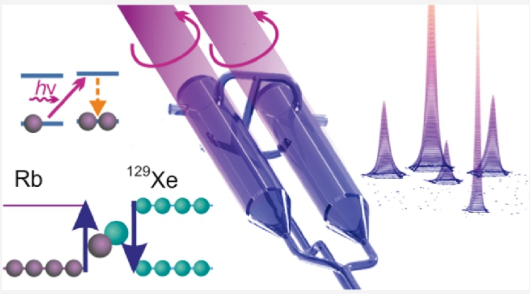

INTRODUCTION

Spin-exchange optical pumping (SEOP) is a powerful way to generate high nonequilibrium nuclear-spin polarization for a noble gas like ^{129}Xe, which enhances its NMR detection sensitivity by up to 5 orders of magnitude.[1] The sensitivity gain, together with the reduction of measurement time, is beneficial for magnetic resonance imaging[2−4] and spectroscopy.[5−9] As such, hyperpolarized ^{129}Xe was used among other things for lung imaging,[2,4,10] highly sensitive, cryptophane-based biosensors,[11−15] protein research,[16−18] the characterization of natural soils[19] and porous materials.[20−24]

To prepare hyperpolarized ^{129}Xe, the first step is to optically pump a gas mixture, containing Xe in addition to a highly reactive alkali metal, an inert buffering agent, and a quenching component, typically Rb, He, and N_2, respectively.[25−27] Circularly polarized laser light is used to transfer its angular momentum to the single valence electron of Rb in the vapor phase.[28] While the high photon flux provided by powerful and tunable diode lasers provides efficient electronic polarization, their characteristically broad laser profile requires pressure broadening of the narrow Rb D1 line, for the supplied laser power to be utilized most effectively.[29] A traditional SEOP ^{129}Xe apparatus operates at elevated pressures (∼3 bar), which allows for high efficiencies and nearly 100% electronic polarization.[30] The recent introduction of line-narrowed diode lasers does now permit low-pressure gas systems to be pumped efficiently.[31] Once the alkali metal vapor is optically pumped, collision of metal atoms with xenon atoms allows for the transfer of the electronic polarization to xenon nuclear spins via the Fermi-contact hyperfine interaction. This transfer is accomplished by Xe−Rb binary collisions (BC) that dominate at high gas pressures and the formation of van der Waals molecules that monopolize at low gas pressures.[26,27,32]

Typically, one of two operational strategies is employed to accumulate hyperpolarized ^{129}Xe: either batch mode or continuous-flow mode. In batch mode, the pumping cell is filled with a small amount of Rb and a gas mixture of He, N_2, and Xe. It is then heated, to provide sufficiently high Rb vapor density, and illuminated with circularly polarized laser light to drive the optical pumping process. Usually, high polarization is achieved, since the necessary residence time in the pumping

Received: February 6, 2022
Revised: March 24, 2022
Published: April 14, 2022

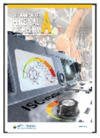

https://doi.org/10.1021/acs.jpca.2c00891
J. Phys. Chem. A 2022, 126, 2578−2589

cell can always be matched, avoiding the premature termination of SEOP.[33−35] Xenon gas is frozen out of the gas mixture with liquid nitrogen and stored under a small magnetic field before utilization. This strategy leads to high ^{129}Xe polarization as losses are minimized. The highest reported values of up to 80%[34] for ^{129}Xe polarization have been achieved in this way.[36−39]

In continuous-flow mode, a constant stream of the gas mixture (He, N_2, and Xe) flows through the pumping cell. While the limited residence time during optical pumping generally leads to lower absolute polarization, more xenon is accumulated due to the larger amount of gas passing through the cell.[40−43] To increase the absolute polarization despite limited residence times of the gas mixture in the pumping cell, various approaches were developed.[39,41,43−50] To decrease depolarization effects, due to collisions of xenon with paramagnetic impurities on the walls of the pumping cell, the surface-to-volume ratio was optimized and the surfaces were coated with a silylation agent to create a protecting layer. While a spherical pumping cell leads to the best S/V ratio, simulations showed that cylindrical cells with a radius-to-length ratio of 0.1 better adapt to the optical pumping rate over the length of the pumping cell.[51]

Although an increase in laser power generally leads to increased Rb and thus ^{129}Xe polarization, a plateau is usually reached, where higher flux cannot be converted into higher polarization due to saturation effects. This is caused by increasing the pumping cell temperature, thereby enhancing polarization destruction rates.[47] Simulations by Fink and Brunner showed that for pressures of 10 bar, the increase in polarization stagnates if the laser power exceeds 100 W.[51,52]

We aim at establishing a continuous-flow polarizer, working in a closed cycle with the sample in the magnet of the NMR spectrometer. The system should allow for performing continuous experiments lasting several hours. Exploring the interconnectivity of pore spaces in porous materials like metal−organic frameworks (MOFs)[20,53,54] and porous polymers (POPs)[55,56] is of particular interest. This requires the sequential collection and quantitative analysis of a series of two-dimensional (2D) ^{129}Xe exchange spectra (EXSY), which can take several hours—as such, ^{129}Xe polarization at the sample is required to be highly stable for the whole experiment time and should exceed 10% to make such analyses possible. In addition, the magnetization production rate (MPR) of the polarizer needs to be large enough to feed a few 100 mg of samples continuously.

The presented polarizer is based on previous findings and reported experiences with the abovementioned polarizers.[44,47,51,52] In particular, we included simulations by Fink and Brunner into the design of the present system.[51,52] Our apparatus utilizes broadband diode laser arrays and is thus based on a high-pressure design.[30] To minimize convection and optimize laser absorption, the pumping cell bodies were kept slim and were arranged vertically.[51,52] The two-bodied pumping cell design aims to increase the total active volume and thereby the magnetization production rates (MPRs). Moreover, it makes the need to focus the two circularly polarized laser beams on one body obsolete.[51,52] By optimizing the optical path length we avoid the use of beam shaping tools like collimators and beam expanders, which unavoidably would reduce the photon flux.[57] Finally, we introduced a separate Rb presaturation chamber, which can be individually heated. The larger distance to the pumping cell will increase the control over the Rb vapor density. Although most of these elements have been used before, their combination in the present system is unique. After a thorough characterization of its performance, we demonstrate its efficiency and stability by collecting 2D exchange spectra (EXSY) for the MOF CAU-1-AmMe.[20] CAU-1-AmMe is characterized by two types of interconnecting pores—a large pore (LP) with a diameter of roughly 1 nm and a small pore (SP) with a diameter of 0.5 nm.

■ THEORY

Phenomenologically, the ^{129}Xe polarization build-up based on SEOP can be described by eq 1[44]

$$P_{\mathrm{Xe}} = P_{\mathrm{Xe}}^{\infty}\left(1 - \mathrm{e}^{-(\gamma_{\mathrm{SE}}+\Gamma_{\mathrm{Xe}})\tau_{\mathrm{res}}}\right) \tag{1}$$

Here, γ_{SE} is the spin-exchange rate, Γ_{Xe} represents the xenon spin destruction (SD) rate, and τ_{res} denotes the residence time Xe spends in the optical pumping cell. The xenon polarization for infinite residence time (P_{Xe}^{∞}), like in a batch mode experiment, is directly proportional to the Rb electronic polarization (P_{Rb}) obtained via the optical pumping process, where $P_{\mathrm{Xe}}^{\infty} = \gamma_{\mathrm{SE}}\cdot(\gamma_{\mathrm{SE}} + \Gamma_{\mathrm{Xe}})^{-1}P_{\mathrm{Rb}}$. The experimentally attainable P_{Rb} is dependent on the relative position of Rb along the path length of the optimal pumping cell (z) parallel to the applied magnetic field and is denoted $P_{\mathrm{Rb}}(z)$, as defined in eq 2. It relies on two factors: the rate at which the Rb electronic polarization builds up, $\gamma_{\mathrm{opt}}(z)$, and its relative depolarization rate (Γ_{SD}) that manifests in the form of collisional mixing. Sources of depolarization are hereby referred to as modes of spin destruction (SD), consistent with the notation introduced in eq 2

$$P_{\mathrm{Rb}}(z) = \left(\frac{\gamma_{\mathrm{opt}}(z)}{\gamma_{\mathrm{opt}}(z) + \Gamma_{\mathrm{SD}}}\right) \tag{2}$$

Here, $\gamma_{\mathrm{opt}}(z)$, also known as the Rb optical pumping rate, is a function of the photon flux (ϕ), the photon frequency ν, and the photon absorption cross section (σ_s), according to $\gamma_{\mathrm{opt}}(\nu,z) = \int\phi(\nu,z)\sigma_s(\nu)\,\mathrm{d}\nu$.[58] The spin destruction rate depends on relaxation rates due to the formation and breakup of van der Waals molecules ($\Gamma_{\mathrm{SD}}^{\mathrm{vdW}}$) and binary collisions of Rb with a buffer gas ($\Gamma_{\mathrm{SD}}^{\mathrm{BC}}$), where $\Gamma_{\mathrm{SD}} = \Gamma_{\mathrm{SD}}^{\mathrm{vdW}} + \Gamma_{\mathrm{SD}}^{\mathrm{BC}}$. As mentioned previously, the relaxation due to binary collisions is the dominant factor in the high-pressure regime, where $\Gamma_{\mathrm{SD}}^{\mathrm{BC}}$ is defined as

$$\Gamma_{\mathrm{SD}}^{\mathrm{BC}} = \sum_i [G_i]\kappa_{\mathrm{SD}}^{\mathrm{Rb}-i} \tag{3}$$

This binary collision spin destruction rate depends on the collisional cross section between Rb and its colliding partner i ($\kappa_{\mathrm{SD}}^{\mathrm{Rb}-i}$) and the vapor density of the said partner, $[G_i]$, within the gas mixture.

While Rb spin destruction rates for collisions with helium and nitrogen are moderate,[32,59] the cross section for Rb−Rb collisions is orders of magnitude higher.[32] Thus, the Rb vapor density strongly influences the electronic equilibrium polarization (eq 2) and hence the ^{129}Xe equilibrium polarization. By controlling the Rb vapor density, an additional degree of freedom is introduced to adjust the ^{129}Xe polarization.

In the high-pressure regime, the spin exchange between the electron spin of Rb atoms and ^{129}Xe nuclei is governed by binary collisions.[60] Thus, the spin-exchange rate (γ_{SE}) can be described as follows:

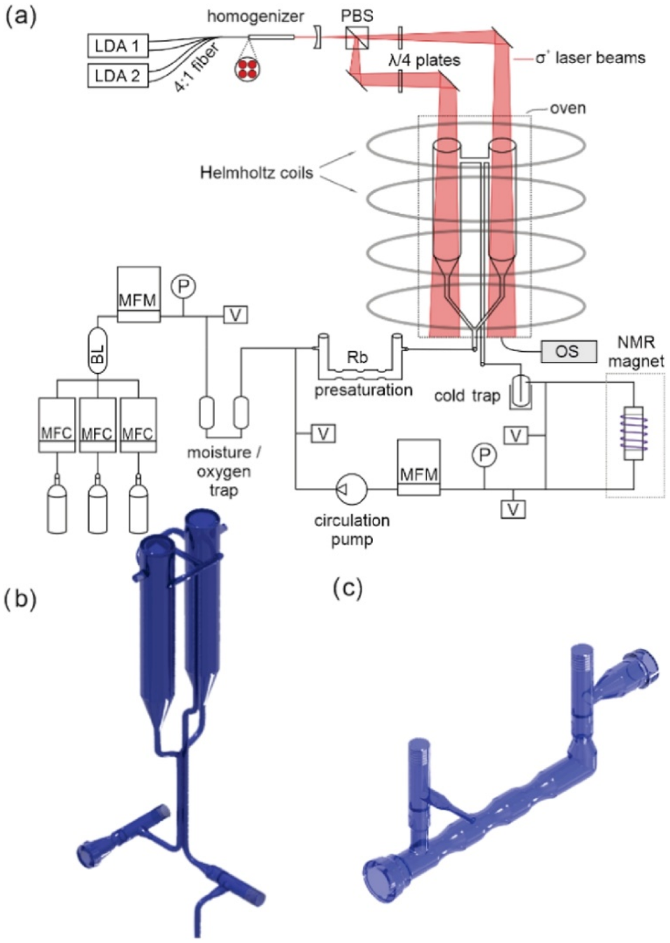

Figure 1. Details of the SEOP polarizer design. (a) Schematic diagram of the polarizer. LDA: laser diode array; PBS: polarizing beam splitter; MFC: mass flow controller; BL: ballast tank; MFM: mass flow meter; P: pressure meter; V: turbo pump; OS: optical spectrometer. (b) Double bodied, vertical optical pumping cell. (c) External presaturation chamber with bulges in the lower part, as Rb reservoirs; CAD illustrations of glass devices are rendered in blue for contrast.

$$\gamma_{\mathrm{SE}} = \kappa_{\mathrm{SE}}^{\mathrm{Rb-Xe}}[\mathrm{Rb}] \tag{4}$$

where $\kappa_{\mathrm{SE}}^{\mathrm{Rb-Xe}}$ is the spin-exchange cross section due to binary collisions between Rb and Xe and [Rb] is the Rb vapor density within the pumping cell. Note that γ_{SE} decreases if the Rb polarization is smaller than unity. Binary collisions and van der Waals molecules also contribute to xenon nuclear-spin relaxation, denoted Γ^{BC} and Γ^{vdW}, respectively. An additional mode of relaxation arises due to collisions with the pumping cell wall (Γ^{W}). These components contribute to the overall nuclear-spin destruction rate of Xe, according to

$$\Gamma_{\mathrm{Xe}} = \Gamma^{\mathrm{BC}} + \Gamma^{\mathrm{vdW}} + \Gamma^{\mathrm{W}} \tag{5}$$

The wall relaxation term is highly influenced by the surface-to-volume ratio of the pumping cell and its surface conditions.[61−63] Binary collisions between Rb and xenon lead to a polarization gain for xenon in case of collisions with polarized Rb. Otherwise, the high collisional cross section maintains xenon spin destruction until Rb is removed from the gas mixture.

To describe ^{129}Xe hyperpolarization at the sample within an NMR spectrometer phenomenologically, two periods need to be considered for a closed-cycle, continuous-flow apparatus. The first is the ^{129}Xe polarization build-up within the pumping cell, described by eq 1; the second is defined as a decay period, where the gas is transported to the sample. As the spin-exchange rate, γ_{SE}, and the spin destruction rate, Γ_{Xe}, influence the polarization build-up in a similar fashion, we combine both parameters in a single time constant: $T_{\mathrm{pb}} = (\gamma_{\mathrm{SE}} + \Gamma_{\mathrm{Xe}})^{-1}$. From here on, this is called the nuclear polarization build-up time. Additionally, we define the residence time in the optical pumping cell (τ_{op}) by $\tau_{\mathrm{op}} = V_{\mathrm{OP}}/\dot{V}$, where V_{OP} and $\dot{V}$ refer to the volume of the optical pumping cell and the volume flow, respectively.

Although the spin-exchange process halts when the gas mixture exits the pumping cell, the spin destruction processes continue during transport to the sample. To account for this,

https://doi.org/10.1021/acs.jpca.2c00891
J. Phys. Chem. A 2022, 126, 2578−2589

we define an average transport relaxation time constant, T_{tr}, to represent the depolarization via Xe−Xe collisions and Xe−wall contacts. Despite similar notation, the transport time for the hyperpolarized gas mixture to reach the sample after leaving the pumping cell is represented by τ_{tr} and is specified by the quotient of the volume of all tubings between the pumping cell and the magnet and the cold trap V_{tr} and the gas flow $\dot{V}$. The combination of these two separate time periods on the overall ^{129}Xe nuclear polarization is described by the following equation

$$P_{Xe} = P_{Xe}^{\infty}(1 - e^{-\tau_{op}/T_{pb}})\, e^{-\tau_{tr}/T_{tr}} \qquad (6)$$

■ METHODS

All ^{129}Xe NMR spectroscopic measurements were carried out on a Bruker AvanceII NMR spectrometer at an external magnetic field of 7.05 T and a Larmor frequency ν_0 of 83.43 MHz. A static H/F−X double-resonance wide-bore probe was used with a home-built sample holder connected to the polarizer via perfluoroalkoxy (PFA) tubing. The poly(ether ether ketone) (PEEK) sample holder is gas tight for pressures up to 12 bar and variable temperatures (130−380 K). Hyperpolarized and thermally polarized ^{129}Xe NMR spectra were measured with 4 and 32 scans, respectively, and gas mixtures as given in the text. The $\pi/2$ pulse was set to 3.5 μs corresponding to a nutation frequency ν_{nut} of ≈72 kHz. Recycle delays were optimized to 1 s for the hyperpolarized gas mixtures and 60 s (fully recovered) for thermally polarized Xe gas. The thermally polarized Xe gas with ^{129}Xe in natural abundance was measured for a system pressure of 11.5 bar and small amounts of oxygen as the relaxation agent. The measurements in thermal polarization are needed to calculate the ^{129}Xe polarization for the experiments with hyperpolarized ^{129}Xe. The chemical shift was referenced to gaseous xenon extrapolated to zero pressure (0 ppm).

^{129}Xe 2D EXSY spectra for CAU-1-AmMe[20] were acquired using a sequence of three consecutive $\pi/2$ pulses separated by an evolution time t_1 and a mixing time t_m. After the third $\pi/2$ pulse, a refocusing π pulse was applied with an interpulse delay of 12 μs to avoid phase errors caused by signal loss within the dead time. The $\pi/2$ and π pulses (ν_{nut} = 62.5 kHz), corresponded to pulse durations of 4 and 8 μs. Two hundred transients were recorded, each with eight scans, a recycle delay of 1 s, and a settling time of 1 s for stopping the gas flow before the measurement. CAU-1-AmMe was synthesized as described by Kemnitzer et al.[20]

The design of the polarizer is schematically depicted in Figure 1a. To generate high laser power, two Duo FAP diode laser arrays (Coherent) are coupled in a 4:1 fiber connector. The optical power is adjustable between 0 and 120 W, as each diode array reaches a power of up to 30 W. The laser beam is then divided by a polarizing beam splitter (PBS in Figure 1a). The two resulting linearly polarized beams are circularly polarized by $\lambda/4$-plates before being redirected into a vertically positioned optical pumping cell (Figure S1). The latter is positioned in an oven, which is heated by hot oil flowing in a copper spiral heater (Figure S2). Around the oven and the pumping cell, four Helmholtz coils are arranged in a Barker coil arrangement[64] for optimized uniformity and homogeneity of the ∼25 G magnetic field.

The gas mixtures are provided by a mixing unit consisting of gas bottles of Xe (Rießner Gase GmbH, 99.998%), N_2 (Rießner Gase GmbH, 99.999%) and He (Rießner Gase GmbH, 99.999%), their respective mass flow controllers (MFC; Bronkhorst EL-FLOW F-201CV), a ballast tank (BL), and a mixing unit. With the MFCs, a broad range of gas compositions is available. The gases are dried and cleaned by a moisture and oxygen trap before being introduced into the recirculating polarizer. Gas circulation is established by an oil-free rotary vane pump with magnet bearing (Gardner Denver Thomas GK-M 24/02).

The pumping cell is a home-built, double bodied, vertically arranged, high-pressure glass body. The gas mixture flows opposite to the propagation of the laser beam (see Figures 1b and S2). The gas stream is divided into two separate gas streams before entering both cylinders of the pumping cell. The pumping cell is heated to a temperature of ∼150 °C. A presaturation chamber (Figures 1c and S3) is connected to the inflow of the pumping cell to saturate the gas mixture with Rb vapor. The presaturation chamber has four bulges in its lower section and is 20 cm long. This maximizes the Rb surface area and thus the exchange rate with the gas phase. The Rb partial pressure is controlled by a heating jacket around the presaturation chamber with a separate temperature controller. The Rb vapor is removed from the gas mixture in a cold trap prior to exposure to the sample region. The cold trap was temperated to 0 °C with a 2-propanol bath that was cooled with dry ice.

■ RESULTS AND DISCUSSION

Building on the general points made about its basic construct (provided in the introduction), additional specifications are provided that inform on experimentally observed trends. First, the pumping cylinders are arranged vertically and the radius-to-length ratio was chosen to be smaller than 0.1 (currently 0.07) to minimize losses with respect to convection. Convection would enhance wall contacts of the hyperpolarized Rb and ^{129}Xe atoms and enhance relaxation. Based on the selected radius-to-length ratio, maintaining a high laser power density and increasing the active volume is possible by splitting the gas flow and directing it through two identical, slim pumping cylinders.

The laminar flow inside the pumping cell requires the gas mixture to be loaded with Rb vapor prior to entering the pumping cell—thus the use of an external presaturation chamber. Unusually high Rb vapor densities within a pumping cell can lead to the accumulation of Rb on the glass surface. This is a common problem when Rb is directly placed inside the pumping cell body; such deposition typically occurs in regions of low photon flux.[52] Here, we placed the presaturation chamber in a separate oven to mitigate this issue, allowing for the temperature of these two units to be controlled independently of each other. The distance between them ensures a homogeneous distribution of Rb vapor in the gas flow and offers the possibility for fine-tuned control of the Rb vapor density within the gas mixture prior to its exposure to the optical pumping cell.

The residence time is managed by a rotary vane pump and monitored by a mass flow meter. Operational volumetric flow rates ($\dot{V}$) range between 200 and 1200 mL/min, calibrated to standard conditions. With a pumping cell volume (V_{OP}) of 387 mL and a transfer volume (V_{tr}) of 129 mL, the total residence time (τ_{res}^{tot}) amounts to

https://doi.org/10.1021/acs.jpca.2c00891
J. Phys. Chem. A 2022, 126, 2578−2589

$$\tau_{\mathrm{res}}^{\mathrm{tot}} = 31\,240\ \mathrm{mL\cdot s/(bar\cdot min)}\cdot\frac{P}{\dot{V}} \tag{7}$$

relative to an absolute pressure, P, of 1 bar. As $V_{\mathrm{OP}} \approx 3\cdot V_{\mathrm{tr}}$, 75% of the total residence time accounts for the time spent within the optical pumping cell. The remaining 25% is attributed to the transport time of the gas mixture to the magnet. For a system pressure of 3 bar, minimal/maximal residence times of 58/349 s in the pumping cell and 20/120 s during transport arise, resulting in $\tau_{\mathrm{res}}^{\mathrm{tot}}$ of 78/469 s.

Two series of measurements are performed to characterize the polarizer proficiency as it relates to the conditions of the presaturation chamber directly. As previously discussed, the Rb vapor density is influenced by both the temperature and surface area of Rb in contact with the gas mixture. For series I, the presaturation chamber was half-filled with two puddles of Rb in two of the four bulges of the chamber. According to simulations of Fink and Brunner,[52] the restricted Rb surface leads to Rb partial pressures lower than the saturation vapor pressure in the gas mixture as the residence time of the gas mixture over the Rb surface is then too short to allow for equilibration. As a consequence of the laminar flow in the pumping cell, deposition of Rb vapor on the glass surface of the pumping cell is minimal and should not influence Rb concentration profiles in the pumping cell. For series II, Rb was filled in all four bulges of the presaturation chamber. The increase in the Rb surface area will result in a higher Rb vapor density in the gas mixture.

For series I, laser output power, flow rate, and system pressure were varied systematically while keeping the composition of the gas mixture (1% Xe, 3% N_2, and 96% He) and the presaturation chamber temperature (180 °C) constant. The trends for ^{129}Xe polarization as a function of the laser output power and the total residence time for selected flow rates and pressures are shown in Figure 2. Additional data supporting these trends are given in the Supporting Information (Figures S4–S10).

Based on eq 2, the ^{129}Xe polarization, P_{Xe}, should scale with increasing laser output power. This is consequent of the Rb optical pumping rate (γ_{opt}), as higher laser output power is expected to lead to larger electronic polarization values, P_{Rb}, which should in turn increase P_{Xe} per eq 1. Furthermore, the residence time and spin-exchange rate, Γ_{Xe}, ought to remain constant as long as the temperature of the pumping cell and the flow rate are not changed. Figure 2a shows that this expectation is matched by the behavior of the polarizer, in particular, for low system pressure. For 3 bar (black lines in Figure 2), the trend for P_{Xe} is almost independent of the flow rates and thus of the residence time. In this regime, the highest observable ^{129}Xe polarization is about 22%. Two effects become obvious with increasing pressure. First, the average ^{129}Xe polarization decreases to about 10% for 4 bar and 5% for 5 bar. Second, while for the largest flow rates (shortest residence times) P_{Xe} still increases steadily with higher laser output power, decreasing the flow leads to a reduction in the slope of the trend curves. Unexpectedly, for 5 bar, the slope becomes negative leading to a less efficient ^{129}Xe polarization at high laser output powers (Figure 2a, blue dashed line) and small flow rates.

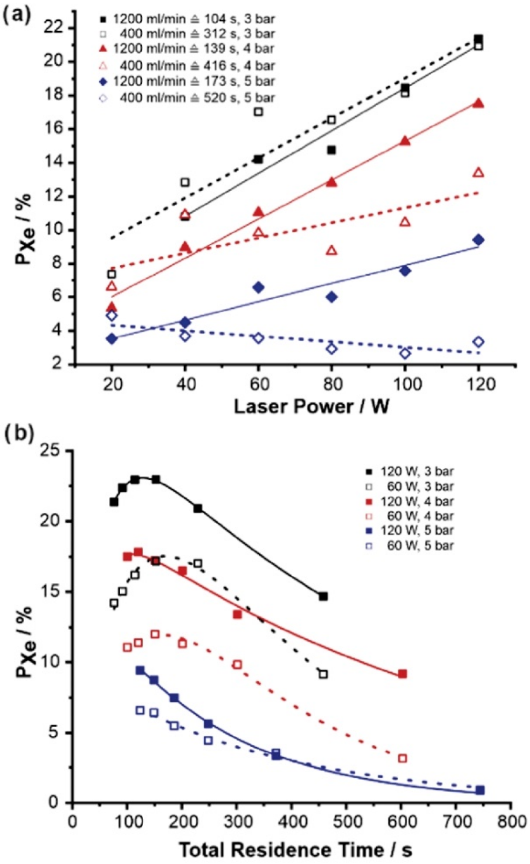

Figure 2. Overview of the trends for the ^{129}Xe polarization obtained for series I. The presaturation chamber is filled with two puddles of Rb, using half of the capacity of the Rb reservoir. (a) Trends as a function of the laser output power for pressures of 3 bar (black), 4 bar (red), and 5 bar (blue) and flow rates of 400 and 1200 mL/min (open and solid symbols). Labels in the figure are given as volume flow rate, total residence time, and system pressure. (b) Trends as a function of the total residence time for pressures of 3 bar (black), 4 bar (red), and 5 bar (blue) and laser powers of 60 and 120 W (open squares with dashed lines and solid squares with solid lines). The trend curves were derived by refining the ^{129}Xe polarization using eq 6. Figure S7 shows exemplarily the build-up and decay branches included in eq 6 for a system pressure of 3 bar and a laser output power of 120 W. The labels provide the laser power and system pressure.

This peculiar effect cannot be explained easily based on eqs 1 and 2. Although larger nuclear-spin destruction rates (Γ_{Xe}) would reduce P_{Xe}, this should influence small and high flow rates in a similar fashion as a function of the laser output power. This trend holds as long as the residence times in the pumping cell are long compared to the ones reported to be necessary for an efficient polarization transfer.[44] Trends shown in Figure 2b demonstrate that this is indeed the case. Thus, we attribute the decrease of P_{Xe} with increasing laser output power for small flow rates to an increase of the pumping cell temperature. This effect will be most severe for long residence times in the pumping cell and higher pressures. Larger pressure leads to more collisions, broadening the Rb D1 line. Thus, a larger part of the laser energy will be absorbed by the system, heating the gas mixture more strongly. Long residence times will enhance the temperature increase. The larger collision rate

https://doi.org/10.1021/acs.jpca.2c00891
J. Phys. Chem. A 2022, 126, 2578−2589

is likely to lead to larger Γ_{Xe} and Γ_{SD} and thus larger polarization relaxation rates for both ^{129}Xe and Rb atoms. For pressures beyond 5 bar and flows below 400 mL/min, even less efficient ^{129}Xe polarization was found with increasing laser output power.

Consequently, for the current dimensions of the pumping cell and accessible flow rates, favorable operating conditions were found at lower system pressures. To separate between processes within the pumping cell and during the transport to the NMR probe, where P_{Xe} is finally detected, the ^{129}Xe polarization is displayed as a function of the total residence time τ_{res}^{tot}, as shown in Figure 2b. The data reveals two regimes for P_{Xe}. For small τ_{res}^{tot}, P_{Xe} first rises as a function of τ_{res}^{tot} and finally decreases in the limit of large τ_{res}^{tot}, resulting in a pronounced maximum of P_{Xe} at intermediate residence times between 80 and 180 s (Figures 2 and S4−S7). This phenomenon matches the behavior predicted by eq 6 and demonstrates that for 3 bar, the smallest τ_{res}^{tot} of 80 s are somewhat small to reach the steady state of P_{Xe}. In this regime, P_{Xe} is sensitive to the time constant T_{pb} for the polarization build-up. In contrast, beyond τ_{res}^{tot} of 300 s, P_{Xe} is dominated by the decay time constant T_{tr}, which is on the order of 100 s (120−150 s).

The results shown in Figure 2b also indicate that the experimentally obtained P_{Xe} decreases with increasing system pressure, while its maximum value shifts toward shorter residence times. For example, at 4 bar, the residence time was determined to be 30 and 60 s, while only the decay branch of eq 6 was observed at 5 bar. In addition, reducing the laser output power also lowers P_{Xe}. Simultaneously, lower laser output powers shift the maximum observed P_{Xe} to larger τ_{res}^{tot}. Consequently, T_{pb} becomes smaller with increasing system pressure and laser output power. In both cases, the collision rates within the gas mixture are enhanced. This is either due to higher pressure or to an increased temperature based on the larger energy absorption. Larger collision rates in turn influence both γ_{SE} and Γ_{Xe}, explaining the reduction in T_{pb}.

For a system pressure of 3 bar, T_{pb} was determined to be 40 and 80 s for a laser output of 120 and 20 W, respectively. For system pressures larger than 4 bar, T_{pb} becomes too short to be determined from the experimental P_{Xe} data. As expected, an increase in system pressure shortens T_{tr} by the increasing collision rate within the gas mixture. While around 130 s at 3 bar, T_{tr} is roughly halved when the pressure is increased to 5 bar.

Figure 3 depicts the ^{129}Xe polarization as a dependence of laser output power and residence time for series II. Here, Rb was filled in all four bulges of the presaturation chamber, which was then heated to 175 °C. The increase in the Rb surface area led to a markedly higher Rb vapor density in the gas mixture,[52] which was required to reduce the presaturation temperature by 5 °C to achieve long-time stable polarization. Adopting the optimal system pressure found for series I, we started the measurements with a system pressure of 3 bar. The full data set is presented in Figures S11−S15. As observed for series I, P_{Xe} increases with increasing laser output power (Figure 3a). However, the polarization values are smaller by 50−70%. Furthermore, P_{Xe} decreases monotonically as a function of τ_{res}^{tot} (Figure 3b) for all laser output powers. The initial polarization build-up, partly observed for series I (Figure 2b), is not visible, which implies that the polarization build-up time T_{pb} (eq 6) is shorter than the one determined for series I. Also, the obtained transport relaxation time constants T_{tr} (eq 6) are roughly five times shorter (20 s for 120 W and 25 s for 30 W), indicating that the polarization decay during transport to the magnet is markedly enhanced.

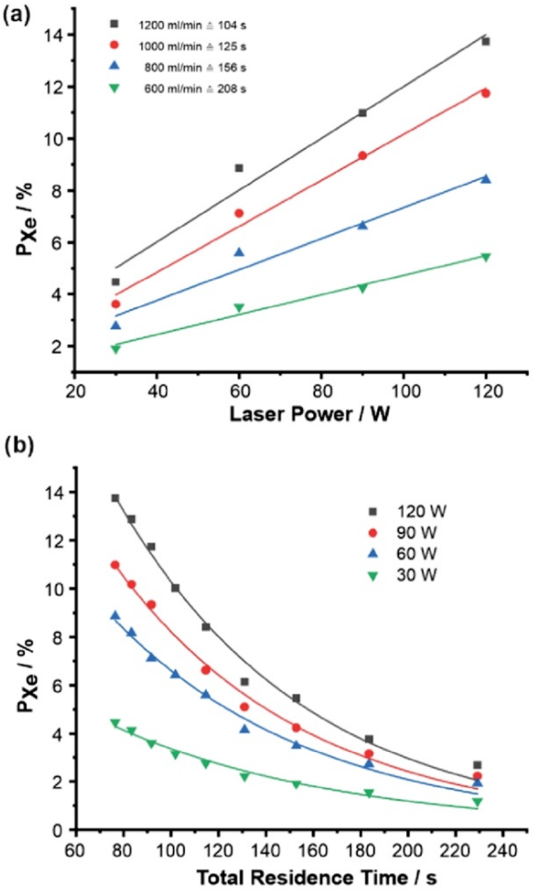

Figure 3. Trends for the ^{129}Xe polarization for series II for a system pressure of 3 bar. The presaturation chamber was filled with four puddles of Rb to 100% of its capacity. (a) Trend as a function of laser output power for flow rates of 1200 mL/min (black), 1000 mL/min (red), 800 mL/min (blue), and 600 mL/min (green). The labels refer to the flow rate and total residence time. (b) ^{129}Xe Polarization for various residence times for laser powers of 120 W (black), 90 W (red), 60 W (blue), and 30 W (green).

These trends can consistently be explained with a higher Rb vapor density, which would increase both the spin-exchange rate, γ_{SE}, and the xenon spin destruction rate, Γ_{Xe}, leading to smaller P_{Xe}^{∞} and shorter T_{pb} and T_{tr}. As the steady state for P_{Xe} is reached faster, the residence time in the pumping cell is now long enough for efficient polarization transfer for all conditions. However, the obtained P_{Xe} value decays faster during transport of the gas mixture to the magnet, which explains the lower observed ^{129}Xe polarization. To avoid such strong depolarization effects, which are most likely caused by binary Rb−Xe collisions, the distance between the pumping cell and cold trap should be kept as short as possible for future experiments.

An evaluation of the pressure dependence of P_{Xe} is provided in Figure 4a, showing a pronounced decrease at elevated

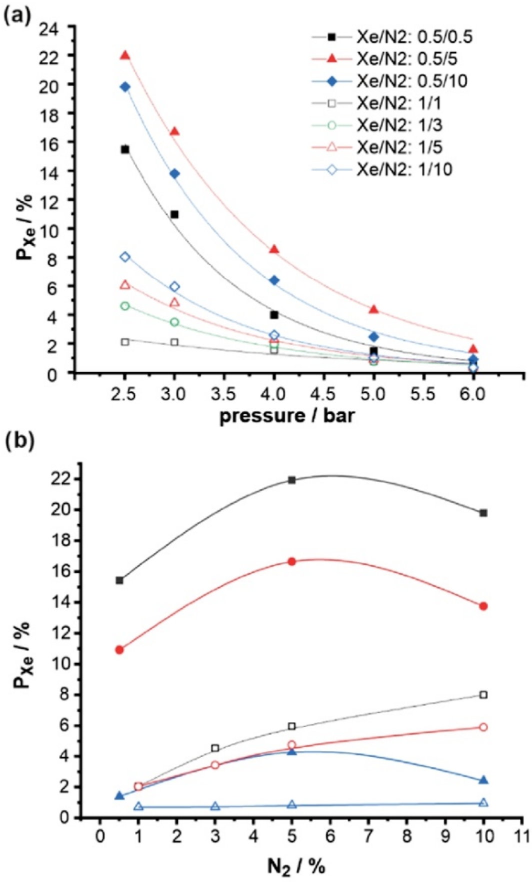

Figure 4. Trends for the ^{129}Xe polarization for a fully filled presaturation chamber (series II) for a laser power of 120 W and various gas compositions. (a) P_{Xe} as a function of the system pressure. The labeling refers to the volume fractions of xenon and nitrogen in percent. (b) P_{Xe} for different nitrogen volume fractions and system pressures of 2.5 bar (black lines and symbols), 3 bar (red lines and symbols), and 5 bar (blue lines and symbols). Solid symbols denote a xenon volume fraction of 0.5% and open symbols a volume fraction of 1%.

system pressures for all gas compositions studied. The largest P_{Xe} value of about 23% was obtained at the lowest pressure of 2.5 bar. In this respect, series II (fully filled presaturation chamber) exhibits a similar trend as series I (half-filled presaturation chamber). The absolute changes are, nevertheless, more pronounced. For the same gas composition and system pressures, higher Rb vapor densities are shown to lead to lower ^{129}Xe polarizations. This observation suggests that for the current polarizer design, the increase of the spin destruction rates (Γ_{Xe} and Γ_{SD}) and the accompanied reduction of P_{Xe}[65,66] outweigh the beneficial effect of pressure broadening.[29,67,68] As before, we attribute this to (i) a temperature increase in the pumping cell due to stronger absorption of the laser light and (ii) relatively long distances between the pumping cell and the cold trap, allowing Rb atoms to depolarize ^{129}Xe after leaving the pumping cell.

This trend is valid for all probed gas compositions (Figures 4 and S13). Lower Xe volume fractions lead to higher P_{Xe}, consistent with the literature.[36,47,69] Furthermore, we observed maximum ^{129}Xe polarization for a N_2 volume fraction roughly 10 times larger than the one for Xe, for all adjusted system pressures (Figure 4b). This trend is most obvious for a Xe volume fraction of 0.5%, as P_{Xe} is largest. The observed trend is in line with previous results, indicating that a higher volume percentage of N_2 is necessary to reach high P_{Xe}. Although N_2/Xe ratios below one were found to be sufficient to prevent energy pooling of excited Rb states in the pumping cell,[70] typical N_2-to-Xe ratios between 1 and 10 are used in high-pressure systems.[40,42,44,71,72] On average, the values are somewhat smaller compared to the observations made in the current study. The increased N_2 fraction necessary for our experiments hints toward higher Rb vapor densities in the pumping cell, and thus a higher demand of quenching gas.

The results for series I and II show that ^{129}Xe polarization for our pumping cell design can be described using eq 6. We demonstrate that changing the Rb vapor density has strong effects on the steady-state xenon polarization P_{Xe}^{∞}, the polarization build-up, and transport relaxation time constants T_{pb} and T_{tr} and thus on P_{Xe}. While restricting the surface area of the Rb pool turned out to be an elegant way to limit the Rb vapor density, its value cannot be changed easily, once the pumping cell is running. Thus, we explored the possibility also to adapt the Rb vapor density via the temperature of the presaturation chamber.

For a fully filled presaturation chamber (series II), the cell temperature was varied between 165 and 190 °C, measured at 5 °C increments and the resulting P_{Xe} determined as a function of the flow rate (Figure 5). P_{Xe} increases markedly with increasing flow rates for all presaturation temperatures. This is expected, as the residence times reduce, providing less time for the achieved ^{129}Xe polarization to decay; T_{pb} is short enough to ensure an efficient polarization build-up even for the shortest

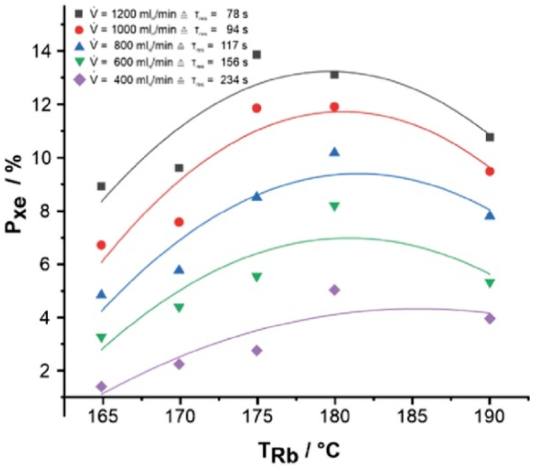

Figure 5. Influence of presaturation chamber temperature on ^{129}Xe polarization for volume flow rates of 1200 (black), 1000 (red), 800 (blue), 600 (green), and 400 mL/min (purple). Measured with a fully filled presaturation chamber (series II) at a system pressure of 3 bar, and a mixture of 1% Xe, 3% N_2, and helium as buffer gas with 120 W laser power. Solid lines are a guide for the eye.

residence times. P_{Xe} expresses a smooth maximum between 175 and 180 °C. As the results discussed above show no indication that the Rb vapor density varies with the volume flow, we attribute this behavior to an increasing Rb vapor density toward higher chamber temperatures. This is favorable for lower temperatures as more Rb is provided and polarized in the pumping cell, thereby increasing P_{Xe}. However, at temperatures above 180 °C, the Rb vapor density is excessive, once again leading to higher pumping cell temperatures, larger relaxation rates (Γ_{Xe}), and consequently a lower degree of long-time stable polarization.

Our results imply that the present polarizer setup provides two handles to adjust, and thus control, the Rb vapor density. Restricting the surface area for the Rb puddles in the presaturation chamber changes the Rb vapor density markedly, which is reflected in the pronounced drop of T_{pb} from 80 s (20 W) for series I to below the detection limit for series II. Raising the presaturation chamber temperature also increases the Rb vapor density and can be used to fine tune the final ^{129}Xe polarization.

^{129}Xe polarization reached in the pumping cell at infinite residence times (P^{∞}_{Xe}) can be estimated by modeling the obtained data series with eq 6. Due to fast polarization build-up for series II, only the decay branch of eq 6 is observed, making the absolute values of T_{pb} unattainable (Figure 3b). Refining the data with eq 6 using T_{pb}, T_{tr}, and P^{∞}_{Xe} leads to small T_{pb} values and thus provides a lower limit for P^{∞}_{Xe}. Refinements with larger but constrained T_{pb} values led to fits with similar quality, but with higher P^{∞}_{Xe}. Deviations occur for T_{pb} values larger than 30 s. This value is roughly the limit from where the build-up branch will show in the trends for P_{Xe} versus τ^{tot}_{res}. P^{∞}_{Xe} obtained for those refinements thus pose the higher limit for the polarization in the pumping cell. We expect the real values to be positioned within this range.

Figure 6 shows the estimated windows for P^{∞}_{Xe} for series II as a function of the presaturation chamber temperature and a laser output power of 120 W. P^{∞}_{Xe} is high for the whole temperature range (165−190 °C), demonstrating that the setup is robust and convenient to handle. ^{129}Xe polarizations between 35 and 50% were reached when measured at the optimal chamber temperature of 175 °C. Interestingly, similarly high ^{129}Xe polarizations were reached when filling the presaturation body half as in series I, albeit for a slightly higher presaturation chamber temperature (blue rectangle in Figure 6). As T_{pb} could be determined (Figure 2b) for this case, this value could be determined with a good confidence.

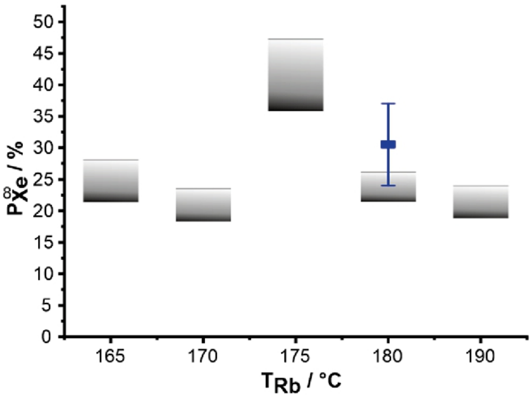

Figure 6. ^{129}Xe polarization in the optical pumping cell determined for series II (boxes) and series I (blue rectangle) using eq 6. Data fitting was based on measurement sets for 120 W laser power, 3 bar absolute pressure, and a gas mixture of 1% Xe, 3% N_2, and He as the buffer gas. The shaded regions mark regions for the extrapolated ^{129}Xe polarization. Its lower limit was obtained from free refinements of the experimental data with eq 6. The upper limit was derived by constraining T_{pb} to 30 s.

To compare different polarizer designs, not only is the net polarization crucial but also the amount of hyperpolarized ^{129}Xe, which is produced in a finite amount of time. For a better comparison, the magnetization production rate (MPR) is defined as

$$\mathrm{MPR} = \dot{V}\cdot x_{Xe}\cdot f\cdot P^{\infty}_{Xe} \tag{8}$$

Here, $\dot{V}$ denotes the volume flow, x_{Xe} is the molar fraction of xenon gas in the gas mixture, and f represents the ^{129}Xe isotope fraction in xenon gas.[71] The volume flow is normalized to standard conditions to obtain comparable results.

A comparison of polarization and MPR values for polarizers presented in the literature is shown in Table 1. Similar to the results obtained for this study, other high-pressure polarizers like the one of Zook et al.[47] showed highest P_{Xe} values for low pressures and lean xenon proportions of 0.6%, reaching values of 67%. MPRs of 100 mL/h were reached for ^{129}Xe gas enriched to 86%. With the present polarizer design, we reached roughly 70 mL/h working with ^{129}Xe in natural abundance and can thus produce roughly twice the amount of ^{129}Xe. The MPRs reached within this study are comparable to other polarizers with similarly sized pumping cells.[43,44,52] Often for these systems, ^{129}Xe polarization is lower, demonstrating that increasing the MPR is paid with a loss within the hyperpolarization efficiency. Nevertheless, the works of Ruset[48] showed that large MPRs and high polarization can be achieved by dramatically increasing the size of the optical pumping cell.

Table 1. Polarization and Magnetization Production Rate (MPR) for Various Polarizer Designs[a]

polarizer	pressure regime	polarization (%)	MPR (mL/h)
Driehuys[44]	hp	5	13
Rosen[45]	hp	7.5	37
Moudrakovski[46]	hp	6	5
Zook[47]	hp	67	26
Zook[47,b]	hp	40[b]	100[b]
Zook[47]	hp	23	27
Zook[47]	hp	12	35
Knagge[43]	hp	69	18
Ruset[48]	lp	64	50
Ruset[48]	lp	50	158
Ruset[48]	lp	22	348
Nikolaou[34]	lp−hp	>80	>76
this work	hp	36−48	68−91

[a] The MPR values were calculated based on the published polarization and experimental details. hp and lp refer to high- and low-pressure designs, respectively. The values for the current study were taken from series II with a flow rate of 1200 mL/min. If not noted otherwise, ^{129}Xe in natural abundance was used (f = 0.2624). [b] The measurement used 86% isotopic enrichment of ^{129}Xe.

Furthermore, by optimizing a batch mode polarizer, Nikolaou[34] showed both high polarization and high MPR due to fast accumulation times. Thus, MPR values of over 76 mL/h were achieved. This shows the potential of large production rates in applications independent of a steady stream of hyperpolarized ^{129}Xe, like MR imaging applications. In the case of research on porous materials and characterization of kinetics, it is of importance to supply a stable stream of xenon with large MPRs and high ^{129}Xe polarization.

To demonstrate the long-time stability of ^{129}Xe polarization, we acquired a series of four 2D EXSY spectra for the model system CAU-1-AmMe (Figure S16).[20] Xenon is adsorbed in its two interconnecting pore types—a large one (LP) with a diameter of roughly 1 nm and a small one (SP) with a diameter of 0.5 nm. At elevated temperatures, only one ^{129}Xe resonance is observed due to fast xenon diffusion within the whole pore system (Figure S17). Toward lower temperatures, more Xe atoms are adsorbed, and the diffusion rates become smaller. Two well-separated resonances occur around 170 K, characteristic for ^{129}Xe residing in the larger (155 ppm) and smaller (230 ppm) pores. In this regime, 2D EXSY spectra acquired as a function of the mixing time allow for the rate constants associated with the exchange of Xe atoms between the two types of pores to be quantified.[73−75] Such quantitative analysis of the corresponding cross-intensities (Figure 7 left) is only possible if the polarization is constant over the whole series of acquired 2D EXSY NMR spectra. Fluctuation of polarization during the experiment will result in signal artifacts.

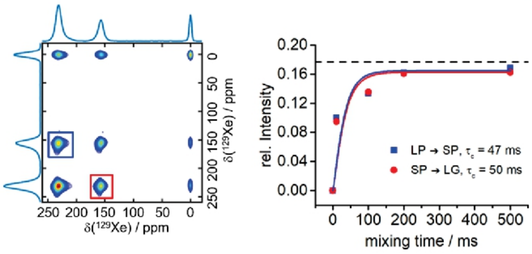

Figure 7. ^{129}Xe 2D-EXSY spectrum of CAU-1-AmMe and build-up curves for the cross-intensities of exchange between large pores (LPs) and small pores (SPs). All 2D spectra were acquired at 160 K with a home-built stop-flow device to stop the flow during the measurement and renew the gas within the waiting time between the transients. Left: EXSY spectrum for a mixing time of 500 ms. Right: Experimental and simulated build-up curves for the cross-intensities as a function of the mixing time. The color code denotes the exchange process: blue and red for Xe exchange between LP ↔ SP and vice versa. The dashed line represents the expected exchange intensity for infinite mixing times.

The ^{129}Xe 2D EXSY NMR spectra, in particular, for longer mixing times, show well-developed cross-intensities, proving exchange of xenon atoms between the gas phase (0 ppm), the small (230 ppm) pores, and large (155 ppm) pores (Figures 7 (left) and S16). While the two cross-peaks for the exchange between the pores are symmetric, the cross-peaks for the exchange of adsorbed xenon with the gas phase are asymmetric. Cross-peaks for xenon atoms being adsorbed from the gas phase are more intense compared to the ones for the desorption process, which is in line with larger spin destruction rates (Γ_{Xe}) for adsorbed ^{129}Xe.

For quantitative analysis of exchange intensities, we take into account only the cross-peaks for the exchange in the pore system (Figure 7 left). The relative 1D intensities for the three main resonances amount to 0.47 (230 ppm), 0.37 (155 ppm), and 0.16 (0 ppm). For infinite mixing times, the cross-intensities for the exchange between the LP and SP amount to 0.173, normalized to a total intensity of 1 for the whole 2D spectrum (Figure 7 right). The observed cross-intensities approach this boundary with excellent agreement. The correlation times, τ_c, were derived by refining the cross-intensities by the master equation approach.[73,76] A detailed description is given in the Supporting Information (Section S3.2). τ_c amounts to 50 ms (SP → LP) and 47 ms (LP → SP). Both values are similar, matching the rate matrix approach for which the same build-up behavior is expected for both cross-intensities. Based on the average distance between both pores and an average τ_c of 49 ms, the diffusion constant for Xe in CAU-1-AmMe is calculated to be 6.24×10^{-18} m^2/s. The high quality of the refinement and the excellent match with the expected exchange intensities demonstrate that the polarization is constant for the whole measurement period. As each spectrum required roughly 1 h of measurement time, this amounts to at least 4 h.

■ CONCLUSIONS

Here, we present an informed, home-built apparatus for polarizing ^{129}Xe by SEOP to support various ^{129}Xe NMR spectroscopic experiments. The design is rooted on a full evaluation of hyperpolarized ^{129}Xe production systems available in the literature to date and is shown to exhibit competitive levels of polarization and magnetization production rates for a high-pressure device (Table 1). The polarizer provides a continuous stream of a gas mixture, consisting of Xe, N_2, and He, which flows in a closed cycle over the sample in the NMR magnet and is designed for uninterrupted NMR spectroscopic measurements as a function of pressure and temperature. Optimal working conditions were derived by varying a broad range of system parameters (e.g., presaturation chamber filling conditions and temperature, system pressure, flow rate, laser output power, and gas composition). The polarizer reaches MPRs of about 70 mL/h and ^{129}Xe pumping cell polarization about 35% for moderate system pressures (≈2.5 bar), large laser output powers (120 W), high flow rates (1200 mL/min), and Xe−N_2 ratios of 1:10 in the gas mixture. At the sample, roughly 50% of the initial ^{129}Xe polarization is maintained, offering a fast and flexible ^{129}Xe NMR spectroscopic characterization. As the polarization remains stable for several hours, even the quantitative analysis of a series of 2D exchange spectra acquired for different mixing times was shown to be possible.

The central parts of the polarizer are a separate Rb presaturation chamber and a pumping cell with two slim and parallel bodies. The latter was positioned vertically in a fluid-heated oven to ensure a homogeneous temperature profile. The laser light of two Duo FAP diode laser arrays was split into two parallel, circularly polarized beams, each illuminating one body of the pumping cell. This design ensures high laser power density over the full length of the pumping cell bodies and allows for increasing the active gas volume, in turn maximizing the MPR of the polarizer. The use of an external Rb presaturation chamber with a separate oven provided two effective handles for controlling the Rb vapor density, improving the long-time stability of the polarization markedly. While spatially restricting the surface area of Rb within the presaturation chamber (partially fill) proved to have a large and discontinuous effect on the Rb vapor density, changing the

https://doi.org/10.1021/acs.jpca.2c00891
J. Phys. Chem. A 2022, 126, 2578−2589

presaturation chamber temperature enables fine tuning of the system. In this way, unwanted accumulation of Rb in the pumping cell with its negative effects on magnitude and stability of ^{129}Xe polarization could be minimized.

^{129}Xe polarization at the sample can be described by a simple phenomenological model (eq 6) that takes into account (i) a polarization build-up and (ii) polarization decay during transport of the gas to the sample. The parametrization helps in setting up and optimizing the system's working conditions, allows for determining the steady-state polarization in the pumping cell, and enables quantification of polarization losses on the gas transport to the sample. In this way, two routes for further improvements become obvious. First, we plan to shorten the distance between the pumping cell and the cold trap to minimize spin destruction rates on the way to the magnet as early as possible. Second, implementing a larger circulation pump, enabling higher flow rates would reduce polarization losses further and improve the MPR.

We built a polarizer that produces high polarization and is robust with respect to fluctuations of important system parameters. Working conditions, where the polarization is high and long-time stable, are easily set up. Due to the compact, transportable build-up, and excellent performance, the polarizer can be used for a broad variety of applications in life, environmental, and materials sciences.

■ ASSOCIATED CONTENT

Supporting Information

The Supporting Information is available free of charge at https://pubs.acs.org/doi/10.1021/acs.jpca.2c00891.

> Pictures and drawings of the polarization optics, pumping cell, and presaturation chamber; and graphs of the dependence of ^{129}Xe polarization on flow velocity/laser power/nitrogen content/system pressure as well as of the structure of CAU-1-AmMe and 1D-^{129}Xe NMR spectra of CAU-1-AmMe at various temperatures (PDF)

■ AUTHOR INFORMATION

Corresponding Authors

Caroline D. Keenan − *Department of Chemistry and Biochemistry, Carson-Newman University, Jefferson City, Tennessee 37760, United States*; Phone: (865)-471-3259; Email: ckeenan@cn.edu

Ernst A. Rössler − *Inorganic Chemistry III and Northern Bavarian NMR Centre, University of Bayreuth, 95447 Bayreuth, Germany*; orcid.org/0000-0001-5586-973X; Email: ernst.roessler@uni-bayreuth.de

Jürgen Senker − *Inorganic Chemistry III and Northern Bavarian NMR Centre, University of Bayreuth, 95447 Bayreuth, Germany*; orcid.org/0000-0002-7278-7952; Phone: +49 (0)921/55-2532; Email: juergen.senker@uni-bayreuth.de

Authors

Robert Stäglich − *Inorganic Chemistry III and Northern Bavarian NMR Centre, University of Bayreuth, 95447 Bayreuth, Germany*

Tobias W. Kemnitzer − *Inorganic Chemistry III and Northern Bavarian NMR Centre, University of Bayreuth, 95447 Bayreuth, Germany*

Marie C. Harder − *Inorganic Chemistry III and Northern Bavarian NMR Centre, University of Bayreuth, 95447 Bayreuth, Germany*

Adrian Schmutzler − *Inorganic Chemistry III and Northern Bavarian NMR Centre, University of Bayreuth, 95447 Bayreuth, Germany*

Marcel Meinhart − *Inorganic Chemistry III and Northern Bavarian NMR Centre, University of Bayreuth, 95447 Bayreuth, Germany*

Complete contact information is available at: https://pubs.acs.org/10.1021/acs.jpca.2c00891

Author Contributions

[§]R.S. and T.W.K. contributed equally to this work. The manuscript was written through contributions of all authors. All authors have given approval to the final version of the manuscript.

Notes

The authors declare no competing financial interest.

■ ACKNOWLEDGMENTS

The authors acknowledge the Deutsche Forschungsgemeinschaft for funding through the Mikroplastik SFB Project Number 391977956—SFB 1357, Subproject B01. The authors also thank Prof. Dr. Eike Brunner for fruitful discussions on the polarizer design.

■ REFERENCES

(1) Walker, T. G.; Happer, W. Spin-Exchange Optical Pumping of Noble-Gas Nuclei. *Rev. Mod. Phys.* **1997**, *69*, 629−642.

(2) Dregely, I.; Mugler, J. P.; Ruset, I. C.; Altes, T. A.; Mata, J. F.; Miller, G. W.; Ketel, J.; Ketel, S.; Distelbrink, J.; Hersman, F. W.; et al. Hyperpolarized Xenon-129 Gas-Exchange Imaging of Lung Microstructure: First Case Studies in Subjects with Obstructive Lung Disease. *J. Magn. Reson. Imaging* **2011**, *33*, 1052−1062.

(3) Mugler, J. P.; Driehuys, B.; Brookeman, J. R.; Cates, G. D.; Berr, S. S.; Bryant, R. G.; Daniel, T. M.; De Lange, E. E.; Downs, J. H.; Erickson, C. J.; et al. MR Imaging and Spectroscopy Using Hyperpolarized ^{129}Xe Gas: Preliminary Human Results. *Magn. Reson. Med.* **1997**, *37*, 809−815.

(4) Mugler, J. P.; Altes, T. A. Hyperpolarized ^{129}Xe MRI of the Human Lung. *J. Magn. Reson. Imaging* **2013**, *37*, 313−331.

(5) Nossov, A.; Guenneau, F.; Springuel-Huet, M. A.; Haddad, E.; Montouillout, V.; Knott, B.; Engelke, F.; Fernandez, C.; Gédéon, A. Continuous Flow Hyperpolarized ^{129}Xe-MAS NMR Studies of Microporous Materials. *Phys. Chem. Chem. Phys.* **2003**, *5*, 4479−4483.

(6) Pawsey, S.; Kalebaila, K. K.; Moudrakovski, I.; Ripmeester, J. A.; Brock, S. L. Pore Structure and Interconnectivity of CdS Aerogels and Xerogels by Hyperpolarized Xenon NMR. *J. Phys. Chem. C* **2010**, *114*, 13187−13195.

(7) Smith, J.; Knagge, K.; Smith, L. J.; MacNamara, E.; Raftery, D. Investigating Hyperpolarized^{129}Xe and CPMAS for Spin Polarization Transfer to Surface Nuclei: A Model Study. *J. Magn. Reson.* **2002**, *159*, 111−125.

(8) Zaheer, M.; Keenan, C. D.; Hermannsdörfer, J.; Roessler, E.; Motz, G.; Senker, J.; Kempe, R. Robust Microporous Monoliths with Integrated Catalytically Active Metal Sites Investigated by Hyperpolarized ^{129}Xe NMR. *Chem. Mater.* **2012**, *24*, 3952−3963.

(9) Keenan, C. D.; Herling, M. M.; Siegel, R.; Petzold, N.; Bowers, C. R.; Rössler, E. A.; Breu, J.; Senker, J. Porosity of Pillared Clays Studied by Hyperpolarized ^{129}Xe NMR Spectroscopy and Xe Adsorption Isotherms. *Langmuir* **2013**, *29*, 643−652.

(10) Norquay, G.; Parnell, S. R.; Xu, X.; Parra-Robles, J.; Wild, J. M. Optimized Production of Hyperpolarized ^{129}Xe at 2 Bars for in Vivo

Lung Magnetic Resonance Imaging. *J. Appl. Phys.* **2013**, *113*, No. 044908.

(11) Witte, C.; Kunth, M.; Rossella, F.; Schröder, L. Observing and Preventing Rubidium Runaway in a Direct-Infusion Xenon-Spin Hyperpolarizer Optimized for High-Resolution Hyper-CEST (Chemical Exchange Saturation Transfer Using Hyperpolarized Nuclei) NMR. *J. Chem. Phys.* **2014**, *140*, No. 084203.

(12) Witte, C.; Schröder, L. NMR of Hyperpolarised Probes. *NMR Biomed.* **2013**, *26*, 788−802.

(13) Wei, Q.; Seward, G. K.; Hill, P. A.; Patton, B.; Dimitrov, I. E.; Kuzma, N. N.; Dmochowski, I. J. Designing ^{129}Xe NMR Biosensors for Matrix Metalloproteinase Detection. *J. Am. Chem. Soc.* **2006**, *128*, 13274−13283.

(14) Spence, M. M.; Rubin, S. M.; Dimitrov, I. E.; Ruiz, E. J.; Wemmer, D. E.; Pines, A.; Yao, S. Q.; Tian, F.; Schultz, P. G. Functionalized Xenon as a Biosensor. *Proc. Natl. Acad. Sci.* **2001**, *98*, 10654−10657.

(15) Schröder, L.; Lowery, T. J.; Hilty, C.; Wemmer, D. E.; Pines, A. Molecular Imaging Using a Targeted Magnetic Resonance Hyperpolarized Biosensor. *Science* **2006**, *314*, 446−449.

(16) Chambers, J. M.; Hill, P. A.; Aaron, J. A.; Han, Z.; Christianson, D. W.; Kuzma, N. N.; Dmochowski, I. J. Cryptophane Xenon-129 Nuclear Magnetic Resonance Biosensors Targeting Human Carbonic Anhydrase. *J. Am. Chem. Soc.* **2009**, *131*, 563−569.

(17) Gomes, M. D.; Dao, P.; Jeong, K.; Slack, C. C.; Vassiliou, C. C.; Finbloom, J. A.; Francis, M. B.; Wemmer, D. E.; Pines, A. ^{129}Xe NMR Relaxation-Based Macromolecular Sensing. *J. Am. Chem. Soc.* **2016**, *138*, 9747−9750.

(18) Rubin, S. M.; Spence, M. M.; Dimitrov, I. E.; Ruiz, E. J.; Pines, A.; Wemmer, D. E. Detection of a Conformational Change in Maltose Binding Protein by ^{129}Xe NMR Spectroscopy. *J. Am. Chem. Soc.* **2001**, *123*, 8616−8617.

(19) Filimonova, S.; Nossov, A.; Dümig, A.; Gédéon, A.; Kögel-Knabner, I.; Knicker, H. Evaluating Pore Structures of Soil Components with a Combination of "Conventional" and Hyperpolarised ^{129}Xe NMR Studies. *Geoderma* **2011**, *162*, 96−106.

(20) Kemnitzer, T. W.; Tschense, C. B. L.; Wittmann, T.; Rössler, E. A.; Senker, J. Exploring Local Disorder within CAU-1 Frameworks Using Hyperpolarized ^{129}Xe NMR Spectroscopy. *Langmuir* **2018**, *34*, 12538−12548.

(21) Springuel-Huet, M.-A.; Nossov, A.; Adem, Z.; Guenneau, F.; Volkringer, C.; Loiseau, T.; Férey, G.; Gédéon, A. ^{129}Xe NMR Study of the Framework Flexibility of the Porous Hybrid MIL-53(Al). *J. Am. Chem. Soc.* **2010**, *132*, 11599−11607.

(22) Weiland, E.; Springuel-Huet, M.-A.; Nossov, A.; Gédéon, A. 129Xenon NMR: Review of Recent Insights into Porous Materials. *Microporous Mesoporous Mater.* **2016**, *225*, 41−65.

(23) Ruckdeschel, P.; Kemnitzer, T. W.; Nutz, F. A.; Senker, J.; Retsch, M. Hollow Silica Sphere Colloidal Crystals: Insights into Calcination Dependent Thermal Transport. *Nanoscale* **2015**, *7*, 10059−10070.

(24) Elfinger, M.; Schönauer, T.; Thomä, S. L. J.; Stäglich, R.; Drechsler, M.; Zobel, M.; Senker, J.; Kempe, R. Co-Catalyzed Synthesis of Primary Amines via Reductive Amination Employing Hydrogen under Very Mild Conditions. *ChemSusChem* **2021**, *14*, 2360−2366.

(25) Appelt, S.; Ünlü, T.; Zilles, K.; Shah, N. J.; Baer-Lang, S.; Halling, H. Experimental Studies of Rubidium Absolute Polarization at High Temperatures. *Appl. Phys. Lett.* **1999**, *75*, 427−429.

(26) Happer, W.; Miron, E.; Schaefer, S.; Schreiber, D.; van Wijngaarden, W. A.; Zeng, X. Polarization of the Nuclear Spins of Noble-Gas Atoms by Spin Exchange with Optically Pumped Alkali-Metal Atoms. *Phys. Rev. A* **1984**, *29*, 3092−3110.

(27) Bhaskar, N. D.; Happer, W.; McClelland, T. Efficiency of Spin Exchange between Rubidium Spins and Xe129 Nuclei in a Gas. *Phys. Rev. Lett.* **1982**, *49*, 25−28.

(28) Walker, T. G.; Happer, W. Spin-Exchange Optical Pumping of Noble-Gas Nuclei. *Rev. Mod. Phys.* **1997**, *69*, 629−642.

(29) Ottinger, C.; Scheps, R.; York, G. W.; Gallagher, A. Broadening of the Rb Resonance Lines by the Noble Gases. *Phys. Rev. A* **1975**, *11*, 1815−1828.

(30) Plummer, J. W.; Emami, K.; Dummer, A.; Woods, J. C.; Walkup, L. L.; Cleveland, Z. I. A Semi-Empirical Model to Optimize Continuous-Flow Hyperpolarized 129Xe Production under Practical Cryogenic-Accumulation Conditions. *J. Magn. Reson.* **2020**, *320*, No. 106845.

(31) Whiting, N.; Nikolaou, P.; Eschmann, N. A.; Barlow, M. J.; Lammert, R.; Ungar, J.; Hu, W.; Vaissie, L.; Goodson, B. M. Using Frequency-Narrowed, Tunable Laser Diode Arrays with Integrated Volume Holographic Gratings for Spin-Exchange Optical Pumping at High Resonant Fluxes and Xenon Densities. *Appl. Phys. B: Lasers Opt.* **2012**, *106*, 775−788.

(32) Appelt, S.; Baranga, A. B.-A.; Erickson, C. J.; Romalis, M. V.; Young, A. R.; Happer, W. Theory of Spin-Exchange Optical Pumping of ^{3}He and ^{129}Xe. *Phys. Rev. A* **1998**, *58*, 1412−1439.

(33) Raftery, D.; Long, H.; Meersmann, T.; Grandinetti, P. J.; Reven, L.; Pines, A. High-Field NMR of Adsorbed Xenon Polarized by Laser Pumping. *Phys. Rev. Lett.* **1991**, *66*, 584−587.

(34) Nikolaou, P.; Coffey, A. M.; Barlow, M. J.; Rosen, M. S.; Goodson, B. M.; Chekmenev, E. Y. Temperature-Ramped ^{129}Xe Spin-Exchange Optical Pumping. *Anal. Chem.* **2014**, *86*, 8206−8212.

(35) Nikolaou, P.; Coffey, A. M.; Walkup, L. L.; Gust, B. M.; Whiting, N.; Newton, H.; Barcus, S.; Muradyan, I.; Dabaghyan, M.; Moroz, G. D.; et al. Near-Unity Nuclear Polarization with an Open-Source ^{129}Xe Hyperpolarizer for NMR and MRI. *Proc. Natl. Acad. Sci. U.S.A.* **2013**, *110*, 14150−14155.

(36) Nikolaou, P.; Coffey, A. M.; Ranta, K.; Walkup, L. L.; Gust, B. M.; Barlow, M. J.; Rosen, M. S.; Goodson, B. M.; Chekmenev, E. Y. Multidimensional Mapping of Spin-Exchange Optical Pumping in Clinical-Scale Batch-Mode ^{129}Xe Hyperpolarizers. *J. Phys. Chem. B* **2014**, *118*, 4809−4816.

(37) Birchall, J. R.; Nikolaou, P.; Coffey, A. M.; Kidd, B. E.; Murphy, M.; Molway, M.; Bales, L. B.; Goodson, B. M.; Irwin, R. K.; Barlow, M. J.; et al. Batch-Mode Clinical-Scale Optical Hyperpolarization of Xenon-129 Using an Aluminum Jacket with Rapid Temperature Ramping. *Anal. Chem.* **2020**, *92*, 4309−4316.

(38) Birchall, J. R.; Irwin, R. K.; Chowdhury, M. R. H.; Nikolaou, P.; Goodson, B. M.; Barlow, M. J.; Shcherbakov, A.; Chekmenev, E. Y. Automated Low-Cost In Situ IR and NMR Spectroscopy Characterization of Clinical-Scale ^{129}Xe Spin-Exchange Optical Pumping. *Anal. Chem.* **2021**, *93*, 3883.

(39) Birchall, J. R.; Irwin, R. K.; Nikolaou, P.; Coffey, A. M.; Kidd, B. E.; Murphy, M.; Molway, M.; Bales, L. B.; Ranta, K.; Barlow, M. J.; et al. XeUS: A Second-Generation Automated Open-Source Batch-Mode Clinical-Scale Hyperpolarizer. *J. Magn. Reson.* **2020**, *319*, No. 106813.

(40) Haake, M.; Pines, A.; Reimer, J. A.; Seydoux, R. Surface-Enhanced NMR Using Continuous-Flow Laser-Polarized Xenon. *J. Am. Chem. Soc.* **1997**, *119*, 11711−11712.

(41) Shah, N. J.; Ünlü, T.; Wegener, H.-P.; Halling, H.; Zilles, K.; Appelt, S. Measurement of Rubidium and Xenon Absolute Polarization at High Temperatures as a Means of Improved Production of Hyperpolarized ^{129}Xe. *NMR Biomed.* **2000**, *13*, 214−219.

(42) Mortuza, M. G.; Anala, S.; Pavlovskaya, G. E.; Dieken, T. J.; Meersmann, T. Spin-Exchange Optical Pumping of High-Density Xenon-129. *J. Chem. Phys.* **2003**, *118*, 1581−1584.

(43) Knagge, K.; Prange, J.; Raftery, D. A Continuously Recirculating Optical Pumping Apparatus for High Xenon Polarization and Surface NMR Studies. *Chem. Phys. Lett.* **2004**, *397*, 11−16.

(44) Driehuys, B.; Cates, G. D.; Miron, E.; Sauer, K.; Walter, D. K.; Happer, W. High-volume Production of Laser-polarized ^{129}Xe. *Appl. Phys. Lett.* **1996**, *69*, 1668−1670.

(45) Rosen, M. S.; Chupp, T. E.; Coulter, K. P.; Welsh, R. C.; Swanson, S. D. Polarized ^{129}Xe Optical Pumping/Spin Exchange and Delivery System for Magnetic Resonance Spectroscopy and Imaging Studies. *Rev. Sci. Instrum.* **1999**, *70*, 1546−1552.

(46) Moudrakovski, I. L.; Lang, S.; Ratcliffe, C. I.; Simard, B.; Santyr, G.; Ripmeester, J. A. Chemical Shift Imaging with Continuously Flowing Hyperpolarized Xenon for the Characterization of Materials. *J. Magn. Reson.* **2000**, *144*, 372−377.

(47) Zook, A. L.; Adhyaru, B. B.; Bowers, C. R. High Capacity Production of >65% Spin Polarized Xenon-129 for NMR Spectroscopy and Imaging. *J. Magn. Reson.* **2002**, *159*, 175−182.

(48) Ruset, I. C.; Ketel, S.; Hersman, F. W. Optical Pumping System Design for Large Production of Hyperpolarized Xe129. *Phys. Rev. Lett.* **2006**, *96*, No. 053002.

(49) Nikolaou, P.; Coffey, A. M.; Walkup, L. L.; Gust, B. M.; Lapierre, C. D.; Koehnemann, E.; Barlow, M. J.; Rosen, M. S.; Goodson, B. M.; Chekmenev, E. Y. A 3D-Printed High Power Nuclear Spin Polarizer. *J. Am. Chem. Soc.* **2014**, *136*, 1636−1642.

(50) Imai, H.; Yoshimura, H.; Kimura, A.; Fujiwara, H. Continuous Flow Production of Concentrated Hyperpolarized Xenon Gas from a Dilute Xenon Gas Mixture by Buffer Gas Condensation. *Sci. Rep.* **2017**, *7*, No. 7352.

(51) Fink, A.; Baumer, D.; Brunner, E. Production of Hyperpolarized Xenon in a Static Pump Cell: Numerical Simulations and Experiments. *Phys. Rev. A: At., Mol., Opt. Phys.* **2005**, *72*, 1−9.

(52) Fink, A.; Brunner, E. Optimization of Continuous Flow Pump Cells Used for the Production of Hyperpolarized ^{129}Xe: A Theoretical Study. *Appl. Phys. B: Lasers Opt.* **2007**, *89*, 65−71.

(53) Koschnick, C.; Stäglich, R.; Scholz, T.; Terban, M. W.; von Mankowski, A.; Savasci, G.; Binder, F.; Schökel, A.; Etter, M.; Nuss, J.; et al. Understanding Disorder and Linker Deficiency in Porphyrinic Zirconium-Based Metal−Organic Frameworks by Resolving the Zr_8O_6 Cluster Conundrum in PCN-221. *Nat. Commun.* **2021**, *12*, No. 3099.

(54) Wittmann, T.; Mondal, A.; Tschense, C. B. L.; Wittmann, J. J.; Klimm, O.; Siegel, R.; Corzilius, B.; Weber, B.; Kaupp, M.; Senker, J. Probing Interactions of N-Donor Molecules with Open Metal Sites within Paramagnetic Cr-MIL-101: A Solid-State NMR Spectroscopic and Density Functional Theory Study. *J. Am. Chem. Soc.* **2018**, *140*, 2135−2144.

(55) Breunig, M.; Dorner, M.; Senker, J. Ultramicroporous Polyimides with Hierarchical Morphology for Carbon Dioxide Separation. *J. Mater. Chem. A* **2021**, *9*, 12797−12806.

(56) Klumpen, C.; Breunig, M.; Homburg, T.; Stock, N.; Senker, J. Microporous Organic Polyimides for CO_2 and H_2O Capture and Separation from CH_4 and N_2 Mixtures: Interplay between Porosity and Chemical Function. *Chem. Mater.* **2016**, *28*, 5461−5470.

(57) Pedrotti, F. L.; Pedrotti, L. M.; Pedrotti, L. S. *Introduction to Optics*; Cambridge University Press, 2017. DOI: 10.1017/9781108552493.

(58) Happer, W.; Van Wijngaarden, W. A. An Optical Pumping Primer. *Hyperfine Interact.* **1987**, *38*, 435−470.

(59) Chen, W. C.; Gentile, T. R.; Walker, T. G.; Babcock, E. Spin-Exchange Optical Pumping of ^{3}He with Rb-K Mixtures and Pure K. *Phys. Rev. A* **2007**, *75*, No. 013416.

(60) Goodson, B. M. Advances in Magnetic Resonance: Nuclear Magnetic Resonance of Laser-Polarized Noble Gases in Molecules, Materials, and Organisms. *J. Magn. Reson.* **2002**, *155*, 157−216.

(61) Hunt, E. R.; Carr, H. Y. Nuclear Magnetic Resonance of Xe129 in Natural Xenon. *Phys. Rev.* **1963**, *130*, 2302−2305.

(62) Chann, B.; Nelson, I. A.; Anderson, L. W.; Driehuys, B.; Walker, T. G. ^{129}Xe - Xe Molecular Spin Relaxation. *Phys. Rev. Lett.* **2002**, *88*, No. 113201.

(63) Driehuys, B.; Cates, G. D.; Happer, W. Surface Relaxation Mechanisms of Laser-Polarized ^{129}Xe. *Phys. Rev. Lett.* **1995**, *74*, 4943−4946.

(64) Barker, J. R. New Coil Systems for the Production of Uniform Magnetic Fields. *J. Sci. Instrum.* **1949**, *26*, 273−275.

(65) Zeng, X.; Wu, Z.; Call, T.; Miron, E.; Schreiber, D.; Happer, W. Experimental Determination of the Rate Constants for Spin Exchange between Optically Pumped K, Rb, and Cs Atoms and ^{129}Xe Nuclei in Alkali-Metal−Noble-Gas van Der Waals Molecules. *Phys. Rev. A* **1985**, *31*, 260−278.

(66) Nelson, I. A.; Walker, T. G. Rb-Xe Spin Relaxation in Dilute Xe Mixtures. *Phys. Rev. A* **2001**, *65*, No. 012712.

(67) Romalis, M. V.; Miron, E.; Cates, G. D. Pressure Broadening of Rb D_1 and D_2 lines by ^{3}He, ^{4}He, N_2, and Xe: Line Cores and near Wings. *Phys. Rev. A* **1997**, *56*, 4569−4578.

(68) Couture, A. H.; Clegg, T. B.; Driehuys, B. Pressure Shifts and Broadening of the Cs D_1 and D_2 Lines by He, N_2, and Xe at Densities Used for Optical Pumping and Spin Exchange Polarization. *J. Appl. Phys.* **2008**, *104*, No. 094912.

(69) Skinner, J. G.; Ranta, K.; Whiting, N.; Coffey, A. M.; Nikolaou, P.; Rosen, M. S.; Chekmenev, E. Y.; Morris, P. G.; Barlow, M. J.; Goodson, B. M. High Xe Density, High Photon Flux, Stopped-Flow Spin-Exchange Optical Pumping: Simulations versus Experiments. *J. Magn. Reson.* **2020**, *312*, No. 106686.

(70) Saha, I.; Nikolaou, P.; Whiting, N.; Goodson, B. M. Characterization of Violet Emission from Rb Optical Pumping Cells Used in Laser-Polarized Xenon NMR Experiments. *Chem. Phys. Lett.* **2006**, *428*, 268−276.

(71) Norquay, G.; Collier, G. J.; Rao, M.; Stewart, N. J.; Wild, J. M. Xe 129 -Rb Spin-Exchange Optical Pumping with High Photon Efficiency. *Phys. Rev. Lett.* **2018**, *121*, No. 153201.

(72) Antonacci, M. A.; Burant, A.; Wagner, W.; Branca, R. T. Depolarization of Nuclear Spin Polarized ^{129}Xe Gas by Dark Rubidium during Spin-Exchange Optical Pumping. *J. Magn. Reson.* **2017**, *279*, 60−67.

(73) Coates, C. S.; Baise, M.; Schmutzler, A.; Simonov, A.; Makepeace, J. W.; Seel, A. G.; Smith, R. I.; Playford, H. Y.; Keen, D. A.; Siegel, R.; et al. Spin-Ice Physics in Cadmium Cyanide. *Nat. Commun.* **2021**, *12*, No. 2272.

(74) Liu, Y.; Zhang, W.; Liu, Z.; Xu, S.; Wang, Y.; Xie, Z.; Han, X.; Bao, X. Direct Observation of the Mesopores in ZSM-5 Zeolites with Hierarchical Porous Structures by Laser-Hyperpolarized ^{129}Xe NMR. *J. Phys. Chem. C* **2008**, *112*, 15375−15381.

(75) Jeener, J.; Meier, B. H.; Bachmann, P.; Ernst, R. R. Investigation of Exchange Processes by Two-dimensional NMR Spectroscopy. *J. Chem. Phys.* **1979**, *71*, 4546−4553.

(76) Senker, J.; Seyfarth, L.; Voll, J. Determination of Rotational Symmetry Elements in NMR Crystallography. *Solid State Sci.* **2004**, *6*, 1039−1052.

Supporting Information

Portable Hyperpolarized Xe-129 Apparatus with Long-Time Stable Polarization Mediated by Adaptable Rb Vapor Density

Robert Stäglich,[‡a] Tobias W. Kemnitzer,[‡a] Marie C. Harder,[a] Adrian Schmutzler,[a] Marcel Meinhart,[a] Caroline D. Keenan,[b]* Ernst A. Rössler,[a]* and Jürgen Senker[a]*

a. Inorganic Chemistry III and Northern Bavarian NMR Centre, University of Bayreuth, Universitätsstraße 30, 95447, Bayreuth, Germany.
b. Department of Chemistry and Biochemistry, Carson-Newman University, 1645 Russel Avenue, Jefferson City, TN37760, USA† These authors contributed equally to this work

S1. Technical Data

In the following paragraph, details of the polarizer equipment are presented. Specially manufactured glass cells for saturation with rubidium, the uniquely shaped pumping cell as well as our approach to laser beam shaping are described in detail.

S1.1 Optics

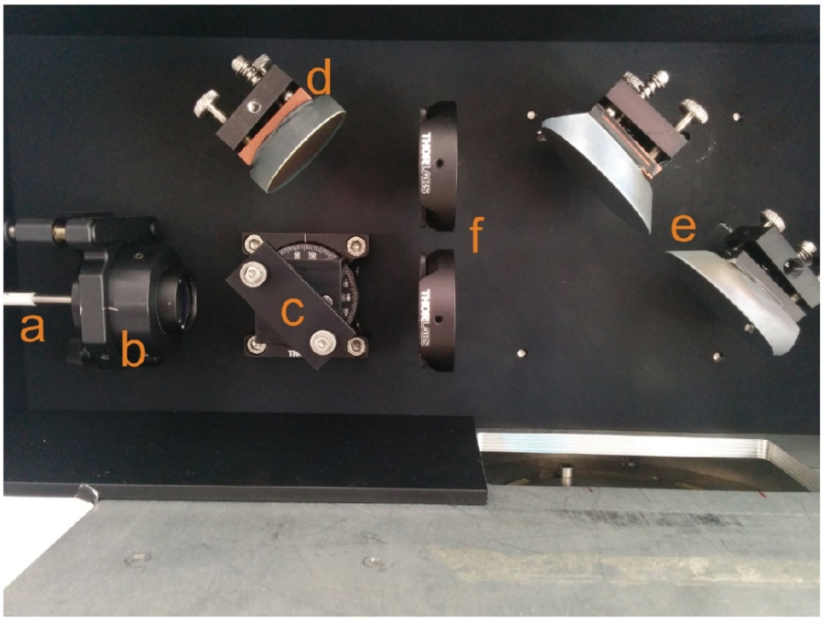

Figure S1. Beam shaping optics. a) Optical fiber combining the beams of the 4 diode lasers to max. 120 W optical output power. b) Beam collimator parallelizing the highly divergent laser beam exiting the optical fiber. c) Polarizing beam splitter, with laser beams exiting to the top and the right. d) and e) Mirrors. f) λ/4 plates for circular polarization of both linearly polarized laser beams.

S1.2 Pumping Cell

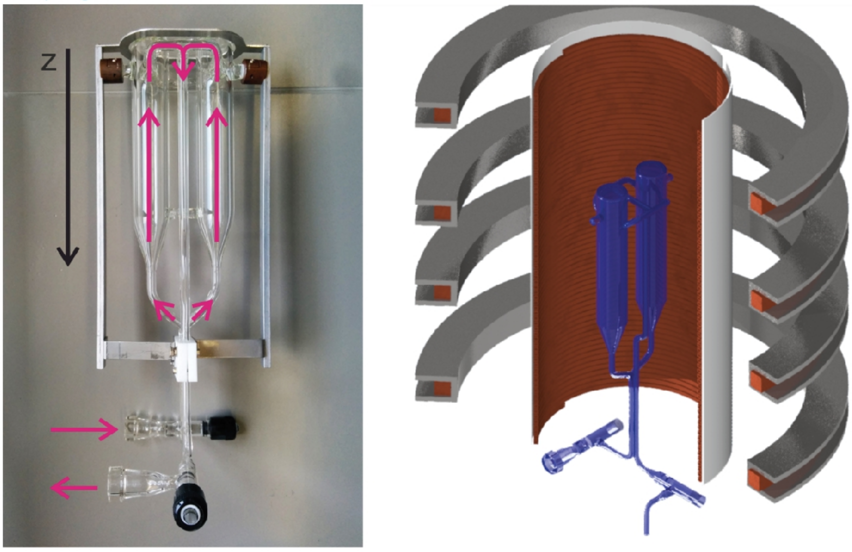

Figure S2. Left: Double bodied optical pumping cell. In pink the direction of gas flow is indicated. Starting in the lower left, the pumping cell is connected via a flange to the presaturation cell, the gas flow is directed upwards and split into two streams. Each gas stream enters an individual optical pumping cylinder with an inner diameter of 30 mm and a length of approximately 30 cm. With a recess of roughly 2 cm, the outflow of the cylinders exits in a 45° angle in respect to the cylinder axis. Both optical pumping cylinders have two outflow pipes which all combine in a single pipe, directed down to another valve and flange. The flat laser entrance windows (top of the cylinders) are made of anti-reflex coated quartz glass. The pumping cell is contained in a scaffold, aligning it in the hot air oven and the laser beams. The black arrow indicates the laser beam direction and the z-direction as indicated in equation 2 in the manuscript. Right: CAD detail of position of the pumping cell (blue for contrast) in the oven (cut copper windings surrounded by aluminum shield). Four copper Helmholtz coils are arranged around the oven to supply a homogenous magnetic field inside the optical pumping cell.

S1.3 Presaturation Cell

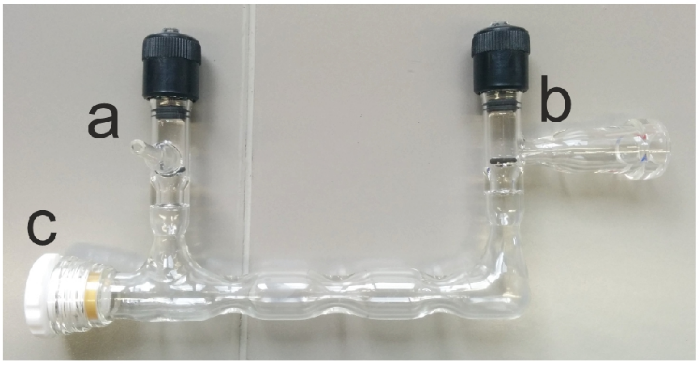

Figure S3. Rubidium presaturation cell. a) Valve and gas inflow. b) Valve for gas outflow. Via the flange a connection to the optical pumping cell is realized. c) Rubidium filling port with PTFE gasket screw. The indentations at the bottom of the cell serve as reservoirs for the Rb. They avoid the Rb to flow and accumulate in the right part of the cell and define the surface area of the Rb, which is exposed to the gas flow. For measurement “series II” the bottom of all four bulges were filled with Rb, while in “series I” only the first two bulges were filled.

S2. Polarizer Performance

^{129}Xe polarization as function of all parameters probed for series I and II are shown in the following.

S2.1 Presaturation cell half-filled with two puddles of Rb (series I)

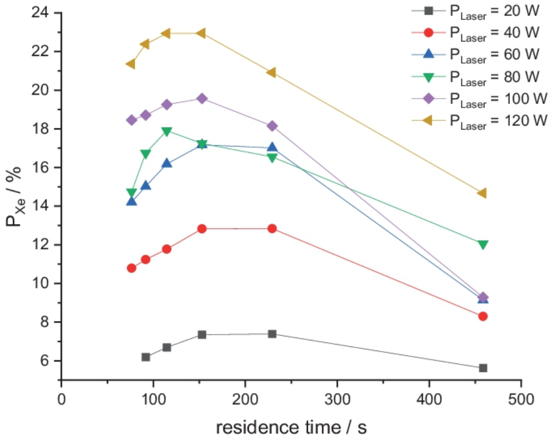

Figure S4. ^{129}Xe polarization in dependence of flow velocity. p = 3 bar.

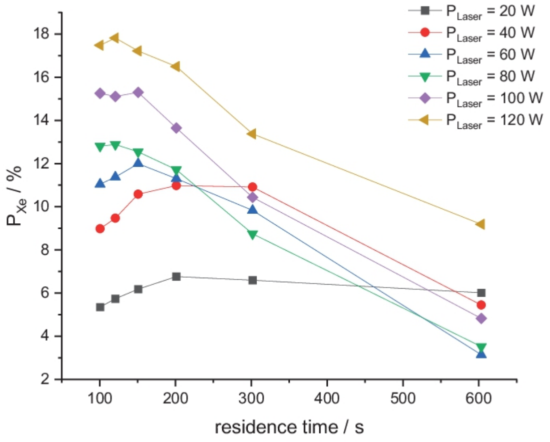

Figure S5. ^{129}Xe polarization in dependence of flow velocity. p = 4 bar.

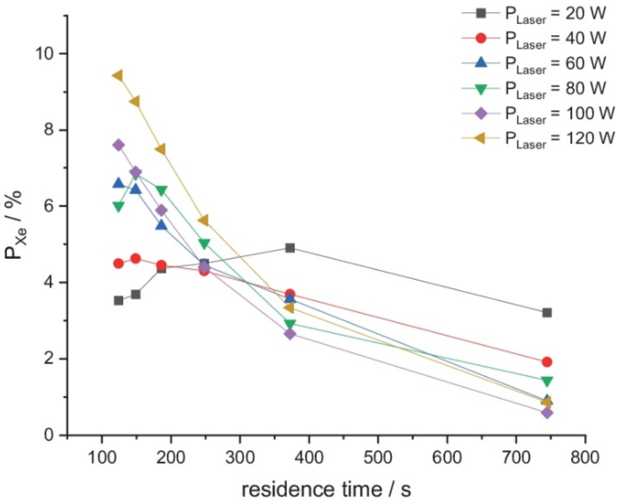

Figure S6. ^{129}Xe polarization in dependence of flow velocity. p = 5 bar.

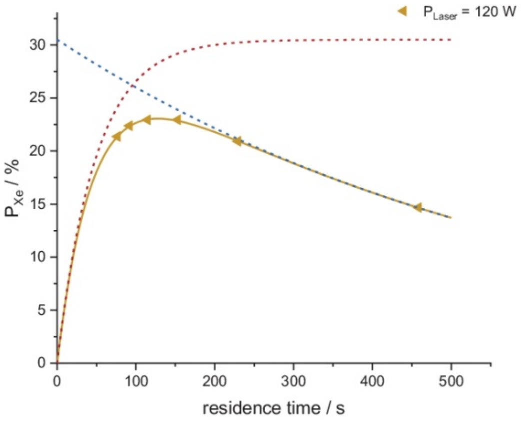

Figure S7. ^{129}Xe polarization as function of the flow velocity with the full trend curve (yellow) refined from equation 6 for a system pressure of p = 3 bar and a laser output power of 120 W. The two branches included in equation 6 are highlighted. The red dashed line represents the build-up branch and the polarization decay is given as a blue dashed line.

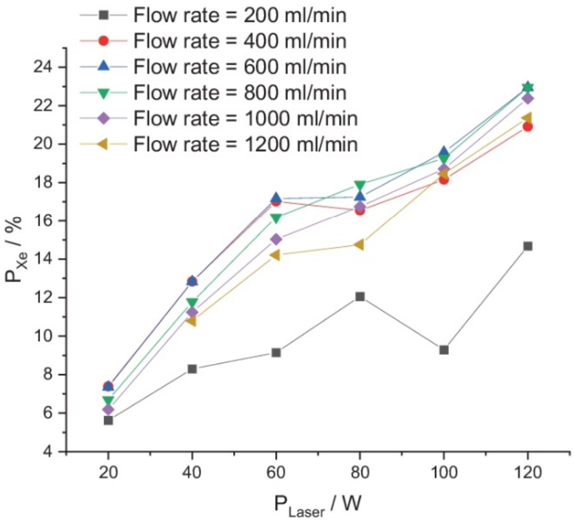

Figure S8. ^{129}Xe polarization in dependence of laser power. p = 3 bar.

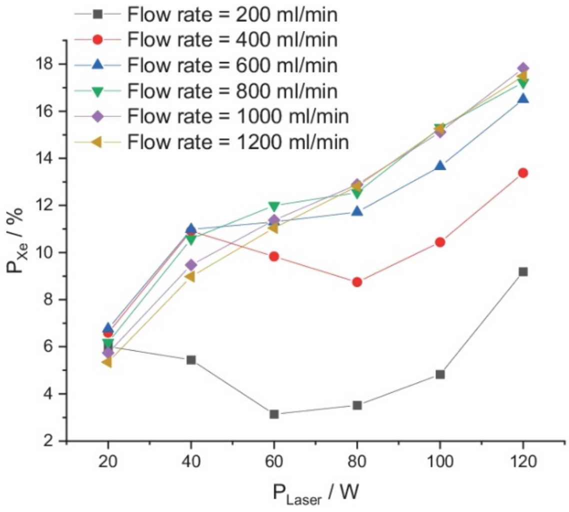

Figure S9. ^{129}Xe polarization in dependence of laser power. p = 4 bar.

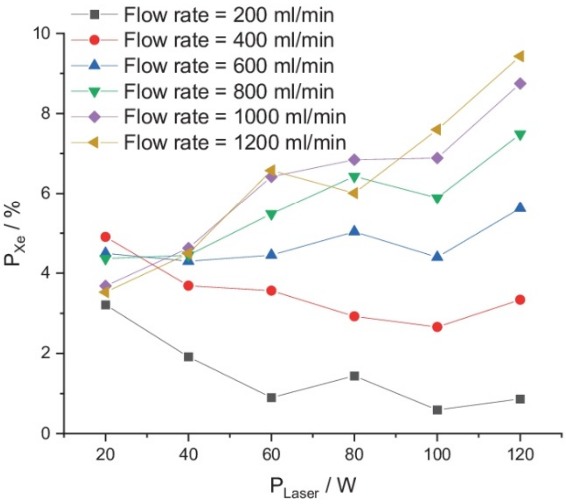

Figure S10. ^{129}Xe polarization in dependence of laser power. p = 5 bar.

S2.2 Presaturation cell fully filled

In Figure S11 the polarization over volume flow is shown for laser powers between 30 and 120 W and for Rb presaturation cell temperatures of 165°C and 170°C. The behavior is identical as depicted in Fig. 2a in the manuscript, furthermore underlining the main dependence on relaxation mechanisms during transport from the polarizer to the pumping cell. Figure S12 also completes the dataset for Figure 2b in the manuscript.

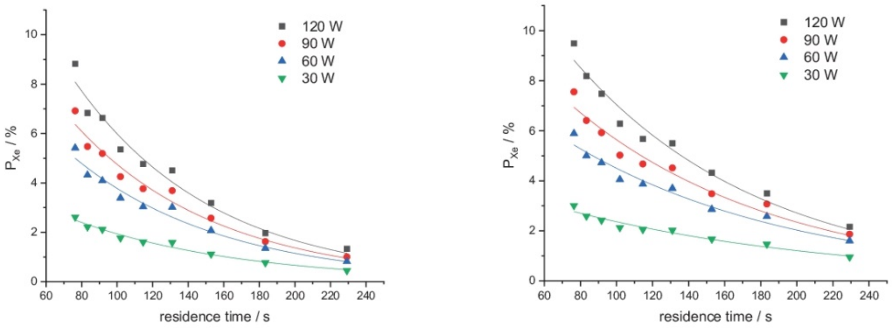

Figure S11. ^{129}Xe polarization in dependence of flow velocity for laser powers of 120 (black), 90 (red), 60 (blue) and 30 (green) W. Left: Temperature of the Rb presaturation cell of 165°C. Right: T_{Rb} = 170°C.

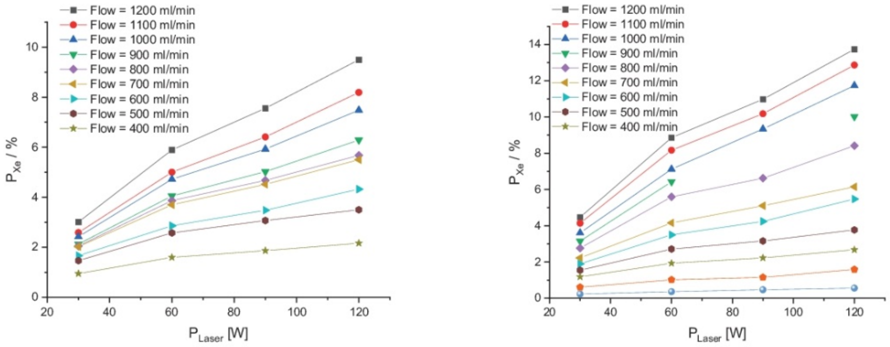

Figure S12. ^{129}Xe polarization in dependence of laser output power. Left: T_{Rb} = 170°C, right: T_{Rb} = 175°C.

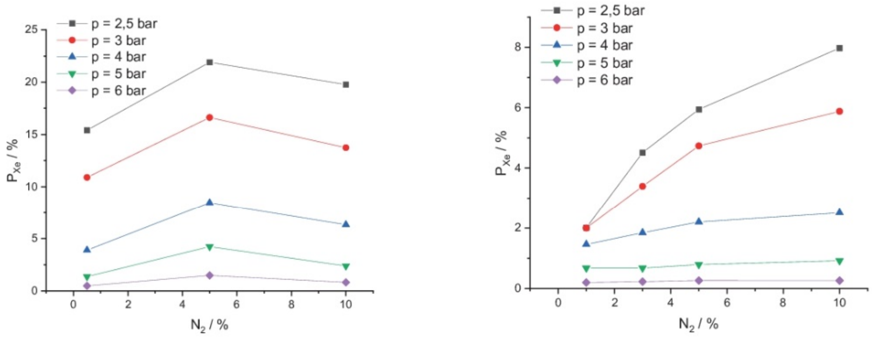

Figure S13. ^{129}Xe polarization in dependence of nitrogen volume fraction Left: Xenon gas content of 0.5%, Right: Xenon gas content of 1%.

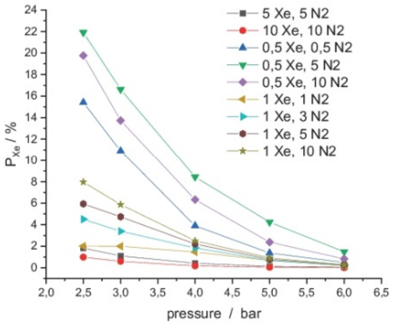

Figure S14. ^{129}Xe polarization in dependence of system pressure.

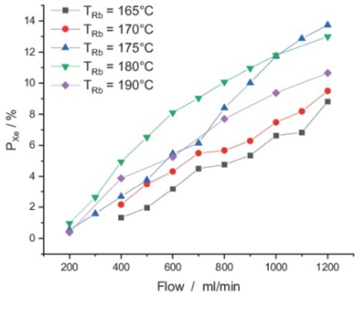

Figure S15. ^{129}Xe polarization in dependence of flow velocity for Rb presaturation temperatures between 165°C and 190°C and a laser power of 120 W.

S3. Application to CAU-1-AmMe

In the following, measurements of hyperpolarized ^{129}Xe NMR spectroscopy are shown and the evaluation strategy for the ^{129}Xe-2D-EXSY NMR experiments is described.

S3.1 Hyperpolarized ^{129}Xe NMR spectroscopy of CAU-1-AmMe

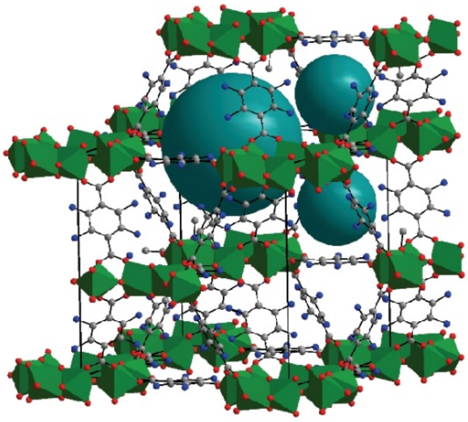

Figure S16. Characteristic cut out depicting the structure model of CAU-1-AmMe. One fourth of all hydrogen atoms at the benzene rings is exchanged by an $NH - CO - CH_3$ group (MaMe).

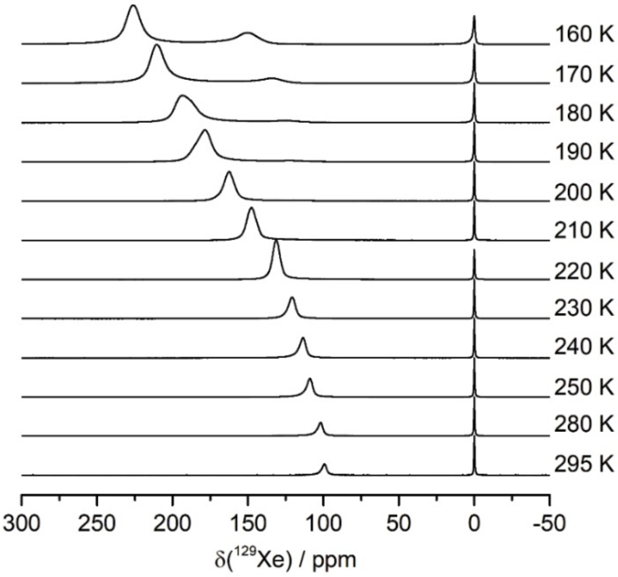

Figure S17. *Variable temperature hp ^{129}Xe NMR spectra of CAU-1-AmMe.*

S3.2 Evaluation of ^{129}Xe-2D-EXSY NMR experiments

In case of slow exchange between Xe sites with different chemical shifts, the normalized intensities of a ^{129}Xe 2D EXSY spectrum correspond to conditional probabilities p_{ab}. The p_{ab} describe the probabilities of finding a xenon atom on site a after the mixing time τ_m, if the same xenon atom was positioned on site b before τ_m.[73, 76] The time-dependent evolution of the p_{ab} follows a master equation:

$$\dot{P} = KP.$$

P is a matrix with elements p_{ab} and K is the kinetic matrix containing the exchange rates k_{ab}. The diagonal elements of K are given by $k_{aa} = -\sum_{b\neq a} k_{ba}$.

The master equation solves to:

$$P(\tau_{mix}) = \exp\,(K\tau_{mix}) \cdot P^0.$$

P^0 is a diagonal matrix containing the initial probabilities p^0_{aa}. For the current case p^0_{aa} corresponds to the equilibrium probability of site *a* e.g. determined from a quantitative 1D spectrum. $p^0_{ab} = 0$.

For the ^{129}Xe EXSY spectra provided in the manuscript, three sites, one for the large pores (LP), one for the small pores (SP) and one for the gas phase (GP) need to be taken into account. Their equilibrium probabilities are $p(LP)$, $p(SP)$ and $p(GP)$, respectively. K amounts to

$$K = \begin{pmatrix} -(k_{LP\to SP} + k_{LP\to GP}) & k_{SP\to LP} & k_{GP\to LP} \\ k_{LP\to SP} & -(k_{SP\to LP} + k_{SP\to GP}) & k_{GP\to SP} \\ k_{LP\to GP} & k_{SP\to GP} & -(k_{GP\to LP} + k_{GP\to SP}) \end{pmatrix}$$

with a detailed balance for the exchange rates

$$k_{LP\to SP} \cdot p(LP) = k_{SP\to LP} \cdot p(SP)$$

$$k_{LP\to GP} \cdot p(LP) = k_{GP\to LP} \cdot p(GP)$$

$$k_{SP\to GP} \cdot p(SP) = k_{GP\to SP} \cdot p(GP).$$

In general, the trend for cross intensities for a three-site jump contain two contributions. The first describes the jumps towards site a and the second accounts for jumps from site a to all other sites. Both are described by exponential functions which are superimposed for the final trend. As neither an overshoot nor a delayed initial increase was observed for the cross intensities describing the exchange between the large and the small pores (Figure 7), the rates for exchange between LP and SP, LP and GP as well as SP and GP will be similar. For simplicity, we chose the same value for all three exchange rates for the all-site exchange model:

$$k = k_{LP\to SP} = k_{LP\to GP} = \ k_{SP\to GP}.$$

The correlation time τ_c for exchange between the large and small pores it thus follows $\tau_c = k^{-1}$.

The cross intensities for the exchange of Xe atoms between the large and the small pores then read as

$$\begin{aligned} & p_{LP\rightarrow SP}(\tau_m) = p_{SP\rightarrow LP}(\tau_m) \\ & = p^{\infty}\left(1 - \frac{1}{p(LP)+p(SP)} e^{-\frac{p(LP)+2p(SP)}{p(SP)}\cdot k\cdot\tau_m} + \frac{p(GP)}{p(LP)+p(SP)} e^{-\frac{1}{p(GP)}\cdot k\cdot\tau_m}\right) \end{aligned}$$

with $p^{\infty} = p(LP)\cdot p(SP)$. *p(LP)*, *p(SP)* and *p(GP)* were derived from the normalized intensities within the 1D ^{129}Xe spectrum.

5.2. Hollow silica sphere colloidal crystals insights into calcination dependent thermal transport

P. Ruckdeschel,[a] T. W. Kemnitzer,[b] F. A. Nutz,[a] J. Senker[b] und M. Retsch[a]*

Erschienen in:

Nanoscale *2015*, *7*, 10059-10070, Copyright Royal Society of Chemistry
DOI: 10.1039/c5nr00435g

[a] Department of Physical Chemistry I, University of Bayreuth, Universitätsstr. 30, 95447 Bayreuth (Germany

[b] Department of Inorganic Chemistry III, University of Bayreuth, Universitätsstr. 30, 95447 Bayreuth (Germany)

* markus.retsch@uni-bayreuth.de

Nanoscale

PAPER

View Article Online
View Journal | View Issue

Cite this: *Nanoscale*, 2015, **7**, 10059

Hollow silica sphere colloidal crystals: insights into calcination dependent thermal transport†

P. Ruckdeschel,[a] T. W. Kemnitzer,[b] F. A. Nutz,[a] J. Senker[b] and M. Retsch*[a]

Received 20th January 2015,
Accepted 27th April 2015

DOI: 10.1039/c5nr00435g

www.rsc.org/nanoscale

Colloidal crystals consisting of monodisperse hollow silica spheres represent a well-defined porous material class, which features a range of interesting optical, mechanical, and thermal properties. These hierarchically structured materials comprise micropores within the silica network, which are confined to a thin shell (tens of nanometers) of a hollow sphere (hundreds of nanometers). Using simple calcination steps, we markedly change the internal microstructure, which we investigate by a multitude of characterization techniques, while the meso- and macrostructure remains constant. Most importantly the rearrangement of the silica condensation network leads to a reduction in the total surface area and loss of micropores as demonstrated by N_2 sorption and hyperpolarized ^{129}Xe NMR studies. Spin-lattice relaxation shows a drastic increase of the rigidity of the amorphous network. These microstructural changes significantly influence the thermal conductivity through such a porous silica material. We demonstrate a remarkably low thermal conductivity of only 71 mW m^{-1} K^{-1} for a material of a comparatively high density of 1.04 kg m^{-3} at 500 °C calcination temperature. This thermal conductivity increases up to 141 mW m^{-1} K^{-1} at the highest calcination temperature of 950 °C. The great strength of hollow silica sphere colloidal crystals lies in their hierarchical structure control, which allows further investigation of how the internal microstructure and the interfacial contact points affect the transport of heat.

Introduction

Thermal insulation is an important and indispensable part of current strategies to lower our total energy consumption worldwide. For insulation applications most commonly highly porous materials are being used such as foams or mineral wool.[1] These materials feature thermal conductivities between 30 and 40 mW m^{-1} K^{-1} due to their combination of an amorphous matrix intercalated by a high volume fraction of air, both being poor heat conductors. Nevertheless, fairly thick layers (tens of cm) of these classic materials are necessary to achieve satisfactorily low values of the overall thermal transmittance for their application in structures and buildings.

Another well investigated class of materials is silica aerogels.[2–4] Quite similar to polymeric foams, they comprise an amorphous skeleton and a particularly low density. The network is composed of amorphous silica, which is massively nanostructured by the presence of micro-, meso-, and macropores. Aerogels feature one of the lowest reported thermal conductivities of all material classes and can reach below 20 mW m^{-1} K^{-1}. They can therefore be considered super-insulation materials, which could make their way into widespread applications.[5] From a scientific point of view the total thermal conductivity κ of such an aerogel material is complex as it is influenced by four individual contributions.

$$\kappa_{\text{total}} = \kappa_{\text{solid conduction}} + \kappa_{\text{gas}} + \kappa_{\text{radiation}} + \kappa_{\text{convection}} \qquad (1)$$

These individual contributions depend critically on the actual porosity and microstructure of the respective aerogel material. Details can be found in the literature,[1,5–9] whereas we only want to give a short overview here. Convection is typically negligible due to the small pore sizes, which are present in aerogels. κ_{gas} greatly depends on the type of gas used to fill the free volume, which can take up to 99% in aerogels. The pressure of the atmosphere determines this contribution, which is completely suppressed in a vacuum. The dependence on the pressure of the atmosphere is expressed by the Knudsen formalism, which relates the mean free path of the gas molecule to the domain size of the pores, based on kinetic theory.[10,11] $\kappa_{\text{radiation}}$ depends on the temperature difference between the two surfaces of the aerogel monolith, the ambient temperature and the emissivity κ of these interfaces, which can

---

[a] *University of Bayreuth, Physical Chemistry 1 – Polymer Systems, Universitaetsstr. 30, 95447 Bayreuth, Germany. E-mail: markus.retsch@uni-bayreuth.de*

[b] *University of Bayreuth, Inorganic Chemistry 3, Universitaetsstr. 30, 95447 Bayreuth, Germany*

† Electronic supplementary information (ESI) available. See DOI: 10.1039/c5nr00435g

be calculated using the Stefan–Boltzmann equation.[8,12] Assuming that all pores are connected in series by air gaps leads to a dependence on the pore size. Ideally, the contribution of thermal radiation becomes less with decreasing pore size. However, it has to be noted that pores much smaller than the wavelength of the IR radiation may be less effective in reducing this contribution.[1] Furthermore, coupling between radiation and solid conduction can significantly alter the temperature distribution between the two material surfaces, which can result in higher contributions from thermal radiation.[8] Ways to suppress radiation contributions are given by the introduction of absorbing or reflecting moieties.[9,12] $\kappa_{\text{solid conduction}}$ increases with increasing density. Thermal energy is transported along the amorphous silica network by vibrational modes, which can be classified into propagons (propagating and delocalized) and diffusons (nonpropagating and delocalized).[13,14] The third class of vibrational modes, locons (nonpropagating and localized), do not contribute significantly to thermal transport.[15] Whereas a full atomistic understanding of thermal transport through amorphous silica still has to be established, Larkin *et al.* calculated that the contribution from propagating modes amounts to only ~6% of the total thermal conductivity.[15] At the same time the thermal conductivity accumulation function saturates at a mean free path (MFP) of only 10 nm for amorphous SiO_2, which is reflected in an independence of the thermal conductivity from the layer thickness of the amorphous film.[15] These calculations fit well to experimental data from Regner *et al.*, who used broadband frequency domain thermoreflectance to measure the thermal conductivity accumulation function.[16] More complicated systems, such as silica films with microporosity, however, are still elusive to be described by molecular dynamics or finite element simulations as shown by Coquil *et al.*[17] Experimentally, no influence of the symmetry of the micropores was observed using the 3ω technique.[18] Considering the situation of silica aerogels, one has to further take the influence of thermal transport across interfaces into account, as the thermal energy has to diffuse through the individual nanoclusters.[19]

Even though much progress has been made to fabricate silica aerogels over the last few decades, the mandatory supercritical drying step still presents an obstacle to their widespread use and implementation in other technologies.[2,3,20] A work-around to this delicate processing step is possible by the use of hollow spheres, which can be used in a vast range of applications by themselves.[21] In particular hollow silica nanoparticles (HSNP) can be conveniently fabricated by a template polystyrene particle process and thereby allow access to monodisperse particles with adjustable size and porosity.[22] Monodisperse hollow silica particles feature intriguing properties such as a coloration effect caused by Mie resonance,[23] as well as rich mechanical properties, both as single spheres[22,24] and in an ensemble structure.[25,26] Such particles can be processed by standard dispersion technologies into various nano- and mesostructured films, or they can be turned into dry nanoparticle powders. Whereas the record low densities of aerogels are hard to achieve in order to retain the structural integrity of the hollow spheres, they yield well-defined porous materials, which comprise a hierarchy of length scales. The silica shell can be as thin as 10 nm with an additional microporosity in the silica network. The size of the particles typically ranges from 100 nm up to several µm, depending on the size of the templating sphere. All these can be adjusted on a single particle level, with an additional length scale and symmetry to be added upon assembling those colloidal building blocks, which can result in crystalline or amorphous meso- or macrostructures.

Despite their structural complexity and ease of fabrication, only a little is known to date on the thermal conductivity of ensembles of hollow silica spheres.[27–30] Previous studies showed indeed the low thermal conductivity of hollow silica powders in the range from 20 to 33 mW m^{-1} K^{-1}. However, using the transient hot disk, the hotwire, or the 3ω technique, the authors did not specify details of the measurement parameters nor of the micro- or mesostructure of the hollow sphere powder under consideration. In such granular materials the contact points and adhesion between the spheres are of particular importance for the overall transport process along the silica network, as has been appreciated in previous studies, too.[19,28] Here, we want to fully capitalize on the well-defined structure of colloidal crystals consisting of hollow spheres. Our aim is not to demonstrate a record breaking ultralow thermal conductivity, but we want to introduce this material class as a platform to study the fundamentals of thermal transport in amorphous particle based materials. Specifically, we want to answer the question of how the internal microstructure of silica and the mutual contact points determine the thermal conductivity of the particle ensemble. We therefore measure specifically the thermal transport processes through the solid silica network by the laser flash technique.

Results and discussion

As outlined in the Experimental section we utilize hollow spheres of 316 nm diameter and 44 nm shell thickness. These are prepared by coating a polystyrene (PS) template with silica and ensuing calcination of the core/shell structure. Decomposition of the PS core sets in at about 300 °C. For quantitative combustion of the PS core, calcination has been carried out at 500 °C for 12 h. Thermal elemental analysis confirmed the complete combustion process by a lack of carbon in the 500 °C calcined spheres (see ESI Table S1†). This is also confirmed by thermogravimetric analysis (TGA), where a loss of ~2% is observed due to the removal of intercalated water (Fig. S5 in the ESI†). Another 1% of mass is lost up to 950 °C, which can be attributed to the removal of trace amounts of silica condensation products like water. During this core-removal calcination step the outer diameter of the core/shell sphere shrinks by about 2% when transitioning into hollow spheres. Uniformity and monodispersity are most important for a good struc-

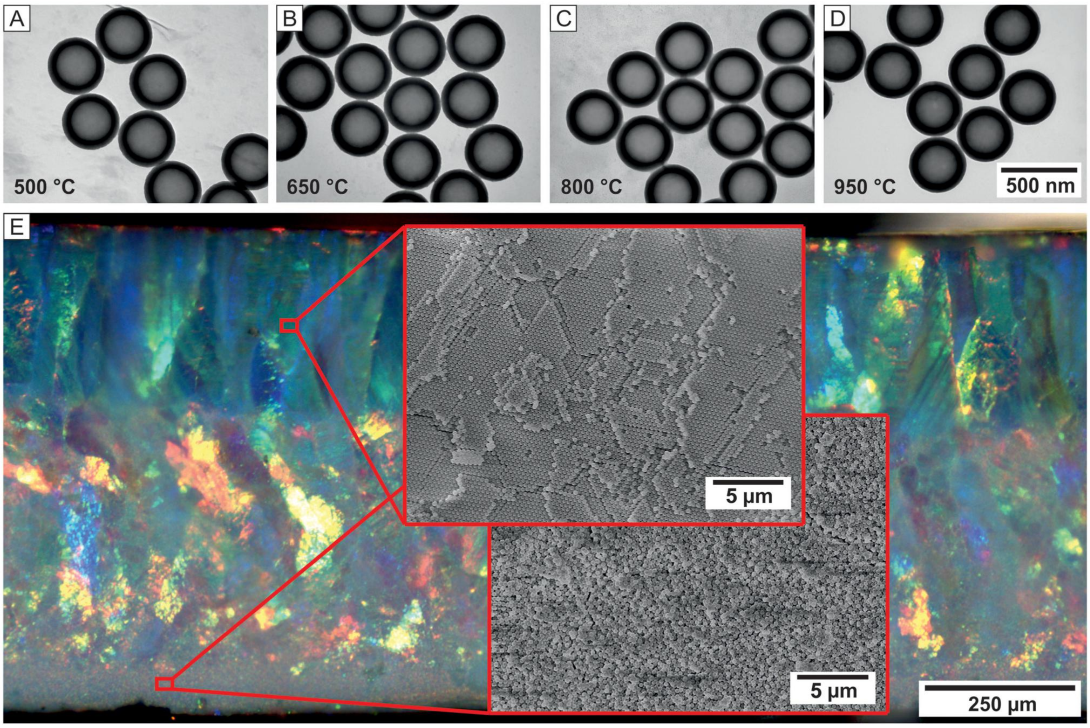

Fig. 1 (A–D) TEM images of hollow silica nanoparticles at different calcination temperatures (500–950 °C). The particle dimensions remain constant for the various calcination temperatures and do not show any clustering. (E) Correlative light and electron microscopy (CLEM) images of a HSNP colloidal crystal calcined at 500 °C. The bright colors are caused by coherent Bragg scattering. Most of the crystal is in a fully crystalline state as confirmed by the scanning electron microscopy (SEM) insets.

tural control of the individual particle, as well as for the assembly into a colloidal crystal, which defines the neighbouring contact points. Transmission electron microscopy (TEM) images demonstrate the size and shape of the hollow spheres (Fig. 1a–d). One can deduce that the spheres remain fully intact during the calcination cycle; they do not feature any cracks or dents. From the projection in the TEM the shell thickness can be measured, which is given by the dark shaded ring that surrounds the hollow core. The surface of the spheres appears smooth (ESI Fig. S1†), and the particles do not form aggregates or clusters. No sinter necks between the spheres or clusters can be seen in the TEM image, but they are rather individually redispersed in ethanol and deposited on the carbon-coated TEM grid. Quite importantly, the hollow spheres demonstrate only a minor shrinkage of their diameter and shell thickness after being subjected to higher calcination temperatures up to 950 °C. As can be seen in Table 1, the diameter slightly shrinks from 316 nm to 310 nm, whereas the shell thickness remains almost constant at 44 nm. In order to further characterize the shape of the hollow spheres, we performed SAXS measurements (ESI Fig. S2a†). A multitude of diffraction orders can be observed, which are fitted using the form factor of a vesicle. The data match well to the TEM measurement and further prove the monodispersity of the hollow spheres.

The functional properties of the hollow spheres only come into play when being assembled into a colloidal superstructure. We therefore used colloidal self-assembly of the core/shell particles as well as hollow spheres calcined at 950 °C, both dispersed in water, in order to fabricate macroscopic monoliths of highly ordered colloidal crystals. Simple drying in PTFE beakers for several days turned out to be the most efficient way to obtain suitable monoliths.

Fig. 1e shows the side-view on a representative colloidal crystal after self-assembly from core/shell particles and calcination at 500 °C. The thicknesses of colloidal crystals under investigation here ranged from about 390 µm to 875 µm. Due to the particle size of 316 nm diameter the crystallinity of the colloidal crystal can be assessed by its bright opalescent colors. Different lattice orientations are exposed to the surface, which causes a multitude of colors observable in Fig. 1e. We used correlative light and electron microscopy to determine the crystallinity of the hollow sphere monolith. Two specific areas are highlighted in Fig. 1e. The top area

Table 1 Summary of data received from TEM, He pycnometry and N_2 sorption measurements

	TEM[a]		Density	N_2 sorption measurement[c]			
	d [nm]	t [nm]	ρ (CC)[b] [g cm^{-3}]	S_{BET} [m^2 g^{-1}]	$V_{tot,DFT}$ [cm^3 g^{-1}]	$V_{mic,DFT}$ [cm^3 g^{-1}]	V_{mic}/V_{tot} [%]
HS-500	316 ± 4	44 ± 2	1.044	113.9	0.101	0.028	27.4
HS-650	316 ± 4	43 ± 2	1.037	70.0	0.087	0.010	11.0
HS-800	314 ± 6	44 ± 2	1.050	26.3	0.053	0	0
HS-950	310 ± 4	43 ± 2	1.047	19.7	0.045	0	0

[a] d: diameter, t: shell thickness. [b] Density of the colloidal crystal (CC) calculated using the density of the silica shell obtained from helium pycnometry measurements ($\rho(SiO_2$, shell) = 2.27 g cm^{-3}) and assuming an fcc packing fraction of 0.74. [c] S_{BET}: surface area calculated by using the BET method, $V_{tot,DFT}$: total pore volume determined by using the NLDFT model on silica at 77 K, $V_{mic,DFT}$: pore volume for pores with diameters smaller than 2 nm determined by using the NLDFT model on silica at 77 K.

with greenish opalescence constitutes highly ordered, hexagonal periodicities of the hollow spheres. Such areas expand over a large range as single crystalline domains. As can be inferred by the opalescence, the vast majority of the hollow sphere ensemble is fully crystalline. Only at the very bottom the long-range crystalline order is compromised and the particles appear to be in a jammed state with only small crystallites persisting. Based on this study, we can safely assume that the volume fraction of the particles in the colloidal crystal is close to its ideal value of 74%. This value represents an upper limit, since the amorphous components will slightly lower the real volume fraction. In combination with He pycnometry measurements, which resulted in a density of the silica shells – independent of the calcination temperature – of $\rho_{\text{silica, shell}} = 2.27$ g cm^{-3}, we can calculate the effective density of the hollow sphere colloidal crystal. For the hollow spheres under consideration here, we obtain $\rho_{\text{HSNP, CC}} \approx 1.04$ g cm^{-3} (see Table 1).

Whereas the geometric structure of a colloidal crystal consisting of hollow sphere particles remains almost identical for a large range of calcination temperatures, the internal structure changes quite considerably. Therefore any changes to the thermal conductivity can be linked to the microstructure of the silica shell. This internal structure is characterized by a certain surface area, a porosity defined by micropores, as well as the degree of condensation and the rigidity of the SiO_x network. We used N_2 adsorption isotherms as well as hyperpolarized ^{129}Xe NMR spectroscopy to characterize the surface area and the pore size distribution within the silica shell (Fig. 2). We find that the particles being calcined at 500 °C feature the largest BET surface area of about 114 m^2 g^{-1}. Please note that we did not add any structure directing agents to the Stöber process to specifically increase the surface area or to template certain types or symmetries of micropores.[18] The isotherms do not show any pronounced hystereses and point towards the presence of micropores (steep slope at low p/p_0), mesopores of small diameter (shallow slope at intermediate p/p_0), and macropores (Fig. 2a). Upon calcination at higher temperatures, these mixed isotherms change considerably. The surface area gradually decreases, leading to a BET surface area of only 19.7 m^2 g^{-1} for the highest calcination temperature used in this study. Estimating the surface area of a hollow sphere powder of our particles leads to a slightly smaller surface area of 12.6 m^2 g^{-1}, when only the outer interface was accessible. Taking into account some surface roughness of the hollow spheres indicates that most of the silica shells are impassable for N_2 after calcination at 950 °C. The drop in the surface area is accompanied by a loss of the total pore volume (from 0.101 cm^3 g^{-1} to 0.045 cm^3 g^{-1}) and micropore volume (Fig. 2c). In particular no micropore volume can be derived from the N_2 isotherms at calcination temperatures beyond 800 °C any more (Table 1).

The pore size distribution obtained by NLDFT analysis, shown in Fig. 2b, confirms the closure of micropores of about 5–8 Å in radius. Exceeding the information accessible by N_2 sorption, the usage of hyperpolarized ^{129}Xe NMR reveals more details of the internal structure at the highest calcination temperatures (Fig. 2d). Two trends become obvious in the ^{129}Xe spectra. Considering the same measurement temperatures the signal intensity decreases with increasing calcination temperatures. This confirms the gradual closure of the micropores with increasing calcination temperature. From the limiting shifts $\delta(^{129}\text{Xe}) \sim 57$ ppm and 105 ppm determined at room temperature for the sample calcined at 500 °C two microporous cavities with diameters of 7 Å and 11 Å, were derived using the Fraissard model for cylindrical pore geometry (compare ESI Table S2†).[31] This is in good agreement with the pore radius distribution calculated from the N_2 sorption measurements. For all calcination temperatures the ^{129}Xe signals shift high-field with increasing measurement temperature due to the reducing Xe–Xe interactions as the pores gradually empty. Although for higher calcination temperatures the limiting shift could not be determined experimentally at room temperature due to the decreasing intensity, this trend indicates that even at 800 °C and 950 °C calcination temperatures some microporous cavities remain (Fig. 2d). This is in line with the decreasing micropore volume derived from the sorption data.

The evolution of an asymmetry for the ^{129}Xe gas peak at 0 ppm for all calcination temperatures is in line with filling mesoporous cavities at lower measurement temperatures (Fig. S3a†).[32] This can be rationalized by the geometry of the

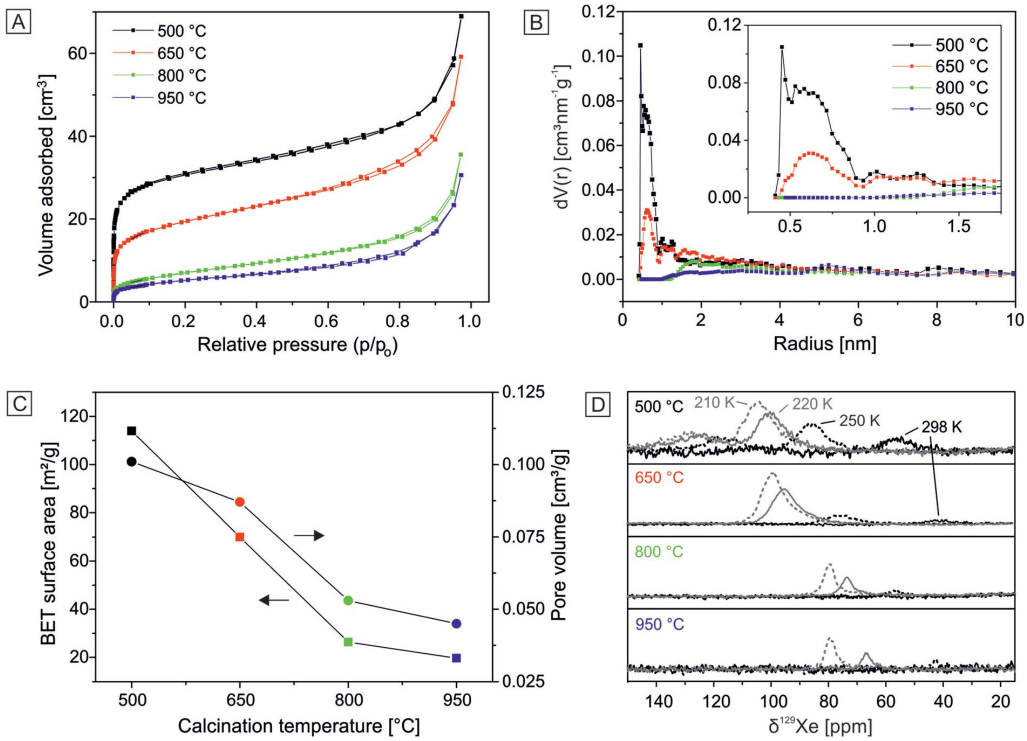

Fig. 2 Internal structural characterization of hollow silica spheres in dependence of the calcination temperature: (A) Nitrogen adsorption and desorption isotherms measured at 77 K allow the determination of pore volume and surface area. (B) Pore radius distributions, calculated by applying the NLDFT silica kernel based on a cylindrical pore model, indicate closure of the micropores at higher calcination temperatures. (C) BET surface area (squares) and pore volume (dots) as a function of calcination temperature. (D) ^{129}Xe NMR spectra of hyperpolarized xenon in silica hollow spheres as a function of the sample temperature. Even for the highest calcination temperatures a small amount of micropores is still present in the silica shell.

contact points between the adjacent spheres, which can be considered to be conical pores.

Despite the rearrangement, which happens during the high temperature calcination, the SiO_2 network remains in its fully amorphous state. Powder XRD measurements on all four samples do not show any onset of crystallization (ESI Fig. S2b†). Only broad halos, indicating the glassy state of the SiO_2 network, can be observed.

As demonstrated by Zhang *et al.*, silica networks obtained by the Stöber method predominantly consist of Si atoms, which are connected to three (Q^3) or four (Q^4) neighbouring –O–Si– units. The ratio between Q^3 and Q^4 changes with increasing calcination temperature and ultimately leads to a fully condensed SiO_2 network.[24] We also characterized our hollow silica spheres by solid state MAS ^{29}Si NMR. The spectrum of a calcined sample at 500 °C is given in Fig. 3a (the other spectra are shown in the ESI in Fig. S4†). By deconvoluting the individual contributions from Q^3 and Q^4 using a pseudo-Voigt function, we determined the ratio of Q^4 to be already 88% in the 500 °C sample. This ratio increases up to 94% for the case of 950 °C calcination (ESI Table S2†). It demonstrates a certain degree of rearrangement within the SiO_2 network upon exposure to higher temperatures, yet the size of the particles stays constant. More prominent are the concomitant changes in the spin-lattice relaxation time T_1 (Fig. 3b). We measured an increase from about 33 s for the hollow spheres calcined at 500 °C up to 6400 s for the highest calcination temperature. This clearly hints towards an increase of the rigidity of the still amorphous silica network, which may also improve the thermal transport capabilities. We confirmed that T_1 is almost independent of the amount of adsorbed water. This was observed at low calcination temperatures by ^{1}H NMR studies (ESI Fig. S3b†). Whereas the broad water peak vanishes in the ^{1}H NMR after the drying procedure, the T_1 changes from 33 s to 20 s for the untreated and predried samples calcined at 500 °C (compare Table S2 in the ESI†).

All these changes to the internal structure (surface area reduction, closure of micropores, increase of Q^4 content and increase of rigidity) happen simultaneously during calcination and are summarized in Fig. 4.

Besides the marked changes to the internal structure of the silica shell, the contact area between the adjacent spheres can

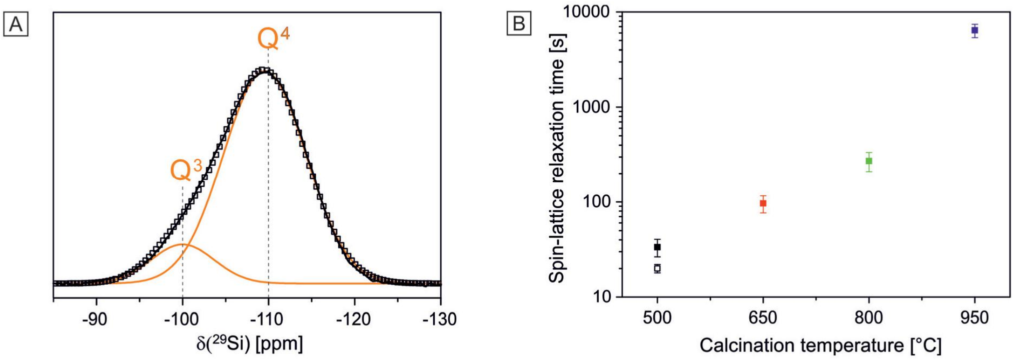

Fig. 3 Internal structural characterization of hollow silica spheres. (A) Deconvoluted projection of the ^{29}Si spectrum of HSNP calcined at 500 °C; measured signal (black line), cumulative fit (open squares), simulated signals (orange lines), (B) Spin-lattice relaxation time of silica hollow spheres calcined at different temperatures. The closed symbols represent untreated and the open symbol pre-dried powder to remove water residues.

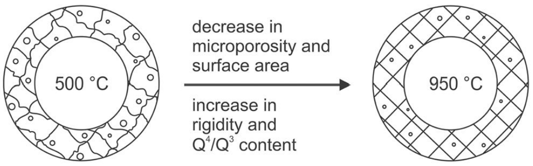

Fig. 4 Schematic representation of the internal structural changes upon high temperature calcination.

also be largely influenced by higher calcination temperatures. Colloidal crystals, with a hexagonally close packed structure, feature twelve neighbouring spheres around each particle. In a vacuum the thermal energy through such a colloidal structure can only be transported along the SiO_2 network. Therefore the contact points between the adjacent spheres play a paramount role. Concomitantly to the changes of the internal structures, the degree of condensation between two spheres at the contact area is also likely to increase. These subtle changes, however, cannot be characterized or quantified, due to the small amount of atoms involved. From the SEM images (ESI Fig. S1†) we merely deduce that the contact points between the spheres increase slightly from (46 ± 13) nm at 500 °C to (64 ± 12) nm at 950 °C. In order to separate these two contributions to thermal transport (internal structural changes and contact area changes), we conducted two separate sets of experiments. In the first one, we assembled a colloidal crystal from core/shell particles. After calcination at 500 °C we obtained the hollow sphere colloidal crystal. This monolith was repeatedly characterized after calcination at different temperatures of 650 °C, 800 °C and 950 °C for 12 hours (solid symbols in Fig. 6b). This experiment is sensitive to both types of internal and interfacial changes at the same time. In the second experiment, we self-assembled hollow silica spheres from an aqueous dispersion, which have beforehand been subjected to calcination at 950 °C. These hollow spheres featured a surface area of roughly 20 $m^2 g^{-1}$, similar to the 950 °C calcined particles of the first experiment, indicating a comparable internal structure. Analogously to the samples of the first experiments (compare Fig. 1e) a colloidal crystal with large monocrystalline areas was obtained (see ESI Fig. S8†). The degree of crystallinity decreases from top to bottom with some amorphous areas at the lower end. The samples of this set of experiment are only sensitive to changes in the interfacial contact areas, since the internal structure already resembles a highly condensed network with a small surface area and closed micropores. Annealing of this colloidal crystal at elevated temperatures will consequently only strengthen the interfacial contact points, but will leave the internal structure unaffected. By these two sets of experiments (calcined and annealed colloidal crystals) we can differentiate between contributions made from the internal structure and interfacial changes.

We performed laser flash analysis (LFA) on both types of hollow sphere colloidal crystals. The principle of measurement is depicted in Fig. S6b in the ESI.† A typical measurement along with its fit is provided in Fig. 5a (further LFA measurements are shown in Fig. S7 in the ESI† along with a description of the radiation fit model). At first we investigated the temperature-dependent thermal diffusivity of a hollow sphere colloidal crystal from room temperature up to 200 °C (note that this sample has been calcined at 500 °C, and was stored under ambient laboratory conditions). The heating and cooling cycles are identical after the initial pre-conditioning as outlined in the Experimental section (ESI Fig. S7b†). The pre-conditioning removes adsorbed water in the silica shell (compare ^{1}H NMR of HSNP calcined at 500 °C in Fig. S3b in the ESI†). We conducted our experiments on at least three distinct samples of the hollow sphere colloidal crystals, each varying slightly with respect to the overall sample thickness. Fig. 5b shows only a small increase in thermal diffusivity

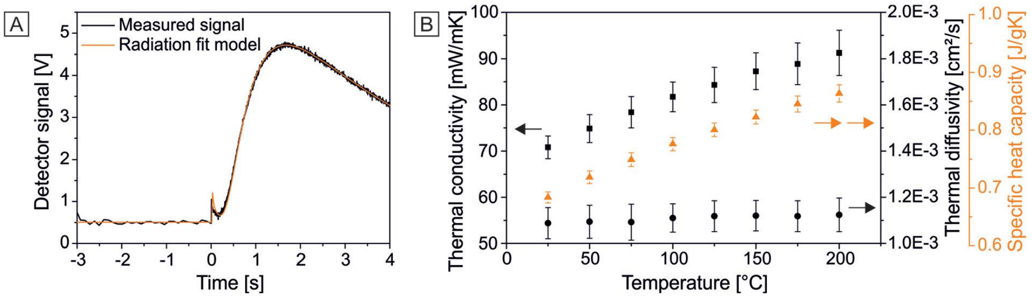

Fig. 5 LFA measurements of HSNP calcined at 500 °C. (A) Measured signal (black line) with the radiation fit model (orange line). (B) Summary of the necessary input parameters (thermal diffusivity – black circles and mean specific heat capacity – orange triangles) to determine the thermal conductivity (black squares).

α along with the specific heat capacity c_p in the temperature range from 25 °C to 200 °C. Using the equation

$$\kappa = \alpha\rho c_p \tag{2}$$

the thermal conductivity κ can be calculated. As demonstrated above, the density ρ of the silica shell and therefore of the hollow sphere colloidal crystal does not change within this temperature range, and stays almost constant up to calcination temperatures of 950 °C. The uncertainty of the density determination is about 9%.

Since we conduct our measurements in a vacuum, we use the c_p obtained from DSC measurements of the silica shell (from compacted hollow spheres). The specific heat capacity shows a monotonic increase in the temperature range of interest, but is hardly influenced by the calcination temperature (see Fig. S5b in the ESI†). We therefore used the same average temperature dependent c_p for all samples under consideration here, which is close to the literature value of quartz glass (c_p = 0.73 J g^{-1} K^{-1}).[33] The standard deviation of the c_p amounts to about 2%. The slightly reduced c_p of our silica shell could be attributed to a small amount of porosity and differences in the network condensation, compared to fused quartz glass reported in the literature. Combining the individual uncertainties of the thermal diffusivity, density, and specific heat, we find that the determination of κ is accurate to within ±5–13% for an individual measurement. Variations from sample to sample during the different calcination steps can be therefore regarded as the main source of error (details are reported in the ESI†: uncertainty analysis of the thermal conductivity determination). We therefore show the average values and standard deviation of at least three independent samples in Fig. 6.

Fig. 6a shows all temperature-dependent thermal conductivities for samples after various calcination temperatures. The thermal conductivity of a 500 °C calcined hollow sphere colloidal crystal consisting of 316 nm diameter and 44 nm shell capsules is very low with κ = 71 mW m^{-1} K^{-1}. The thermal conductivity increases monotonically to a value of κ = 91 mW m^{-1} K^{-1} at 200 °C, which is known for glassy materials at high temperatures.[34,35] It is higher compared to most bulk silica aerogels and previously reported hollow spheres, however, the effective density of the colloidal crystal under investigation here is relatively high with ρ = 1.044 g cm^{-3}. Calcination at elevated temperatures leads to a systematic increase in thermal conductivity, the absolute magnitude doubles at room temperature from κ = 71 mW m^{-1} K^{-1} (calcination at 500 °C) to κ = 140 mW m^{-1} K^{-1} (calcination at 950 °C). In comparison with calcination dependent investigations that have been carried out on silica aerogel samples we attribute this increase not to a loss in methyl groups or increase in density, but solely to microstructural changes, since the density of our silica shell is constant from calcination between 500 °C and 950 °C.[36] This is corroborated by a thermogravimetric analysis of the 500 °C calcined hollow spheres (ESI Fig. S5a†).

In the further discussion we only want to focus on the thermal conductivity at 25 °C. Concomitant with the increase in thermal conductivity at higher calcination temperatures, the standard deviation also increases. This can be understood by small, but random changes from sample to sample during the calcination process. These changes can be the evolution of cracks or line defects, or a change in the adhesion between the neighbouring spheres. As outlined above, the individual spheres remain almost constant in size even at high calcination temperatures. However, within an ensemble of particles these minute changes can accumulate to distinct defects. Such changes are small and we could not observe any structural changes by optical microscopy or SEM (see Fig. S1 in the ESI†). Since the samples of annealed colloidal crystals also demonstrate the same amount of increase in data scattering, the evolution of the mutual contact points seems to be the major source for this scattering. In addition, an increase in thermal conductivity can lead to higher losses into the sample holder during the LFA measurement. This in turn can reduce the accuracy of the radiation fit model.

Despite some scatter in the data, the unambiguous trend of an increase in thermal conductivity can be inferred from the inset of Fig. 6b (closed symbols). Due to the well-defined struc-

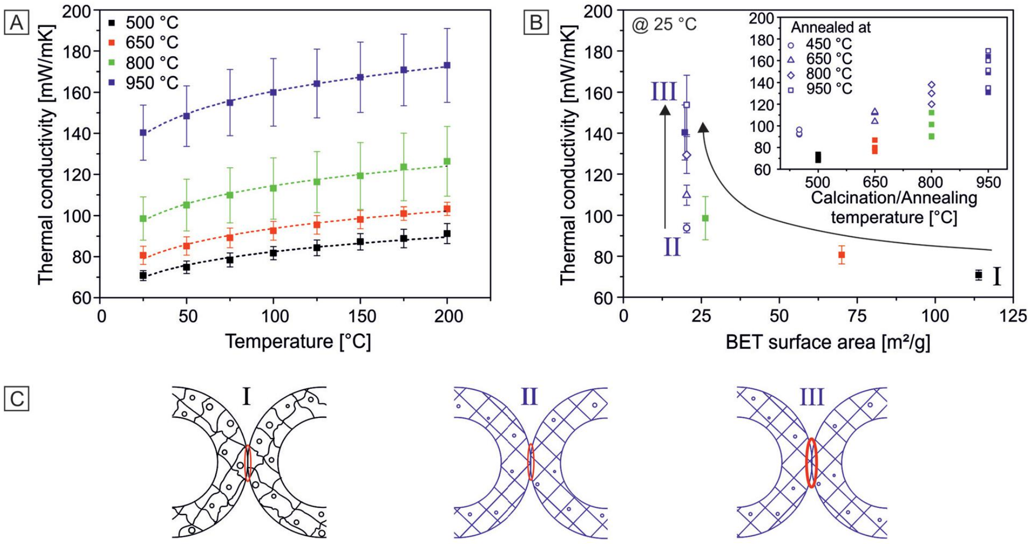

Fig. 6 Thermal conductivity of calcined (closed symbols) and annealed HSNP colloidal crystals (open symbols). (A) Thermal conductivity of HSNP monoliths calcined at different temperatures (500–950 °C) as a function of the measurement temperature. The dashed lines represent $\kappa \sim T^x$. (B) BET surface area and calcination temperature (inset) as a function of the thermal conductivity at 25 °C measurement temperature. (C) Schematic representation of the internal structural changes and the increase in interfacial adhesion within a colloidal crystal ensemble.

ture, we can now relate this apparent increase to microstructural changes in the SiO$_2$ network. We therefore plot the same data against the BET surface area, which changes sensitively with the calcination temperature as shown above. The reduction in the surface area by a factor of almost six leads to a doubling of the thermal conductivity (Fig. 6b solid symbols). However, this change is accompanied by the closure of micropores, a small increase in Q^4 Si atoms (ESI Fig. S7c†), a large increase in spin-lattice relaxation time, and most importantly an increase of the interfacial adhesion between the spheres. These changes are schematically shown in Fig. 6c. The relative area (based on the total particle surface) involved in interfacial contact points, increases with higher calcination temperatures from ~6% at 500 °C to ~13% at 950 °C (see Fig. S1†). This can additionally contribute to an improved thermal transport between the individual particles due to less constriction resistance. We therefore also investigated the thermal transport properties of annealed colloidal crystals as outlined above. Fig. S7d in the ESI† shows all temperature-dependent measurements of the annealed samples, similar to Fig. 6a. The data from the 450 °C up to 950 °C annealed colloidal crystals are shown with open symbols in Fig. 6b and correspond to a transition from Fig. 6c II to III. The BET surface area of the hollow spheres and therefore of the colloidal crystal has already been reduced to only 20.3 m^2 g^{-1} prior to the colloidal crystal formation. This surface area does not change with increasing annealing temperatures any more, as the SiO$_2$ network has already been brought into its highly condensed form. Consequently, the data lie on a straight vertical line in Fig. 6b (open symbols). One recognizes that the loss of micropores and increase in the rigidity of the silica network (*i.e.* the T_1 relaxation) lead to a distinct increase in thermal conductivity from κ = 71 mW m^{-1} K^{-1} to κ = 92 mW m^{-1} K^{-1} – while the interfacial contact between the spheres can be regarded similar to the 500 °C calcined crystal (closed black square). In contrast it also demonstrates the large influence of interfacial adhesion as the thermal conductivity is drastically reduced compared to the fully annealed case (open blue circles, κ = 154 mW m^{-1} K^{-1}). Annealing at 650 °C, 800 °C, and ultimately 950 °C strengthens the covalent linkage at the contact points of the adjacent spheres, but will not change the internal structure any further (transition from Fig. 6c II to III). This increase in adhesion is reflected in a marked increase in thermal conductivity of the annealed hollow sphere monoliths (open symbols) from κ = 94 mW m^{-1} K^{-1} (500 °C) to κ = 110 mW m^{-1} K^{-1} (650 °C), κ = 129 mW m^{-1} K^{-1} (800 °C), and κ = 154 mW m^{-1} K^{-1} (950 °C). The final value of 154 mW m^{-1} K^{-1} is a little higher, compared to the calcined colloidal crystal (κ = 140 mW m^{-1} K^{-1}). This could be due to the absence of shrinkage in the case of annealing in contrast to calcination where the spheres shrink slightly from 316 nm to 310 nm (compare Table 1). This could be reflected in less defects and broken contact points.

What do we learn about the transport of thermal energy through such an amorphous, nanostructured silica material? The transport of thermal energy in this amorphous material is influenced by two distinct contributions: the microstructure of the "bulk" silica network (the thickness is only 44 nm) and the interfacial contact between the adjacent spheres. The influence of the bulk silica network can be seen by the difference between the colloidal particles calcined after (Fig. 6b solid symbols) and before (Fig. 6b open symbols) the assembly process. Assuming a comparable adhesion between the silica spheres at the respective calcination and annealing temperatures, the annealed colloidal crystals always demonstrate a higher thermal conductivity. Apparently, the minimum amount of micropores in combination with a higher degree of Q^4 atoms and a smaller BET surface area leads to less scattering of delocalized modes at point defects or interfaces. Furthermore, the increase in spin-lattice relaxation time can be interpreted as a measure to increase the coherence length of the vibrational modes in the amorphous network, which will result in an increased thermal transport. A similar effect has been reported for amorphous polymers, where weak van der Waals bonds have been replaced by stronger hydrogen bonds.[37] Accordingly, we also observe a decrease in the temperature dependence from $\kappa \sim T^{0.5}$ for 500 °C calcination to $\kappa \sim T^{0.4}$ for 950 °C calcination (determined by a linear fit to a double-log plot of the κ *vs.* T graph). The annealed samples show a $\kappa \sim T^{0.4}$ dependency, which slightly decreases with higher annealing temperatures (see ESI Fig. S7d†). As a reference, fused quartz glass demonstrates a proportionality of $\kappa \sim T^{0.3}$ in the respective temperature range between 0 °C and 200 °C. The temperature dependence of the thermal conductivity can provide insights on how thermal energy is transported. For crystalline materials the temperature-dependent thermal conductivity is known to scale with T^{-1} (at high temperatures) due to phonon–phonon Umklapp scattering.[34,38] For disordered materials the scaling behaviour exhibits typically a positive slope due to an increase in heat capacity and the diffusive thermal conduction of propagons and diffusons. In our amorphous material, we find the expected increase in thermal conductivity with increasing temperatures. This dependency, however, decreases slightly from $T^{0.5}$ to $T^{0.4}$ with increasing calcination temperature. We attribute this decrease to an increased anharmonic coupling between localized modes or between localized and delocalized modes, caused by the microstructural changes during the calcination.[39]

Even more important, particularly when considering the small amount of atoms involved, are the interfacial contact points between the adjacent spheres. Due to the fcc structure, each particle contacts twelve neighbouring particles. For the case of annealed colloidal crystals, the adhesion and the degree of crosslinking between the spheres govern predominantly the thermal transport, since the internal structure is already fully condensed. Whereas we cannot quantify the bonding strength between the hollow silica particles, one can deduce from Fig. 6b (open symbols) that the thermal conductivity can be increased by more than 160%, when strengthening the contact points. Analogously to the calcined samples, a slight increase in the mutual particle contact area may also contribute to the enhanced thermal transport.

The absolute thermal insulation properties of the hollow silica colloidal crystals presented here are less compared to their aerogel analogues; however, they still demonstrate a very low thermal conductivity in particular in the light of the relatively high density ($\rho \approx 1.04$ g cm^{-3}).

Conclusion

Colloidal crystals consisting of hollow silica nanoparticles represent a porous material class, with very well defined nano- and mesostructures. The monodispersity of the constituting building blocks, which comprise two distinct length scales (44 nm shell thickness and 316 nm diameter), translates into highly ordered colloidal crystals. Yet, for thermal transport applications, this material can be considered entirely amorphous, due to the glassy microstructure of the condensed silica network. We employed a range of characterization techniques to determine the structural entities from the nano- to the macroscale. SAXS, electron and optical microscopy showed the structural integrity even after calcination up to 950 °C, whereas NMR, N_2 sorption, and XRD demonstrated significant changes on the nanoscale. These changes result in an increase in thermal conductivity through this porous material. We identified two distinct contributions to this increase in thermal conduction. The first being internal structural changes of the condensed silica network, which are: loss of micropores, loss of BET surface areas, increase in Q^4 Si atoms and increase in spin-lattice relaxation time. The second being an increase in interfacial bonding between the individual spheres. Both result in a higher thermal conductivity of our porous silica material. Even though only a fraction of the total amount of Si and O atoms contribute to interfacial adhesion, the thermal conductivity predominantly depends on it. Combining low adhesion forces and microstructure leads consequently to the lowest thermal conductivity of κ = 71 mW m^{-1} K^{-1} for the system under investigation here. Colloidal crystals of hollow silica nanoparticles not only represent a highly insulating material. The well-defined structure further allows us to thoroughly investigate thermal transport processes in amorphous silica materials. Further research will build upon these concepts and may lead to extremely efficient insulation layers.

Experimental section

Materials

Styrene (≥99%, Aldrich), 2,2′-azobis(2-methylpropionamidine) dihydrochloride (AIBA; 97%, Aldrich), 2-methacryloxy-ethyltrimethylammonium chloride (MTC; 70% solution in water, Polyscience), polyvinylpyrrolidone K30 (PVP; $M_w \sim 55$ kg mol^{-1}, Aldrich), Tetraethyl orthosilicate (TEOS; ≥99%, Aldrich) and ammonium hydroxide solution (30–33% in water, Aldrich) were used as received. Ethanol (EtOH) was used in technical grade and water was taken from a Millipore Direct Q3UV unit for the entire synthesis and purification steps.

Synthesis of monodisperse hollow silica nanoparticles

The synthesis of monodisperse hollow silica nanoparticles comprises three steps. First monodisperse polystyrene (PS) latex particles were synthesized by emulsifier-free emulsion polymerization. The reaction was carried out in a 500 mL three-neck flask, equipped with a gas inlet and a reflux condenser. Solid chemicals were dissolved in water prior to addition. Firstly 200 mL water, 26 mL styrene, 1.8 g PVP and 100 μL MTC were heated to the reaction temperature of 70 °C at a stirring speed of 850 rpm using a large egg-shaped magnetic stirring bar. After equilibrating for 20 min, 600 mg AIBA initiator, dissolved in 40 mL water, was quickly added to initiate the polymerization. After nucleation, the stirring speed was reduced to 450 rpm and the polymerization was allowed to continue overnight at 70 °C under a slight inert gas flow. In the second step the PS template particles were coated with a silica shell to obtain core/shell particles. The silica coating was achieved by a Stöber condensation process.[40] Therefore 17.5 mL neat PS dispersion (9.14 wt%) were diluted with 122.5 mL ethanol and 9.1 mL ammonium hydroxide solution and stirred at 500 rpm. After stepwise addition of 13 mL TEOS the reaction was stirred overnight at room temperature. The core/shell particles were purified by repeated centrifugation and redispersion in water. In order to prepare hollow spheres, the sample was dried and kept in a furnace (Nabertherm L5/11/P33) at 500 °C, 650 °C, 800 °C or 950 °C in air for 12 h. The hollow spheres could be redispersed in water using mild sonication in a sonication bath.

Colloidal crystal *via* evaporation induced self-assembly of hollow silica nanoparticles

To obtain colloidal crystals a concentrated aqueous solution of core shell particles (~7 wt%) or hollow silica spheres (~5 wt%) was slowly evaporated in a Teflon beaker with a diameter of 2 cm for several days.

Characterization

Transmission electron microscopy (TEM) images were taken on a Zeiss CEM 902 instrument in bright field imaging mode at an acceleration voltage of 80 kV.

Elemental analysis (EA) was performed on a Vario Elementar EL III apparatus.

Nitrogen sorption measurements were carried out on a Quantachrome Autosorb AS-1 pore analyzer at 77 K. Prior to the measurements, all samples were preconditioned in a vacuum at 350 °C for 12 hours. For the analysis, the Quantachrome ASiQ v3.0 software was used. The specific surface areas were calculated using the BET method. Pore volumes and pore size distributions were obtained by applying the nonlocal density functional theory (NLDFT) adsorption branch model for silica materials with cylindrical pore geometry.

Solid-state ^{29}Si NMR and hyperpolarized ^{129}Xe NMR measurements were carried out on a Bruker Avance II spectrometer in combination with a 7.05 T magnet (Oxford) corresponding to a Larmor frequency ω_0 = 59.6 MHz for ^{29}Si and 83.0 MHz for ^{129}Xe equipped with a BVT 3000 VT-Unit (Bruker). ^{29}Si spectra were recorded with single pulse excitation using a 7 mm triple resonance probe at a spinning frequency of 5 kHz. The chemical shifts were referenced to tris(trimethylsilyl)amine (2.4 ppm) relative to tetramethylsilane (TMS). A 90° pulse at a nutation frequency of 38 kHz was used. The repetition times were set to 60 s. The number of scans was adapted such that a sufficient S/N ratio was obtained. Spin-lattice relaxation was measured by using a saturation recovery experiment with a pulse train of 5 90° pulses to ensure complete saturation of the system. The spectra were deconvoluted using a pseudo-Voigt profile by fitting to the least squares. The formula of the applied profile is expressed by

$$I(\delta) = A\left\{\eta\frac{\sqrt{4\log 2}}{\sqrt{\pi}w}\exp\left[-\frac{4\log 2}{w^2}(\delta-\delta_0)^2\right] + (1-\eta)\frac{2}{\pi}\frac{w}{\left[4(\delta-\delta_0)\right]^2+w^2}\right\} \tag{3}$$

where A is the amplitude of the peak, δ_0 is its center, η is the weight factor (1: Gaussian function, 0: Lorentzian function) and w is the full width at half maximum (FWHM).

For variable-temperature (VT) hyperpolarized ^{129}Xe NMR measurements a 5 mm wideline double resonance probe (Bruker) was used. The NMR chemical shifts were referenced to the signal of gaseous xenon at 0 ppm. The probe was modified with a 3 mm inner diameter PEEK sample holder to incorporate hyperpolarized ^{129}Xe in continuous flow mode to the sample. The spectra were acquired with single pulse excitation using 52.62 kHz nutation frequency and 32 to 128 transients. The recycle time was set to 1 s and is not dependent on the spin-lattice relaxation but limited by the flow rate and the exchange between hyperpolarized and depolarized ^{129}Xe in the pore.[41] The hyperpolarized ^{129}Xe was generated using a self-built polarizer. A gas mixture of $Xe : N_2 : He = 1 : 2 : 97$ (vol%) at an overall pressure of 5 bar was irradiated with an 80 W diode laser (Coherent Inc.) at a central frequency of the Rb D_1-line (l = 794.8 nm). The polarized gas was exchanged over the sample with a flow rate of about 200 cm^3 min^{-1}. A polarization of ~5% was reached.

Solid-state ^{1}H NMR measurements were carried out on a Bruker Avance III HD spectrometer using a 14.1 T magnet (Bruker Ascent) corresponding to a Larmor frequency of ω_0 = 600.1 MHz and a 1.3 mm double resonance probe at a spinning frequency of 62.5 kHz. Spectra were acquired with 8 transients at a nutation frequency of 161 kHz and a repeating time of 5 s.

Small-angle X-ray scattering (SAXS) data reported here were measured using the small-angle-X-ray system Double Ganesha AIR (SAXSLAB, Denmark). The X-ray source of this laboratory-based system is a rotating anode (copper, MicroMax 007HF, Rigaku Corporation, Japan) providing a micro-focused beam at l = 0.154 nm. The data were recorded by a position sensitive detector (PILATUS 300 K, Dectris). To cover the range of scattering vectors between 0.026 and 2.6 nm^{-1} different detector positions were used. The measurement was recorded using a powder of hollow silica nanoparticles between two Kapton foils at room temperature. The scattering curve was evaluated with a vesicle fit in the program SCATTER.[42]

Powder X-ray diffraction (XRD) measurements were performed using a STOE STADI P (CuK$_{\alpha1}$ radiation, transmission geometry) diffractometer equipped with a fast, high resolution silicon strip detector DECTRIS Mythen1 K. The samples were mounted on a flat disk using Scotch® tape. A stepsize of 0.2° and an integration time of 20 s were used.

Differential scanning calorimetry (DSC) measurements were recorded using a Q1000 DSC (TA Instruments). Compressed powders of the hollow spheres (12–15 mg) were scanned in covered aluminium pans under dry nitrogen purge (50 mL min^{-1}) over a temperature range from −50 °C to 200 °C with a heating rate of 10 °C min^{-1}. The heat flow and heat capacity were calibrated using a standard sapphire sample. The received data were evaluated with Universal Analysis 2000 2.5A software.

Thermogravimetric analysis (TGA) was performed with a Mettler Toledo TGA/STDA 851^{e} Star System at a heating rate of 10 K min^{-1} under air flow. The initial sample weight was 16.8018 mg.

Thermal diffusivity of the colloidal crystals was measured by laser flash analysis (LFA) on a XFA 500 XenonFlash apparatus (Linseis) with an InSb infrared detector. The measurements were taken over a temperature range from 25 to 200 °C in a vacuum. Prior to the measurements the samples were coated with approximately 15 μm of graphite on each side. In order to eliminate any potential contribution from intercalated water inside the SiO_2 network, we pre-heated the samples up to 200 °C for 15 min in a vacuum. The received data were evaluated by the software AproSoft Laser Flash Evaluation v1.06. The thicknesses of the colloidal crystals were determined with a Litematic VL-50 (Mitutoyo).

Correlative light-electron microscopy (CLEM) images were recorded on an Axio Imager.A2 m (Carl Zeiss Microscopy) equipped with a motorized stage and a digital camera AxioCam ICc 1. Using the shuttle & find module the samples were transferred into a scanning electron microscope (SEM) Zeiss Ultraplus mounted on the sample holder KorrMik MAT universal B. SEM images were recorded on pre-defined spots based on the optical light microscopy image using acceleration voltages between 2 and 3 kV and InLens SE detection as well as Everhart–Thornley detection (80/20 or 70/30 ratio).

Acknowledgements

The authors thank Lena Geiling and Nadine Popp for BET, Anna-Maria Dietel for EA, Markus Drechsler for TEM, Martin Dulle for SAXS, Ute Kuhn for DSC, and Beate Förster for CLEM measurements. This project was funded by the Volkswagen foundation. SFB 840 is acknowledged for financial support. P.R. acknowledges support by the Elite Network Bavaria (ENB). M.R. thanks the VCI for financial support.

Notes and references

1 B. P. Jelle, A. Gustavsen and R. Baetens, *J. Build. Phys.*, 2010, **34**, 99–123.
2 A. S. Dorcheh and M. H. Abbasi, *J. Mater. Process. Technol.*, 2008, **199**, 10–26.
3 N. Hüsing and U. Schubert, *Angew. Chem., Int. Ed.*, 1998, **37**, 22–45.
4 S. S. Kistler, *J. Phys. Chem.*, 1931, **36**, 52–64.
5 M. Koebel, A. Rigacci and P. Achard, *J. Sol-Gel Sci. Technol.*, 2012, **63**, 315–339.
6 U. Heinemann, *Int. J. Thermophys.*, 2008, **29**, 735–749.
7 D. M. Smith, A. Maskara and U. Boes, *J. Non-Cryst. Solids*, 1998, **225**, 254–259.
8 U. Heinemann, R. Caps and J. Fricke, *Int. J. Heat Mass Transfer*, 1996, **39**, 2115–2130.
9 L. W. Hrubesh and R. W. Pekala, *J. Mater. Res.*, 1994, **9**, 731–738.
10 M. Knudsen, *Ann. Phys.*, 1911, **339**, 593–656.
11 S. N. Schiffres, K. H. Kim, L. Hu, A. J. H. McGaughey, M. F. Islam and J. A. Malen, *Adv. Funct. Mater.*, 2012, **22**, 5251–5258.
12 X. Lu, M. C. Arduini-Schuster, J. Kuhn, O. Nilsson, J. Fricke and R. W. Pekala, *Science*, 1992, **255**, 971–972.
13 P. Allen and J. Feldman, *Phys. Rev. B: Condens. Matter*, 1993, **48**, 12581–12588.
14 P. B. Allen, J. L. Feldman, J. Fabian and F. Wooten, *Philos. Mag. B*, 2009, **79**, 1715–1731.
15 J. M. Larkin and A. J. H. McGaughey, *Phys. Rev. B: Condens. Matter*, 2014, **89**, 144303.
16 K. T. Regner, D. P. Sellan, Z. Su, C. H. Amon, A. J. H. McGaughey and J. A. Malen, *Nat. Commun.*, 2013, **4**, 1640–1647.
17 T. Coquil, J. Fang and L. Pilon, *Int. J. Heat Mass Transfer*, 2011, **54**, 4540–4548.
18 T. Coquil, E. K. Richman, N. J. Hutchinson, S. H. Tolbert and L. Pilon, *J. Appl. Phys.*, 2009, **106**, 034910.
19 T. G. Desai, *Appl. Phys. Lett.*, 2011, **98**, 193107.
20 J. Fricke and T. Tillotson, *Thin Solid Films*, 1997, **297**, 212–223.
21 M. Chen, C. Ye, S. Zhou and L. Wu, *Adv. Mater.*, 2013, **25**, 5343–5351.
22 L. Zhang, M. D'Acunzi, M. Kappl, G. K. Auernhammer, D. Vollmer, C. M. van Kats and A. van Blaaderen, *Langmuir*, 2009, **25**, 2711–2717.
23 M. Retsch, M. Schmelzeisen, H.-J. Butt and E. L. Thomas, *Nano Lett.*, 2011, **11**, 1389–1394.
24 L. Zhang, M. D'Acunzi, M. Kappl, A. Imhof, A. van Blaaderen, H.-J. Butt, R. Graf and D. Vollmer, *Phys. Chem. Chem. Phys.*, 2010, **12**, 15392.
25 J. Yin, M. Retsch, E. L. Thomas and M. C. Boyce, *Langmuir*, 2012, **28**, 5580–5588.

26 J. Yin, M. Retsch, J.-H. Lee, E. L. Thomas and M. C. Boyce, *Langmuir*, 2011, **27**, 10492–10500.

27 L. I. C. Sandberg, T. Gao, B. P. Jelle and A. Gustavsen, *Adv. Mater. Sci. Eng.*, 2013, **2013**, 1–6.

28 T. Gao, B. P. Jelle, L. I. Sandberg and A. Gustavsen, *ACS Appl. Mater. Interfaces*, 2013, **5**, 761–767.

29 Q. Yue, Y. Li, M. Kong, J. Huang, X. Zhao, J. Liu and R. E. Williford, *J. Mater. Chem.*, 2011, **21**, 12041.

30 Y. Liao, X. Wu, H. Liu and Y. Chen, *Thermochim. Acta*, 2011, **526**, 178–184.

31 J. Demarquay and J. Fraissard, *Chem. Phys. Lett.*, 1987, **136**, 314–318.

32 I. L. Moudrakovski, V. V. Terskikh, C. I. Ratcliffe, J. A. Ripmeester, L.-Q. Wang, Y. Shin and G. J. Exarhos, *J. Phys. Chem. B*, 2002, **106**, 5938–5946.

33 Y. S. Touloukian, *Thermophysical properties of matter: Specific heat/Nonmetallic Solids*, IFI Plenum, New York, 1970.

34 D. G. Cahill and R. O. Pohl, *Annu. Rev. Phys. Chem.*, 1988, **39**, 93–121.

35 D. Cahill and R. Pohl, *Phys. Rev. B: Condens. Matter*, 1987, **35**, 4067–4073.

36 P. E. Hopkins, B. Kaehr, E. S. Piekos, D. Dunphy and C. Jeffrey Brinker, *J. Appl. Phys.*, 2012, **111**, 113532.

37 G. H. Kim, D. Lee, A. Shanker, L. Shao, M. S. Kwon, D. Gidley, J. Kim and K. P. Pipe, *Nat. Mater.*, 2015, **14**, 295–300.

38 C. Kittel, *Einführung in die Festkörperphysik*, Oldenbourg, Wien, 14th edn, 2005.

39 S. Shenogin, A. Bodapati, P. Keblinski and A. J. H. McGaughey, *J. Appl. Phys.*, 2009, **105**, 034906.

40 W. Stöber, A. Fink and E. Bohn, *J. Colloid Interface Sci.*, 1968, **26**, 62–69.

41 B. M. Goodson, *J. Magn. Reson.*, 2002, **155**, 157–216.

42 S. Förster, L. Apostol and W. Bras, *J. Appl. Crystallogr.*, 2010, **43**, 639–646.

Electronic Supplementary Material (ESI) for Nanoscale.

Supporting Information

Hollow Silica Sphere Colloidal Crystals: Insights into Calcination Dependent Thermal Transport

Pia Ruckdeschel,[1] Tobias W. Kemnitzer,[2] Fabian A. Nutz,[1] Jürgen Senker,[2] Markus Retsch[1,]*

[1]University of Bayreuth, Physical Chemistry 1, Universitätsstr. 30, 95447 Bayreuth

[2]University of Bayreuth, Inorganic Chemistry 3, Universitätsstr. 30, 95447 Bayreuth

[*] markus.retsch@uni-bayreuth.de

Table S1. Elemental analysis – N, C, O content in HSNP calcinated at different temperatures.

	N content [%]	C content [%]	O content [%]
HSNP-500	0.054	0.254	0.317
HSNP-650	0.021	0.067	0.106
HSNP-800	0.026	0.035	0.010
HSNP-950	0.025	0.069	0.002

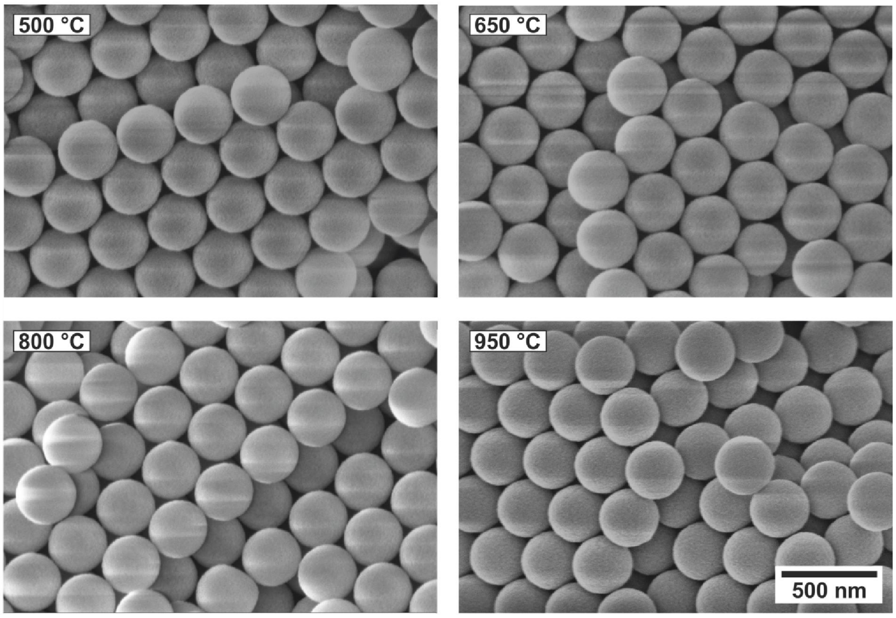

Figure S1. High magnification SEM images of HSNP calcinated at different temperatures (500 – 950 °C). No sinter necks between adjacent spheres can be observed, the particles retain their spherical shape and hexagonal assembly symmetry.

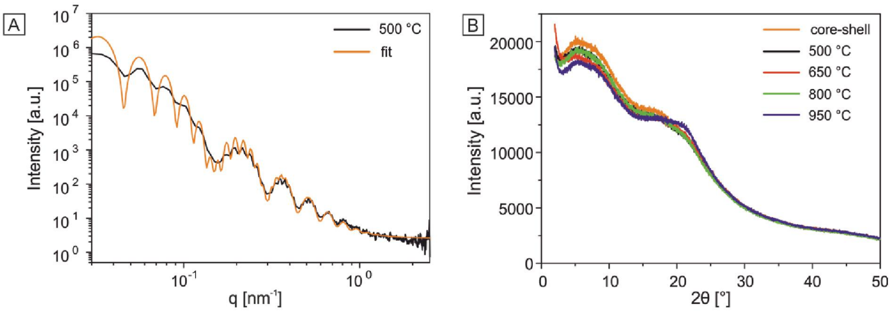

Figure S2. Internal structural characterization of HSNP. A) SAXS pattern for hollow silica nanoparticles calcinated at 500 °C: experimental scattering profile (black line) and the fitting curve (orange line). The fit parameters are 315 nm diameter and 42.5 nm shell thickness, B) XRD measurements of HSNP calcinated at different temperatures (500 – 950 °C).

Table S2. Summary of data received from NMR measurements.

	^{29}Si NMR [a]		*^{129}Xe NMR* [c]	
	$Q^4/(Q^3+Q^4)$	**T_1 relaxation time [s]**	**Delta [ppm]**	**Cylindrical pore [nm]**
HSNP-500	0.88	33 ± 7 (20 ± 2)[b]	57, 105	1.11, 0.71
HSNP-650	0.92	96 ± 20	42, 105	1.42, 0.71
HSNP-800	0.94	272 ± 60	-	-
HSNP-950	0.94	6400 ± 1000	-	-

[a] Relative amount of Q^4 units and spin-lattice relaxation times obtained from solid state ^{29}Si NMR, [b] Spin-lattice relaxation time of HSNP-500 after drying to remove water residues, [c] Limiting shift of ^{129}Xe and corresponding pore sizes according to the Fraissard model for cylindrical pore geometries.

$$D(\partial) = \frac{243 \cdot 2.054}{\delta} - 2.054 + D_{Xe}$$

δ = Limiting shift, D_{Xe} = VdW-Diameter of Xe

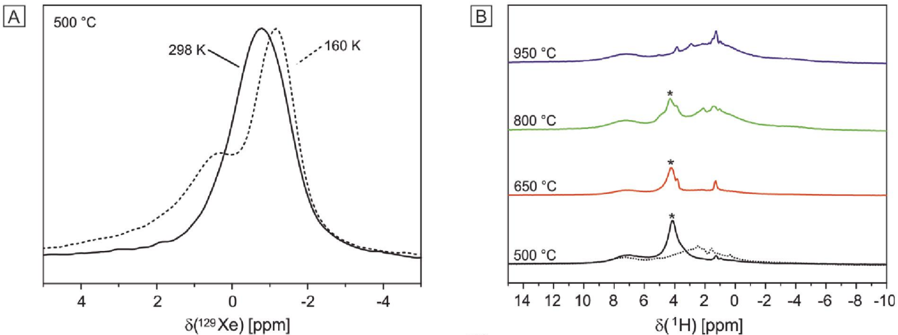

Figure S3. NMR characterization of HSNP. A) ^{129}Xe NMR: Single xenon gas peak at 0 ppm of silica hollow spheres at a measurement temperature of 298 K and 160 K, B) ^{1}H NMR spectra of silica hollow spheres calcinated at different temperatures (500 – 950 °C). The dotted line shows a pre-dried sample. The stars mark the peak caused by adsorbed water.

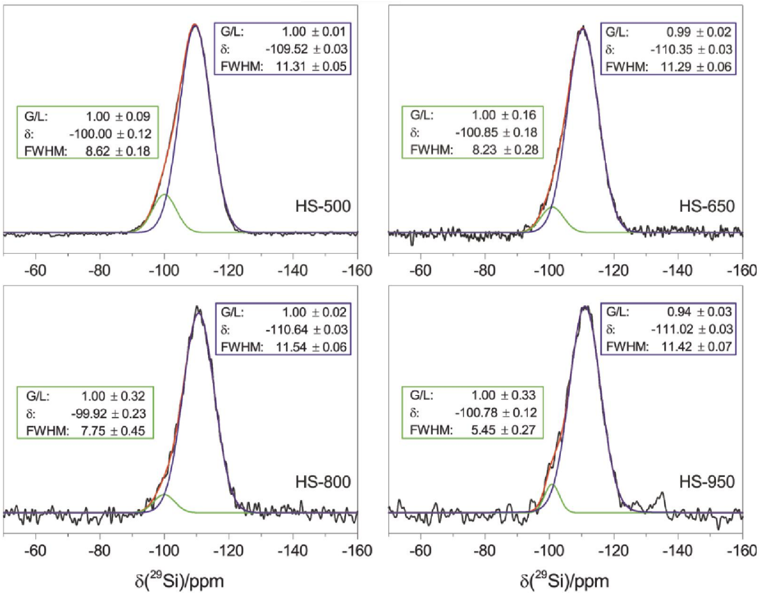

Figure S4. Deconvoluted projection of the ^{29}Si spectra of HSNP calcinated at 500 – 950 °C; measured signal (black), cumulative fit (red), simulated signals (green, blue).

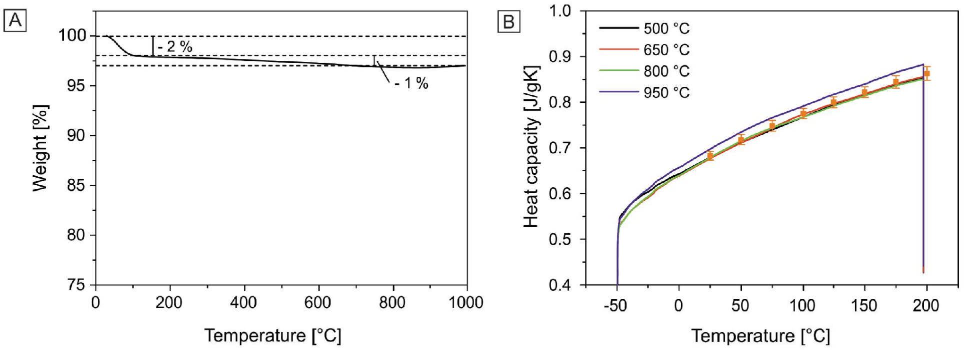

Figure S5. A) Thermogravimetric analysis (TGA) results of silica hollow spheres calcinated at 500 °C. The weight loss step (~ 2 %) at temperature up to 100 °C relates to the loss of adsorbed water. Another 1 % of mass is lost up to 950 °C, which can be attributed to the removal of trace amounts of silica condensation products. B) Differential scanning calorimetry (DSC) measurements of the compacted silica hollow spheres calcinated at 500 - 950 °C and the corresponding mean values (orange dots).

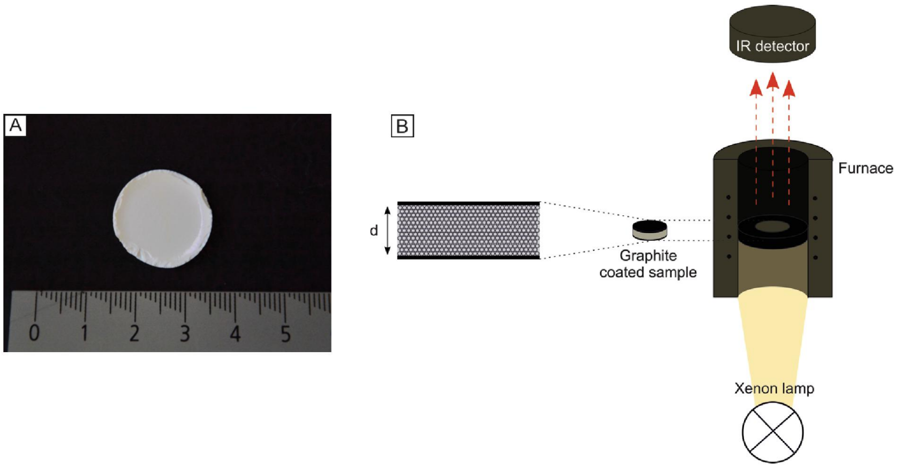

Figure S6. A) Photograph of a silica hollow sphere colloidal crystal with a diameter of 2 cm, B) LFA measurement principle and sample setup.

In brief, the colloidal crystals were coated on the top and bottom side with a thin graphitic layer (< 20 µm). Using a short light flash from a Xe white light source (2 ms) the bottom side of the sample is subjected to a temperature increase. The absorbed heat diffuses through the sample and consequently heats the top surface. An IR detector measures this time-dependent temperature increase. Using a radiation fit model the thermal diffusivity of the hollow sphere colloidal crystal sample can be extracted.

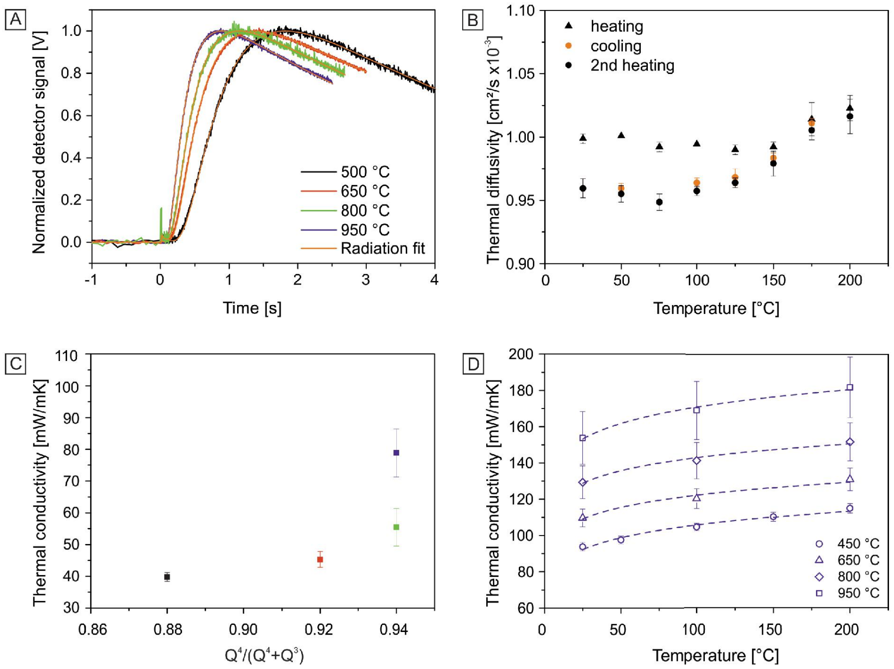

Figure S7. Laser flash analysis (LFA) of silica hollow sphere colloidal crystals A) Examples of LFA measurement signals of HSNP monoliths after calcination at elevated temperatures and the corresponding radiations fits (orange lines). The raw data were normalized to (0,1). Sample thicknesses were: 500 °C: 812 µm, 650 °C: 686 µm, 800 °C: 654 µm, 950 °C: 665 µm. B) Thermal diffusivity as a function of temperature of a HSNP colloidal crystal calcinated at 500 °C with heating (black) and cooling cycles (orange). C)Thermal conductivity of HSNP crystals calcinated at different temperatures in dependence of the degree of condensation, D)Thermal conductivity of annealed colloidal crystals (450 – 950 °C), calcinated at 950 °C prior to the assembly of the monoliths. The dashed lines represent $\kappa \sim T^x$.

The radiation fit model represents an expansion to the finite-pulse and heat-loss corrections implemented in the Combined fit model from Dusza (L. Dusza, High Temperatures - High Pressures, 1995, 27, 467-473). It accounts for a portion of the Xe flash to be directly transmitted to the top surface, leading to an instantaneous temperature jump analogous to Blumm *et al.*.(J. Blumm, J. Henderson, O. Nilsson and J. Fricke, High Temperatures-High Pressures, 1997, 29, 555-560).

Uncertainty analysis of the thermal conductivity determination

In the following, the uncertainty analysis of an individual sample based on independent measurements for the 500 °C calcinated HSNP colloidal crystal is shown exemplarily. The different contributions will be introduced separately:

Thermal conductivity κ:

$$\kappa = \alpha \cdot c_p \cdot \rho = \left(\frac{0.138 \cdot d^2}{t_{\frac{1}{2}}}\right) \cdot c_p \cdot \left(\frac{(r^3 - (r-t)^3) \cdot \rho_{SiO_2}}{r^3}\right)$$

Thermal diffusivity determination: $\alpha = \frac{0.138 \cdot d^2}{t_{\frac{1}{2}}}$

$$\sigma_\alpha = \sqrt{\left(\frac{\sigma\alpha}{\sigma t_{\frac{1}{2}}}\right)^2 \cdot \sigma_{t_{\frac{1}{2}}}^2 + \left(\frac{\sigma\alpha}{\sigma d}\right)^2 \cdot \sigma_d^2 = \left(-\frac{0.138 \cdot d^2}{\left(t_{\frac{1}{2}}\right)^2}\right)^2 \cdot \sigma_{t_{\frac{1}{2}}}^2 + \left(\frac{2 \cdot 0.138 \cdot d}{t_{\frac{1}{2}}}\right)^2 \cdot \sigma_d^2}$$

Measured parameters and their standard deviation:

Half-rise time $t_{1/2}$: (0.926 ± 0.009) s

Layer thickness d: (812 ± 8) µm

Average thermal diffusivity and standard deviation:

α= (9.83 ± 0.22) ·10^{-8} m²/s

i) Heat capacity c_p determination: $\sigma_{c_p} = \sqrt{\frac{\sum(x-\bar{x})^2}{n-1}}$

Average c_p and standard deviation:

c_p: (0.683 ± 0.010) J/gK

ii) Particle density ρ determination: $\rho = \left(\frac{(r^3-(r-t)^3) \cdot \rho_{SiO_2}}{r^3}\right)$

$$\sigma_\rho = \sqrt{\begin{gathered}\left(\frac{\sigma\rho}{\sigma r}\right)^2 \cdot \sigma_r^2 + \left(\frac{\sigma\rho}{\sigma t}\right)^2 \cdot \sigma_t^2 + \left(\frac{\sigma\rho}{\sigma\rho_{SiO2}}\right)^2 \cdot \sigma_{\rho_{SiO2}}^2 = \\ \left(-3 \cdot t(t-r)^2 \cdot \frac{\rho}{r^4}\right)^2 \cdot \sigma_r^2 + \left(3 \cdot (r-t)^2 \cdot \frac{\rho}{r^3}\right)^2 \cdot \sigma_t^2 + \left(\frac{(r^3 - (r-t)^3)}{r^3}\right)^2 \cdot \sigma_{\rho_{SiO2}}^2\end{gathered}}$$

Measured parameters and their standard deviation:

Shell thickness t: (43.7 ± 1.6) nm

Particle radius r: (157.9 ± 1.9) nm

Density of the shell by He pycnometry ρ_{SiO2}: (2.27 ± 0.13) g/cm³

Average density and standard deviation:

ρ= (1.044 ± 0.089) g/cm³

Calculation of the thermal conductivity κ:

$$\kappa = \alpha \cdot c_p \cdot \rho$$

Standard deviation of κ:

$$\sigma_\kappa = \sqrt{\left(\frac{\sigma\kappa}{\sigma\alpha}\right)^2 \cdot \sigma_\alpha^2 + \left(\frac{\sigma\kappa}{\sigma c_p}\right)^2 \cdot \sigma_{c_p}^2 + (\frac{\sigma\kappa}{\sigma\rho})^2 \cdot \sigma_\rho^2}$$

Average thermal conductivity and standard deviation:

κ= (70.1 ± 6.3) mW/mK

We determined the standard deviation for each calcination dependent thermal conductivity measurement of our samples and confirmed that the relative error is < 10 % for most of the cases. The highest uncertainty was found to be 13 %.
We therefore conclude that the major source of uncertainty is given by variations from sample to sample. This is the data and uncertainty that we present in our manuscript, which is based on at least three independent samples at each calcination temperature.

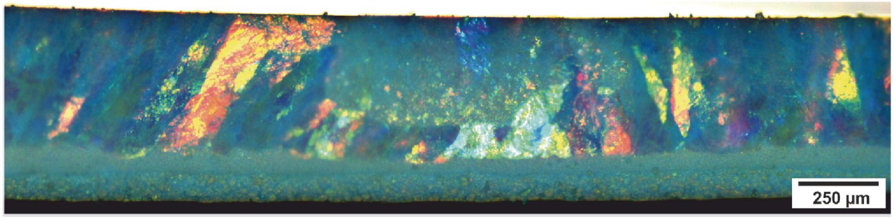

Figure S8. Bright field microscopy image of a colloidal crystal consisting of HSNP calcinated prior to the assembly process (annealed colloidal crystal).

5.3. Exploring Local Disorder within CAU-1 Frameworks Using Hyperpolarized ^{129}Xe-NMR Spectroscopy

T. W. Kemnitzer,[a] C. B. L. Tschense,[a] T. Wittmann,[a] E. A. Rössler[b] und J. Senker[a]*

Erschienen in:

Langmuir **2018**, *34(42)*, 12538-12548

DOI: 10.1021/acs.langmuir.8b02592

[a] Department of Inorganic Chemistry III, University of Bayreuth, Universitätsstr. 30, 95447 Bayreuth (Germany)

[b] Department of Experimental Physics II, University of Bayreuth, Universitätsstr. 30, 95447 Bayreuth (Germany)

* juergen.senker@uni-bayreuth.de

LANGMUIR Article
Cite This: Langmuir 2018, 34, 12538−12548 pubs.acs.org/Langmuir

Exploring Local Disorder within CAU-1 Frameworks Using Hyperpolarized ^{129}Xe NMR Spectroscopy

Tobias W. Kemnitzer,[†] Carsten B. L. Tschense,[†] Thomas Wittmann,[†] Ernst A. Rössler,[‡] and Jürgen Senker*,[†]

[†]Inorganic Chemistry III and [‡]Experimental Physics II, University of Bayreuth, 95447 Bayreuth, Germany

Supporting Information

ABSTRACT: The sorption properties of metal−organic frameworks (MOFs) can be influenced by introducing covalently attached functional side chains, which make this subclass of porous materials promising for applications as diverse as gas storage and separation, catalysis, and drug delivery. The incorporation of side groups usually comes along with disorder, as the synthesis procedures rarely allow for one specific position among a larger group of equivalent sites to be selected. For a series of isoreticular CAU-1 frameworks, chosen as model compounds, one out of four positions at every linker is modified with equal probability. Here, we investigate the influence of this disorder on Ar sorption and ^{129}Xe nuclear magnetic resonance spectroscopy using hyperpolarized ^{129}Xe gas. Models used for predicting the pore dimensions as well as their distributions were derived from the unfunctionalized framework by replacing one proton at every linker with either an amino, an acetamide, or a methyl urea functionality. The resulting structures were optimized using density functional theory (DFT) calculations. Results from void analyses and Monte Carlo force field simulations suggest that for available Ar nonlocal DFT (NLDFT) kernels, neither the pore dimensions nor the distributions induced by the side-chain disorder are well-reproduced. By contrast, we found the ^{129}Xe chemical shift analysis for the shift observed at high temperature to be well-suited to develop a detailed fingerprint of the porosity and side-chain disorder within the isoreticular CAU-1 series. After calibrating the ^{129}Xe limiting shift of the amino-functionalized framework with DFT calculations, the downfield shifts for the other two derivatives are an excellent measure for the reduction of the accessible pore space and reveal a strong preference for the side chains toward the octahedral voids for both cases. We expect that the strategy presented here can be commonly applied to disorder phenomena within MOFs in the future.

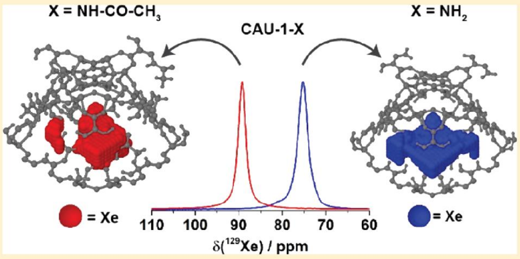

■ INTRODUCTION

Porosity is essential for a broad variety of applications ranging from gas storage[1−3] and separation[4−6] over ion exchange and water purification[7,8] to drug delivery[9−11] and catalysis.[12,13] Among the class of porous materials, metal−organic frameworks (MOFs) are promising because of their rational design, straightforward synthesis, and chemical flexibility.[14,15] This allows for the introduction of specific functional groups either by direct synthesis or postsynthetic modification (PSM) and thus tune the pore sizes and inner surfaces toward selective interactions and size selectivity.[16] As such, the long-term stability against water can be increased or the introduction of chiral groups can create a heterogeneous catalyst framework.[17,18]

MOFs feature well-defined compositions; they are mostly crystalline and combine structural stability with the flexibility of the framework.[14] They are composed of highly charged metal-oxide clusters based of divalent, trivalent, or tetravalent cations (e.g., Zn^{2+}, Cu^{2+}, Al^{3+}, Fe^{3+}, Cr^{3+}, and Zr^{4+})[19−24] called inorganic building units (IBUs). The IBUs are interconnected by linkers, which are often multivalent carboxylic acids such as terephthalic (bdc) and trimesic (btc) acid. MOFs realize large inner surface areas up to 6000 m^2/g and, therefore, provide high pore volumes and reaction spaces.[25]

Because of the hybrid character of MOFs, the inner surfaces are, although long-range ordered, heterogeneous, which is challenging for the characterization of the underlying porosity.[26] Nanoporous materials are most frequently analyzed using Ar and N_2 physisorption. Herein, sorption isotherms are fitted by Langmuir[27] or Brunauer−Emmett−Teller (BET)[28] models and density functional theory (DFT) methods to obtain specific surface areas, pore volumes, and pore size distributions (PSDs). Although the physical interpretation significantly depends on the material class, these data are commonly used as a benchmark for the porosity. In particular, the quality of the DFT analysis including the PSDs is directly linked to available kernels, which encode pore geometry, surface roughness, and chemical structure.[29−31] Whereas for

Received: August 2, 2018
Revised: September 21, 2018
Published: September 24, 2018

DOI: 10.1021/acs.langmuir.8b02592
Langmuir 2018, 34, 12538−12548

the most frequently used materials such as porous carbon and silica as well as zeolites such kernels are available, it is challenging to generate similar models with a reasonable effort for MOFs because of their structural versatility and flexibility. Thus, for understanding the sorption properties, an alternative method such as ^{129}Xe nuclear magnetic resonance (NMR) spectroscopy is beneficial.[32,33] However, ^{129}Xe NMR spectroscopy suffers from low sensitivity. In this context, the sensitivity enhancement by 4−5 orders of magnitude using hyperpolarized (HP) ^{129}Xe is highly attractive.[34−43] Then, two-dimensional exchange spectroscopy can be used to provide information about the pore interconnectivity, which is of great importance, in particular, when hierarchically structured materials[44] are studied to obtain information about adsorption and transport kinetics.

Because of the highly polarizable electron cloud of Xe atoms, the chemical shift of ^{129}Xe shows a strong dependency on its environment. In addition, Xe gas is easily adsorbed in porous materials even at high temperatures. Moreover, the smallest pores where Xe atoms are adsorbed are on the order of the Xe van der Waals diameter (4.4 Å) and thus allows the upper part of the ultramicroporous region (d < 0.7 nm) to be probed.[45] As such, ^{129}Xe NMR spectroscopy is an alternative to the frequently used CO_2 sorption experiments. Because of its quadrupole moment, CO_2 interacts more strongly with the polar parts of the framework, whereas Xe atoms are more sensitive to hydrophobic environments.[46] The largest pores leading to a specific ^{129}Xe chemical shift for adsorbed Xe atoms were reported for mesoporous silica materials with pore sizes of around 10 nm.[41]

For adsorbed Xe, the chemical shift δ is influenced by several interactions, additive in nature. Usually, the xenon−wall interactions (δ_s), Xe−Xe interactions (δ_{Xe}), strong adsorption sites (δ_{SAS}), and the influence of electric (δ_e) or magnetic (δ_m) fields are distinguished (eq 1).

$$\delta = \delta_s + \delta_{Xe} + \delta_{SAS} + \delta_e + \delta_m \quad (1)$$

In the so-called limiting shift region, δ_{Xe} is minimized by reducing the Xe adsorption at high temperatures. If additionally, the influence of δ_{SAS} as well as δ_e and δ_m can be neglected, which is true for diamagnetic and homogeneous materials with low charge densities, the ^{129}Xe chemical shift is connected only to xenon−wall interactions.

A prominent work in this field was published by Demarquay and Fraissard,[47] who developed a model to calculate the mean free path within the pores of zeolites from the ^{129}Xe NMR chemical shift. For a given pore geometry, the average mean free path is directly connected to the pore size itself. This analysis was successfully used for pillared clays to obtain the pore size of the interlayer space.[48] A similar correlation was published on mesoporous silica materials.[49]

However, for materials as heterogeneous as MOFs with highly charged IBUs, we expect that neither the influence of δ_e and δ_m can be neglected nor is δ_s constant, as required for the abovementioned model. Nevertheless, the experimental database for ^{129}Xe chemical shifts of MOFs is rather limited, and only for a few examples such as IRMOFs,[50] ZIF-8,[45] MIL-53,[51] or UiO-66,[52] ^{129}Xe NMR spectra have been published so far. In particular, very few systematic studies between the ^{129}Xe isotropic chemical shift and the pore size were reported, which probe correlations between both observables, such as the Fraissard model, without finding any obvious relationships.[50] Therefore, in the current work, we develop a microscopic picture of the ^{129}Xe chemical shift of Xe atoms adsorbed in a isoreticular series of CAU-1-X derivatives, with X = $-NH_2$, $-NH-CO-CH_3$, and $-NH-CO-NH-CH_3$, by DFT calculations, as first done by Jameson and de Dios.[53]

CAU-1[54] was chosen as a model system as it has diamagnetic metal centers and its structure is rigid. CAU-1 (Figure 1) is composed of AlO_6 octahedra that are connected to eight rings alternately sharing corners and edges. These IBUs are interconnected by twelve 2-aminoterephthalate ions (bdc-NH_2), forming a tetragonal structure with two distinct cavities.

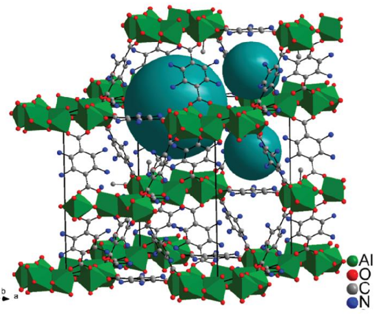

Figure 1. Crystal structure of CAU-1 as solved by Ahnfeldt et al.[54] Cyan spheres indicate the two different pores. Nitrogen sites are occupied by a probability of 25%.

The interactions and dynamics of an isolated Xe atom are modeled by a high number of possible adsorptions sites within a representative part of the network. With DFT calculations, we then create a three-dimensional (3D) map of Xe positions assigning two hypersurfaces, one for the energy and one for the ^{129}Xe chemical shift. These maps allow the experimental ^{129}Xe chemical shift to be modeled as the average over all Xe positions. This approach is a valid alternative to the molecular dynamics (MD) studies published by Trepte et al.,[52] as long as the Xe dynamics is in the fast motion limit. It offers the advantage, however, that significantly fewer calculations have to be performed, thus keeping the calculation cost at a reasonable level. The results are compared to Xe adsorption isotherms as a function of temperature in order to quantify the amount of adsorbed Xe and determine the onset of Xe−Xe interactions.

■ EXPERIMENTAL SECTION

Preparation of MOF. CAU-1 was synthesized according to a protocol of Ahnfeldt et al.[54] Aluminum chloride hexahydrate (232 mg, 0.96 mmol) and 2-aminoterephthalic acid (58 mg, 0.32 mmol) were dissolved in methanol (3.175 mL) and stirred for 5 min at 145 °C in a Biotage Initiator+ microwave reactor (400 W). The yellowish suspension was cooled to room temperature, centrifuged, and washed three times in a mixture (1:1) of dry methanol and chloroform to remove unreacted, incorporated bdc-NH_2. The product was then dried at 100 °C under reduced pressure.

Postsynthetic Modification of CAU-1. CAU-1-AmMe (Scheme 1) was obtained after suspending CAU-1 (100 mg) in chloroform (5 mL), adding acetic anhydride (0.4 mL 4.23 mmol), and stirring for 24 h at 100 °C in a 10 mL Duran screw cap glass bottle. For CAU-1-UrMe (Scheme 1), methyl isocyanate was synthesized by adding acetyl chloride (2, 8 mL, 40 mmol) dropwise to a stirred solution of sodium azide (2, 6 g, 40 mmol) in freshly distilled acetonitrile (40 mL) at 50 °C within 5 h.

DOI: 10.1021/acs.langmuir.8b02592
Langmuir 2018, 34, 12538−12548

Scheme 1. Schematic Postsynthetic Modification of 2-Aminotherephtalic Acid at the Linker in CAU-1[a]

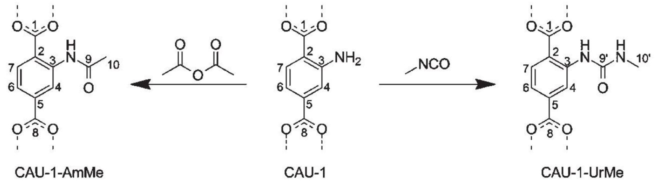

[a] All carbon atoms are numbered for easier description.

Then, the freshly prepared methyl isocyanate was added dropwise into a suspension of CAU-1 (100 mg) in chloroform (5 mL) immediately after its synthesis and subsequent distillation from the reaction mixture. After stirring the CAU-1 suspension for 24 h at room temperature, the mixture was filtered off and washed with chloroform. The yellow powder was then dried at 100 °C under reduced pressure.

Powder X-ray Diffraction (PXRD). Powder X-ray diffractograms were recorded on a STOE Stadi P diffractometer equipped with a Mythen 1K detector [Debye−Scherrer geometry, Cu Kα_1 radiation (λ = 1.54056 Å), Ge monochromator 111-direction]. Samples were prepared in a glass capillary with an outer diameter of 0.5 mm. The experimental powder X-ray diffractograms were fitted to the theoretical structure,[54] including preferred orientation, using the Pawley method in TOPAS Academic.

Ar/Xe Physisorption. Both Ar and Xe physisorption experiments were performed on a Quantachrome Autosorb 1 analyzer. Prior to measurements, all samples were dried at 110 °C for 24 h at reduced pressure. Ar physisorption experiments were carried out at 87.35 K. Xe physisorption was performed at temperatures of 298, 273, 240, 220, 200, 180, and 160 K in a pressure range of 0−100 kPa. Specific surface areas were determined using a five-point BET model in a p/p_0 range of 0.008−0.5. A nonlocal DFT (NLDFT) kernel (Quantachrome ASiQwin 3.0 software, Ar on carbon, slit pore) for the calculation of PSDs and pore volumes was used because it obtained the smallest fitting errors to the isotherms.

Liquid-State NMR Spectroscopy. Solution ^{1}H NMR spectra were obtained using a Bruker DRX 500 spectrometer operating at a proton frequency of 500.13 MHz in combination with an implemented standard sequence using 30° excitation pulses. The samples were digested in a solution of 5 wt % CsF in dimethyl sulfoxide (DMSO)-d_6/D_2O (5:1).

Solid-State NMR Spectroscopy. All NMR spectra were acquired on an AVANCE III HD spectrometer (Bruker) at a B_0 field of 9.4 T. ^{13}C{^{1}H} (100.6 MHz) magic-angle spinning (MAS) spectra were obtained using a ramped cross-polarization experiment, where the nutation frequency ν_{nut} on the proton channel was varied linearly by 50%. The samples were spun at 12.5 kHz in a 4 mm MAS double-resonance probe (Bruker). Excitation of the proton spin bath was carried out with ν_{nut} = 100 kHz. The corresponding ν_{nut} on the ^{13}C channel and the contact time were adjusted to 70 kHz and 3 ms, respectively. The spectra were acquired over 3072 transients with a recycle delay of 1 s. During acquisition, proton broadband decoupling was applied using a spinal-64[55] sequence with ν_{nut} = 70 kHz. ^{13}C spectra were referenced indirectly with respect to tetramethylsilane using adamantane as the secondary reference.

HP Continuous Flow ^{129}Xe NMR Spectroscopy. ^{129}Xe NMR experiments were performed using a home-built hyperpolarizer equipped with two Duo-FAP diode laser arrays (Coherent Inc.) at an output power of 100 W. A gas mixture with a volume ratio Xe/N_2/He = 1%:3%:96% was used at an absolute pressure of 5 bar. The laser line was tuned to the Rb-D_1 line (794.8 nm) while light absorption was checked continuously by an optical charge-coupled device spectrometer (Avantes). Spin exchange optical pumping (SEOP) provided ^{129}Xe polarization of about 15−20%. The gas flow was held constant at a rate of around 300 sccm.

HP-^{129}Xe NMR spectra were obtained on an Avance II spectrometer (Bruker) combined with a 7.05 T magnet (Oxford) working at a resonance frequency of 83.4 MHz. A double-resonance wideband probe (Bruker) was used, which was modified with a 3 mm inner diameter PEEK sample holder incorporating a constant stream of HP-^{129}Xe to the sample within the coil. Variable temperature (VT) experiments were performed using a BVT 3000 unit (Bruker) providing a temperature-controlled N_2 stream on the sample holder. The temperature was changed in 10 K steps and allowed to equilibrate for 10 min before starting the measurements. The samples were dried in high vacuum at 110 °C prior to measurements to remove any moisture residue inside the pores. One-dimensional NMR spectra were recorded using a single pulse excitation with a $\pi/2$ pulse length of 4.75 μs with 8−64 transients to acquire a constant signal-to-noise ratio and compensate the variations of the hyperpolarization rate. The recycle delay of HP-Xe was set between 1 and 32 s to adjust for smaller diffusion rates at lower temperatures.

Ab Initio Calculations. Calculations were carried out using the CASTEP DFT code (version 8.0)[56] using the generalized gradient approximation (GGA) functional, Perdew−Burke−Ernzerhof (PBE), and semiempirical dispersion correction Grimme06.[57,58] Pseudopotentials with a plane wave cutoff of 900 eV and 1 k point within the Brillouin zone were applied. Because only relative energy values between each calculation are relevant, the lowest obtained energy was set arbitrary to 0, so all other denoted energy values are in relation to this minimum.

Geometry optimizations were carried out after adding pending side chains to the framework in all possible permutations to an energy and force minimum using the Broyden−Fletcher−Goldfarb−Shanno (BFGS) minimization algorithm. For these calculations, no constraints were used, and both lattice parameters and atomic positions were allowed to relax freely. For calculating the energy and shift hypersurfaces as a function of the Xe position within the pore space, no geometry optimization was performed and lattice parameters and atomic positions were kept constant.

Chemical shieldings were calculated using the gauge including projector augmented waves (GIPAW) method.[59,60] To transform the isotropic part of the chemical shielding σ into a chemical shift δ, the following equation was used

$$\delta_{\text{iso}} = \sigma_{\text{ref}} - \sigma_{\text{iso}} \tag{2}$$

σ_{ref} was determined by matching the experimental chemical shifts with the simulated shieldings. For comparison, a shielding for gaseous Xe extrapolated to zero pressure was derived by placing a single Xe atom inside a cubic unit cell with an axis length of 15 Å. The resulting shielding $\sigma_{\text{Xe(gas)}}$ amounts to 5924 ppm.

■ RESULTS AND DISCUSSION

The PXRD patterns of CAU-1 (-NH_2), CAU-1-AmMe (NH−CO−CH_3), and CAU-1-UrMe (NH−CO−NH−CH_3) (Figure S1) exhibit sharp reflexes, which were indexed based on the structure model of CAU-1 published in ref 54. Together with the good match between the observed and simulated reflex intensities (Figure S1), this confirms that all three derivatives crystallize in the CAU-1 topology with good crystallinity.

Deviations of the expected reflex intensities are attributed to preferred orientation. The cell parameters obtained by refining the powder patterns with the Pawley method are very similar to the ones given in ref 54 (Table 1) and do not change significantly upon PSM. The absence of any nonindexed and superstructure reflections asserts the radiographic purity and suggests local disorder for the position of the functional groups at the bdc units and their orientation within the framework.

Table 1. Refined Lattice Constants and R_{wp} Values of CAU-1 and Modified Structures Obtained from Fitting the PXRDs (Figures S2−S4) via the Pawley Method

sample	a/Å	b/Å	c/Å	R_{wp}/%
CAU-1	18.342(3)	18.324(5)	17.732(2)	1.743
AmMe	18.361(2)	18.349(3)	17.738(1)	2.398
UrMe	18.336(3)	18.343(4)	17.753(2)	1.834

The ^{13}C MAS NMR spectra (Figure S5) for all three compounds exhibit a resonance at 48 ppm, typical for methanolate ions coordinated to Al^{3+}.[54] For CAU-1, the resonances of the aromatic carbon atoms are well-resolved, with resonances at 151 ppm (3, Scheme 1), 137 and 131 ppm (5, 7), and 117 ppm (2, 4) as well as 171/173 ppm for the carboxylate groups (2, 5). The ^{13}C MAS NMR spectra of CAU-1-AmMe and CAU-1-UrMe exhibit additional peaks characteristic for the new anchor groups $-NH-CO-CH_3$ and $-NH-CO-NH-CH_3$, for example, the $-CH_3$ group of the anchors (10, 10′) resonate at 24 ppm. The signal of the aromatic carbon atom 3 next to the amino group is shifted highfield after PSM and overlaps with the other aromatic signals. The nearly complete absence of the original signal at 151 ppm demonstrates almost complete linker conversion via PSM for all derivatives.

These results agree well with the data from liquid-state ^{1}H NMR spectroscopy (Figure S6) after dissolution of the framework in a basic solution. The ^{1}H chemical shift of the aromatic proton in the meta position to the amino group of 2-aminotherepthalic acid changes its value from 7.56 to 7.81 ppm during chemical modification of $-NH_2$ and can thus be used for quantifying the ratio of modified and unmodified linker molecules. With the higher degree of modification, the integral of the modified linker molecules increases, whereas that of the original linker decreases. For both CAU-1-AmMe and CAU-1-UrMe, a conversion degree of 93% results. Summarizing, we prepared CAU-1, CAU-1-AmMe, and CAU-1-UrMe with high yield, high purity, and excellent conversion degrees of 93% for the modified networks.

To derive the influence of the anchor group disorder on the porosity of the CAU-1 derivatives, a set of structure models was created. The amino groups of each linker molecule in the reference crystal structure have four possible positions with an occupation probability of 25%. Thus, we created several models by positioning the amino groups to possible linker sites of the framework. Although the resulting number of structural isomers is relatively low, we expect the variation to be large enough to model the distribution of the pore sizes induced by the disorder of the side groups.

The relevant information and details for the construction of these models are described in detail in Figures S7 and S8 of the Supporting Information. On the basis of the symmetry of the unit cell, the configuration of the amino groups placed on the cell edges and pointing into the octahedral cavity allows for only four different configurations (Figure 2A).

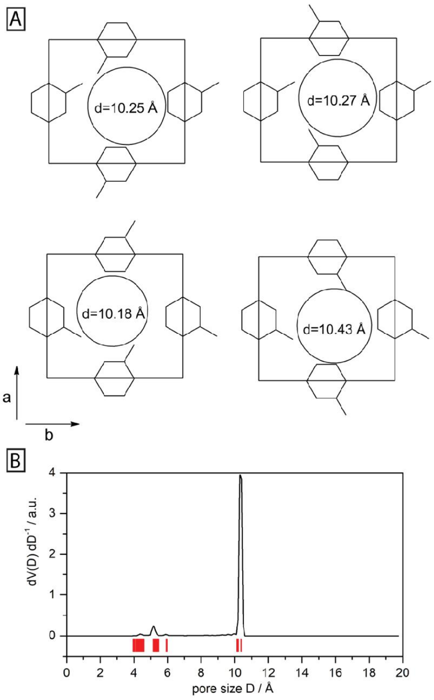

Figure 2. (A) Schematic cross-section of the unit cell with c = 0 to demonstrate all possible configurations of the amino groups. The calculated pore sizes using the Platon cavity plot are placed into the models. Details about the construction can be found in Figures S7/S8. (B) Calculated mean ⟨PSD⟩ compared to the discrete pore sizes (red lines) obtained from the Platon cavity module.

Additionally, for the amino groups attached to the linkers defining the tetrahedral pores (TPs), a total of 55 configurational isomers are possible in the lower or upper half of the unit cell (Figure S9). In total, this leads to 4 × 55 × 55 = 12100 anchor group configurations. Because the configurations of the octahedral and tetrahedral voids of the upper and lower part of the unit cell are independent of each other, it is sufficient to analyze the 4 octahedral and 55 tetrahedral configurations in terms of free volume. The corresponding structure models were optimized with DFT methods to an energy and force minimum without any restrictions. Whereas the positions of the amino groups were relaxed, the overall structure as well as the lattice parameters stayed constant during the optimization. To create CAU-1 structure models after PSM, the NH_2 groups were exchanged by the bulkier functional groups and optimized in a similar way. For all models, the pore sizes of these structures were determined using the cavity tool of Platon[61] assuming spherical pore shapes. Hereby, the potential free volume inside the unit cell is analyzed with hard spheres. The radii and positions are moved until the surface of these spheres overlaps with the vdW radii of the framework and the side-chain atoms, respectively. This method generates discrete pore sizes, which, for example, vary

Table 2. Comparison of Pore Size D of OPs (oct) and TPs (tet) Obtained from Ar Physisorption (NLDFT) and from the Modeled Crystal Structures (Platon)[a]

sample	D_{oct} (Platon)	D_{tet} (Platon)	D_{oct} (NLDFT)	D_{tet} (NLDFT)
CAU-1	10.18−10.43	3.99−6.02	6.28−11.30	4.79−6.00
CAU-1-AmMe	7.79−8.59	2.74−4.53	6.28−8.99	4.58−6.00
CAU-1-UrMe	7.45−8.19	2.59−4.22	5.90−8.52	4.84−5.90

[a] Values are given in Å.

Table 3. Surface Area and Pore Volume Obtained from Ar Physisorption Using the BET Model and the NLDFT Kernel

sample	V_{mic}[a]/cm^3 g^{-1}	$V_{mic\ DFT}$[b]/cm^3 g^{-1}	V_{tot}[c]/cm^3 g^{-1}	$V_{tot\ DFT}$[d]/cm^3 g^{-1}	S_{BET}/m^2 g^{-1}	S_{DFT}/m^2 g^{-1}
CAU-1	0.569	0.424	0.759	0.880	1432.54	1199.2
AmMe	0.456	0.436	0.556	0.654	1241.34	1294.19
UrMe	0.398	0.295	0.537	0.676	999.78	911.86

[a] Calculated pore volume at $p/p_0 = 0.15$. [b] Pore volume for pores with diameters smaller than 2 nm calculated from the Ar NLDFT model at 87 K. [c] Calculated total pore volume at $p/p_0 = 0.8$. [d] Total pore volume from the Ar NLDFT model at 87 K.

for the conformational isomers of the octahedral pores (OPs) between 10.2 and 10.5 Å (Figure 2A). Additionally, PSDs for N_2 adsorption at 77 K were calculated based on the UFF forcefield[62] using Poreblazer[63] for each structure model. These PSDs were then averaged to derive the mean distribution ⟨PSD⟩. The calculated pore sizes obtained from both methods for the structure of CAU-1 (Figure 2B) are in good agreement with each other. As expected, the pore sizes for both the tetrahedral and the octahedral cavities (Table 2) decrease with increasing size of the functional group, although the effect is more pronounced for the OPs. The cavity plot leads to average pore diameters between 10.18 (CAU-1) and 7.45 Å (CAU-1-UrMe) with a spread of less than 1 Å for the OPs and values of 5.2−4.2 Å for the TPs.

In parallel, Ar physisorption isotherms (Figure S10A) were obtained to derive surface areas, pore volumes, and PSDs (Figure S10B) of all three frameworks. All isotherms are type I, as expected for microporous materials. A small hysteresis in combination with a sudden increase of the adsorption volume is observed in the range of $p/p_0 = 0.8−0.97$. This is most probably caused by adsorption within the intergranular space between the crystallites, which is typical for powdered samples. Both the apparent BET surface area and V_{tot} decrease from 1432 m^2/g and 0.759 cm^3/g for CAU-1 to 1000 m^2/g with 0.537 cm^3/g for CAU-1-UrMe (Table 3), which is in line with the larger required space and increasing molar mass for AmMe ($1.14 \times M_{CAU\text{-}1}$) and UrMe ($1.20 \times M_{CAU\text{-}1}$). The decrease of the total pore volume V_{tot} upon PSM is also reflected by the trend of the micropore volume V_{mic}. With an exception for CAU-1 where S_{BET} is significantly smaller, S_{BET} and S_{DFT} are comparable (Table 3). By contrast, the PSDs (Figure S10B) reveal significant differences compared to the structural pore analysis. The PSD for CAU-1 exhibits three distinct maxima for cavity diameters of 5.1, 7.8, and 10 Å, whereas the cavity plot analysis as well as the simulated PSD suggests only two cavities with diameters of around 10.0 and 5.2 Å. The most intense volume fraction of the PSD around 7.8 Å is not reflected in the cavity plot analysis.

For CAU-1-AmMe and CAU-1-UrMe, only two volume fractions with diameters of about 5.3/5.2 and 7.8/7.2 Å were resolved (Figure S10). From the cavity plot analysis, average diameters of 4.5/4.2 and 7.6/6.4 Å were derived. Although both methods suggest a larger influence of the cavity sizes for the OPs upon PSM, the absolute values differ markedly. The discussed deviations of the data derived from the NLDFT kernel provide a good example for the limited suitability of available DFT kernels for MOFs. This is accompanied by a pore size reduction within the octahedral cavities of roughly 35% for the cavity plot and only 10% for the PSD analysis. For the TPs, a diameter of 5.2 Å with a reduction of about 20% upon PSM was determined by the cavity plot method, whereas the PSD revealed similar values (≈4.8 Å) and no size reduction for all three derivatives. We attribute these deviations mainly to the nature of the NLDFT kernel, which is optimized for homogeneous carbon surfaces and not for a hybrid material such as CAU-1.

^{129}Xe NMR spectroscopy presents an alternative approach toward the porosity of the CAU-1 derivatives as the chemical shift is sensitive to the nature of the pore walls, the pore size, and the interpore diffusivity. Here, we explore further how far these influences on the chemical shift can be singled out to derive information about the pore structure of the targeted frameworks. Therefore, we measured ^{129}Xe NMR spectra as a function of temperature for all three compounds. Using HP ^{129}Xe produced by SEOP allowed all measurements to be performed in a reasonable time frame. VT ^{129}Xe NMR spectra for CAU-1 are depicted in Figure 3 and show two well-separated signals at room temperature. The resonance at 0 ppm is assigned to free gaseous Xe within the coil and is used as the internal reference. The second signal shifts with temperature and corresponds to Xe adsorbed within the framework and is characteristic of the interaction of Xe with the host.[64] At elevated temperatures (240−360 K), the observed shift does not change with temperature, which is usually referred to as the limiting shift range.[64] In this range, the ^{129}Xe isotropic chemical shift is supposed to be influenced only by interactions between Xe atoms and the framework and not by Xe−Xe interactions. Xe physisorption measurements (Figure S11) show that for this temperature range, the amount of adsorbed Xe atoms per unit cell is below three. Thus, only less than 10% of the free pore volume is populated by Xe, which is small enough to reduce Xe−Xe interactions effectively.

Below 240 K, the signal for ^{129}Xe adsorbed in the pore space starts to move to larger shift values and broadens significantly (Figure 3). The spectra were acquired down to a temperature of 140 K to avoid the formation of Xe ice at about 130 K. Around 200 K, the peak splits into two asymmetric resonances, which merge into one asymmetric resonance again below 180 K. At the same time, the amount of adsorbed Xe atoms

DOI: 10.1021/acs.langmuir.8b02592
Langmuir 2018, 34, 12538−12548

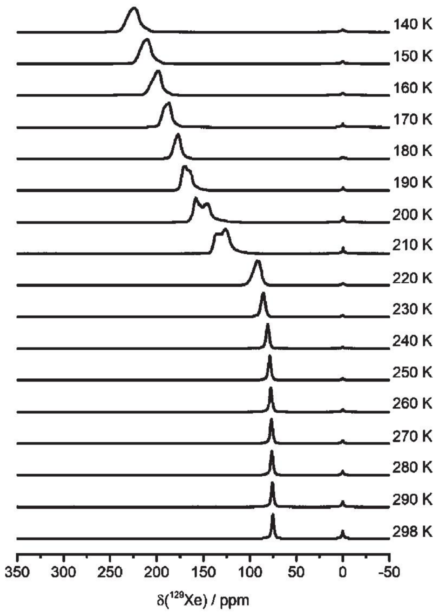

Figure 3. ^{129}Xe NMR spectra of CAU-1 as function of temperature.

increases continuously to 24 per unit cell at 180 K, as derived again from the Xe-physisorption isotherms (Figure S12). This value corresponds to a packing efficiency of 83%, which is slightly larger than expected for an ideal close packing (74%, 22 Xe atoms) and indicates a complete filling of the pore volume below 180 K under the experimental Xe partial pressure (5 kPa) adjusted within the NMR sample holder. This is corroborated by the shape of the Xe isotherm at 180 K, which has already started to saturate under these conditions (Figure S11). We attribute the two different ^{129}Xe resonances at 200 K to the two pore geometries (TP/OP). The shifts for both cavities exhibit slightly different temperature dependencies explaining the coalescence of the corresponding resonances toward lower temperatures. A more detailed analysis of the ^{129}Xe chemical shift in this region, however, has to be based on a complex combination of the Xe−Xe and Xe framework interactions, which is beyond the scope of this work. Similar behavior is observed for the isoreticular AmMe and UrMe species (Figures S13 and S14).

For the prediction of the ^{129}Xe isotropic chemical shift on the DFT level, we focus on the limiting shift region because only xenon−wall interactions have to be considered. This allows for the exploration of the energy and shift hypersurfaces of Xe atoms moving through the pore space, keeping the computational costs at a reasonable level. The fact that within the limiting shift region only one resonance is observed (Figures 3, S13, S14) demonstrates that under these conditions, the Xe dynamics within the pores is fast enough to explore both TP and OP environments for all CAU-1 derivatives during the acquisition time (fast motion limit). Therefore, the ^{129}Xe chemical shift is calculated as the average over a number of Xe positions within the framework. These scenarios might be created by MD simulations to describe the thermal motion of the Xe atoms. However, to reach sufficient statistics for a Boltzmann weighting of the simulated chemical shifts, a considerable number of calculation steps have to be carried out, which is time-consuming, in particular, because simulations have to be carried out on the DFT level to allow for chemical shift calculations.

Therefore, we used an alternative strategy to explore the inner pore volume of CAU-1. We partition the pore space in a fine 3D mesh with a defined and equal step size in all directions. On each grid point, one Xe atom is placed, and the chemical shift as well as the energy of the system were calculated without geometry optimization. It is justified to treat the framework as a rigid body because large-angle linker rotations are significantly slower compared to the Xe dynamics and can thus be neglected for modeling the ^{129}Xe chemical shift.[65] To minimize the number of required positions and thus the calculation time, the smallest volume within the unit cell representing the whole system—the asymmetric unit—was used. It represents a cuboid with an axis length of $a/2$, $b/2$, and $c/2$ starting at the origin of the unit cell, which represents 1/8 of the cell volume.

This creates a one-to-one correlation between the energy and the shift hypersurfaces. As the thermal energy is high enough for a given Xe atom to explore the complete hypersurface, its energy is then used to predict the probability to find a Xe atom located at a certain position. This probability was then used to calculate the average chemical shift. Although the disorder of the anchor groups in principle increases this volume to at least one unit cell or beyond, we found it to be sufficient to explore the asymmetric unit to reproduce the observed chemical shift with a reasonable accuracy.

To create a sufficiently large number of Xe sites on the 3D grid of the asymmetric unit for an accurate Boltzmann weighting, we chose a step size of 0.5 Å in each direction. Xe positions with a distance to the neighboring framework atoms below 75% of the sum of the vdW radii were excluded from the calculations resulting in 781 model structures. For a first comparison, the calculated shielding values were transformed into chemical shifts using a shielding of 5924 ppm calculated for Xe gas (see the Experimental Section) based on nonrelativistic DFT calculations. This is convenient as the experimental isotropic chemical shift of Xe gas is usually set to 0 ppm. A similar procedure, however with a different program code for nonrelativistic DFT calculations, led to a comparable shielding for Xe gas of 6192 ppm.[52] The correlations between the position and energy E_i on the one hand and chemical shift values δ_i on the other hand are depicted in Figure 4.

Xe positions with the lowest relative energies are found close to the electron cloud of the aromatic system of the bdc units. Here, the energetically most favored position for Xe atoms is the middle of the TPs sandwiched between two bdc linkers (Figure 4 top). These regions thus pose the most attractive adsorption sites in CAU-1. For instance, Xe atoms in the OPs are 20 kJ/mol less favored compared to the ones located on the tetrahedral adsorption sites. Significantly, higher energy values up to 100 kJ/mol are observed, if the Xe atoms are close to the IBUs. By contrast, the ^{129}Xe isotropic chemical shift for Xe atoms in the middle of the TPs is 162 ppm and, therefore, in a range of elevated chemical shifts. Whereas Xe atoms in the middle of the OPs exhibit the lowest chemical shift of 0 ppm. The highest chemical shift values of about 600 ppm are realized close to the IBUs. As a consequence, there is no unambiguous relation between the energy and the isotropic chemical shift, as shown in Figure 5A.

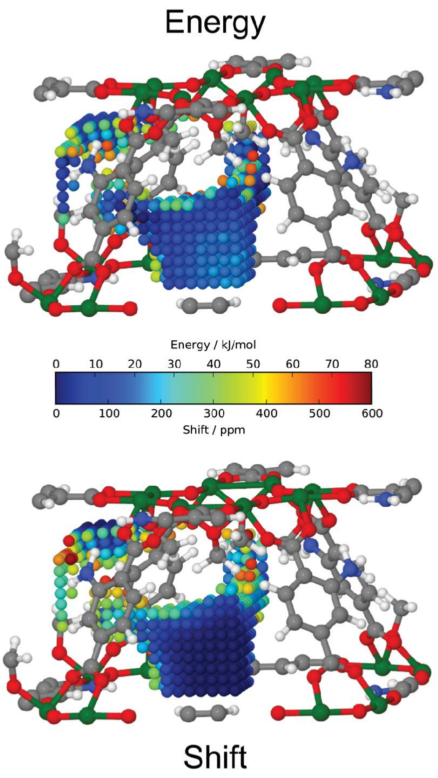

Figure 4. Grid of Xe positions within the selected fraction of the unit cell. Energy (top) and ^{129}Xe isotropic chemical shift (bottom) are color coded with the color bar shown below. For a better overview, only half of the unit cell is shown. The complete structure is given in Figures S15 and S16.

The energy hypersurface allows a probability P_i of finding a Xe atom on a specific grid position to be defined. Because the translational dynamics of the Xe atoms is fast compared to the NMR timescale, we assume that the whole ensemble of grid points is explored within the acquisition time. P_i is then given as a simple Boltzmann weighting and is defined by eq 3 with Z being the sum of states.

$$P_i = \frac{e^{-E_i/RT}}{Z}, \qquad Z = \sum_i e^{-E_i/RT} \tag{3}$$

$$\bar{\delta} = \sum_i \delta_i \cdot P_i \tag{4}$$

As for every grid point a chemical shift was calculated, the experimental shift can be modeled as the average over all grid positions. $\bar{\delta}$ is thus given by eq 4 and is depicted in Figure 5B (magenta line). By referencing $\bar{\delta}$ to the experimental data in the limiting shift region (240−360 K), σ_{ref} of 5882.5 ppm was obtained. This value is 41.5 ppm smaller compared to the nonrelativistic shielding value calculated for Xe gas (5924 ppm). This offset is attributed to an overestimation of the chemical shift within the DFT calculations and the omission of relativistic effects as shown for ^{129}Xe chemical shift calculations for the MOFs, UiO-66, and UiO-67.[52] The inclusion of relativistic effects by adapting the pseudopotentials (SR-ZORA)[68] for selected calculations resulted in a correction of about 10 ppm and thus accounts only for roughly 25% of the relativistic effects. Similar results were found for the theoretical prediction of ^{129}Xe shifts for clathrates and organic cages.[66,67] For the present study, we thus used the experimentally determined reference value of 5882.5 ppm for further analysis.

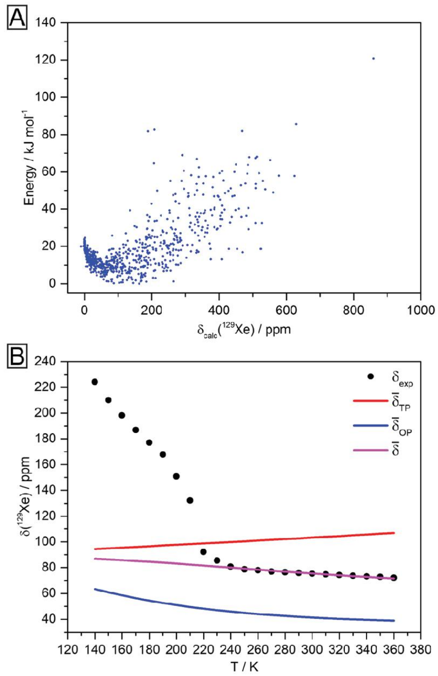

Figure 5. (A) ^{129}Xe shift and corresponding energy for each position on the grid within CAU-1. (B) Experimental δ_{exp} and theoretical ($\bar{\delta}$) values of the isotropic ^{129}Xe chemical shift for each measured temperature. Averaged contributions of the octahedral ($\bar{\delta}_{OP}$) and tetrahedral ($\bar{\delta}_{TP}$) are shown. Isotropic shifts were corrected with a constant value of 41.5 ppm to match the experimental data.

The calculated $\bar{\delta}$ exhibits a very similar temperature dependency compared to the experimental limiting shifts (Figure 5B, magenta line and black circles) at high temperatures (220−360 K). The small but significant increase of the chemical shift values with decreasing temperature is a consequence of a higher population of energetically favored Xe adsorption sites. The excellent agreement between the experimental (−0.0532 ppm/K) and calculated (−0.0731 ppm/K) slopes in this temperature region demonstrate that it is justified to assume thermal equilibrium within the given ensemble.

In a next step, we divided the 3D grid into two parts—one for the TPs and one for the OPs. This was done by splitting the volume of the asymmetric unit into four cuboids with edge lengths of $a/4$, $b/4$, and $c/2$ according to Figure S17. Whereas the green cuboids are representative for TPs, the blue ones account for OPs. Averaging the chemical shifts and the probabilities corresponding to grid points either belonging to green or blue cuboids allows for deriving $\bar{\delta}_{OP}$ and $\bar{\delta}_{TP}$ (Figure 5B) as well as the corresponding occupancies (Figure S18).

DOI: 10.1021/acs.langmuir.8b02592
Langmuir 2018, 34, 12538−12548

Although only 20% of all Xe grid positions are assigned to the TP space, Xe atoms within the TPs have a significantly higher influence on the overall shift because they are energetically favored and thus have a higher population probability; for example, at 360 and 240 K, the TPs are populated by 48 and 63%, respectively (Figure S18).

The averaged chemical shift of the TPs decreases with decreasing temperature, whereas the trend of the OP is opposing. This trend arises as the less favored positions of the TP have high chemical shifts, whereas in the OP, these positions exhibit low chemical shifts. Below 220 K, the experimentally observed ^{129}Xe chemical shift values strongly increases and do not match the trend of the calculated $\overline{\delta}$ any longer. The steep increase indicates the onset of Xe−Xe interactions, as confirmed by the increased width and shape formation in the experimental NMR spectra (Figure 3) and Xe physisorption (Figure S11). The calculations are based on one Xe atom only, and thus the corresponding chemical shift values do not reflect this trend.

For CAU-1-AmMe and CAU-1-UrMe, the ^{129}Xe spectra and the limiting shifts at room temperature are downfield-shifted by 14 and 16 ppm compared to CAU-1 (Figure 6). This trend can be explained by the larger space requirement of the AmMe and UrMe functional groups. The additional occupied pore space obviously blocks areas with lower shift values compared to CAU-1, which are not accessible for the Xe atoms any longer and thus increase the mean chemical shift. As such, the anchor groups must predominantly point into the OP space (Figure 7).

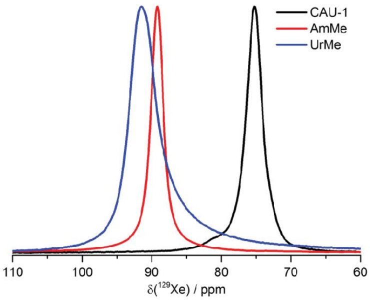

Figure 6. ^{129}Xe NMR resonances of adsorbed Xe in CAU-1 and isoreticular frameworks at 298 K.

Indeed, the cavity plot method demonstrates a significantly stronger reduction of the pore diameter of the OPs up to 25%. Compared to this, the TPs exhibit a maximum reduction of 16%. Neglecting the smaller space reduction within the TPs, the increasing shift might be explained by the blocking of low-shift regions within the OPs by sterically demanding anchor groups. Therefore, a second set of ^{129}Xe chemical shift calculations was performed for one structure of CAU-1-AmMe. The number of possible Xe positions within the volume fraction of the unit cell reduces from 781 for CAU-1 to 504 for CAU-1-AmMe (Figure 7), demonstrating a pore volume, which is reduced by roughly 35%.

This matches well with the results from the cavity plot method. The calculated chemical shift was referenced using the same correction value as for CAU-1 (41.5 ppm). The values for energy and chemical shift at each chosen Xe position is comparable with the previous calculations, confirming that the anchor groups themselves have essentially no influence on the ^{129}Xe chemical shift or the adsorption energy. Again, the center of the TP represents the most attractive adsorption site in terms of an energy minimum. The overall averaged chemical shift for this system is now dependent on the orientation of the anchor groups pointing into the OPs. Different orientations and tilting angles of the NH−CO−CH_3 groups in relation to the phenyl rings of the linkers result in the omission of certain Xe positions. As a consequence, the calculated averaged shift is a function of the anchor group orientation with two limit values given as blue and red lines in Figure 8.

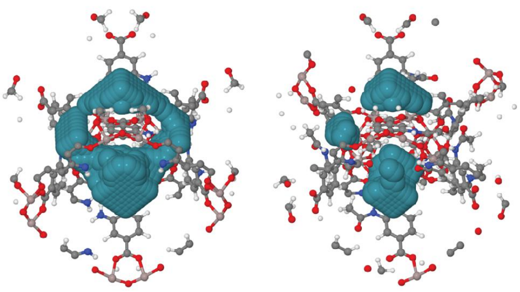

Figure 7. Demonstration of the reduction of free pore volume by the introduction of longer functional groups via PSM. Teal colored spheres represent possible Xe positions set for chemical shift calculations within the framework of CAU-1 (left) and CAU-1-AmMe (right).

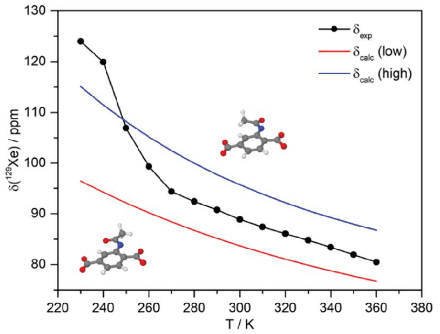

Figure 8. Experimental δ_{exp} and ranges for calculated values (δ_{calc}) of the isotropic ^{129}Xe chemical shift of CAU-1-AmMe. Given ranges are the boundaries of the calculated chemical shift depending on the orientation of the anchor groups.

The data suggest that the experimental and the averaged calculated ^{129}Xe chemical shifts can be matched by removing specific points from the Xe grid derived for CAU-1 according to the space demand of the side chains as a function of their orientation. In this way, ^{129}Xe NMR spectroscopy becomes sensitive to the side-chain disorder as it allows the local alignment of the anchor groups to be derived.

■ CONCLUSIONS

We synthesized a series of isoreticular CAU-1 framework by the postsynthetic modification of the amino groups with acetic anhydride and methyl isocyanate separately. In this way, acetamide and methyl urea functionalities could be introduced into the framework with a functionalization degree of about 93%. Besides a thorough structural characterization based on PXRD and infrared and solid-state NMR spectroscopies, all three frameworks were analyzed using Ar physisorption and ^{129}Xe NMR spectroscopy to study the influence of the side-chain disorder on the porosity. CAU-1 frameworks crystallize in a distorted cubic close packing with two interconnecting cavities—a larger octahedral-type and a smaller tetrahedral-type one. Available kernels for calculating PSDs from the Ar sorption data revealed significant deviations for the absolute cavity sizes and the expected trends as a function of the space demand of the side chains. Compared to a structure-based void analysis and PSDs derived from Monte Carlo force field simulations with nitrogen as the probe molecule, the pore sizes are underestimated by 10−15% for the OPs. By contrast, for the TPs, the pore sizes are overestimated by up to 40%. Additionally, the predicted trend for the distribution of the pore diameters induced by the side-chain disorder is not well-reflected within the Ar PSDs. The models used for predicting the pore dimensions were derived from the crystal structure data by positioning the side chains on one of the four possible positions of the bdc linkers. Afterward, geometry optimization was carried out using quantum mechanical calculations on the DFT level.

By contrast, we found the ^{129}Xe chemical shift analysis to be well-suited to track the local framework environment. After calibrating the limiting shift of CAU-1 with DFT calculations of the unfunctionalized framework, the downfield ^{129}Xe shifts for CAU-1-AmMe (14 ppm) and CAU-1-UrMe (16 ppm) could be used to predict the reduction of the accessible pore volume, which is on the same order of magnitude as for the results from the cavity plot method. Additionally, the change of the ^{129}Xe shift allowed to locate the excluded regions in the OPs suggesting that the side chains preferentially point into these voids for both cases. The measured chemical shifts were interpreted using quantum mechanical calculations by screening the accessible pore volume in a representative part of the unit cell. For this, a 3D grid with a step size of 0.5 Å was defined resulting in 781 calculations. As the Xe atoms move fast enough to ensure the fast motion limit, the ^{129}Xe shifts were calculated as an average using the Boltzmann factor for each position. By partitioning the grid points into octahedral and tetrahedral cavities, we could, furthermore, determine the occupation probabilities of a Xe atom in one of the two pores as a function of the temperature. As such, ^{129}Xe NMR spectroscopy enabled to develop a detailed fingerprint of the porosity and side-chain disorder for all three isoreticular CAU-1 frameworks. We expect that the strategy presented here can be commonly applied to disorder phenomena within MOFs in the future, in particular, if the data acquisition is combined with SEOP for hyperpolarizing the ^{129}Xe probe gas.

■ ASSOCIATED CONTENT

Supporting Information

The Supporting Information is available free of charge on the ACS Publications website at DOI: 10.1021/acs.langmuir.8b02592.

> PXRD pattern of CAU-1 species including simulated pattern; refinement of the PXRD pattern using the Pawley method; solid-state $^{13}C\{^{1}H\}$ NMR spectra; liquid-state ^{1}H NMR spectra of CAU-1 species; structural permutation of possible NH_2 positions; Ar physisorption experiments; Xe physisorption experiments; Xe loading of CAU-1; ^{129}Xe VT NMR spectra from 298 to 140 K; color-coded DFT-based energy and chemical shift for CAU-1; geometric pore assignment; and calculated pore occupation probabilities (PDF)

■ AUTHOR INFORMATION

Corresponding Author

*E-mail: juergen.senker@uni-bayreuth.de.

ORCID

Carsten B. L. Tschense: 0000-0002-8082-2244
Ernst A. Rössler: 0000-0001-5586-973X
Jürgen Senker: 0000-0002-7278-7952

Author Contributions

The manuscript was written through contributions of all authors. All authors have given approval to the final version of the manuscript.

Notes

The authors declare no competing financial interest.

■ ACKNOWLEDGMENTS

The authors thank Marco Schwarzmann for performing physisorption measurements and Beate Bojer and Renée Siegel for solid-state MAS NMR measurements. We gratefully thank Prof. Josef Breu for access to the gas sorption instruments. We thank the Deutsche Forschungsgemeinschaft for the funding of this work in the course of SFB 840 and SE 1417/8-1.

■ ABBREVIATIONS

bdc, benzyl dicarboxylate; BET, Brunauer−Emmett−Teller; BFGS, Broyden−Fletcher−Goldfarb−Shanno; CP, cross polarization; CF, continuous flow; DFT, density function theory; GIPAW, gauge including projector augmented wave; GGA, general gradient approximation; HP, hyperpolarized; MOF, metal−organic framework; NMR, nuclear magnetic resonance; OP, octahedral pore; PBE, Perdew−Burke−Ernzerhof; PSD, pore size distribution; PSM, postsynthetic modification; PXRD, powder X-ray diffraction; SEOP, spin exchange optical pumping; TP, tetrahedral pore; VT, variable temperature

■ REFERENCES

(1) Ma, S.; Zhou, H.-C. Gas storage in porous metal-organic frameworks for clean energy applications. *Chem. Commun.* **2010**, *46*, 44−53.

(2) Huang, S.-J.; Huh, S.; Lo, P.-S.; Liu, S.-H.; Lin, V. S.-Y.; Liu, S.-B. Hyperpolarized 129Xe NMR investigation of multifunctional organic/inorganic hybrid mesoporous silica materials. *Phys. Chem. Chem. Phys.* **2005**, *7*, 3080.

(3) Zhang, Q.; Uchaker, E.; Candelaria, S. L.; Cao, G. Nanomaterials for Energy Conversion and Storage. *Chem. Soc. Rev.* **2013**, *42*, 3127.

(4) Li, J.-R.; Kuppler, R. J.; Zhou, H.-C. Selective gas adsorption and separation in metal-organic frameworks. *Chem. Soc. Rev.* **2009**, *38*, 1477.

(5) Liebl, M. R.; Senker, J. Microporous Functionalized Triazine-Based Polyimides with High CO2 Capture Capacity. *Chem. Mater.* **2013**, *25*, 970−980.

(6) Phan, A.; Doonan, C. J.; Uribe-Romo, F. J.; Knobler, C. B.; O'Keeffe, M.; Yaghi, O. M. Synthesis, Structure, and Carbon Dioxide Capture Properties of Zeolitic Imidazolate Frameworks. *Acc. Chem. Res.* **2010**, *43*, 58−67.

(7) Sharma, V. K.; Feng, M. Water Depollution Using Metal-Organic Frameworks-Catalyzed Advanced Oxidation Processes: A Review. *J. Hazard. Mater.* **2017**, DOI: 10.1016/j.jhazmat.2017.09.043.

(8) Lee, A.; Elam, J. W.; Darling, S. B. Membrane Materials for Water Purification: Design, Development, and Application. *Environ. Sci.: Water Res. Technol.* **2016**, *2*, 17−42.

(9) Horcajada, P.; Serre, C.; Vallet-Regí, M.; Sebban, M.; Taulelle, F.; Férey, G. Metal-Organic Frameworks as Efficient Materials for Drug Delivery. *Angew. Chem., Int. Ed. Engl.* **2006**, *45*, 5974−5978.

(10) Horcajada, P.; Chalati, T.; Serre, C.; Gillet, B.; Sebrie, C.; Baati, T.; Eubank, J. F.; Heurtaux, D.; Clayette, P.; Kreuz, C.; Chang, J.-S.; Hwang, Y. K.; Marsaud, V.; Bories, P.-N.; Cynober, L.; Gil, S.; Férey, G.; Couvreur, P.; Gref, R. Porous metal-organic-framework nanoscale carriers as a potential platform for drug delivery and imaging. *Nat. Mater.* **2010**, *9*, 172−178.

(11) Gordon, J.; Kazemian, H.; Rohani, S. MIL-53(Fe), MIL-101, and SBA-15 Porous Materials: Potential Platforms for Drug Delivery. *Mater. Sci. Eng., C* **2015**, *47*, 172−179.

(12) Liang, J.; Liang, Z.; Zou, R.; Zhao, Y. Heterogeneous Catalysis in Zeolites, Mesoporous Silica, and Metal-Organic Frameworks. *Adv. Mater.* **2017**, *29*, 1701139.

(13) Hartmann, M.; Fischer, M. Amino-Functionalized Basic Catalysts with MIL-101 Structure. *Microporous Mesoporous Mater.* **2012**, *164*, 38−43.

(14) Férey, G. Hybrid Porous Solids: Past, Present, Future. *Chem. Soc. Rev.* **2007**, *37*, 191.

(15) Furukawa, H.; Cordova, K. E.; O'Keeffe, M.; Yaghi, O. M. The Chemistry and Applications of Metal-Organic Frameworks. *Science* **2013**, *341*, 1230444.

(16) Tanabe, K. K.; Cohen, S. M. Postsynthetic modification of metal-organic frameworks-a progress report. *Chem. Soc. Rev.* **2011**, *40*, 498−519.

(17) Wittmann, T.; Siegel, R.; Reimer, N.; Milius, W.; Stock, N.; Senker, J. Enhancing the Water Stability of Al-MIL-101-NH2via Postsynthetic Modification. *Chem.—Eur. J.* **2015**, *21*, 314−323.

(18) Banerjee, M.; Das, S.; Yoon, M.; Choi, H. J.; Hyun, M. H.; Park, S. M.; Seo, G.; Kim, K. Postsynthetic Modification Switches an Achiral Framework to Catalytically Active Homochiral Metal−Organic Porous Materials. *J. Am. Chem. Soc.* **2009**, *131*, 7524−7525.

(19) Kaye, S. S.; Dailly, A.; Yaghi, O. M.; Long, J. R. Impact of Preparation and Handling on the Hydrogen Storage Properties of Zn4O(1,4-benzenedicarboxylate)3(MOF-5). *J. Am. Chem. Soc.* **2007**, *129*, 14176−14177.

(20) Cavka, J. H.; Jakobsen, S.; Olsbye, U.; Guillou, N.; Lamberti, C.; Bordiga, S.; Lillerud, K. P. A New Zirconium Inorganic Building Brick Forming Metal Organic Frameworks with Exceptional Stability. *J. Am. Chem. Soc.* **2008**, *130*, 13850−13851.

(21) Loiseau, T.; Serre, C.; Huguenard, C.; Fink, G.; Taulelle, F.; Henry, M.; Bataille, T.; Férey, G. A Rationale for the Large Breathing of the Porous Aluminum Terephthalate (MIL-53) Upon Hydration. *Chem.—Eur. J.* **2004**, *10*, 1373−1382.

(22) Wittmann, T.; Mondal, A.; Tschense, C. B. L.; Wittmann, J. J.; Klimm, O.; Siegel, R.; Corzilius, B.; Weber, B.; Kaupp, M.; Senker, J. Probing Interactions of N-Donor Molecules with Open Metal Sites within Paramagnetic Cr-MIL-101: A Solid-State NMR Spectroscopic and Density Functional Theory Study. *J. Am. Chem. Soc.* **2018**, *140*, 2135−2144.

(23) Chui, S. S. A Chemically Functionalizable Nanoporous Material [Cu3(TMA)2(H2O)3]n. *Science* **1999**, *283*, 1148−1150.

(24) Horcajada, P.; Surblé, S.; Serre, C.; Hong, D.-Y.; Seo, Y.-K.; Chang, J.-S.; Grenèche, J.-M.; Margiolaki, I.; Férey, G. Synthesis and Catalytic Properties of MIL-100(Fe), an Iron(III) Carboxylate with Large Pores. *Chem. Commun.* **2007**, 2820−2822.

(25) Wang, T. C.; Bury, W.; Gómez-Gualdrón, D. A.; Vermeulen, N. A.; Mondloch, J. E.; Deria, P.; Zhang, K.; Moghadam, P. Z.; Sarjeant, A. A.; Snurr, R. Q.; Stoddart, J. F.; Hupp, J. T.; Farha, O. K. Ultrahigh Surface Area Zirconium MOFs and Insights into the Applicability of the BET Theory. *J. Am. Chem. Soc.* **2015**, *137*, 3585−3591.

(26) Sudik, A. C.; Côté, A. P.; Wong-Foy, A. G.; O'Keeffe, M.; Yaghi, O. M. A Metal-Organic Framework with a Hierarchical System of Pores and Tetrahedral Building Blocks. *Angew. Chem., Int. Ed.* **2006**, *45*, 2528−2533.

(27) Langmuir, I. The Adsorption Of Gases On Plane Surfaces Of Glass, Mica And Platinum. *J. Am. Chem. Soc.* **1918**, *40*, 1361−1403.

(28) Brunauer, S.; Emmett, P. H.; Teller, E. Adsorption of Gases in Multimolecular Layers. *J. Am. Chem. Soc.* **1938**, *60*, 309−319.

(29) Neimark, A. V.; Lin, Y.; Ravikovitch, P. I.; Thommes, M. Quenched Solid Density Functional Theory and Pore Size Analysis of Micro-Mesoporous Carbons. *Carbon* **2009**, *47*, 1617−1628.

(30) Ravikovitch, P. I.; Vishnyakov, A.; Russo, R.; Neimark, A. V. Unified Approach to Pore Size Characterization of Microporous Carbonaceous Materials from N2, Ar, and CO2Adsorption Isotherms. *Langmuir* **2000**, *16*, 2311−2320.

(31) Ravikovitch, P. I.; Neimark, A. V. Density Functional Theory of Adsorption in Spherical Cavities and Pore Size Characterization of Templated Nanoporous Silicas with Cubic and Three-Dimensional Hexagonal Structures. *Langmuir* **2002**, *18*, 1550−1560.

(32) Wang, L.-Q.; Wang, D.; Liu, J.; Exarhos, G. J.; Pawsey, S.; Moudrakovski, I. Probing Porosity and Pore Interconnectivity in Crystalline Mesoporous TiO2 Using Hyperpolarized 129Xe NMR. *J. Phys. Chem. C* **2009**, *113*, 6577−6583.

(33) Pawsey, S.; Kalebaila, K. K.; Moudrakovski, I.; Ripmeester, J. A.; Brock, S. L. Pore Structure and Interconnectivity of CdS Aerogels and Xerogels by Hyperpolarized Xenon NMR. *J. Phys. Chem. C* **2010**, *114*, 13187−13195.

(34) Weiland, E.; Springuel-Huet, M.-A.; Nossov, A.; Guenneau, F.; Quoineaud, A.-A.; Gédéon, A. Exploring the Complex Porosity of Transition Aluminas by 129Xe NMR Spectroscopy. *J. Phys. Chem. C* **2015**, *119*, 15285−15291.

(35) Anedda, R.; Soldatov, D. V.; Moudrakovski, I. L.; Casu, M.; Ripmeester, J. A. A New Approach to Characterizing Sorption in Materials with Flexible Micropores. *Chem. Mater.* **2008**, *20*, 2908−2920.

(36) Meersmann, T.; Logan, J. W.; Simonutti, R.; Caldarelli, S.; Comotti, A.; Sozzani, P.; Kaiser, L. G.; Pines, A. Exploring Single-File Diffusion in One-Dimensional Nanochannels by Laser-Polarized129Xe NMR Spectroscopy. *J. Phys. Chem. A* **2000**, *104*, 11665−11670.

(37) Springuel-Huet, M. A.; Fraissard, J. 129Xe NMR of Xenon Adsorbed on the Molecular Sieves AlPO4-11 and SAPO-11. Chemical Shift Anisotropy Related to the Asymmetry of the Adsorption Zones. *Chem. Phys. Lett.* **1989**, *154*, 299−302.

(38) Oschatz, M.; Hoffmann, H. C.; Pallmann, J.; Schaber, J.; Borchardt, L.; Nickel, W.; Senkovska, I.; Rico-Francés, S.; Silvestre-Albero, J.; Kaskel, S.; Brunner, E. Structural Characterization of Micro- and Mesoporous Carbon Materials Using In Situ High Pressure 129Xe NMR Spectroscopy. *Chem. Mater.* **2014**, *26*, 3280−3288.

(39) Fraissard, J. Microporous Materials and Xenon-129 NMR. *Encyclopedia of Magnetic Resonance*; John Wiley & Sons, Ltd: Chichester, U.K., 2007.

(40) Brunner, E. Applications of laser-polarized129Xe under continuous flow. *Magn. Reson. Chem.* **1999**, *37*, S14−S22.

(41) Cros, F.; Korb, J.-P.; Malier, L. Spectroscopic Mesopore Size Characterization and Diffusion Measurement in Closed Porosity by Xenon NMR. *Langmuir* **2000**, *16*, 10193−10197.

(42) Moudrakovski, I. L.; Lang, S.; Ratcliffe, C. I.; Simard, B.; Santyr, G.; Ripmeester, J. A. Chemical Shift Imaging with Continuously Flowing Hyperpolarized Xenon for the Characterization of Materials. *J. Magn. Reson.* **2000**, *144*, 372−377.

(43) Ruset, I. C.; Ketel, S.; Hersman, F. W. Optical Pumping System Design for Large Production of Hyperpolarized ^{129}Xe. *Phys. Rev. Lett.* **2006**, *96*, 053002.

(44) Guo, Q.; Chen, C.; Zhou, L.; Li, X.; Li, Z.; Yuan, D.; Ding, J.; Wan, H.; Guan, G. Design of ZIF-8/Ion Copolymer Hierarchically Porous Material: Coordination Effect on the Adsorption and Diffusion for Carbon Dioxide. *Microporous Mesoporous Mater.* **2018**, *261*, 79−87.

(45) Springuel-Huet, M.-A.; Nossov, A.; Guenneau, F.; Gédéon, A. Flexibility of ZIF-8 materials studied using 129Xe NMR. *Chem. Commun.* **2013**, *49*, 7403.

(46) Bhunia, A.; Boldog, I.; Möller, A.; Janiak, C. Highly Stable Nanoporous Covalent Triazine-Based Frameworks with an Adamantane Core for Carbon Dioxide Sorption and Separation. *J. Mater. Chem. A* **2013**, *1*, 14990.

(47) Demarquay, J.; Fraissard, J. 129Xe NMR of Xenon Adsorbed on Zeolites. *Chem. Phys. Lett.* **1987**, *136*, 314−318.

(48) Keenan, C. D.; Herling, M. M.; Siegel, R.; Petzold, N.; Bowers, C. R.; Rössler, E. A.; Breu, J.; Senker, J. Porosity of Pillared Clays Studied by Hyperpolarized 129Xe NMR Spectroscopy and Xe Adsorption Isotherms. *Langmuir* **2013**, *29*, 643−652.

(49) Terskikh, V. V.; Moudrakovski, I. L.; Breeze, S. R.; Lang, S.; Ratcliffe, C. I.; Ripmeester, J. A.; Sayari, A. A General Correlation for the129Xe NMR Chemical Shift−Pore Size Relationship in Porous Silica-Based Materials. *Langmuir* **2002**, *18*, 5653−5656.

(50) Ooms, K. J.; Wasylishen, R. E. 129Xe NMR study of xenon in iso-reticular metal-organic frameworks. *Microporous Mesoporous Mater.* **2007**, *103*, 341−351.

(51) Boutin, A.; Springuel-Huet, M.-A.; Nossov, A.; Gédéon, A.; Loiseau, T.; Volkringer, C.; Férey, G.; Coudert, F.-X.; Fuchs, A. H. Breathing Transitions in MIL-53(Al) Metal-Organic Framework Upon Xenon Adsorption. *Angew. Chem., Int. Ed.* **2009**, *48*, 8314−8317.

(52) Trepte, K.; Schaber, J.; Schwalbe, S.; Drache, F.; Senkovska, I.; Kaskel, S.; Kortus, J.; Brunner, E.; Seifert, G. The Origin of the Measured Chemical Shift of ^{129}Xe in UiO-66 and UiO-67 Revealed by DFT Investigations. *Phys. Chem. Chem. Phys.* **2017**, *19*, 10020−10027.

(53) Jameson, C. J.; de Dios, A. C. Xe Nuclear Magnetic Resonance Line Shapes in Nanochannels. *J. Chem. Phys.* **2002**, *116*, 3805−3821.

(54) Ahnfeldt, T.; Guillou, N.; Gunzelmann, D.; Margiolaki, I.; Loiseau, T.; Férey, G.; Senker, J.; Stock, N. [Al4(OH)2(OCH3)4-(H2N-bdc)3]·x H2O: A 12-Connected Porous Metal-Organic Framework with an Unprecedented Aluminum-Containing Brick. *Angew. Chem., Int. Ed.* **2009**, *48*, 5163−5166.

(55) Fung, B. M.; Khitrin, A. K.; Ermolaev, K. An Improved Broadband Decoupling Sequence for Liquid Crystals and Solids. *J. Magn. Reson.* **2000**, *142*, 97−101.

(56) Clark, S. J.; Segall, M. D.; Pickard, C. J.; Hasnip, P. J.; Probert, M. I. J.; Refson, K.; Payne, M. C. First Principles Methods Using CASTEP. *Z Kristallogr Cryst Mater.* **2005**, *220*, 567−570.

(57) Grimme, S. Semiempirical GGA-Type Density Functional Constructed with a Long-Range Dispersion Correction. *J. Comput. Chem.* **2006**, *27*, 1787−1799.

(58) McNellis, E. R.; Meyer, J.; Reuter, K. Azobenzene at Coinage Metal Surfaces: Role of Dispersive van Der Waals Interactions. *Phys. Rev. B* **2009**, *80*, 205414.

(59) Yates, J. R.; Pickard, C. J.; Mauri, F. Calculation of NMR Chemical Shifts for Extended Systems Using Ultrasoft Pseudopotentials. *Phys. Rev. B* **2007**, *76*, 024401.

(60) Pickard, C. J.; Mauri, F. All-Electron Magnetic Response with Pseudopotentials: NMR Chemical Shifts. *Phys. Rev. B* **2001**, *63*, 245101.

(61) Spek, A. L. Structure Validation in Chemical Crystallography. *Acta Crystallogr., Sect. D: Biol. Crystallogr.* **2009**, *65*, 148−155.

(62) Rappe, A. K.; Casewit, C. J.; Colwell, K. S.; Goddard, W. A.; Skiff, W. M. UFF, a Full Periodic Table Force Field for Molecular Mechanics and Molecular Dynamics Simulations. *J. Am. Chem. Soc.* **1992**, *114*, 10024−10035.

(63) Sarkisov, L.; Harrison, A. Computational Structure Characterisation Tools in Application to Ordered and Disordered Porous Materials. *Mol. Simul.* **2011**, *37*, 1248−1257.

(64) Springuel-Huet, M.; Demarquay, J.; Ito, T.; Fraissard, J. 129Xe-NMR of Xenon Adsorbed on Zeolites: Determination of the Dimensions of the Void Space from the Chemical Shift δdL(129Xe). *Stud. Surf. Sci. Catal.* **1988**, *37*, 183−189.

(65) Damron, J. T.; Ma, J.; Kurz, R.; Saalwächter, K.; Matzger, A. J.; Ramamoorthy, A. The Influence of Chemical Modification on Linker Rotational Dynamics in Metal-Organic Frameworks. *Angew. Chem., Int. Ed.* **2018**, *57*, 8678−8681.

(66) Komulainen, S.; Roukala, J.; Zhivonitko, V. V.; Javed, M. A.; Chen, L.; Holden, D.; Hasell, T.; Cooper, A.; Lantto, P.; Telkki, V.-V. Inside Information on Xenon Adsorption in Porous Organic Cages by NMR. *Chem. Sci.* **2017**, *8*, 5721−5727.

(67) Selent, M.; Nyman, J.; Roukala, J.; Ilczyszyn, M.; Oilunkaniemi, R.; Bygrave, P. J.; Laitinen, R.; Jokisaari, J.; Day, G. M.; Lantto, P. Clathrate Structure Determination by Combining Crystal Structure Prediction with Computational and Experimental 129 Xe NMR Spectroscopy. *Chem.—Eur. J.* **2017**, *23*, 5258−5269.

(68) Lenthe, E.; Baerends, E. J.; Snijders, J. G. Relativistic regular two-component Hamiltonians. *J. Chem. Phys.* **1993**, *99*, 4597−4610.

DOI: 10.1021/acs.langmuir.8b02592
Langmuir 2018, 34, 12538−12548

Supporting Information of

Exploring local disorder within CAU-1 frameworks using hyperpolarized ^{129}Xe NMR spectroscopy

Tobias W. Kemnitzer[†], *Carsten B. L. Tschense*[†], *Thomas Wittmann*[†], *Ernst A. Rössler*[‡], *Jürgen Senker*[†]*

[†]Inorganic Chemistry III, University of Bayreuth, 95447 Bayreuth, Germany

[‡]Experimental Physics II, University of Bayreuth, 95447 Bayreuth, Germany

* juergen.senker@uni-bayreuth.de

The supporting information contains:
16 pages
18 Figures

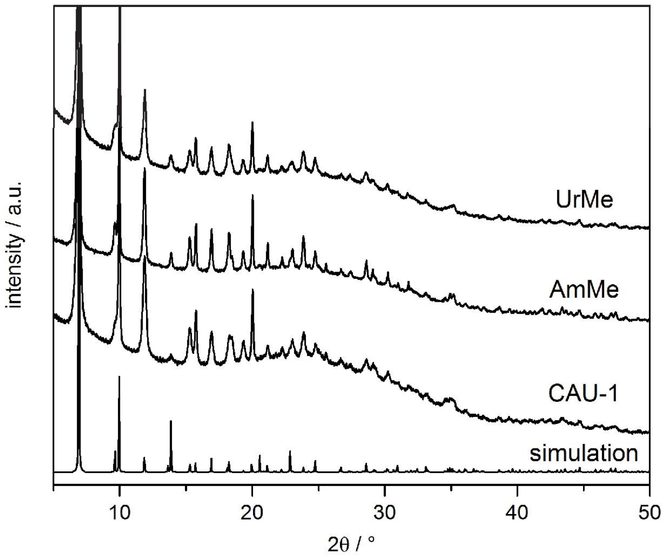

Figure S1. Measured PXRDs for all CAU-1 derivatives. For comparison a simulated pattern using the reference structure of CAU-1 was added.

A complete structure solution of the modified structures via Rietveld refinement is not possible because of the high disorder and statistic distribution of the functional groups within the crystal structure. Therefore, the diffractogramms were fitted with the Pawley-method considering the lattice constants of the literature structure.

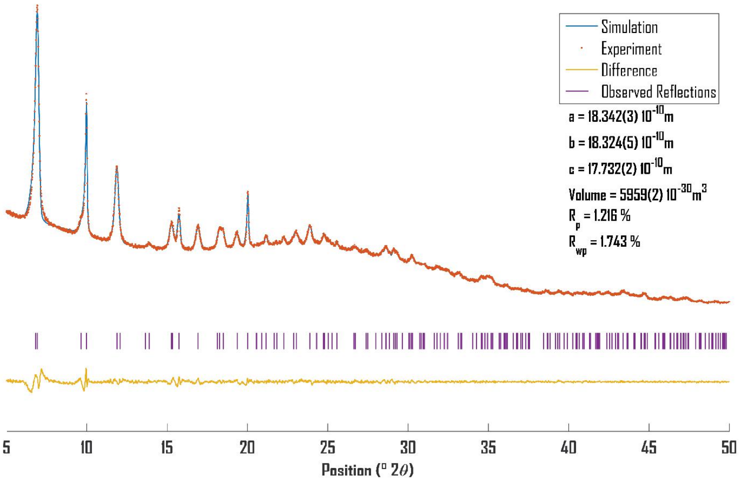

Figure S2. PXRD and corresponding Pawley fit of CAU-1.

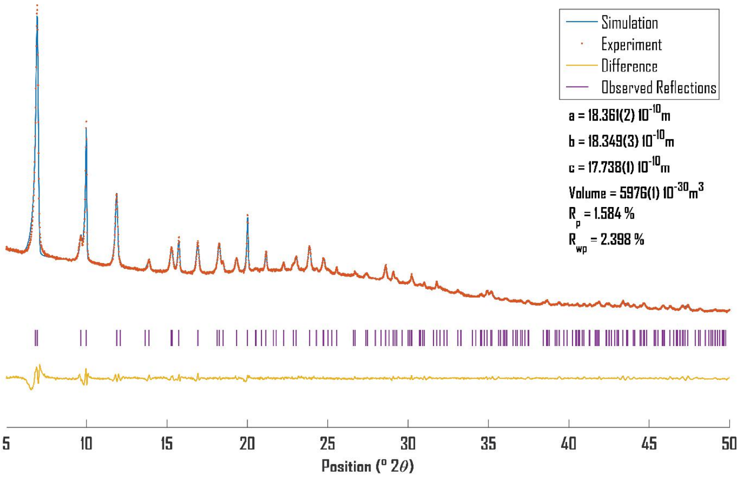

Figure S3. PXRD and corresponding Pawley fit of CAU-1-AmMe.

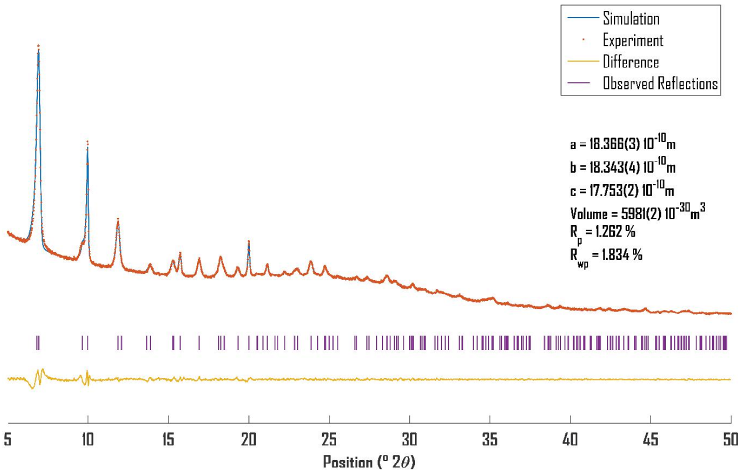

Figure S4. PXRD and corresponding Pawley fit of CAU-1-UrMe.

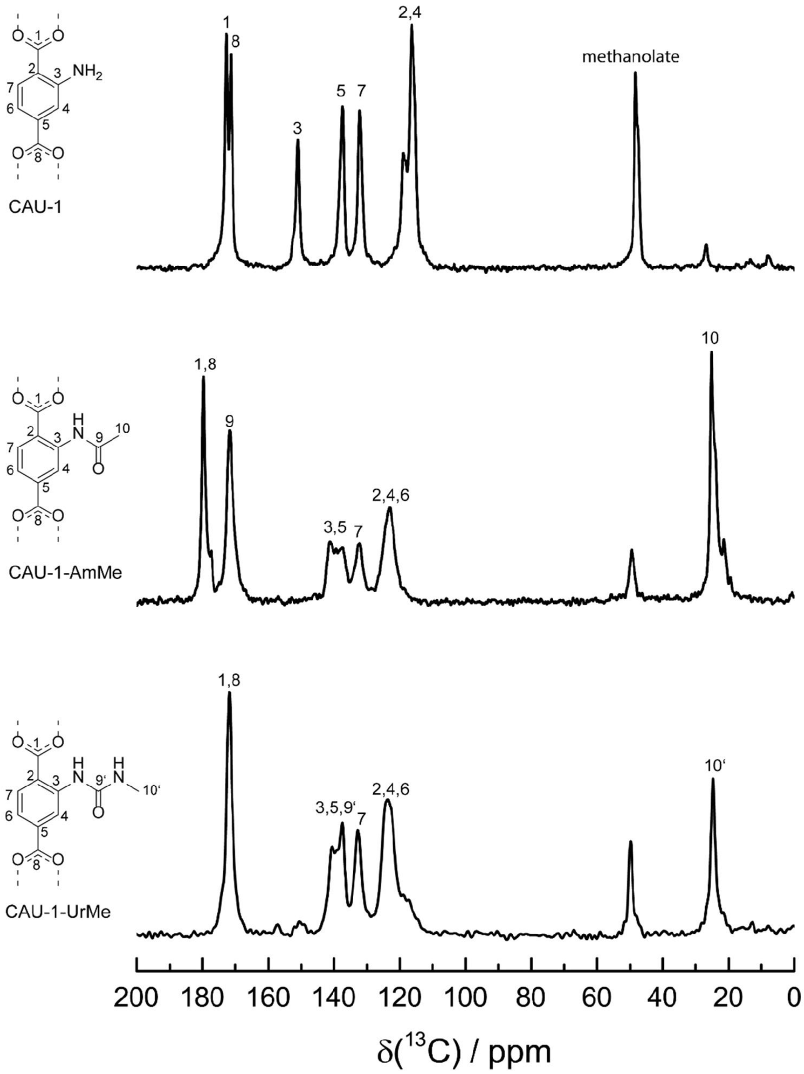

Figure S5. Solid state ^{13}C MAS NMR spectra.

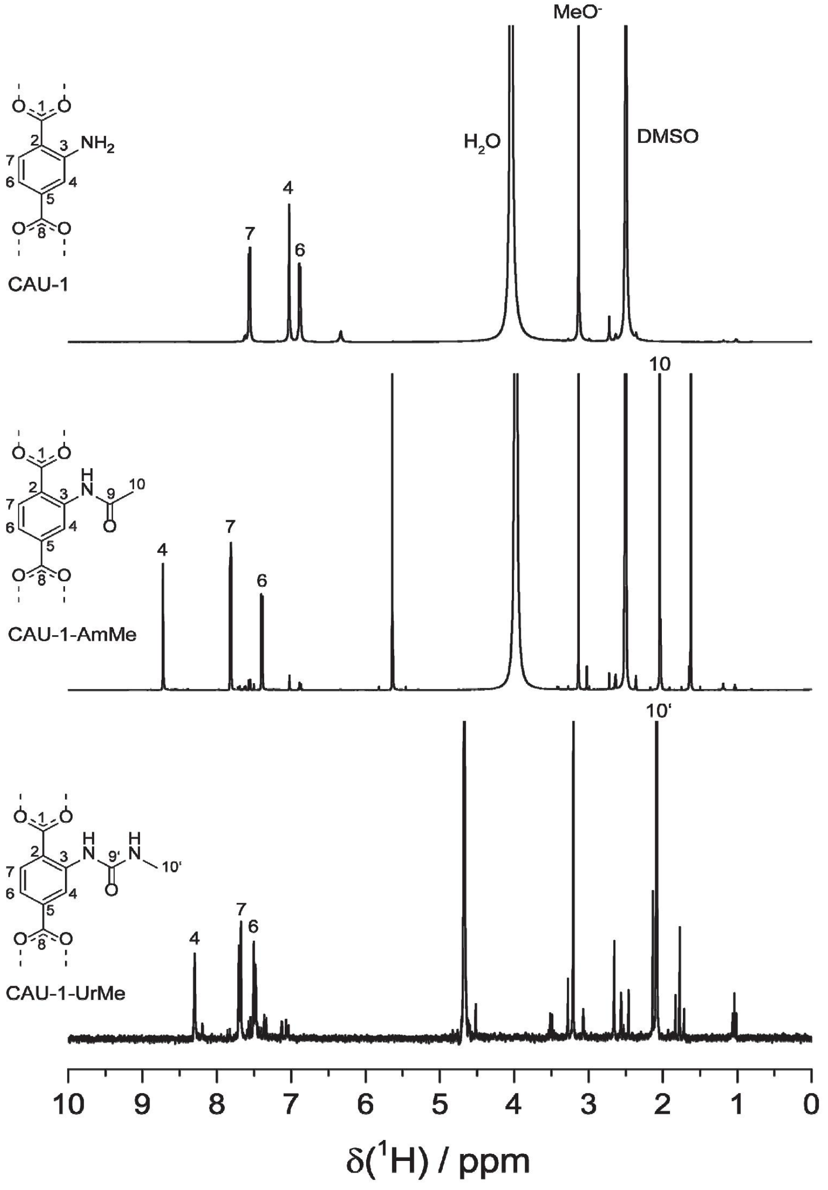

Figure S6. Liquid state ^1H NMR spectra.

In order to obtain pore sizes out of the crystal structure of CAU-1 a number of different models were created concerning the position and orientation of the NH_2-groups. Due to the alignment of the individual linkers the side groups point either into the octahedral or the tetrahedral pores.

The linker molecules placed on the cell edges at c = 0 / c = 1 (Figure 1, Figure S7) as well as the ones penetrating the middle of the a- and b-faces of the unit cell (at c = ½) connected to the central Al 8-rings are assigned to the octahedral pore. Due to the space symmetry only four possible configurations with an overall number of two octahedra per unit cell are possible as it can be seen in the Figures S7 and 2A.

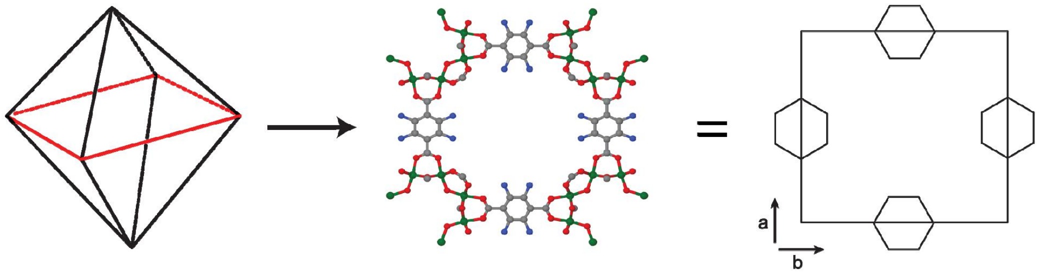

Figure S7. Schematic representation of the bdc units and NH_2-positions relevant for the octahedral pore. Each line of the octahedron represents one bdc unit.

All bdc units are also part of the tetrahedral pores and are represented as the edges of a tetrahedron. All bdc molecules, which are not part of the basal plane of the octahedron (black lines Figure S7) will be assigned to the tetrahedral pore since their NH_2-groups are pointing into them.

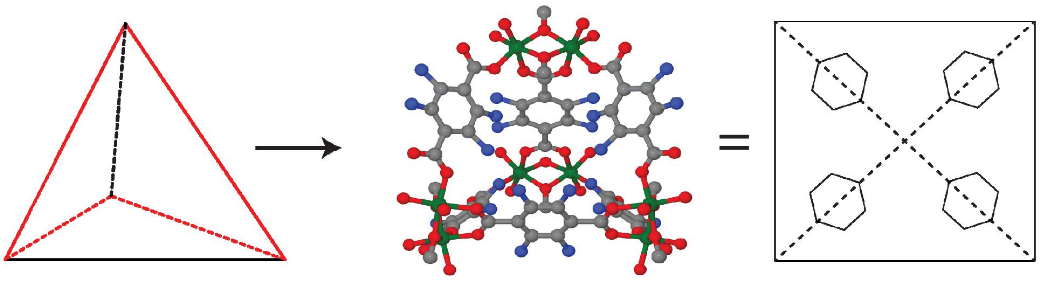

Figure S8. Schematic representation of the bdc units relevant for the tetrahedral pore. The relevant positions are shown by benzyl rings in top view of the unit cell.

Taking all possible positions into account an overall number of 256 combinations are possible reduced to a number of 55 due to the symmetry. These 55 models are shown in Figure S9. This constellation of linkers exists two times within the unit cell. On from c = 0 – ½ and c = ½ - 1.

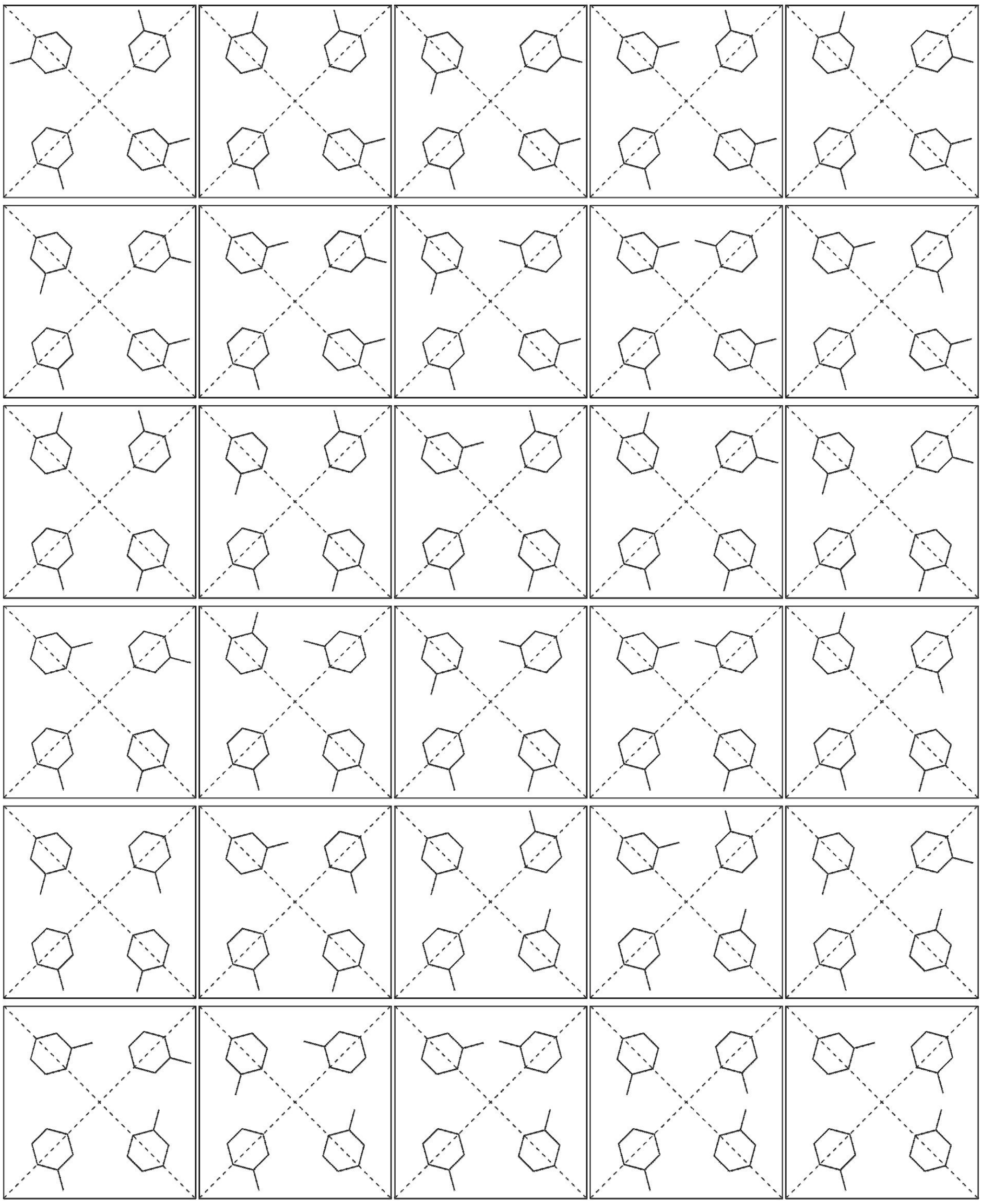

S.9

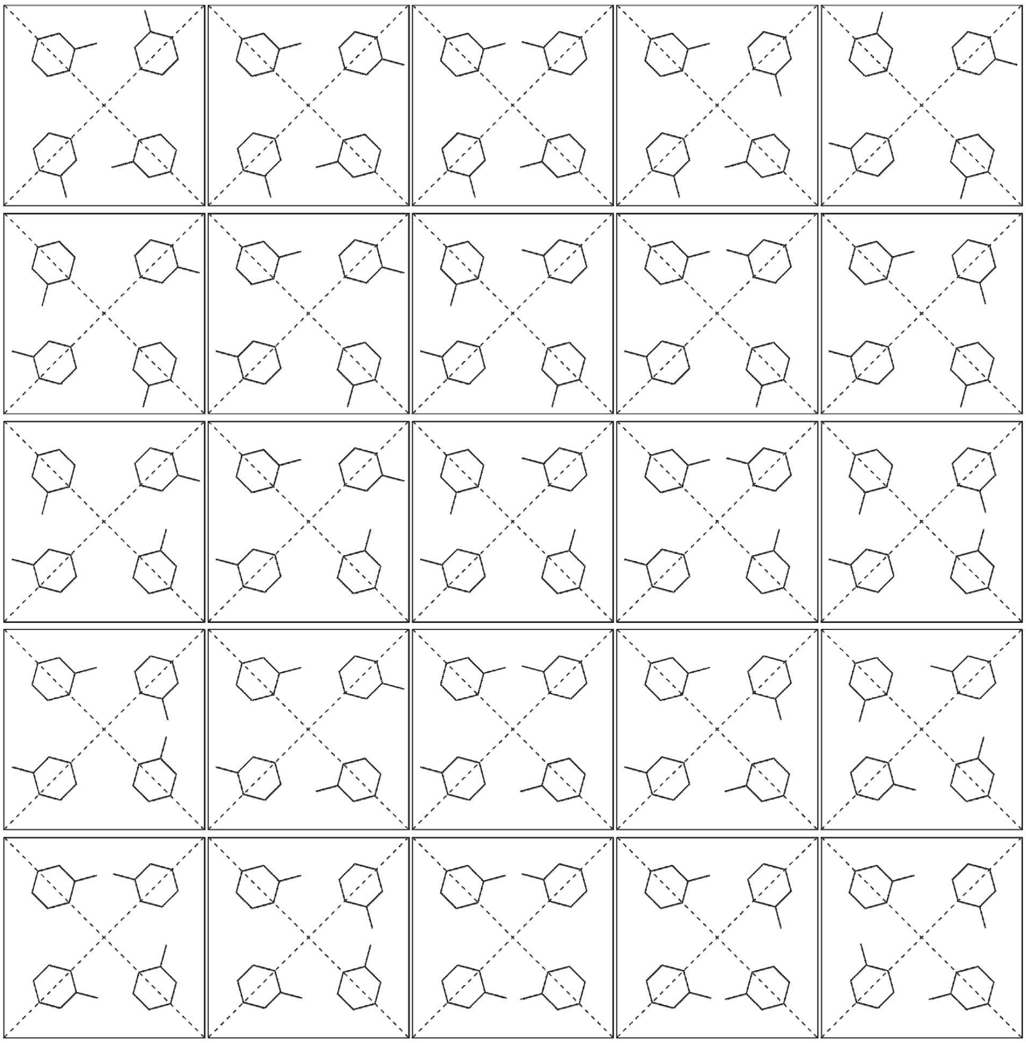

Figure S9. Overview of all possible anchor group positions pointing into the tetrahedral pore.

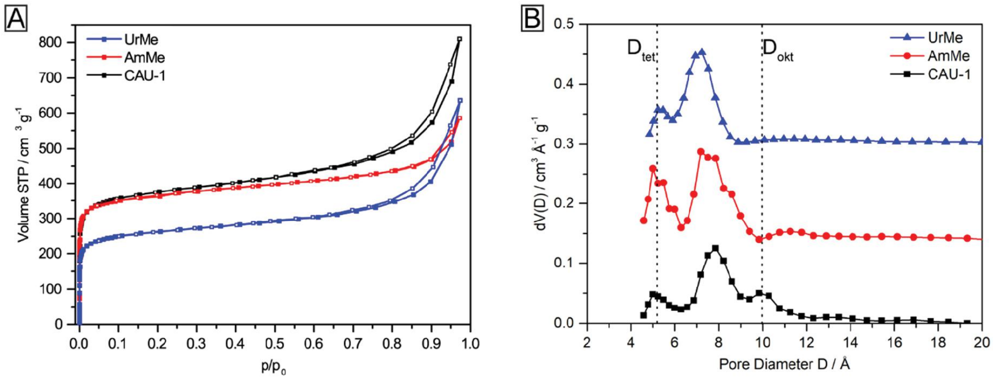

Figure S10. A: Ar adsorption isotherms for all samples at 87.35 K. B: Pore size distribution of all samples obtained from a NLDFT kernel for carbon slit pores. The datasets of CAU-1 derivatives AmMe and UrMe were plotted with a vertical offset of 0.14 and 0.30, respectively. Black dotted lines indicate the average pore sizes for the tetrahedral (left) and octahedral pore (right) of CAU-1.

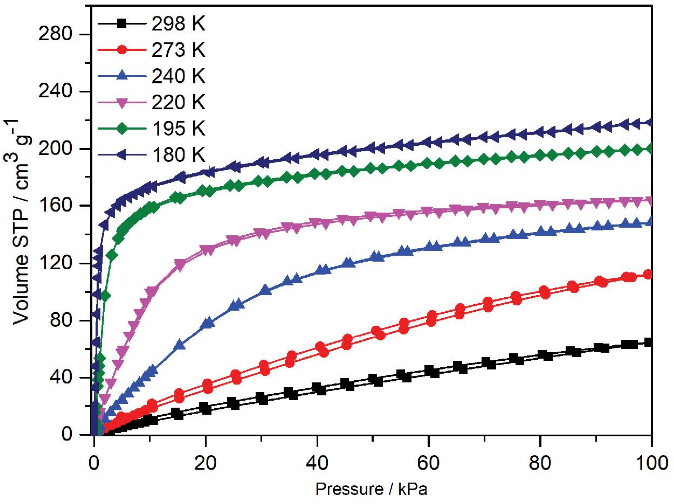

Figure S11. Xe physisorption experiments of CAU-1 at different temperatures.

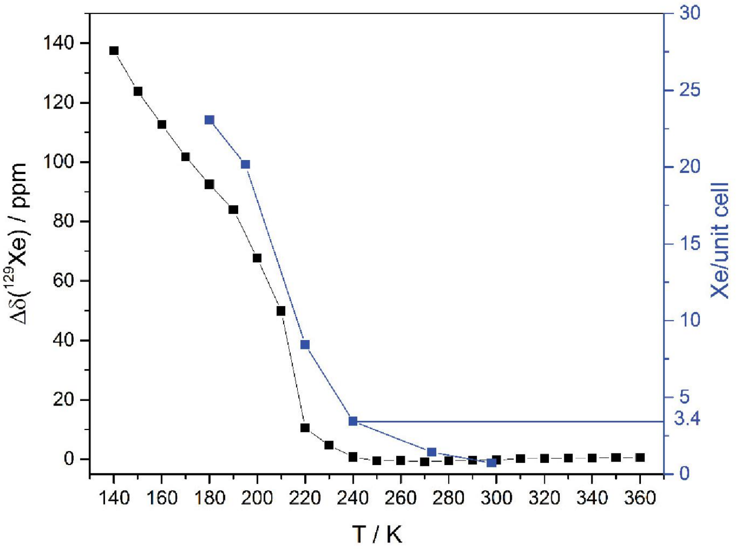

Figure S12. Comparison between temperature dependent ^{129}Xe chemical shift and Xe adsorption for CAU-1. The chemical shift represents the difference between experimental and calculated values.

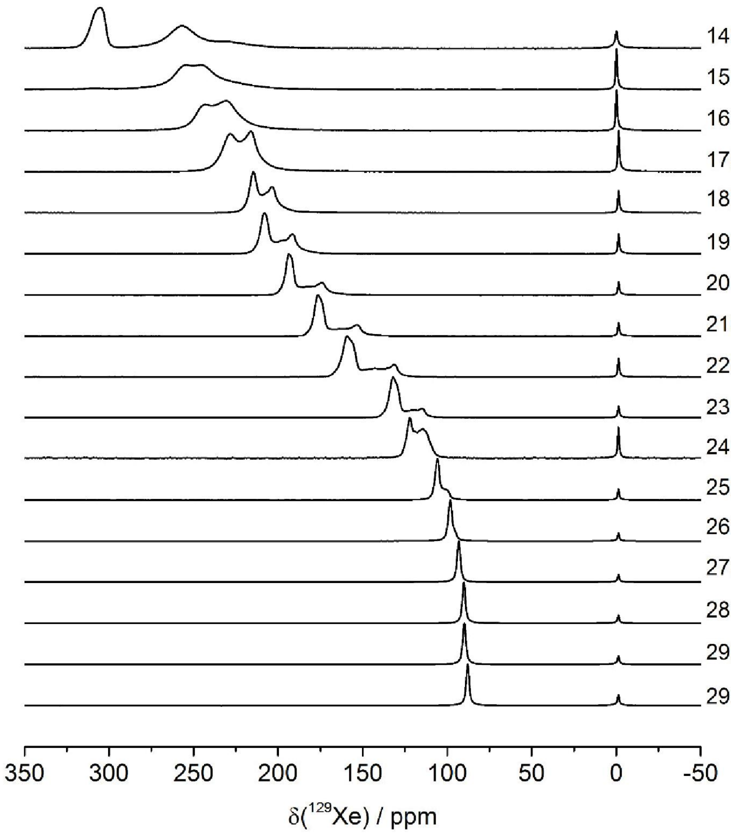

Figure S13. ^{129}Xe VT-NMR spectra of CAU-1-AmMe.

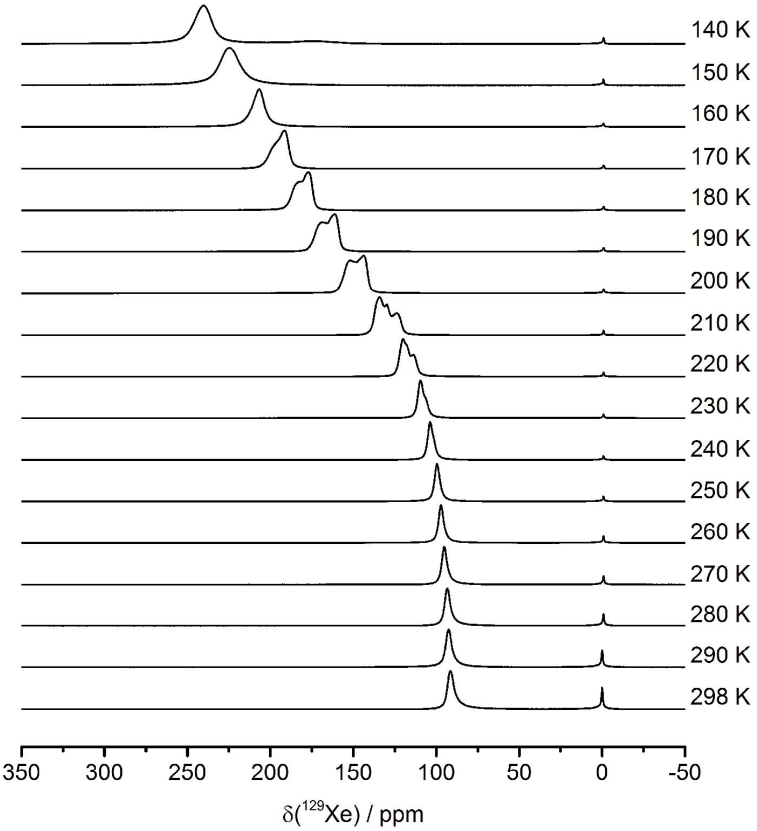

Figure S14. ^{129}Xe VT-NMR spectra of CAU-1-UrMe.

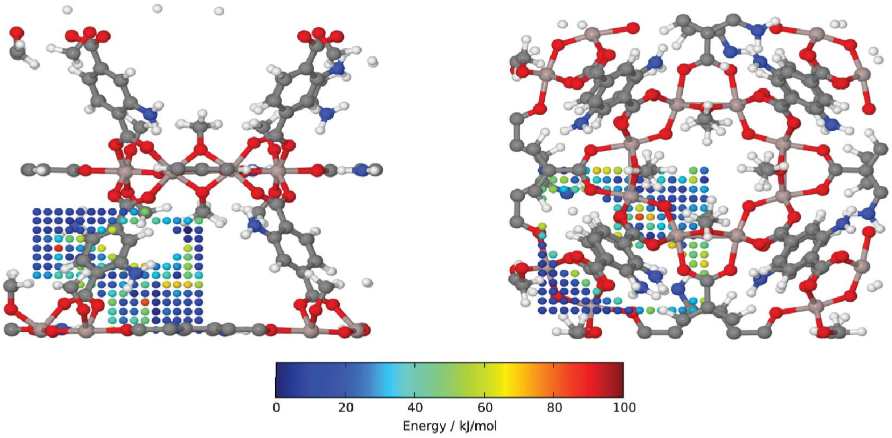

Figure S15. Mapping of calculated energy for each Xe position in CAU-1.

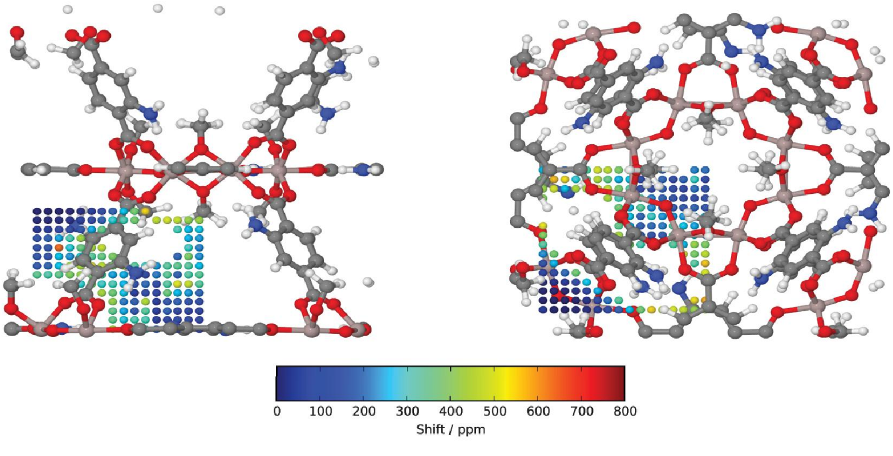

Figure S16. Mapping of calculated chemical ^{129}Xe shifts for each Xe position in CAU-1.

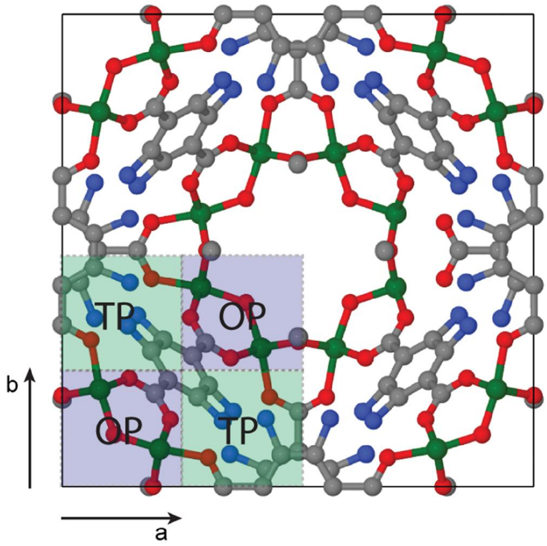

Figure S17. Assignment for Xe positions to the octahedral pore (OP) or the tetrahedral pore (TP) in dependence of the atomic coordinates in a/b-direction.

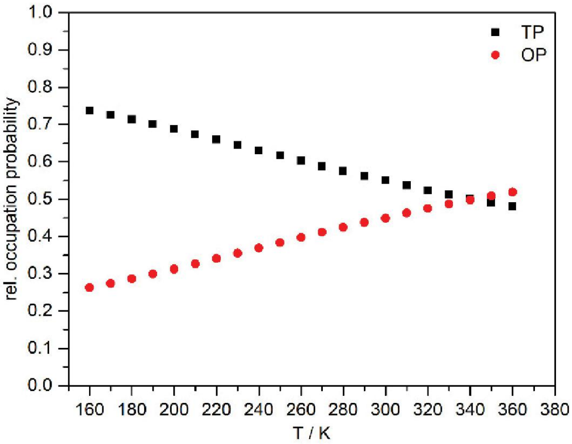

Figure S18. Calculated occupation probability for tetrahedral pores (TP) and octahedral pores (OP) relative to each other as a function of temperature.

S.16

5.4. Probing the Structural Bi-stability during Gate-Opening of MIL-53(Al) via Hyperpolarized ^{129}Xe and Chemical Modelling

T. W. Kemnitzer,[a] C. D. Keenan, [b] R. Siegel, [a] E. A. Rössler[c] und J. Senker[a]*

to be submitted

[a] Department of Inorganic Chemistry III, University of Bayreuth, Universitätsstr. 30, 95447 Bayreuth (Germany)

[b] Department of Chemistry and Biochemistry, Carson-Newman University, Jefferson City, Tennessee 37760 (United States of America)

[c] Department of Experimental Physics II, University of Bayreuth, Universitätsstr. 30, 95447 Bayreuth (Germany)

* juergen.senker@uni-bayreuth.de

Probing the Structural Bi-stability during Gate-Opening of MIL-53(Al) via Hyperpolarized ^{129}Xe and Chemical Modelling

Tobias W. Kemnitzer,[†] Caroline D. Keenan,[‡] Renee Siegel,[†] Ernst Roessler,[§] and Juergen Senker[†]

[‡]Department of Chemistry, Carson-Newman University, Jefferson City, Tennessee 37760, USA

[†]Inorganic Chemistry III, Universität Bayreuth, Bayreuth 95447, Germany

[§]Experimental Physics II, Universität Bayreuth, Bayreuth 95447, Germany

KEYWORDS . metal-organic frameworks, MIL-53, breathing, sorption, xenon, hyperpolarization, chemical shift simulations.

ABSTRACT: The adsorption-induced, reversible breathing of the MIL-53 family of MOFs is known to lead to structural transformations that are accompanied by large changes in both the internal pore and the unit cell volumes which are both guest and temperature dependent. While the adsorption behavior is well characterized by isotherm data for small molecules such as H2O, CO2, CH4 and Xe, little is understood about the microscopic mechanisms of the phase transition responsible for the seemingly bi-stable behavior of the large and narrow pore structures at intermediate guest loading. Here we use continuous-flow hyperpolarized ^{129}Xe NMR methods paired with solid-state 27Al NMR spectroscopy to elucidate underlying features of the guest-induced structural changes with Xe adsorption. Based on 1D ^{129}Xe wideline and MAS NMR spectra we could follow the phase behavior of MIL-53(Al) over a broad temperature range. Lineshape analyses based on results of quantum mechanical simulations demonstrate the formation of Xe pairs and small clusters in the narrow pore structure with increasing Xe uptake. The life-time of these objects is long on the NMR time scale, on the order of a few ms. Here, 2D 129Xe EXSY measurements were performed to investigate the interconnectivity of coexisting large and narrow pore structures within the bi-stability regime, providing a detailed look at Xe chemical exchange processes at various loadings. Under similar conditions, the exchange from the bulk gas to the narrow pores is slowed down by at least one order of magnitude. The chronology of Xe adsorption and diffusion processes suggests a phase transformation mechanism where narrow pore structures are protected by their large pore counterparts. The Al-metal centers are also probed at various guest loading using 27Al NMR QCPMG methods in tandem with variable pressure ^{129}Xe NMR measurements to provide insight into the evolution of Xe's lineshape with changing morphology and loading.

1. INTRODUCTION

Metal organic frameworks (MOFs) belong to an emerging class of crystalline hybrid materials known for their high surface areas, permanent porosity, ion mobility as well as exchange ability and large adsorption capacity for small molecules.[1–5] Considered metal-organic analogs of zeolites, their molecular architecture is constructed of metal ions (or clusters) coordinated to organic building blocks in two or three dimensions. The primary advantage of these hybrid materials over zeolites is the possibility of chemical modification[6–12] of the organic moieties responsible for the networks dimensionality, functionality and reactivity.[13–15] The potential for controlled synthetic changes at the surface on the molecular level offers promising advances for the development of MOFs, expanding their potential applications to biomedical[16–18] and industrial[19–24] use like drug delivery[25,26], gas storage[27,28], separation[29–31], and catalysis[32,33].

In terms of tuneability, flexible MOFs are most intriguing since their morphology responds to external stimuli such as temperature and pressure.[34–36] Such behavior has been shown to be reversible and adaptive to both the size and shape of the guest molecules—distinctive features of the "breathing" or the "gate-opening" phenomena[37–44] The Mil-53 class of flexible MOFs is one of the most well studied third generation structures owing to its ability to maintain a highly ordered structure throughout the dynamic structural modifications associated with the breathing effect.[38,39,45–49] Tethered together by benzenedicarboxylate (BDC) ligands, the trivalent metal (M) centers of the MIL-53 (M = Al^{3+}, Cr^{3+}, Fe^{3+}, Ga^{3+}) network forms a three dimensional arrangement of square- shaped channels in the absence of guest molecules, in a large pore (LP) conformation. The onset of a distorted, narrower pore (NP) structure is triggered by exposure to external stimuli such as gas adsorption,[46,50] temperature,[45] forming a rhombus-shaped network of channels. Further elevation in stress, be it mechanical,[51] thermal, or steric in nature, eventually leads to the reopening of the framework back to the LP state.[36,39,46,52] According to the stress model derived by Boutin et al. MIL-53 changes from the LP (V ≈ 1500Å^3) to the NP (V ≈ 1000Å^3) and back to the LP phase during guest adsorption resulting in an increase in the guest-adsorption capacity and producing multi-step shaped adsorption profiles that can be initiated by a wide variety of adsorbents.[52,53] The most notable adsorption induced change of Mil-53 structure beside water[39,48] was shown by the Ferey group on the co-adsorption of CO_2/CH_4 binary mixtures truly highlight the potential utility of the flexible MOFs in the gas storage/separations industry.[46,54] CO_2 is preferably adsorbed within the NP form while CH_4 does not enter this form.

While guest-responsive selectivity by flexible MOFs is not uncommon—bi-stabilitiy is. Remarkably, this specific LP → NP structural conversion is progressive in nature; both LP and NP forms may coexist as thermodynamically stable structures. Computational work by Ghysels et al.[36] has shown that the relative extent of guest-induced deformation within MIL-53 is subject to size, shape and the dynamics of the guest species as well as to the host-guest interactions within the framework. To further complicate matters, the degree to which guest-guest interactions become a relevant factor to the transition mechanism increases with loading. As such, both guest-guest and guest-host interactions contribute to the adsorption energy in MIL-53. Such thermodynamic approaches, however, do not provide information about the phase transition mechanism. In analogy to a first order phase transition it is debated that the NP phase, and upon reopening the LP phase, nucleates and growths resulting in a spatially inhomogeneous model where crystallites of both phases coexist. In contrast the stress model of Triguero et al. considers shear forces on individual crystals to be the main driving force for the phase transition.[55] They allow to switch whole domains from LP to NP forms or vice versa within each crystallite resulting in a spatially homogeneous mechanism.

Using conventional crystallographic modelling, this model cannot be proved since only small growing domains within the crystallites will build-up and the coherence length of diffraction methods are not able to resolve such effects. Therefore, methods to analyze the local structure on a microscopic scale has to be used. A prominent example for this application is the use of hyperpolarized ^{129}Xe NMR spectroscopy. Hyperpolarized (HP) methods via spin exchange optical pumping (SEOP) enable pore characterization studies and allow for the monitoring of inter-pore and inter-particle diffusion. The heightened sensitivity afforded to ^{129}Xe nuclei by SEOP allows for measurements to be performed at very low Xe densities, effectively minimizing contributions of guest-guest interactions to the observed chemical shift (CS) and enabling the study of surface properties with changing environmental conditions.

In this work, we focus our efforts on elucidating the origins of the LP/NP structural bi-stability within the MIL-53(Al) framework using hyperpolarized ^{129}Xe NMR spectroscopy in combination with in-situ ^{27}Al solid-state NMR and quantum mechanical calculations. Expanding on work previously done by Springuel-Huet[56] and Giovine et al.[57], we use continuous-flow (CF) HP ^{129}Xe 2D exchange spectroscopy (EXSY) to probe the interconnectivity of the coexisting LP/NP states at intermediary loading and employ variable temperature (VT) CF-HP ^{129}Xe magic angle spinning (MAS) to suppress broadening introduced by the chemical shift anisotropy (CSA) in order to gain insight into the potential environmental factors leading to the closing and reopening mechanism of the MIL-53(Al) framework. Using ab-initio calculations the ^{129}Xe NMR spectra were modeled to understand the local arrangement of Xe atoms within the pores under consideration of the gas loading obtained from physisorption experiments. Furthermore, static ^{27}Al solid-state NMR is measured using QCPMG methods to monitor the structural integrity of the Al metal centers and thus the framework during various stages of the adsorption-induced structural.

2. EXPERIMENTAL METHODS

Materials. Mil-53(Al) was produced according to a synthesis route published by Loiseau et al.[39] The activation of the raw material was performed via solvent exchange with repetitive heating with methanol in an autoclave, allowing for any excess bdc molecules remaining within the pores to be replaced with methanol. Afterward, the sample was heated to 110 °C and placed under high vacuum for approximately 12 hours to ensure complete desolvation of methanol. The resulting material was found to be highly crystalline and phase pure as indicated by powder X-ray diffraction (Figure S1), TGA, elemental analysis and solid-state NMR spectroscopy (Figure S2). Further handling and sample preparation were strictly carried out in dry argon atmosphere in a glove box.

Powder X-ray diffraction. The PXRD data were acquired on a STOE Stadi P powder diffractometer equipped with a curved germanium monochromator (oriented according to the (111) plane) creating $CuK_{\alpha1}$ radiation (λ = 1.5406 Å). The samples were filled in a 0.7 mm capillary tube and measured in Debye-Scherrer geometry. The powder pattern was fully handled using the commercial program package Accelrys MS Modeling (version 5.0). All atomic positions were taken from ref. 31 and then optimised during refinement. To reduce the degrees of freedom the benzene rings of bdc linkers were combined in one motion group.

CF-HP ^{129}Xe NMR Spectroscopy. All hyperpolarized ^{129}Xe NMR experiments were performed using a home built SEOP device constructed at the University of Bayreuth. A premixed gas composition of 1% Xe, 2% N_2 and 97% He (by vol.) was utilized for all measurements. The gas mixture was polarized using 15-60 W of laser diode array power (Coherent Inc.) tuned to a wavelength of 794.8 nm (Rb D_1 line). While an absolute pressure of 6.2 bar was maintained within the pumping cell throughout. 1D CF-HP ^{129}Xe NMR spectra were measured at an average flow-rate of 300 sccm while the flow-rate of the 2D EXSY experiments was limited to 180 sccm with the aim to enhance off diagonal peak intensities. Typical polarization values under such operating conditions were between 5-8%.

The 1D variable temperature CF-HP ^{129}Xe NMR experiments were conducted on an AvanceII 300 Bruker spectrometer at a frequency of 83.47 MHz in a double resonance wideline probe. Using a PEEK sample holder adapted for continuous gas flow, spectra were recorded using a single-pulse (SP) excitation with a length of 3 µs (ν_{nut} = 83.3 kHz) under static conditions. The freshly filled sample holder was evacuated at high vacuum at 350K for approximately 1 hour prior to being exposed an overpressure of inert gas and the Xe gas mixture, respectively. The hyperpolarized Xe gas peak was used as an internal standard (0 ppm) throughout. Samples were slowly cooled (~1 K/min) by 5 K intervals with a cooled steam of N_2 and allowed to equilibrate for 10 minutes at each temperature before data acquisition. Spectral deconvolution was performed using DMFit software.[58]

The 2D EXSY spectra were acquired using a standard three pulse sequence $(\pi/2-\tau_1-\pi/2-\tau_m-\pi/2-\tau_2)$ in TPPI mode. The pulse lengths were adjusted to match a nutation frequency of 62.5 kHz. Four transients were acquired for each τ_1 step to account for 180° phase shifts on the first and third impulse to reduce the influence of relaxation and pulse imperfections.[59] Mixing times (τ_m) varied between 200 µs and 2 s in order to explore the full range of exchange at various Xe loadings. A recycle delay of 2 seconds was used for all measurements. The number of data points was 1200 and 56 along the t_2 and t_1 domains, respectively. The cross-peaks (off-diagonal elements) were evaluated using a home-build MATLAB script that allowed for sectional integration and improved baseline correction.

CF-HP ^{129}Xe MAS spectroscopy. A 7 mm Xe-MASCAT probe[60] (Bruker) with modified 7 mm zirconia rotors was used for all VT CF-HP ^{129}Xe MAS NMR measurements. Spectra were obtained at various rotation frequencies (2.0–4.0 kHz) as the probe temperature is regulated by cold bearing and drive nitrogen gas streams. Higher rotation frequencies were necessary to achieve lower sample temperatures. The gas mixture containing the HP ^{129}Xe was vented to atmosphere wherein the gas flow is created by the pressure difference between the pumping cell (pressure maintained at 6.2 bar) and atmosphere (at rotor). Flow-rates were controlled using a teflon needle valve. SP ^{129}Xe NMR spectra were acquired with a pulse length 4.5 µs (ν_{nut} = 55.56 kHz) and recycle delays of 3-5 seconds (depending on the sample temperature). Lower sample temperatures required longer delays between scans as the replenishment rate of the gas decreased with cooling. While it was difficult to gauge the actual flow-rate, an initial change in the MAS rotation frequency (about −5 Hz) signaled adequate flow necessary for sufficient signal to noise. We attribute the change to added force along the magic angle introduced by the HP gas stream.

Solid-State ^{27}Al NMR Spectroscopy. All ^{27}Al solid-state experiments were measured under the same sample and probe setup as the CF-HP ^{129}Xe experiments. This time all the measurements were carried out at room temperature in the presence of only thermally polarized gas. A series of ^{27}Al and ^{129}Xe spectra were collected for a set of parameters for comparison. For the ^{27}Al experiments the probe was tuned to a Larmor frequency of 78.2 MHz. A HS-QCPMG (hyperbolic Secant Quadrupolar Carr-Purcell-Meiboom-Gill) pulse sequence was used to enhance the signal-to-noise ratio. Experiments were run using an HS converging sweep of 20 ms with a bandwidth of 1.4 MHz, centered at +/- 750 kHz and an rf field of 18 kHz to invert the population of the satellite transitions and enhance the central transition. For the QCPMG a $\pi/2$ and π central transition selective pulses with a nutation frequency of 55.56 kHz were employed. The recycle delay was set to 20 seconds. Chemical shifts are reported with respect to a solution of $AlCl_3$ adjusted to a pH of 1 with HCl. Spectral simulations of the static 1D ^{27}Al QCPMG NMR spectra were performed with SIMPSON. The fitted spectra were visually compared to the experimental one to judge for the accuracy of the fit.

Xe Physisorption. Physisorption experiments were carried out on an Autosorb 1 MP (Quantachrome) equipped with a Cryostat (Oxford). All samples were dried for 12 h at 110 °C under reduced pressure prior to the measurements. Isotherms were measured at 180 K, 195 K, 220 K and 255 K in a pressure range of 0 – 100 kPa.

Ab Initio Calculations. All calculations were performed using the CASTEP 17.2 DFT code.[61] As exchange-correlation functional the generalized gradient approximation functional Perdew-Burke-Ernzerhof (PBE) was used in combination with a semi-empirical dispersion correction of Tkatchenko and Scheffler.[62,63] The electronic density was calculated using pseudopotentials of 0.07 Å^{-1} within the Brillouin zone created by the Monkhorst-Pack algorithm.[64] Both parameters were sufficient to converge the ^{129}Xe chemical shielding to an accuracy method (GIPAW).[65,66] with a plane wave cutoff of 900 eV and a k point spacing. of 0.5 ppm. ^{129}Xe chemical shieldings (σ) were calculated using the gauge including projector augmented waves.

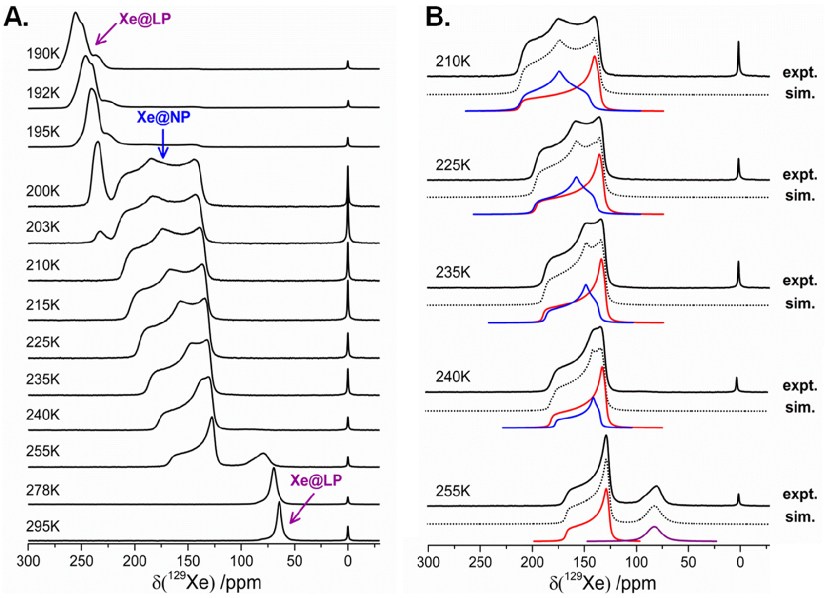

Figure 1. Temperature dependent HP ^{129}Xe NMR wideline spectra of xenon confined within the large-pore (Xe@LP) and narrow-pore (Xe@NP) environments of MIL-53(Al). (A.) Aquired spectra over a temperature range of 295 K – 190 K. (B) Deconvolutions of selected VT-HP ^{129}Xe NMR spectra with two distinct CSA pattern (NP$_1$: red; NP$_2$: blue) representing inequivalent Xe environments within the NP phase.

For transforming the isotropic shielding σ_{iso} into the isotropic chemical shift δ_{iso} equation (1) was used

$$(\delta_{iso} = (-\sigma_{ref} + \sigma_{iso})) \qquad (1)$$

with σ_{ref} determined to 5924 ppm by matching δ_{iso} of gaseous ^{129}Xe at 0 ppm to σ_{iso} values derived from calculations of a single Xe atom inside a cube with 15 Å axis length. All structure models for Xe adsorbed either in the LP or the NP phases were created using a 3 x 1 x 1 supercell to avoid overlap of the wave functions of Xe atoms within neighboring unit cells. Space- and linescans with step sizes of 0.5 Å in all directions were used to sample engery and CS for the structure models to account for the nonuniformity of the inner surfaces of the framework.

3. RESULTS AND DISCUSSION

Variable Temperature 1D NMR Experiments. Variable-temperature, static HP ^{129}Xe NMR experiments of dehydrated MIL-53(Al) were carried out under CF conditions at temperatures ranging from 190-298 K (**Figure 1A**). At ambient temperature a temperature-independent limiting ^{129}Xe chemical shift of about 64.8 ppm is observed. This suggests that the Xe density within the framework is sufficiently low to minimize Xe-Xe interactions, which is in accordance with Xe physisorption isotherms (**Figure S6**) resulting in Xe loadings below one Xe atom per unit cell for this temperature region. The symmetric nature and narrow linewidth of the ^{129}Xe NMR lineshape at 298 K indicates a rather homogeneous sampling of the LP conformation. This resonance shifts steadily downfield with cooling due to increasing Xe-Xe interactions, becoming slightly broader and more depressed when a second, axially-symmetric CSA broadened peak emerges downfield of the main resonance, signifying the beginning of the LP-to-NP structural transition at 255 K. Results indicate a full conversion between structures, as evidenced by the complete disappearance of the LP associated peak below 240 K.

The broad ^{129}Xe NMR lineshape, characteristic of Xe confined within the NP environment, further evolves with decreasing temperature, manifesting a distinct anisotropic character of the spin interactions with loading. The reappearance of a small isotropic peak (≈ 230 ppm) at 203 K indicates the reopening of the NP structure to the original LP conformation. Interestingly, the initial symmetry exhibited in Xe resonance upon the reopening of the MIL-53(Al) structure (at 200-203 K) is lost once the NP/LP bi-phase stability is removed. Below 195 K the spectral lineshape is best described by a superposition of at least three resonances indicating different degrees of reopening. We attribute this to a distribution of crystallite sizes as it is well known that the flexibility of the MIL-53 framework is sensitive to this parameter.[46]

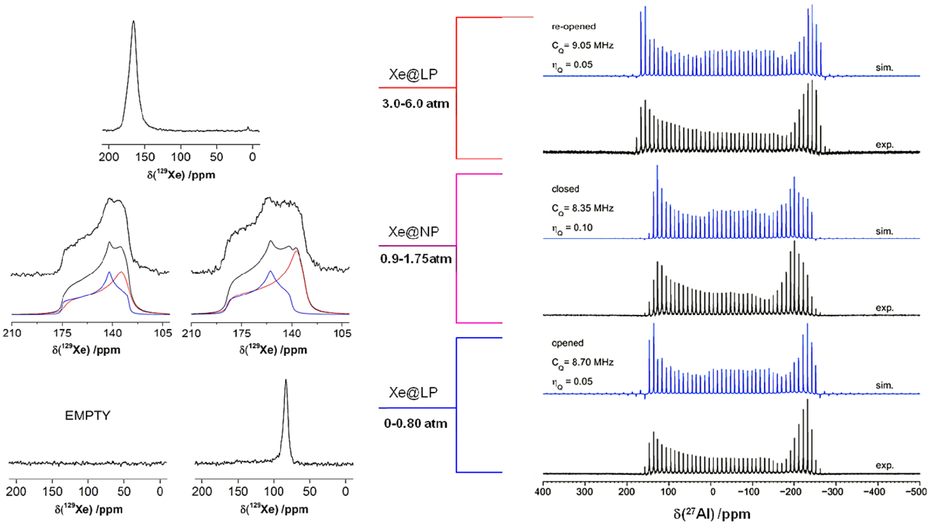

Figure 2. Pressure dependent static ^{129}Xe NMR spectra measured at 298K using thermally polarized Xe for various loading regimes: low (bottom spectra), intermediate (middle spectra), and high loading (top spectrum). Corresponding experimentally determined in situ ^{27}Al QCPMG static NMR spectra (black) were recorded for structure analysis. Simulated static powder pattern lineshapes (using SIMPSON) and the estimated quadrupolar coupling parameters are provided for comparison.

The LP associated ^{129}Xe isotropic shift changes drastically from ~ 90 ppm, just prior to closing (at 255 K), to about 233 ppm in its reopened state (at 200 K). This substantial change reflects the Xe density increasing from about 1.5 to 7.5 in the same temperature region (**Figure S6**).

As previously shown in literature,[56,57] the orientation dependence of the ^{129}Xe nuclear shielding tensor within the NP structure leads to complex spectra. The axially symmetric lineshape observed at 255 K is consistent with previously published results[56,57] and is characteristic of Xe in a spatially restricted environment at low loading. Despite the fact that Xe NMR powder pattern becomes progressively broader and more asymmetric with cooling, well-defined spectral features are identifiable due to the high crystallinity achieved in our MIL-53(Al) samples (**Figure S1**). The better resolved spectra for the NP phase allow for the identification of overlapping anisotropic chemical shift tensor elements that report on the local Xe shielding response to changing chemical and/or structural environments. Spectral analysis of the VT HP ^{129}Xe spectra between 240-210K shows evidence of two inequivalent adsorption sites within the NP structure with cooling (**Figure 1B**). Each spectrum is well characterized by two apparent lineshapes (NP_1 and NP_2 represented by the red and blue spectra in **Figure 1B**), the sums of which are found to be in good agreement with the experimental data.

The progression of the LP-to-NP structural transition, the occurrence of two distinctly different xenon environments (NP1 and NP2) as well as the reopening process over the explored temperature range are also observed in the temperature dependent ^{129}Xe NMR MAS spectra for hyperpolarized Xe adsorbed in MIL-53(Al) (**Figure 3, S3, S4**). The ^{129}Xe MAS spectra of Xe adsorbed within the large-pore (LP) structure of MIL-53(Al) is characterized by a single resonance, reflecting a narrow pore size distribution and isotropic shielding. However, the NP conformation is not initiated until 225 K, approximately 30 K lower than observed for static measurements. Reopening of the LP structure requires similarly reduced temperatures, signifying lower Xe adsorption. This is likely due to the reduced pressure of the gas mixture over the sample (roughly 1 atm) on account that the gas mixture is expanded before being exposed to the MASCAT probe. The LP/NP bi-phase stability is marked by the appearance of two separate, distinguishable peaks at 225 K, indicated by purple and red arrows in **Figure 3**. A shoulder emerges downfield of the NP state at 185 K, verifying the presence of the NP_2 predicted by deconvolution of the static spectra (**Figure 1B**). We attribute the lack of distinct separation of the NP_1 and NP_2 associated resonances to reduced Xe uptake under these experimental conditions.

In particular, for the wideline ^{129}Xe NMR experiments a clear trend for the intensity ratios of the spectral fingerprints for the NP_1 and NP_2 environments is observed as function of temperature. If the depolarization effects of

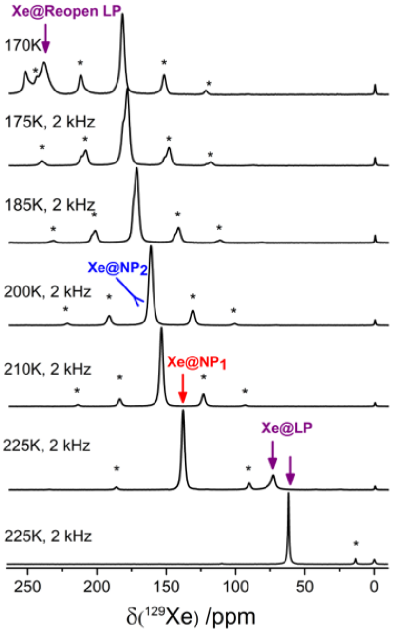

Figure 3. MAS spectra of xenon confined within MIL-53(Al). The purple, red and blue arrows within the spectra denote Xe associated with the LP, NP_1 and NP_2 environments, respectively. Spinning sidebands (ssb) are indicated by asterisks (to left and right of main resonance); rotational frequencies (ν_{rot}) ranged from 2 to 4 kHz.

hyperpolarized ^{129}Xe nuclei adsorbed in either of these two environments are similar, the intensity ratios are representative for the fraction of Xe atoms adsorbed in NP_1 or NP_2 environments. As a 2D exchange experiments suggest that all Xe species are in thermal equilibrium with each other (see below) the trend for the intensity ratios I_i as a function of temperature allows to derive the differences between the enthalpies and entropies of the NP_1 and NP_2 environments. According to:

$$\mu_{Xe@NP_1} = \mu_{Xe@NP_2} \tag{2}$$

$$\Delta\mu^{o}_{Xe@NP_1} - \Delta\mu^{o}_{Xe@NP_2} = \Delta H^{o} + T\Delta S^{o} = RT \cdot ln\frac{I_{Xe@NP2}}{I_{Xe@NP1}} \tag{3}$$

Fitting the trend of $ln\frac{I_{Xe@NP2}}{I_{Xe@NP1}} = \ln(k)$ versus 1/T shows that Xe adsorbed in the NP_2 environment is favored by 10.5 ± 0.6 kJ/mol. Its smaller entropy contribution (ΔS^{o} = -37.7 ± 2.7 J/mol) furthermore suggests that Xe atoms in this environment exihibit less degrees of freedom. These values may account for the fluctuation in the isosteric heat of adsorptions observed by Springuel-Huet et al.[56] for the narrow pore structure occupied by 1-3 atoms per unit cell.

Variable Pressure 1D NMR Experiments. As already shown by Springel-Huet et al.[56] LP-to-NP transition can also be triggered by the Xe pressure at RT and followed by ^{129}Xe NMR spectroscopy. The larger sample amounts for these kind of experiments allow to additionally acquire ^{27}Al NMR spectra which are sensitive to distortions at the AlO_6 octahedra and thus to the state of the framework. In this way the framework properties can be linked to the behavior of the adsorbed Xe atoms. The ^{129}Xe 1D NMR spectra collected for thermally polarized Xe over a pressure range of 0-6 atm (**Figures S5**) exhibit similar features observed for the temperature dependent HP ^{129}Xe NMR spectra (**Figure 1**). Up to 0.8 atm Xe pressure the LP form is stable. The CSA broadened static ^{129}Xe NMR spectra (0.8 – 1.75 atm), characteristic of the NP conformation, are found to be consistent with those observed using HP methods. However, results suggest that the reopening mechanism NP→LP (above 1.75 atm) proceeds at a lower adsorbed Xe density compared to variable temperature measurements—the ^{129}Xe isotropic peak for the reopened LP phase appears around 150 ppm (2.2 atm) instead 233 ppm (203 K). This is probably caused by the higher mobility of the framework at RT reducing the force needed to reopen MIL-53.

The ^{27}Al QCPMG NMR spectra recorded for the same Xe pressures can be grouped into three distinct regions (**Figure 2 right**). For the LP phase at low Xe loading a typical second order quadrupolar shape for the central transition with a coupling constant of C_Q = 8.70 MHz was observed. The transition to the NP phase is accompanied by a reduction of 0.3 MHz (C_Q = 8.4 MHz) and the reopened phase is characterized by an increase of C_Q to 9.1 MHz. Interestingly, despite evidence of a second NP phase indicated by static ^{129}Xe NMR measurements (**Figure 2 left**), no discernible change could be detected in the ^{27}Al QCPMG spectral profile, suggesting that this feature within the ^{129}Xe spectra is unique for different Xe-Xe interactions without changing the framework geometry. This may reflect additional structural strains imposed by the high Xe uptake. Similar trends have been observed for the adsorption of o-xylene in MIL-53(Al) using ^{27}Al MAS NMR.

Ab-initio ^{129}Xe chemical shift calculations. In order to develop a microscopic picture for the LP and NP phases and in particular for the NP_1 and NP_2 environments, we carried out quantumchemical ^{129}Xe CS calculations for a suite of structure models as function of Xe loading and position.

As a first step, in analogy to ref. 67, the expected CS for the limiting shift region was calculated. For this a single Xe atom was placed in the asymmetric unit of both volume. For each position both energy and CS were calculated. Considering that the Xe mobility within the channel is high enough to explore the pore space, the resulting spectral signature is derived by averaging all CS tensors according to a Boltzmann scheme (**Figure S7**). Exept for an overestimation of the isotropic shift, which is explained by relativistic effects not included in

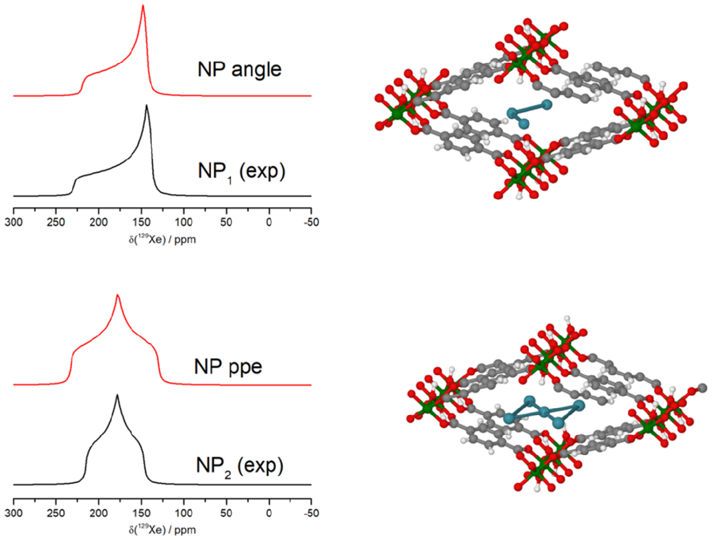

Figure 4. Comparison of measured CSA lineshapes between two distinct NP phases and calculated spectra from Xe atom arrangements within the NP form of MIL-53. The angled model represents NP1, while the ppe model corresponds to NP2, providing the best match to experimental data. The corresponding CSA values can be found in Table S10.

the calculations[67,68], the calculated spectral lineshape matches the experimental data for the LP phase at RT very well. In contrast, striking differences were observed for the NP form (255 K) with main deviations in both magnitude and sign of the CSA. As a consequence, only the ^{129}Xe NMR spectra of the LP phase above 255 K can be described without Xe-Xe interactions. For all simulations of the NP form Xe-Xe interactions play an important role to understand the spectral shape.

A row of geometrical arrangements of Xe atoms within one channel was created which accounts for the higher Xe denisty within the NP phase. The Xe density was adjusted around the experimental value of 2.6 Xe atoms/unit cell determined from Xe physisorption experiments (**Figure S6**). Variations in terms of position and densityof the Xe atoms were allowed to be able to model differences between the NP_1 and NP_2 environments as the lower energy and entropy of the latter one suggest a slightly denser packing. To keep the calculation time reasonable, the CS and energy. Sampling for the Xe clusters were reduced to line scans along the channel axis. Simulations for isolated Xe atoms, however, show that line scans and sampling the full free space (see above) led to almost identical spectral lineshapes.

In the case of the np-form the measured CSA parameters can be compared directly with the calculated chemical shift of an isolated Xe atom within the pore. The anisotropy values are comparable with the experimental data and the isotropic shift appears in the same region, respectively (Table S10).

Nevertheless, the anisotropy shows the wrong sign which hints for a higher influence of Xe-Xe interactions along the channel axis beside the effect of the Xe-wall interaction. This is comparable with the influence of chemical shielding calculations parallel and perpendicular to infinite channels as published by Jameson.[69].

To model these parameters with the correct signs and values, a number of Xe were arragend in differents manners to fulfill both conditions the Xe loading as well as the appearing Xe-Xe interactions. This modeling can be extended to the second CSA lineshape appearing at lower temperatures and higher Xe loading (**Figure 1B** at 210K), respectively. Arranging an infinite linear chain of Xe atoms along the pore with a distance of 4.4 Å results in positive δ_{aniso} comparable to the experiment at 255 K (**Table S10**). If the distance between the atoms is getting slightly larger, the interaction with the framework already dominates and values comparable to isolated atoms are calculated. On the other hand with smaller distances the shift increases to values much higher than measured. To refine the arrangement and model the experimental data as precise as possible, the calculated values were compared with a number of different configurations of Xe atoms. The resulting spectra and Xe atom arrangements can be seen in **Figure 4**. The best results for the NP 1 signal were obtained if the Xe atoms are slightly shifted of from the center of the pore axis (**Figure S8**). The higher isotropic shift of this model can be explained by the static character of the simulations. While here only single configuration were modeled, the real system posseses a high dynamic and the Xe moves fast through the pore.

At lower temperatures and high loading rates of Xe the NP2 CSA appears and can be correlated with models which appear with a different arrangement of Xe atoms. Here, the best overlapping with the experimental values could be achieved with a model of pairs of single Xe atoms in an alternate way (**Figure S9**). The shown results confirm, that the high density of Xe within the pores and therefore the higher frequency of Xe collisions along the pore create a CSA lineshape with high asymmetry. Hereby, both forms NP1 and NP2 coexist and can be still separated well on the timeframe of the NMR experiment. The isotropic chemical shift, which consistently exhibit the measured values, can be corrected by at least 42 ppm to lower values. This correction is necessary because it has been demonstrated in earlier works, that ab intio calculations of the ^{129}Xe isotropic shift is overestimated in case of MOFs.

^{129}Xe 2D EXSY Experiments. The experimentally observed LP/NP bi-stability within the Mil-53 framework is perhaps one of the most intriguing aspects of the breathing phenomenon. The question of whether both phases can coexist within a single crystallite has been highly debated in recent years. 2D exchange spectroscopy (EXSY) offers a simple method to map out chemical exchange pathways by establishing correlations between different adsorption sites. Such techniques are applied here to resolve diffusion processes within the MIL-53(Al) pore system using CF-HP ^{129}Xe NMR.

Initial 2D EXSY measurements were performed on the singular phase of both LP and NP structures to investigate changing dynamics at various loadings (**Figure S11**). The exchange between the different adsorption zones are denoted numerically from 1-4, represented by different colored boxes. In the absence of LP/NP phase coexistence, data suggests fast diffusion times (on the order of a few ms) between the bulk phase HP ^{129}Xe and the LP and NP absorption sites, indicating easy access to both environments independently. This is evidenced by the emergence of off-diagonal elements (cross-peaks) at mixing times as short as 5 ms. The existence of a butterfly pattern around the NP diagonal is characteristic of inter-particle exchange; Xe can diffuse between different NP crystallites within 20 ms. This inter-particle exchange remains evident even in the apparent absence of gas phase Xe↔NP cross peaks. The disappearance of cross peaks between the gas phase Xe and the NP environments (zone-3) at 200 K are damped, barely discernible from the noise due to a drop in polarization at the end of the experiment.

Figure S11 shows a series of 2D EXSY spectra for Xe adsorbed within both NP and LP conformations at 263 K for mixing times ranging from 2-250 ms; the sample is within the bi-stable region of the phase diagram under these experimental conditions. Similar to the VT CF-HP ^{129}Xe NMR spectra in **Figure 1A**, the two-phase region corresponding to the LP/NP coexistence was verified by the appearance of two inequivalent peaks in the 1D NMR spectra, as evident in the projections along each axis. Diagonal and cross peak intensities are a measure of the degree of chemical exchange between different adsorption sites and vary with the mixing time (τ_m). The absence of off diagonal peaks indicates the lack of exchange on the time scale of the experiment, while longer mixing times tend to reveal slower diffusion processes.

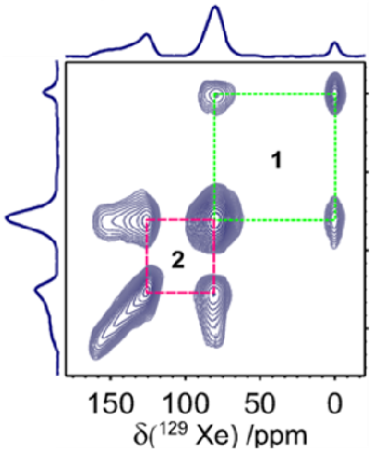

Figure 5. Static CF-HP ^{129}Xe 2D EXSY NMR spectrum of MIL-53(Al) recorded with a mixing time of 20 ms at 263 K. Here the bi-stability can be clearly seen, since only exchange between gas phase and LP-form (1) exists while NP-form is only accessible via LP-form (2).

The Xe spin system is composed of three groups of peaks along the diagonal corresponding to bulk phase Xe gas, LP and NP associated phases of Xe. Subtle structural features can be distinguished upon closer examination of the multiple exchange processes in **Figure S12**. Fresh HP xenon gas is able to diffuse freely from the gas phase to both LP and NP channels, though on different time scales. Considering zone-1, cross-peaks begin to manifest in a few milliseconds (**Figure 5**). Consistent with measurements performed on the sole LP structure at low loading, the large aperture of the LP channel allows easy access to gas phase Xe on the order of a few tens of ms. The elongated nature of the NP phase along the diagonal indicates is characteristic of CSA broadened lineshapes, indicating a lack of exchange between different types of NP adsorption sites at short mixing times below 50 ms. Interestingly, the off-diagonal elements of zone-2 become evident at τ_m< 1 ms, suggesting intimate connectivity of the LP and NP channels. Cross-peak intensities of both processes increase progressively with longer mixing times (**Figure S12B**). As shown in **Figures S12C** and S12**D**, slower diffusion processes become visible at $\tau_m \geq 100$ ms; NP to gas phase exchange is accompanied by the diffusion Xe between different orientations of the NP crystallite

Results suggest a unique hierarchical order of events. The rapid exchange between the LP and NP pore environments suggests that they coexist within a single crystallite. The lengthy diffusion times associated with the NP structure during the LP/NP bi-stability suggests longer diffusion paths compared to the LP structure. This is further substantiated by the short mixing times observed once the Mil-53(Al) has been fully converted the NP structure. Since CF-HP ^{129}Xe NMR methods are is not performed under equilibrium conditions, quantitative analysis of the exchange kinetics is therefore not possible. However, the integrated diagonal and cross-peak intensities of the 2D ^{129}Xe EXSY experiments are provided in **Figure s13** for review as the observed time-scales provide a qualitative picture of the series of events.

4. CONCLUSIONS

The phase behavior of MIL-53(Al) was studied in situ using CF-HP ^{129}Xe NMR methods combined with 27Al QCMPG NMR spectroscopy. The near complete removal of water from the pores led to better resolved ^{129}Xe static spectra, allowing us to identify key features of the breathing mechanism. Variable temperature studies under static and MAS conditions suggest the presence of multiple adsorption sites within the NP structure. Once the narrow pore structure begins to collapse, an axially symmetric lineshape, characteristic of a moderately filled channel possessing an elliptical cross section, is observed in the static ^{129}Xe NMR spectrum at 225 K. That this lineshape persists despite the increase in Xe adsorption at reduced temperatures is curious. The emergence of a second ^{129}Xe NMR lineshape that possesses chemical shift tensor elements that evolve with loading likely reflects the systematic increase in the Xe-Xe interactions with Xe uptake. The +47 ppm shift in the CSA tensor element is attributed to the pair-wise additive contribution due to higher instances of Xe_2 formation within the pores structure. This should not be surprising since the saturation Xe uptake within the NP structure is 2.5 atoms per unit cell according to adsorption isotherm measurements.

Recent work by Bousquet et al. investigating the thermodynamic multi-stability of intermediate structures have shown that variations in the network geometry (opening angle of the channel structure) can lead to differences in the Henry's law constant. Packing defects due to step-by-step filling can lead an irregular evolution in the saturation uptake as the guest is reorganized between multiple stable arrangements within the host volume. Monte-Carlo simulations performed by Bojan and Steele suggest that adsorption within pores with rectangular dimensions can be considered to be heterogeneous in nature; simulations indicate strong adsorption sites at the pore corners and much weaker interactions along the pore walls. As no discernible change in the ^{27}Al quadrupolar coupling constant or asymmetry parameter is observed within NP phase with loading, deviations in the pore geometry would have to be rather small. Thus, we tentatively attribute the overlapping anisotropic broadened lineshapes to packing defects brought on by the inhomogeneous distribution of adsorbed Xe within the NP structure.

2D ^{129}Xe EXSY experiments performed at various temperatures and loading conditions indicate full accessibility of the individual LP and NP structures with the gas phase Xe in the absence of LP/NP coexistence. That the exchange of Xe between two distinct environments within the NP structure (NP_1, NP_2) manifest on the order of 1 ms suggests intimate connectivity of the two domains and intra-particle exchange. Contrary to the stress-based model, which attributes the LP/NP bi-stability to distributions in the stress threshold due to variations in the crystalline size, our 2D EXSY measurements during the LP/NP phase coexistence indicates that two structures are in rather close proximity to each other; exchange is evident at mixing times < 1 ms. Interestingly, results suggest a longer diffusion path for Xe adsorbed within the NP structure when the LP structure is present in appreciable amounts. This is apparent by the lengthy experiment times necessary for interparticle exchange between multiple NP environments. Such behavior points to existence of both LP and NP structures within a single crystallite and demonstrates the cooperative nature of the LP→NP transition.

ASSOCIATED CONTENT

Supporting Information. Additional experimental details as described in the text. This material is available free of charge via the Internet at http://pubs.acs.org.

AUTHOR INFORMATION

Corresponding Author

* E-mail: juergen.senker@uni-bayreuth.de. Phone: +49 921 55 2532. Fax: +49 921 55 2788.

Author Contributions

The manuscript was written through contributions of all authors. All authors have given approval to the final version of the manuscript.

Notes

The authors declare no competing financial interest.

ACKNOWLEDGMENTS

The authors thank Dr. Tim Ahnfeldt for the synthesis of the discussed networks. We greatfully thank Prof. Dr. Josef Breu for access to the gas sorption instrument. We thank the

Deutsche Forschungsgesmeinschaft for the funding of this work in the course of SFB 840 and SE 1417/8-1.

ABBREVIATIONS

MOF, metal organic framework; NMR, nuclear magnetic resonance, LP, large pore; NP, narrow pore; SEOP, spin exchange optical pumping; Xe, xenon; CF, continuous flow; HP, hyperpolarized; VT, variable temperature; DFT, density functional theory; CSA; chemical shift anisotropy; MAS, magic angle spinning; QCPMG, VP, variable pressure; Carr-Purcell-Meiboom-Gill pulse sequence; ssb, spinning sidebands; EXSY, exchange spectroscopy.

REFERENCES

(1) Furukawa, H.; Cordova, K. E.; O'Keeffe, M.; Yaghi, O. M. The Chemistry and Applications of Metal-Organic Frameworks. *Science* **2013**, *341* (6149), 1230444. https://doi.org/10.1126/science.1230444.

(2) Tranchemontagne, D. J.; Mendoza-Cortés, J. L.; O'Keeffe, M.; Yaghi, O. M. Secondary Building Units, Nets and Bonding in the Chemistry of Metal–Organic Frameworks. *Chem. Soc. Rev.* **2009**, *38* (5), 1257. https://doi.org/10.1039/b817735j.

(3) Farha, O. K.; Eryazici, I.; Jeong, N. C.; Hauser, B. G.; Wilmer, C. E.; Sarjeant, A. A.; Snurr, R. Q.; Nguyen, S. T.; Yazaydın, A. Ö.; Hupp, J. T. Metal–Organic Framework Materials with Ultrahigh Surface Areas: Is the Sky the Limit? *J. Am. Chem. Soc.* **2012**, *134* (36), 15016–15021. https://doi.org/10.1021/ja3055639.

(4) Furukawa, H.; Ko, N.; Go, Y. B.; Aratani, N.; Choi, S. B.; Choi, E.; Yazaydin, A. Ö.; Snurr, R. Q.; O'Keeffe, M.; Kim, J.; Yaghi, O. M. Ultrahigh Porosity in Metal-Organic Frameworks. *Science (80-.).* **2010**, *329* (5990), 424–428. https://doi.org/10.1126/science.1192160.

(5) Banerjee, D.; Simon, C. M.; Elsaidi, S. K.; Haranczyk, M.; Thallapally, P. K. Xenon Gas Separation and Storage Using Metal-Organic Frameworks. *Chem* **2018**, *4* (3), 466–494. https://doi.org/10.1016/j.chempr.2017.12.025.

(6) Rowsell, J. L. C.; Yaghi, O. M. Effects of Functionalization, Catenation, and Variation of the Metal Oxide and Organic Linking Units on the Low-Pressure Hydrogen Adsorption Properties of Metal–Organic Frameworks. *J. Am. Chem. Soc.* **2006**, *128* (4), 1304–1315. https://doi.org/10.1021/ja056639q.

(7) Wang, Z.; Cohen, S. M. Postsynthetic Modification of Metal–Organic Frameworks. *Chem. Soc. Rev.* **2009**, *38* (5), 1315. https://doi.org/10.1039/b802258p.

(8) Farrusseng, D.; Canivet, J.; Quadrelli, A. Design of Functional Metal-Organic Frameworks by Post-Synthetic Modification. In *Metal-Organic Frameworks*; Wiley-VCH Verlag GmbH & Co. KGaA: Weinheim, Germany, 2011; pp 23–48. https://doi.org/10.1002/9783527635856.ch2.

(9) Ramsahye, N. A.; Trung, T. K.; Bourrelly, S.; Yang, Q.; Devic, T.; Maurin, G.; Horcajada, P.; Llewellyn, P. L.; Yot, P.; Serre, C.; Filinchuk, Y.; Fajula, F.; Férey, G.; Trens, P. Influence of the Organic Ligand Functionalization on the Breathing of the Porous Iron Terephthalate Metal Organic Framework Type Material upon Hydrocarbon Adsorption. *J. Phys. Chem. C* **2011**, *115* (38), 18683–18695. https://doi.org/10.1021/jp205369t.

(10) Tanabe, K. K. K.; Cohen, S. M. M. Postsynthetic Modification of Metal–Organic Frameworks—a Progress Report. *Chem. Soc. Rev.* **2011**, *40* (2), 498–519. https://doi.org/10.1039/C0CS00031K.

(11) Liu, H.; Zhao, Y.; Zhang, Z.; Nijem, N.; Chabal, Y. J.; Peng, X.; Zeng, H.; Li, J. Ligand Functionalization and Its Effect on CO_2 Adsorption in Microporous Metal-Organic Frameworks. *Chem. - An Asian J.* **2013**, *8* (4), 778–785. https://doi.org/10.1002/asia.201201081.

(12) Wittmann, T.; Siegel, R.; Reimer, N.; Milius, W.; Stock, N.; Senker, J. Enhancing the Water Stability of Al-MIL-101-NH_2 via Postsynthetic Modification. *Chem. - A Eur. J.* **2015**, *21* (1), 314–323. https://doi.org/10.1002/chem.201404654.

(13) Kitagawa, S.; Kitaura, R.; Noro, S. Functional Porous Coordination Polymers. *Angew. Chem. Int. Ed. Engl.* **2004**, *43* (18), 2334–2375. https://doi.org/10.1002/anie.200300610.

(14) Morris, R. E.; Wheatley, P. S. Gas Storage in Nanoporous Materials. *Angew. Chemie Int. Ed.* **2008**, *47* (27), 4966–4981. https://doi.org/10.1002/anie.200703934.

(15) Férey, G. Hybrid Porous Solids: Past, Present, Future. *Chem. Soc. Rev.* **2008**, *37* (1), 191–214. https://doi.org/10.1039/B618320B.

(16) Horcajada, P.; Serre, C.; Vallet-Regí, M.; Sebban, M.; Taulelle, F.; Férey, G. Metal-Organic Frameworks as Efficient Materials for Drug Delivery. *Angew. Chem. Int. Ed. Engl.* **2006**, *45* (36), 5974–5978. https://doi.org/10.1002/anie.200601878.

(17) Nguyen, J. G.; Tanabe, K. K.; Cohen, S. M. Postsynthetic Diazeniumdiolate Formation and NO Release from MOFs. *CrystEngComm* **2010**, *12* (8), 2335. https://doi.org/10.1039/c000154f.

(18) Keskin, S.; Kızılel, S. Biomedical Applications of Metal Organic Frameworks. *Ind. Eng. Chem. Res.* **2011**, *50* (4), 1799–1812. https://doi.org/10.1021/ie101312k.

(19) Umeyama, D.; Horike, S.; Inukai, M.; Hijikata, Y.; Kitagawa, S. Confinement of Mobile Histamine in Coordination Nanochannels for Fast Proton Transfer. *Angew. Chemie* **2011**, *123* (49), 11910–11913. https://doi.org/10.1002/ange.201102997.

(20) Czaja, A. U.; Trukhan, N.; Müller, U. Industrial Applications of Metal–Organic Frameworks. *Chem. Soc. Rev.* **2009**, *38* (5), 1284. https://doi.org/10.1039/b804680h.

(21) D'Alessandro, D.; Smit, B.; Long, J. Carbon Dioxide Capture: Prospects for New Materials. *Angew. Chemie Int. Ed.* **2010**, *49* (35), 6058–6082. https://doi.org/10.1002/anie.201000431.

(22) Li, J.-R. R. J. R.; Kuppler, R. J. J.; Zhou, H.-C. C. H. C. Selective Gas Adsorption and Separation in Metal-Organic Frameworks. *Chem. Soc. Rev.* **2009**, *38* (5), 1477–1504. https://doi.org/10.1039/b802426j.

(23) Yamada, T.; Otsubo, K.; Makiura, R.; Kitagawa, H. Designer Coordination Polymers: Dimensional Crossover Architectures and Proton Conduction. *Chem. Soc. Rev.* **2013**, *42* (16), 6655–6669. https://doi.org/10.1039/c3cs60028a.

(24) Li, S. L.; Xu, Q. Metal-Organic Frameworks as Platforms for Clean Energy. *Energy and Environmental Science*. The Royal Society of Chemistry 2013, pp 1656–1683. https://doi.org/10.1039/c3ee40507a.

(25) Gordon, J.; Kazemian, H.; Rohani, S. MIL-53(Fe), MIL-101, and SBA-15 Porous Materials: Potential Platforms for Drug Delivery. *Mater. Sci. Eng. C* **2015**, *47*, 172–179. https://doi.org/10.1016/J.MSEC.2014.11.046.

(26) Horcajada, P.; Gref, R.; Baati, T.; Allan, P. K.; Maurin, G.; Couvreur, P.; Férey, G.; Morris, R. E.; Serre, C. Metal-Organic Frameworks in Biomedicine. *Chemical Reviews*. February 8, 2012, pp 1232–1268. https://doi.org/10.1021/cr200256v.

(27) Chavan, S.; Vitillo, J. G.; Gianolio, D.; Zavorotynska, O.; Civalleri, B.; Jakobsen, S.; Nilsen, M. H.; Valenzano, L.; Lamberti, C.; Lillerud, K. P.; Bordiga, S. H_2 Storage in Isostructural UiO-67 and UiO-66 MOFs. *Phys. Chem. Chem. Phys.* **2012**, *14* (5), 1614. https://doi.org/10.1039/C1CP23434J.

(28) Si, X.; Jiao, C.; Li, F.; Zhang, J.; Wang, S.; Liu, S.; Li, Z.; Sun, L.; Xu, F.; Gabelica, Z.; Schick, C. High and Selective CO_2 Uptake, H_2 Storage and Methanol Sensing on the Amine-Decorated 12-Connected MOF CAU-1. *Energy Environ. Sci.* **2011**, *4* (11), 4522. https://doi.org/10.1039/c1ee01380g.

(29) Devic, T.; Horcajada, P.; Serre, C.; Salles, F.; Maurin, G.; Moulin, B.; Heurtaux, D.; Clet, G.; Vimont, A.; Grenèche, J.-M.; Ouay, B. Le; Moreau, F.; Magnier, E.; Filinchuk, Y.;

Marrot, J.; Lavalley, J.-C.; Daturi, M.; Férey, G. Functionalization in Flexible Porous Solids: Effects on the Pore Opening and the Host–Guest Interactions. *J. Am. Chem. Soc.* **2010**, *132* (3), 1127–1136. https://doi.org/10.1021/ja9092715.

(30) Horcajada, P.; Salles, F.; Wuttke, S.; Devic, T.; Heurtaux, D.; Maurin, G.; Vimont, A.; Daturi, M.; David, O.; Magnier, E.; Stock, N.; Filinchuk, Y.; Popov, D.; Riekel, C.; Férey, G.; Serre, C. How Linker's Modification Controls Swelling Properties of Highly Flexible Iron(III) Dicarboxylates MIL-88. *J. Am. Chem. Soc.* **2011**, *133* (44), 17839–17847. https://doi.org/10.1021/ja206936e.

(31) Wack, J.; Siegel, R.; Ahnfeldt, T.; Stock, N.; Mafra, L.; Senker, J. Identifying Selective Host–Guest Interactions Based on Hydrogen Bond Donor–Acceptor Pattern in Functionalized Al-MIL-53 Metal–Organic Frameworks. *J. Phys. Chem. C* **2013**, *117* (39), 19991–20001. https://doi.org/10.1021/jp4063252.

(32) Yuan, S.; Zou, L.; Li, H.; Chen, Y.-P.; Qin, J.; Zhang, Q.; Lu, W.; Hall, M. B.; Zhou, H.-C. Flexible Zirconium Metal-Organic Frameworks as Bioinspired Switchable Catalysts. *Angew. Chemie Int. Ed.* **2016**, *55* (36), 10776–10780. https://doi.org/10.1002/anie.201604313.

(33) Sharma, V. K.; Feng, M. Water Depollution Using Metal-Organic Frameworks-Catalyzed Advanced Oxidation Processes: A Review. *J. Hazard. Mater.* **2017**. https://doi.org/10.1016/j.jhazmat.2017.09.043.

(34) Coudert, F.-X.; Mellot-Draznieks, C.; Fuchs, A. H.; Boutin, A. Prediction of Breathing and Gate-Opening Transitions Upon Binary Mixture Adsorption in Metal–Organic Frameworks. *J. Am. Chem. Soc.* **2009**, *131* (32), 11329–11331. https://doi.org/10.1021/ja904123f.

(35) Wieme, J.; Lejaeghere, K.; Kresse, G.; Van Speybroeck, V. Tuning the Balance between Dispersion and Entropy to Design Temperature-Responsive Flexible Metal-Organic Frameworks. *Nat. Commun.* **2018**, *9* (1), 4899. https://doi.org/10.1038/s41467-018-07298-4.

(36) Ghysels, A.; Vanduyfhuys, L.; Vandichel, M.; Waroquier, M.; Van Speybroeck, V.; Smit, B. On the Thermodynamics of Framework Breathing: A Free Energy Model for Gas Adsorption in MIL-53. *J. Phys. Chem. C* **2013**, *117* (22), 11540–11554. https://doi.org/10.1021/jp311601q.

(37) Kitagawa, S.; Uemura, K. Dynamic Porous Properties of Coordination Polymers Inspired by Hydrogen Bonds. *Chem. Soc. Rev.* **2005**, *34* (2), 109–119. https://doi.org/10.1039/b313997m.

(38) Serre, C.; Millange, F.; Thouvenot, C.; Noguès, M.; Marsolier, G.; Louër, D.; Férey, G. Very Large Breathing Effect in the First Nanoporous Chromium(III)-Based Solids: MIL-53 or Cr III (OH)·{O 2 C–C 6 H 4 –CO 2 }·{HO 2 C–C 6 H 4 –CO 2 H} x ·H 2 O Y. *J. Am. Chem. Soc.* **2002**, *124* (45), 13519–13526. https://doi.org/10.1021/ja0276974.

(39) Loiseau, T.; Serre, C.; Huguenard, C.; Fink, G.; Taulelle, F.; Henry, M.; Bataille, T.; Férey, G. A Rationale for the Large Breathing of the Porous Aluminum Terephthalate (MIL-53) Upon Hydration. *Chem. - A Eur. J.* **2004**, *10* (6), 1373–1382. https://doi.org/10.1002/chem.200305413.

(40) Férey, G.; Serre, C. Large Breathing Effects in Three-Dimensional Porous Hybrid Matter: Facts, Analyses, Rules and Consequences. *Chem. Soc. Rev.* **2009**, *38* (5), 1380–1399. https://doi.org/10.1039/b804302g.

(41) Alhamami, M.; Doan, H.; Cheng, C. H. A Review on Breathing Behaviors of Metal-Organic-Frameworks (MOFs) for Gas Adsorption. *Materials*. April 2014, pp 3198–3250. https://doi.org/10.3390/ma7043198.

(42) Aguado, S.; Bergeret, G.; Pera-Titus, M.; Moizan, V.; Nieto-Draghi, C.; Bats, N.; Farrusseng, D. Guest-Induced Gate-Opening of a Zeolite Imidazolate Framework. *New J. Chem.* **2011**, *35* (3), 546–550. https://doi.org/10.1039/c0nj00836b.

(43) Nijem, N.; Wu, H.; Canepa, P.; Marti, A.; Balkus, K. J.; Thonhauser, T.; Li, J.; Chabal, Y. J. Tuning the Gate Opening Pressure of Metal-Organic Frameworks (MOFs) for the Selective Separation of Hydrocarbons. *J. Am. Chem. Soc.* **2012**, *134* (37), 15201–15204. https://doi.org/10.1021/ja305754f.

(44) Schneemann, A.; Bon, V.; Schwedler, I.; Senkovska, I.; Kaskel, S.; Fischer, R. A. Flexible Metal–Organic Frameworks. *Chem. Soc. Rev.* **2014**, *43* (16), 6062–6096. https://doi.org/10.1039/C4CS00101J.

(45) Liu, Y.; Her, J.-H.; Dailly, A.; Ramirez-Cuesta, A. J.; Neumann, D. A.; Brown, C. M. Reversible Structural Transition in MIL-53 with Large Temperature Hysteresis. *J. Am. Chem. Soc.* **2008**, *130* (35), 11813–11818. https://doi.org/10.1021/ja803669w.

(46) Boutin, A.; Coudert, F. X.; Springuel-Huet, M. A.; Neimark, A. V; Férey, G.; Fuchs, A. H. The Behavior of Flexible MIL-53(Al) upon CH4 and CO2adsorption. *J. Phys. Chem. C* **2010**, *114* (50), 22237–22244. https://doi.org/10.1021/jp108710h.

(47) Lieder, C.; Opelt, S.; Dyballa, M.; Henning, H.; Klemm, E.; Hunger, M. Adsorbate Effect on AlO4(OH)2 Centers in the Metal-Organic Framework MIL-53 Investigated by Solid-State NMR Spectroscopy. *J. Phys. Chem. C* **2010**, *114* (39), 16596–16602.

(48) Salles, F.; Bourrelly, S.; Jobic, H.; Devic, T.; Guillerm, V.; Llewellyn, P.; Serre, C.; Ferey, G.; Maurin, G. Molecular Insight into the Adsorption and Diffusion of Water in the Versatile Hydrophilic/Hydrophobic Flexible MIL-53(Cr) MOF. *J. Phys. Chem. C* **2011**, *115* (21), 10764–10776. https://doi.org/10.1021/jp202147m.

(49) Wack, J.; Siegel, R.; Ahnfeldt, T.; Stock, N.; Mafra, L.; Senker, J. Identifying Selective Host-Guest Interactions Based on Hydrogen Bond Donor-Acceptor Pattern in Functionalized Al-MIL-53 Metal-Organic Frameworks. *J. Phys. Chem. C* **2013**, *117* (39), 19991–20001. https://doi.org/10.1021/jp4063252.

(50) Boutin, A.; Couck, S.; Coudert, F.-X.; Serra-Crespo, P.; Gascon, J.; Kapteijn, F.; Fuchs, A. H.; Denayer, J. F. M. Thermodynamic Analysis of the Breathing of Amino-Functionalized MIL-53(Al) upon CO2 Adsorption. *Microporous Mesoporous Mater.* **2011**, *140* (1–3), 108–113. https://doi.org/http://dx.doi.org/10.1016/j.micromeso.2010.07.009.

(51) Beurroies, I.; Boulhout, M.; Llewellyn, P. L.; Kuchta, B.; Férey, G.; Serre, C.; Denoyel, R. Using Pressure to Provoke the Structural Transition of Metal-Organic Frameworks. *Angew. Chemie - Int. Ed.* **2010**, *49* (41), 7526–7529. https://doi.org/10.1002/anie.201003048.

(52) Neimark, A. V; Coudert, F.-X.; Boutin, A.; Fuchs, A. H. Stress-Based Model for the Breathing of Metal-Organic Frameworks. *J. Phys. Chem. Lett.* **2010**, *1* (1), 445–449. https://doi.org/10.1021/jz9003087.

(53) Boutin, A.; Springuel-Huet, M. A.; Nossov, A.; Gédéon, A.; Loiseau, T.; Volkringer, C.; Férey, G.; Coudert, F. X.; Fuchs, A. H. Breathing Transitions in MIL-53(A1) Metal-Organic Framework upon Xenon Adsorption. *Angew. Chemie - Int. Ed.* **2009**, *48* (44), 8314–8317. https://doi.org/10.1002/anie.200903153.

(54) Hamon, L.; Llewellyn, P. L.; Devic, T.; Ghoufi, A.; Clet, G.; Guillerm, V.; Pirngruber, G. D.; Maurin, G.; Serre, C.; Driver, G.; Van Beek, W.; Jolimaître, E.; Vimont, A.; Daturi, M.; Férey, G. Co-Adsorption and Separation of CO2-CH4mixtures in the Highly Flexible MIL-53(Cr) MOF. *J. Am. Chem. Soc.* **2009**, *131* (47), 17490–17499. https://doi.org/10.1021/ja907556q.

(55) Triguero, C.; Coudert, F.-X.; Boutin, A.; Fuchs, A. H.; Neimark, A. V. Mechanism of Breathing Transitions in Metal–Organic Frameworks. *J. Phys. Chem. Lett.* **2011**, *2* (16), 2033–2037. https://doi.org/10.1021/jz2008769.

(56) Springuel-Huet, M.-A.; Nossov, A.; Adem, Z.; Guenneau, F.; Volkringer, C.; Loiseau, T.; Férey, G.; Gédéon, A.; Ferey, G.; Gedeon, A. 129 Xe NMR Study of the Framework Flexibility of the Porous Hybrid MIL-53(Al). *J. Am. Chem. Soc.* **2010**, *132* (33), 11599–11607. https://doi.org/10.1021/ja103105y.

(57) Giovine, R.; Volkringer, C.; Springuel-Huet, M.-A.; Nossov, A.; Blanc, F.; Trébosc, J.; Loiseau, T.; Amoureux, J.-P.; Lafon, O.; Pourpoint, F. Study of Xenon Mobility in the Two Forms of MIL-53(Al) Using Solid-State NMR Spectroscopy. *J. Phys. Chem. C* **2017**, *121* (35), 19262–19268. https://doi.org/10.1021/acs.jpcc.7b06006.

(58) Massiot, D.; Fayon, F.; Capron, M.; King, I.; Le Calvé, S.; Alonso, B.; Durand, J.-O.; Bujoli, B.; Gan, Z.; Hoatson, G. Modelling One- and Two-Dimensional Solid-State NMR Spectra. *Magn. Reson. Chem.* **2002**, *40* (1), 70–76. https://doi.org/10.1002/mrc.984.

(59) Senker, J.; Seyfarth, L.; Voll, J. Determination of Rotational Symmetry Elements in NMR Crystallography. *Solid State Sci.* **2004**, *6* (10), 1039–1052. https://doi.org/10.1016/j.solidstatesciences.2004.07.001.

(60) Hunger, M.; Horvath, T. A New MAS NMR Probe for in Situ Investigations of Hydrocarbon Conversion on Solid Catalysts under Continuous-Flow Conditions. *J. Chem. Soc. Chem. Commun.* **1995**, No. 14, 1423–1424.

(61) Clark, S. J. J.; Segall, M. D. D.; Pickard, C. J. J.; Hasnip, P. J. J.; Probert, M. I. J. I. J.; Refson, K.; Payne, M. C. C. First Principles Methods Using CASTEP. *Zeitschrift für Krist. - Cryst. Mater.* **2005**, *220* (5/6), 567–570. https://doi.org/10.1524/zkri.220.5.567.65075.

(62) Perdew, J. P.; Burke, K.; Ernzerhof, M. Generalized Gradient Approximation Made Simple. *Phys. Rev. Lett.* **1996**, *77* (18), 3865–3868. https://doi.org/10.1103/PhysRevLett.77.3865.

(63) Tkatchenko, A.; Scheffler, M. Accurate Molecular van Der Waals Interactions from Ground-State Electron Density and Free-Atom Reference Data. *Phys. Rev. Lett.* **2009**.

(64) Monkhorst, H. J.; Pack, J. D. Special Points for Brillouin-Zone Integrations. *Phys. Rev. B* **1976**, *13* (12), 5188–5192. https://doi.org/10.1103/PhysRevB.13.5188.

(65) Yates, J. R. R.; Pickard, C. J. J.; Mauri, F. Calculation of NMR Chemical Shifts for Extended Systems Using Ultrasoft Pseudopotentials. *Phys. Rev. B* **2007**, *76* (2), 024401. https://doi.org/10.1103/PhysRevB.76.024401.

(66) Pickard, C. J.; Mauri, F. All-Electron Magnetic Response with Pseudopotentials: NMR Chemical Shifts. *Phys. Rev. B* **2001**, *63* (24), 245101. https://doi.org/10.1103/PhysRevB.63.245101.

(67) Kemnitzer, T. W.; Tschense, C. B. L.; Wittmann, T.; Rössler, E. A.; Senker, J. Exploring Local Disorder within CAU-1 Frameworks Using Hyperpolarized 129 Xe NMR Spectroscopy. *Langmuir* **2018**, *34* (42), 12538–12548. https://doi.org/10.1021/acs.langmuir.8b02592.

(68) Trepte, K.; Schaber, J.; Schwalbe, S.; Drache, F.; Senkovska, I.; Kaskel, S.; Kortus, J.; Brunner, E.; Seifert, G. The Origin of the Measured Chemical Shift of 129 Xe in UiO-66 and UiO-67 Revealed by DFT Investigations. *Phys. Chem. Chem. Phys.* **2017**, *108*, 4751–4758. https://doi.org/10.1039/C7CP00852J.

(69) Jameson, C. J.; de Dios, A. C. Xe Nuclear Magnetic Resonance Line Shapes in Nanochannels. *J. Chem. Phys.* **2002**, *116* (9), 3805–3821. https://doi.org/10.1063/1.1446424.

Probing the Bi-stability of MIL-53(Al) via 1D and 2D NMR Spectroscopy Employing Hyperpolarized ^{129}Xe and Quantum Mechanical Simulations

Tobias W. Kemnitzer,[†] Caroline D. Keenan,[‡] Renee Siegel,[†], Ernst Roessler[§] and Juergen Senker[†]

[‡]Chemistry Department, Carson-Newman University, Jefferson City, Tennessee 37830, USA
[†]Inorganic Chemistry III, Universität Bayreuth, Bayreuth 95447, Germany
[§]Experimental Physics II, Universität Bayreuth, Bayreuth 95447, Germany

X-ray powder diffraction of Mil-53(Al)

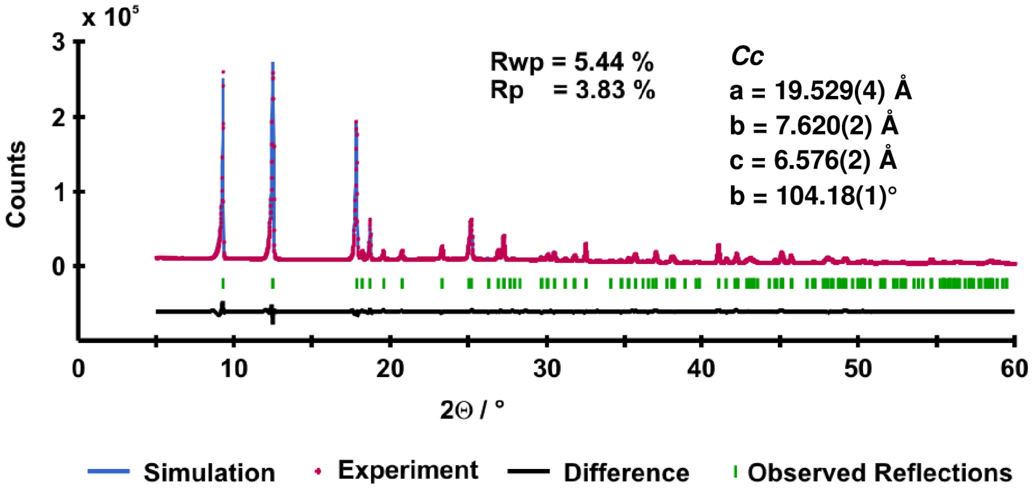

Figure S1. Rietveld profile plot of MIL-53(Al) after activation.

Solid-state NMR spectroscopic characterization of MIL-53(Al)

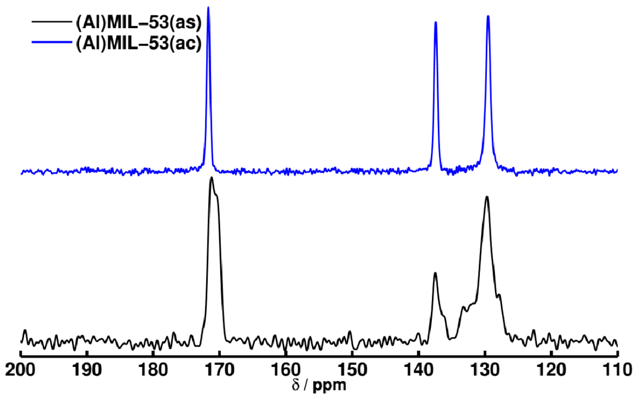

Figure S2. ^{13}C MAS solid-state NMR of MIL-53(as) (black) and the activated form of MIL-53 (blue).

Variations in the HP ^{129}Xe MAS lineshapes with cooling.

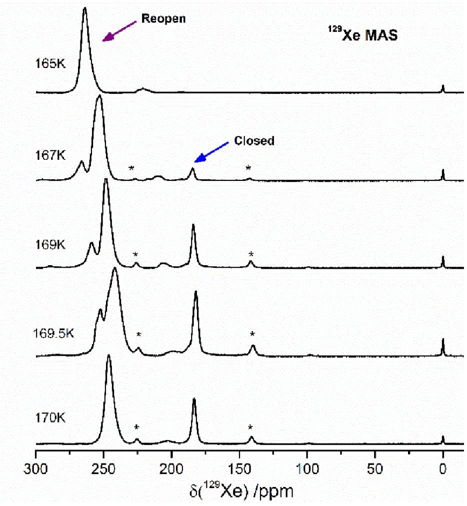

Figure S3. Deconvolution of the ^{129}Xe MAS spectra at temperatures ranging from 175 to 190 K. The emergence of a secondary peak, downfield of the main peak suggests the formation of a secondary environment within the NP conformation.

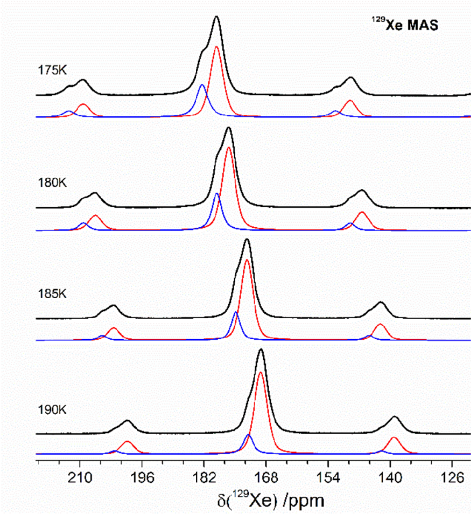

Figure S4. Deconvolution of the ^{129}Xe MAS spectra at temperatures ranging from 175 to 190 K. The emergence of a secondary peak, downfield of the main peak suggests the formation of a secondary environment within the NP conformation.

Development of the ^{129}Xe thermally polarized NMR lineshape with pressure.

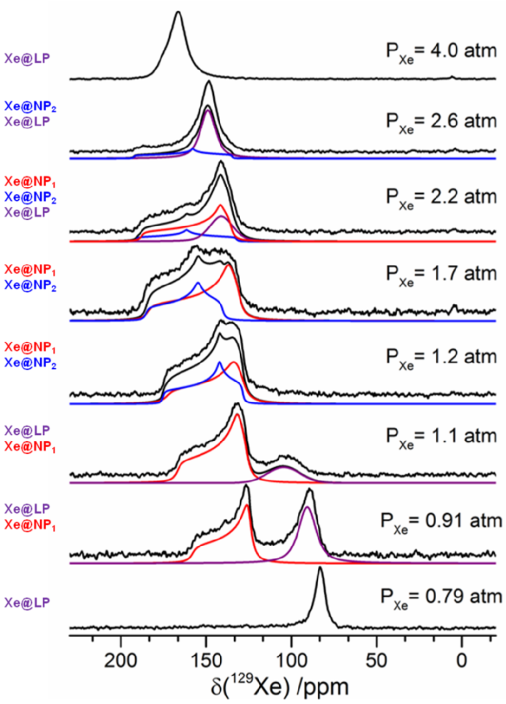

Figure S5. Deconvoluted thermally polarized ^{129}Xe spectra as a function of Xe overpressure (P_{Xe}). General trends are consistent to those observed for VT, HP ^{129}Xe NMR. However, contrary to HP ^{129}Xe static and MAS spectra, the reopening of the LP state does not appear to emerge as a distinctly separate phase.

Xenon physisorption experiments for calculation of network loading.

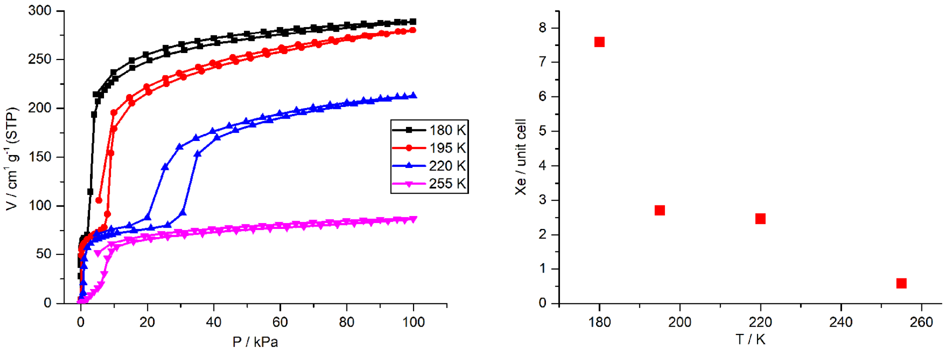

Figure S6. Left: Xe physisorption isotherms of MIL-53. Right: Calculated Xe loading per unit cell of MIL-53 for a partial pressure of 6 kPa according to the theoretical pressure of Xe within the NMR experiment.

Ab-initio calculations to model the ^{129}Xe chemical shift inside MIL-53.

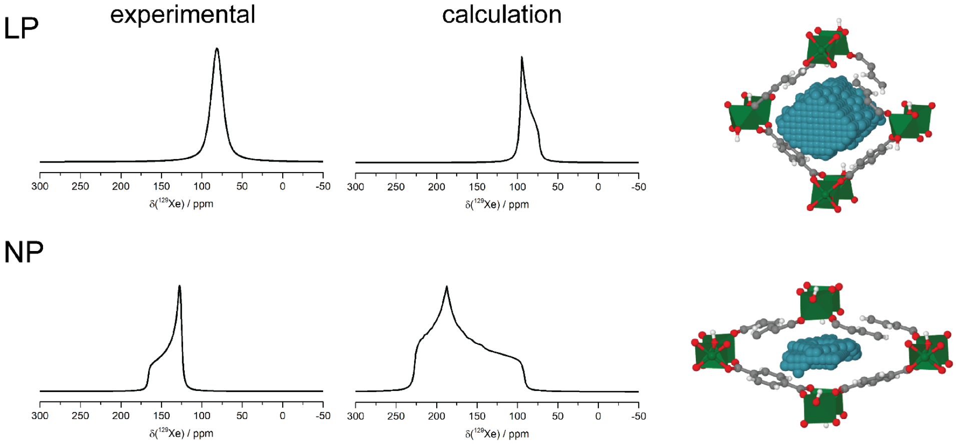

Figure S7. Grid of possible Xe positions (teal colored atoms) within the NP and LP form of MIL-53 and resulting ^{129}Xe NMR spectra. For each position the ^{129}Xe chemical shift as well as the correlated energy was calculated and a resulting Boltzmann weighted shift was calculated, this is compared with the experimental obtained CSA lineshapes.

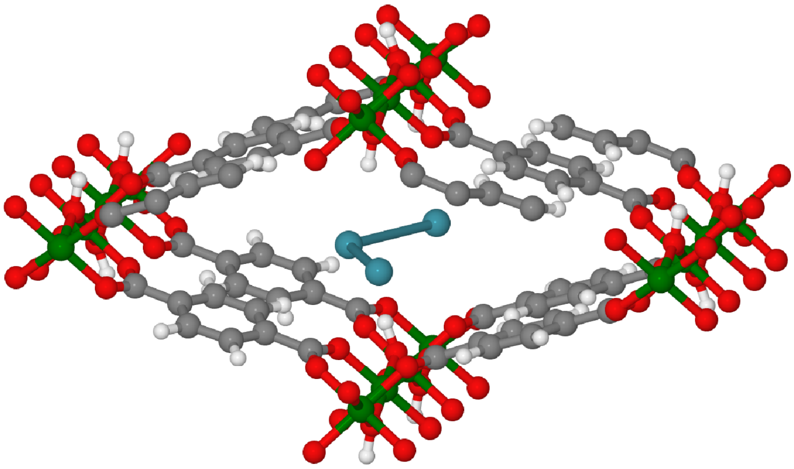

Figure S8. Configuration of a row of Xe atoms (teal) within the NP form of MIL-53 which are slightly shifted from the center of the pore along the a-axis (pore axis). The picture represents an infinite long chain of Xe atoms.

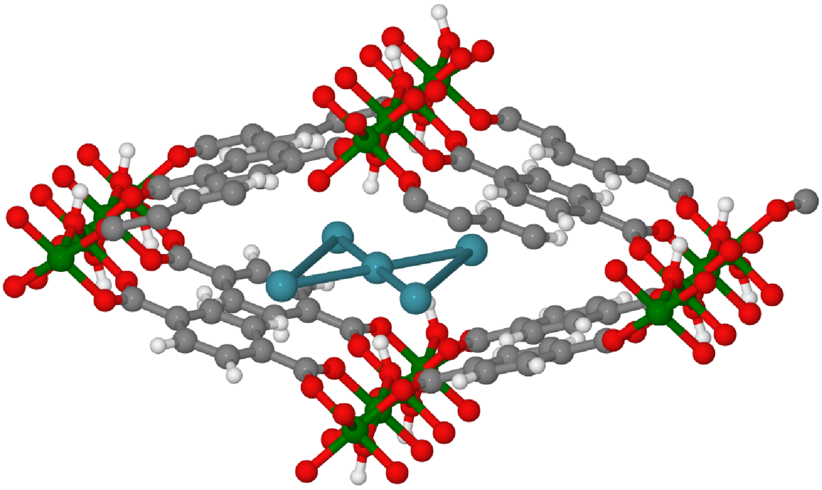

Figure S9. Configuration of a number of Xe atoms (teal) within the NP form of MIL-53 as a representation for the infinite long pore channels. Here the configurations changes between pairs of Xe atoms arranged perpendicular to the a-axis (pore axis) and a single Xe atom in the center of the pore.

Table S10: CSA paramters of static ^{129}Xe spectra (exp) and ab-initio simulations. For the experimental data the limit values of all forms were taken into account.

Configuration	δ_{iso} / ppm	δ_{aniso} / ppm	η
LP (exp)	65	-	-
NP1 (exp)	170	49	0.1
NP2 (exp)	180	35	0.9
LP isolated	89	15	0.1
NP isolated	169	-77	0.512
NP line	235	56	0.44
NP angle	328	59	0.1
NP ppe	262	53	0.9

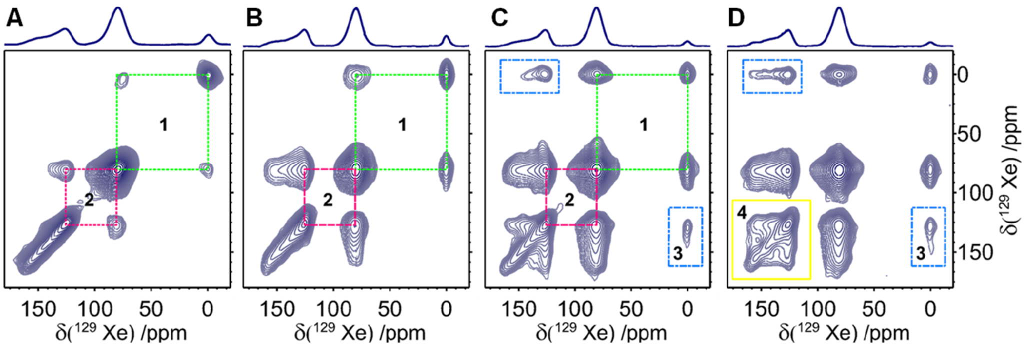

Figure S11. 2D CF-HP ^{129}Xe EXSY spectra obtained under static conditions. Measurements were performed at 263 K with various mixing times: A) 1 ms, B) 20 ms, C) 100 ms, and C) 250 ms. Zones 1-4 describe different exchange processes between three distinct sites. As shown in the projections along the axis, the smallest symmetric peak corresponds to the gas phase Xe, the resonance directly downfield of it is Xe@LP, while the axially symmetric lineshape is Xe@NP.

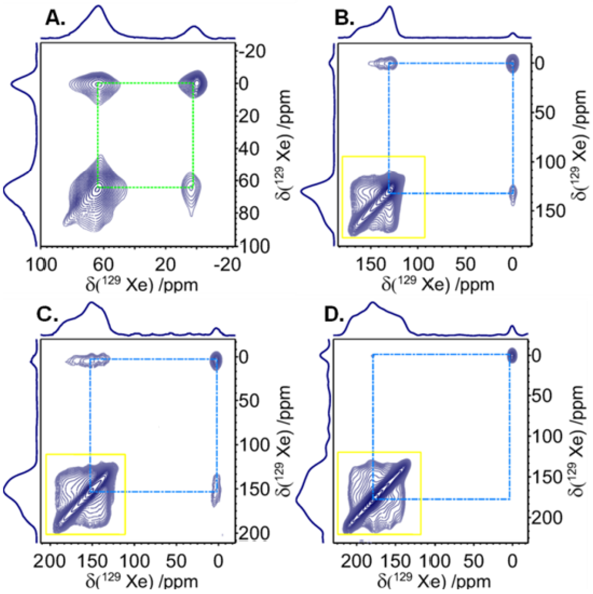

Figure S12. Static CF-HP ^{129}Xe 2D EXSY NMR spectra of MIL-53(Al) recorded with a mixing time of 20 ms at various temperatures: A) 298 K, B) 252 K, C) 225 K, and D) 200 K.

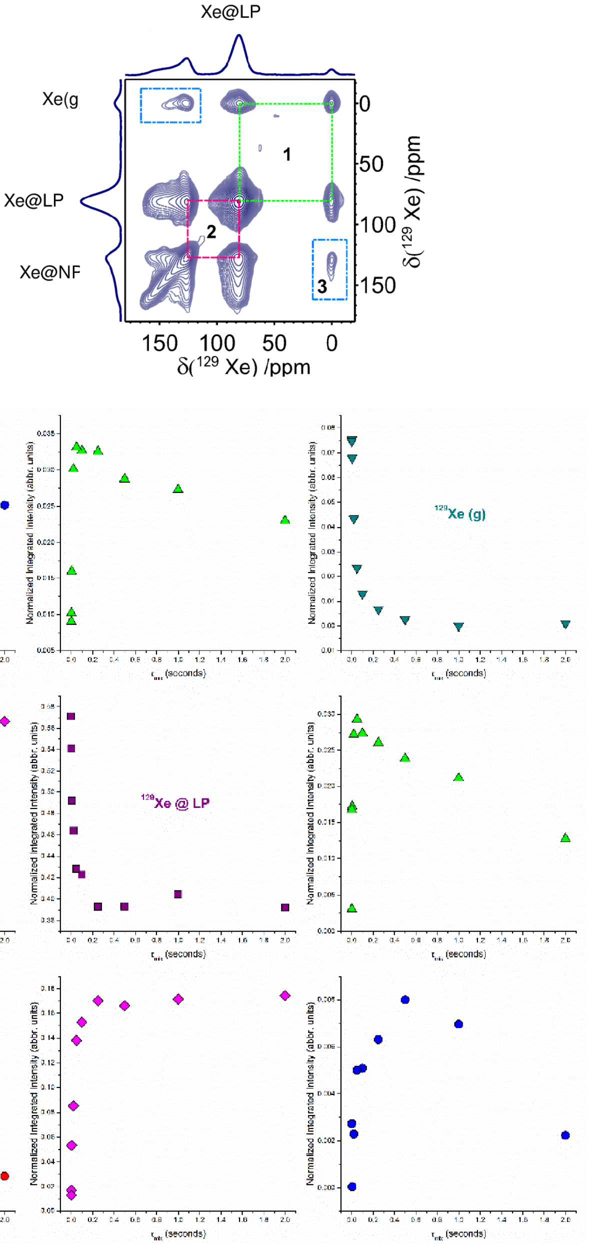

Figure S13. The normalized, integrated diagonal and cross-peak intensities of the 2D ^{129}XeEXSY spectrum shown in Figure 5 of the main text, with mixing times ranging from 2-250 ms. All three environments (bulk ^{129}Xe gas, LP, and NP) were maintained through the course of the experiment; measurements were performed at 263 K.

6. Publikationsliste

1. Ruckdeschel, P.; Kemnitzer, T. W.; Nutz, F. A.; Senker, J.; Retsch, M. Hollow Silica Sphere Colloidal Crystals: Insights into Calcination Dependent Thermal Transport. *Nanoscale* **2015**, *7* (22), 10059–10070. DOI: 10.1039/c5nr00435g

2. Kemnitzer, T. W.; Tschense, C. B. L.; Wittmann, T.; Rössler, E. A.; Senker, J. Exploring Local Disorder within CAU-1 Frameworks Using Hyperpolarized 129 Xe-NMR Spectroscopy. *Langmuir* **2018**, *34* (42), 12538–12548. DOI: 10.1021/acs.langmuir.8b02592

3. Stäglich, R.; Kemnitzer, T. W.; Harder, M. C.; Schmutzler, A.; Meinhart, M.; Keenan, C. D.; Rössler, E. A.; Senker, J. Portable Hyperpolarized Xe-129 Apparatus with Long-Time Stable Polarization Mediated by Adaptable Rb Vapor Density. *J. Phys. Chem. A* **2022**, *126* (16), 2578–2589. DOI: 10.1021/acs.jpca.2c00891

4. Kemnitzer, T. W.; Keenan, C. D.; Siegel R.; Ahnfeldt, T.; Rössler E. A.; Senker, J.; Probing the Structural Bi-stability during Gate-Opening of MIL-53(Al) via Hyperpolarized ^{129}Xe and Chemical Modelling. to be submitted

Nicht in diese Dissertation aufgenommene Publikationen:

5. Bärwinkel, K.; Herling, M. M.; Rieß, M.; Sato, H.; Li, L.; Avadhut, Y. S.; Kemnitzer, T. W.; Kalo, H.; Senker, J.; Matsuda, R.; Kitagawa, S.; Breu, J. Constant Volume Gate-Opening by Freezing Rotational Dynamics in Microporous Organically Pillared Layered Silicates. *J. Am. Chem. Soc.* **2017**, *139* (2), 904–909. DOI: 10.1021/jacs.6b11124

Eidesstattliche Versicherungen und Erklärungen

(§ 8 Satz 2 Nr. 3 PromO Fakultät)

Hiermit versichere ich eidesstattlich, dass ich die Arbeit selbstständig verfasst und keine anderen als die von mir angegebenen Quellen und Hilfsmittel benutzt habe (vgl. Art. 64 Abs. 1 Satz 6 BayHSchG).

(§ 8 Satz 2 Nr. 3 PromO Fakultät)

Hiermit erkläre ich, dass ich die Dissertation nicht bereits zur Erlangung eines akademischen Grades eingereicht habe und dass ich nicht bereits diese oder eine gleichartige Doktorprüfung endgültig nicht bestanden habe.

(§ 8 Satz 2 Nr. 4 PromO Fakultät)

Hiermit erkläre ich, dass ich Hilfe von gewerblichen Promotionsberatern bzw. –vermittlern oder ähnlichen Dienstleistern weder bisher in Anspruch genommen habe noch künftig in Anspruch nehmen werde.

(§ 8 Satz 2 Nr. 7 PromO Fakultät)

Hiermit erkläre ich mein Einverständnis, dass die elektronische Fassung der Dissertation unter Wahrung meiner Urheberrechte und des Datenschutzes einer gesonderten Überprüfung unterzogen werden kann.

(§ 8 Satz 2 Nr. 8 PromO Fakultät)

Hiermit erkläre ich mein Einverständnis, dass bei Verdacht wissenschaftlichen Fehlverhaltens Ermittlungen durch universitätsinterne Organe der wissenschaftlichen Selbstkontrolle stattfinden können.

………………………………………………………………………………….

Ort, Datum, Unterschrift